SLITS IN PARABOLIC REFLECTOR ANTENNAS

A thesis submitted for the Degree

of

Doctor of Philosophy in Electrical Engineering

by

E.J. Hamilton, B.E. (Hons)

University of Canterbury

1981

ABSTRACT

Diffraction by slits and scattering by antennas with slits in their reflectors are investigated.

Attempts are made to engineer nulls in the rear radiation patterns of relatively small (ten wavelength) aperture reflector antennas by changing the size and position of slits in the reflectors.

Diffraction by sharp edges are considered using a modified form of the Geometrical Theory of Diffraction and also reflector surface currents are studied from an integral equation standpoint via the Method of Moments and hybridised forms of the Method of Moments.

Both amplitude and phase of electromagnetic fields are measured by the use of a Microwave Homodyne Detection System, and experimental results are presented along with theoretical results.

ACKNOWLEDGEMENTS

I am pleased to acknowledge the contributions of the people who have helped in the production of this thesis.

People to whom special thanks must go to are my Supervisor, Dr. V. Kerdemelidis (Basil) who gave me enough rope to hang myself on occasions, but also gave much useful guidance; Mr. A. Vernon, who constructed, repaired and maintained much of the experimental range equipment; Professor Ray J. King, who gave the groundwork on Homodyne Detection Systems; the students who shared my room, (Ern Brown, Michael Hamilton-Jenkins, Tom Halliburton, Trevor Lord) and gave me space to experiment; Mrs Gloria Nicol for her typing of a sometimes unintelligible manuscript; John Stark, my running partner, who served to keep me mentally and physically healthy and of course my wife, Maggie, who gave continuous support and showed great patience. This work is as much a result of her efforts as of mine.

TABLE OF CONTENTS

CHAPTER ONE:

INTRODUCTION

'If a man will begin with certainties, he shall end in doubts, but if he will be content, to begin with doubts, he shall end in certainties.'

Francis Bacon, 1561-1626

Microwaves, with a wavelength of less than a metre and greater than a millimetre, exhibit many of the properties of visible light. Microwave reflector antennas are analogous to mirrors, and can produce pencil beams of electromagnetic energy. Microwave antennas, however, produce sidelobes and backlobes because of the finite size of their reflectors. Much work has been done to analyse microwave reflector antennas, which really only came into general use during the Second World War, (Silver, 1949).

Work is continuing on receiving antennas on reducing the effects of interference from non-isotropic sources. In this thesis we will study the problems of placing nulls in the rear field of the parabolic cylinder reflector antenna by the placement of small slits in the reflector, following the suggestion of Sletten and Blacksmith, (Sletten and Blacksmith, 1965). These slits are located so as to allow leakage into the rear field in antiphase to the field diffracted around the edges of the reflector.

Some workers have investigated modification of the reflector edges, i.e., (Cornbleet, 1967), (Lewin, 1972), (Bucci and Franceschetti, 1980), while others have suggested placing screens behind the reflector, (Corona et al, 1971).

Progress in analysis of scattering by reflector antennas had been stilted due to the lack of exact solution techniques, but the Geometrical Theory of Diffraction (GTD), introduced by Keller, (Keller, 1957) has led to many useful approximations.

Solution by Integral Equation techniques were limited to the most simple cases, until the Method of Moments approximation was introduced in the early sixties, i.e., (Mei and Van Bladel, 1963b), (Richmond, 1965), (Harrington, 1967), (Harrington, 1968), (Waterman, 1965).

In this thesis we will apply both GTD and the Method of Moments to the reflector problem, and modifications to both will be introduced.

The thesis is laid out in the following manner:

Chapter 2 is devoted to introducing background material on electromagnetic propagation, and expands upon exact solutions, GTD, Physical Optics and the Method of Moments. The diffraction of an electromagnetic wave by a half plane is used as a reference example. The information in Chapter 2 is applied to the problem of the inclined plane slit in Chapter 3. Each approach in Chapter 2 is applied and compared with experimental results. We see where methods are relevant and how plane inclination affects the electromagnetic properties of the slit.

In Chapter 4 we consider the scattering from a parabolic reflector, with and without slits. We repeat the procedure of Chapter 3, comparing theoretical results with experiment.

In Chapter 5 we discuss Homodyne Detection, (King, 1978), and how it is applied to measuring both the amplitude and phase of the electromagnetic field transmitted through a slit and scattered off a reflector antenna. Information on the experiments undertaken in the course of this project is included in this chapter.

Finally in Chapter 6 we present conclusions on the work in the preceding chapters.

One paper has been accepted for publication, based on some of the topics in this thesis, (Hamilton and Kerdemelidis, 1981), and has been included as an Appendix. Two further papers are in preparation.

CHAPTER TWO: BACKGROUND

'He that talketh what he knoweth, will also talk what he knoweth not.'

Francis Bacon, 1561-1626.

2.1 INTRODUCTION

In this chapter we will study the theories behind the propagation of Electromagnetic fields. In the first part there is a short study of the equations of propagation followed by a look at the Separation of Variables Technique of solution of these equations.

Diffraction by conducting edges is then examined, with the specific example of diffraction by a semi-infinite half plane, of a cylindrical source wave. This example is used to introduce High Frequency concepts, leading to various forms of the Geometrical Theory of Diffraction.

Another approach to diffraction is to consider the currents set up at and about the diffracting edges of the obstacle. This introduces a description of Physical Optics and edge currents. We eventually look into the calculation of surface currents around diffracting edges and surfaces by the Method of Moments Technique.

2.2 ELECTROMAGNETIC FIELDS

Electromagnetic field strength can be expressed in terms of magnetic vector potentials and electric vector potentials, which are obtained from the source currents. Define a magnetic vector potential $\underline{A}$, and an electric vector potential $\underline{F}$. These potentials are related to $\underline{E}$ and $\underline{H}$ as:

$$\underline{E} = -\nabla \times \underline{F} - j\omega\mu\underline{A} + \frac{1}{j\omega\varepsilon}\nabla(\nabla.\underline{A})$$

$$\underline{H} = \nabla \times \underline{A} - j\omega\varepsilon\underline{F} + \frac{1}{j\omega\mu}\nabla(\nabla.\underline{F}) \qquad (2.1)$$

where $\underline{E}$ is Electric field Intensity Vector

$\underline{H}$ is Magnetic field Intensity Vector

μ is permeability of medium of transmission

ε is permittivity of medium of transmission.

where

$$\nabla^2\underline{A} + k^2\underline{A} = -\underline{Je}$$

$$\nabla^2\underline{F} + k^2\underline{F} = -\underline{Jm} \qquad (2.2)$$

$\underline{Je}$ is the Electric Source Current Density Vector

$\underline{Jm}$ is the Magnetic Source Current Density Vector.

The electromagnetic field strengths, source currents and source charges are related by Maxwells Equations, i.e.

$$\nabla \times \underline{E} = -(j\omega\underline{B} + \underline{Jm})$$

$$\nabla \times \underline{H} = j\omega\underline{D} + \underline{Je}$$

$$\nabla . \underline{B} = \rho_m$$

$$\nabla . \underline{D} = \rho_e \qquad (2.3)$$

where $\underline{B}$ is the Magnetic Field Flux Density Vector

$\underline{D}$ is the Electric Field Flux Density Vector

ρ_m is the Magnetic Source Charge Density

ρ_e is the Electric Source Charge Density.

Sources are characterized by the positioning and sizes of the source currents and charges, and surface currents and charges may be placed at boundaries to account for any sudden changes in the propogation medium, i.e. at reflecting infinite conducting surfaces.

For a radiation problem, the actual sources of a field can be replaced by equivalent sources constrained to the surface of a region which contains the sources.

Magnetic source currents and charges have no physical basis, but can be used to aid the analysis.

The relations in Equation (2.2) can be solved by the use of Greens Functions, i.e. where the geometry of Figure 2.1 applies.

$$\underline{A}(\underline{r}) = \int_{V'} \underline{Je}(\underline{r}') \cdot G(\underline{r},\underline{r}')\, dV'$$

$$\underline{F}(\underline{r}) = \int_{V'} \underline{Jm}(r') \cdot G(\underline{r},\underline{r}')\, dV' \qquad (2.4)$$

where $G(\underline{r},\underline{r}')$ is a Greens Function which is a solution of the homogeneous Helmholtz Equation.

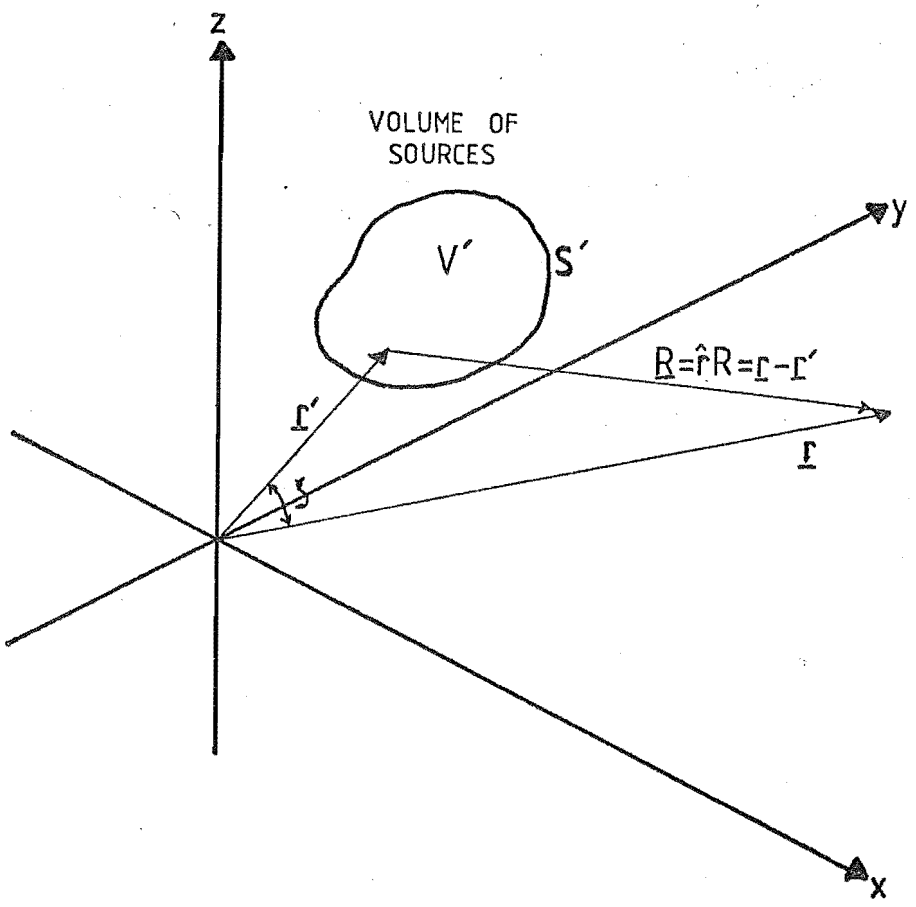

Figure 2.1 Sources in a Volume V', Field Evaluated at $\underline{r}$.

In the situation where the potentials in Equation (2.2) are linearly polarized, we can write them as $\underline{F} = \underline{m}\,\psi_f$, $\underline{A} = \underline{m}\,\psi_a$, where $\underline{m}$ is the unit vector in the direction of polarization. In a source free region, $\underline{Je} = \underline{Jm} = 0$, hence Equation (2.2) reduces to,

$$\nabla^2\psi_{\substack{a\\f}} + k^2\psi_{\substack{a\\f}} = 0, \tag{2.5}$$

the scalar Helmholtz Equation.

If the sources within the region V' of Figure 2.1 are replaced by currents on the surface S', Equations (2.2) and (2.4) become

$$\underline{A}(\underline{r}) = \int_{S'} \underline{Jes}\,(\underline{r}_s')\,.\,G\,(\underline{r},\underline{r}_s')\,dS'$$

$$\underline{F}(\underline{r}) = \int_{S'} \underline{Jms}\,(\underline{r}_s')\,.\,G\,(\underline{r},\underline{r}_s')\,dS' \tag{2.6}$$

$$\nabla^2\underline{A}+k^2\underline{A} = -\underline{Jes}$$

$$\nabla^2\underline{F}+k^2\underline{F} = -\underline{Jms} \tag{2.7}$$

The electromagnetic field at $\underline{r}$ can be found by using Equations (2.1) and (2.4) or alternatively, in the case of equivalent surface sources being used, Equations (2.1) and (2.6), i.e.

$$\underline{E}(\underline{r}) = \int_{X'} \left[\underline{Jm}'x\nabla\underline{G} - j\omega\mu\underline{Je}'\underline{G} + \frac{1}{j\omega\varepsilon}\,\underline{Je}'.\,\nabla\nabla\underline{G}\right]dX',$$

$$\underline{H}(\underline{r}) = \int_{X'} \left[-\underline{Je}'x\nabla\underline{G} - j\omega\varepsilon\underline{Jm}'\underline{G} + \frac{1}{j\omega\mu}\,\underline{Jm}'.\,\nabla\nabla\underline{G}\right]dX', \tag{2.8}$$

where

X' - may be either a Volume V' or a Surface S'

$\underline{Je}'$- may be a Volume Electric Current Density $\underline{Je}(\underline{r}')$, or a Surface Electric Current density $\underline{Jes}(\underline{r}'_s)$

$\underline{Jm}'$- may be a Volume Magnetic Current Density $\underline{Jm}(\underline{r}')$ or a Surface Magnetic Current density $\underline{Jms}(\underline{r}'_s)$

$\underline{G}$ - A shortened form of $G(\underline{r},\underline{r}')$ or $G(\underline{r},\underline{r}'_s)$

For a two dimensional current distribution the vector potentials are,

$$\underline{A}(\underline{\rho}) = \int_{A'} \underline{Je}(\underline{\rho}') \cdot g(\underline{\rho},\underline{\rho}')\, dA',$$

$$\underline{F}(\underline{\rho}) = \int_{A'} \underline{Jm}(\underline{\rho}') \cdot g(\underline{\rho},\underline{\rho}')\, dA', \qquad (2.9)$$

where A' is the area occupied by the cross-section of the sources, and, $g(\underline{\rho},\underline{\rho}')$ is a two dimensional Greens Function. Working along the same lines as the transformation from Equations (2.4) to (2.7); (2.9) becomes,

$$\underline{A}(\underline{\rho}) = \int_{C'} \underline{Jec}(\underline{\rho}'_c) \cdot g(\underline{\rho},\underline{\rho}'_c)\, dC',$$

$$\underline{F}(\underline{\rho}) = \int_{C'} \underline{Jmc}(\underline{\rho}'_c) \cdot g(\underline{\rho},\underline{\rho}'_c)\, dC', \qquad (2.10)$$

The integrals over C' in Equation (2.10) are around the perimeter of the area A', as in Figure 2.2.

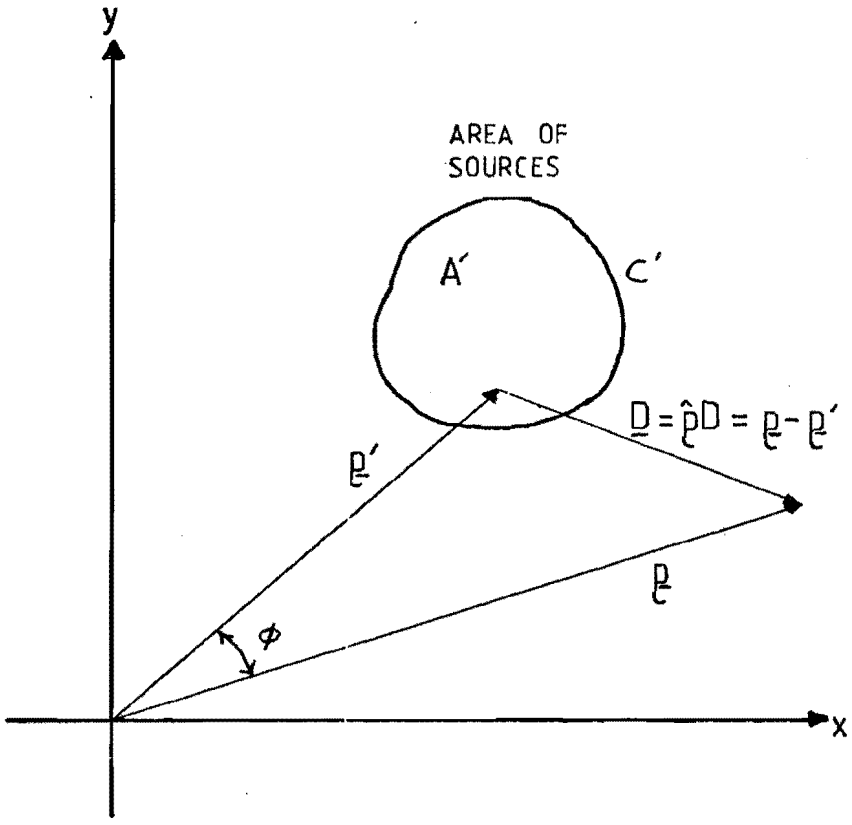

Figure 2.2 Sources in an Area A', Field Evaluated at $\underline{\rho}$.

The electromagnetic field at $\underline{\rho}$ can be expressed by using a combination of the Equations (2.1) and (2.9) or (2.1) and (2.10), depending upon the choice of source distribution, i.e.,

$$\underline{E}(\underline{\rho}) = \int_{Y'} \left[\underline{Jm}' x \nabla \underline{g} - j\omega\mu \underline{Je}' . \underline{g} + \frac{1}{j\omega\varepsilon} \underline{Je}' . \nabla\nabla \underline{g} \right] dY',$$

$$\underline{H}(\underline{\rho}) = \int_{Y'} \left[-\underline{Je}' x \nabla \underline{g} - j\omega\varepsilon \underline{Jm}' . \underline{g} + \frac{1}{j\omega\mu} \underline{Jm}' . \nabla\nabla \underline{g} \right] dY', \qquad (2.11)$$

where, Y' - may be either an Area A', or a Perimeter C'

$\underline{Je}'$ - may be an Area Electric Current Density $\underline{Je}(\underline{\rho}')$, or a Perimeter Electric Current Density, $\underline{Jec}(\underline{\rho}')$

$\underline{Jm}'$ - may be an Area Magnetic Current Density $\underline{Jm}(\underline{\rho}')$, or a Perimeter Magnetic Current Density $\underline{Jmc}(\underline{\rho}')$

$\underline{g}$ - A shortened form of $g(\underline{\rho}, \underline{\rho}')$ or $g(\underline{\rho}, \underline{\rho}_c')$.

2.2.1 GREENS FUNCTIONS

The Greens Functions used in Section 2.2, $G(\underline{r},\underline{r}')$ and $g(\underline{\rho},\underline{\rho}')$ are solutions of the Helmholtz Equation (2.2) for a point source in three dimensions and a line source in two dimensions respectively.

In the three dimentional case, referring to Figure 2.1,

$$G(\underline{r},\underline{r}') = \frac{e^{-jk|\underline{r}-\underline{r}'|}}{4\pi\ |\underline{r}-\underline{r}'|} \quad . \tag{2.12}$$

In the radiation zone, where $|\underline{r}| \gg |\underline{r}'\ \max|$; $|\underline{r}| \gg \lambda o$,

λ_o = free space wavelength and

$$|\underline{r}-\underline{r}'| = |\underline{R}| \approx r - r' \cos\xi \tag{2.13}$$

the three dimensional Greens Function becomes

$$G(\underline{r},\underline{r}') = \frac{e^{-jk(r-r'\cos\xi)}}{4\pi r}$$

$$= e^{jkr'\cos\xi} \cdot \frac{e^{-jkr}}{4\pi r} \quad . \tag{2.14}$$

The multiplier $\frac{e^{-jkr}}{4\pi r}$ is independent of $\underline{r}'$ and can be placed outside of any integrations of source distributions. Only the phase is affected by $\underline{r}'$ in Equation (2.14), the approximation (2.13) has negligible effect on the amplitude term.

Thus from Equation (2.8), the electromagnetic field from a current distribution is, in the far zone,

$$\underline{E}(\underline{r}) = -j\omega\mu \cdot \frac{e^{-jkr}}{4\pi r} \int_{X'} \left[\sqrt{\frac{\epsilon}{\mu}}\, \underline{Jm}' \times \hat{r} + \underline{Je}' - (\underline{Je}' \cdot \hat{r})\hat{r} \right] e^{jkr'\cos\xi} dX',$$

$$\underline{H}(\underline{r}) = j\omega\epsilon \cdot \frac{e^{-jkr}}{4\pi r} \int_{X'} \left[\sqrt{\frac{\mu}{\epsilon}}\, \underline{Je}' \times \hat{r} - \underline{Jm}' + (\underline{Jm}' \cdot \hat{r})\hat{r} \right] e^{jkr'\cos\xi} dX', \tag{2.15}$$

where X' - is either a surface or a volume

$\underline{Je}'$ - is either a surface or volume electric current density

$\underline{Jm}'$ - is either a surface or volume magnetic current density

$\hat{r}$ - is the unit vector in the directior of $\underline{R}$.

In the near zone, close to volume V', Equations (2.13) and (2.14) are not valid. This means that no approximations can be made in the evaluations of the electromagnetic field in Equation (2.11), thus increasing its computational complexity.

Between the near zone and the radiation zone is the 'Fresnel' Zone. The conditions leading to Equation (2.13) still hold, but are such that (2.13) is not valid.

In this case,

$$|\underline{R}| = r - \hat{r}\cdot\underline{r} + \frac{1}{2r}\left[r'^2 - (\hat{r}\cdot\underline{r}')^2\right], \tag{2.16}$$

and the corresponding Greens function differs in the phase term from the far zone Greens Function, i.e.

$$G(\underline{r},\underline{r}')_{\text{Fresnel}} = \frac{e^{-jkr}}{4\pi r}\cdot e^{jk\left(\hat{r}\cdot\underline{r} + \frac{(\hat{r}\cdot\underline{r}')^2}{2r} - \frac{r'^2}{2r}\right)} \tag{2.17}$$

Which may be substituted into Equation (2.8).

This Greens Function will produce a different electromagnetic field from Equation (2.14) due to the extra phase terms. It is a reasonable approximation to replace the phase exponential in the integrals of Equation (2.15) by the phase exponential of Equation (2.17). Generally the Fresnel zone field will vary with direction and distance in a manner different from the far zone field.

For the two-dimensional case,

$$g(\underline{\rho},\underline{\rho}') = \frac{1}{4j} H_o^{(2)}\left(k|\underline{\rho} - \underline{\rho}'|\right), \tag{2.18}$$

where $H_o^{(2)}$ is a zero order Hankel Function of the second kind.

In the far zone, the conditions $|\underline{\rho}| >> |\underline{\rho}\ '_{max}|$ and $|\underline{\rho}| >> \lambda_o$ hold, hence,

$$|\underline{D}| = |\underline{\rho} - \underline{\rho}'| \approx \rho - \rho' \cos\phi. \tag{2.19}$$

For a large argument the Hankel function reduces to,

$$H_o^{(2)}(\gamma) = \sqrt{\frac{2j}{\pi\gamma}}\ e^{-jk\gamma}, \tag{2.20}$$

and Equation (2.18) becomes

$$g(\underline{\rho}, \underline{\rho}') \approx \frac{e^{-jk\rho}}{\sqrt{8\pi jk\rho}}\ e^{jk\rho'\cos\phi}. \tag{2.21}$$

In the far zone, the electromagnetic field from a two dimensional source becomes,

$$\underline{E}(\underline{\rho}) = j\omega\mu\ \frac{e^{-jk\rho}}{(8\pi jk\rho)^{\frac{1}{2}}} \int_{y'} \left[\sqrt{\frac{\varepsilon}{\mu}}\ \underline{Jm}' x\, \hat{\rho} + \underline{Je}' - (\underline{Je}'\cdot\hat{\rho})\,\hat{\rho}\right] e^{jk\rho'\cos\phi} dy',$$

$$\underline{H}(\underline{\rho}) = j\omega\varepsilon\ \frac{e^{-jk\rho}}{(8\pi jk\rho)^{\frac{1}{2}}} \int_{y'} \left[\sqrt{\frac{\mu}{\varepsilon}}\ \underline{Je}' x\hat{\rho} - \underline{Jm}' + (\underline{Jm}'\cdot\hat{\rho})\,\hat{\rho}\right] e^{jk\rho'\cos\phi} dy', \tag{2.22}$$

where Y' - is either the perimeter or area of the source

$\underline{Je}'$ - is either the perimeter or area electric current density

$\underline{Jm}'$ - is either the perimeter or area magnetic current density

$\hat{\rho}$ - is the unit vector in the direction of $\underline{D}$

The relations in Equation (2.22) are found from Equation (2.11).

In the case where condition (2.19) does not hold, the Hankel Function cannot be approximated by Equation (2.20). This increases the complexity of evaluation of Equation (2.11).

In the Fresnel zone the phase term of the condition (2.19) has to be more accurate. This phase term* then may be substituted into the integrals of Equation (2.22).

2.3 SEPARATION OF VARIABLES TECHNIQUES

The Helmholtz equation, Equation (2.5) is a partial differential equation, in either two or three dimensions, depending upon whether it is scalar or vector.

If, by luck, or by good management the variables of the Helmholtz Equation are independent, then it may be possible to split the Equation up into two or three independent ordinary differential equations. Other methods can then be applied to the solution of these equations.

The Helmholtz Equation, repeated below, has an infinite number of solutions for any point. This corresponds to an infinite combination of sources which may produce a specified field. One way to severely restrict the number of solutions is to specify certain a priori boundary conditions.

$$\nabla^2\psi + k^2\psi = 0$$

k - constant

ψ - A solution to the Helmholtz Equation (2.23)

A further simplification is to force boundary surfaces to correspond with coordinate surfaces, hence it is usual to choose the coordinate system which best fits the boundary surfaces. Thus, in the case of three dimensions, solutions may be separated into a product of two or three factors.

---

* Equation (2.17).

$$\psi = F_1(\xi_1) \cdot \Phi\ (\xi_2, \xi_3) \tag{2.24}$$

or

$$\psi = F_1(\xi_1) \cdot F_2(\xi_2) \cdot F_3(\xi_3) \tag{2.25}$$

and in two dimensions, separated solutions may be

$$\psi = F_1(\xi_1) \cdot F_2(\xi_2) \tag{2.26}$$

All solutions of the partial differential equation can be built up out of linear combinations of the members of the family of separated solutions.

In the case of rectangular coordinates, Equation (2.25) becomes

$$\frac{d^2\psi}{dx^2} + \frac{d^2\psi}{dy^2} + \frac{d^2\psi}{dz^2} + k^2\psi = 0 \tag{2.27}$$

and separated solutions are of the form,

$$\psi = X(x) \cdot Y(y) \cdot Z(z), \tag{2.28}$$

Substituting Equation (2.28) into (2.27) and dividing by ψ yields

$$\frac{1}{X}\frac{d^2X}{dx^2} + \frac{1}{Y}\frac{d^2Y}{dy^2} + \frac{1}{Z}\frac{d^2Z}{dz^2} + k^2 = 0, \tag{2.29}$$

Each term depends upon only one coordinate, and Equation (2.29) will sum to zero only if each term is independent, thus,

$$\begin{aligned}
\frac{1}{X}\frac{d^2X}{dx^2} &= -k_x, & \frac{d^2X}{dx^2} + k_x^2 X &= 0, \\
\frac{1}{Y}\frac{d^2Y}{dy^2} &= -k_y, & \frac{d^2Y}{dy^2} + k_y^2 Y &= 0, \\
\frac{1}{Z}\frac{d^2Z}{dz^2} &= -k_z, & \frac{d^2Z}{dz^2} + k_z^2 Z &= 0,
\end{aligned} \tag{2.30}$$

where k_x, k_y, k_z are constants, and

$$k_x^2 + k_y^2 + k_z^2 = k^2 \tag{2.31}$$

Equation (2.31) is called the separation equation, and the relations in Equation (2.30) are the wave equation.

Boundary conditions can take several forms. A common boundary condition is that $\psi = 0$ as the wave tends to infinity. This usually implies a $\frac{1}{R^n}, n>0$ term in the solution, where R is a measure of the radial distance from the source to the measurement point. Further boundary conditions affect ψ at surfaces.

For instance Dirichlet boundary conditions apply if the restriction

$$\psi_{\text{tangential}} = 0, \tag{2.32}$$

is set at a boundary surface.

Similarly Neumann Boundary conditions apply if the restriction

$$\frac{d\psi_{\text{normal}}}{dn} = 0, \tag{2.33}$$

is set at a boundary surface.

Cauchy Boundary conditions,

$$(\psi_{\text{tangential}} + \frac{d\psi_{\text{normal}}}{dn}) = 0, \tag{2.34}$$

over specify the problem, as in the case of an electromagnetic wave, one boundary condition applied to one polarization controls the other polarization too.

As an example, we can apply boundary conditions in the case of a parallel-plane wave-guide, where TEM transmission is required. This application of the Separation of Variables Technique is given in an Appendix.

The Separation of Variables Technique can be applied to many shapes which coincide with coordinate surfaces, such as planes, half-planes, strips, cylinders and spheroids. In many cases, where boundaries

cannot be fitted to coordinate surfaces, the solution of the Helmholtz Equation by the Separation of Variables Technique becomes intractable. Under such circumstances other ad hoc methods must be used.

2.4 EDGE DIFFRACTION

An antenna system in its entirety can be thought of as a collection of sources. Once these sources have been either completely or approximately characterized, the properties of the system can be discovered by the superposition of the effects of the sources.

A reflector antenna usually has one driving source and reflecting surfaces. Geometrical optics or physical optics techniques can be used to find the principle parts of the radiation pattern of the source and reflector, but are unuseable where diffraction effects are required. The inclusion of passive sources* at surface discontinuities in reflecting surfaces to some extent rectifies the shortcomings of the method, but in some cases those passive sources are not a good enough description to correctly predict rear direction fields or fields in the penumbral region.

The passive sources strengths and phasing are found by the use of canonical problems which approximate the problem under study to some extent. The sources are then applied to the problem as required.

Many reflector antennas have discontinuous edges. If the radius of curvature of the reflector is large, it is usually a good approximation to model the edge as a half plane, if the edge is isolated from other discontinuities.

A study of half plane diffraction will facilitate review of various descriptions of diffraction, while being able to compare results with exact solutions.

---

* see Section 2.5 and James (1976)

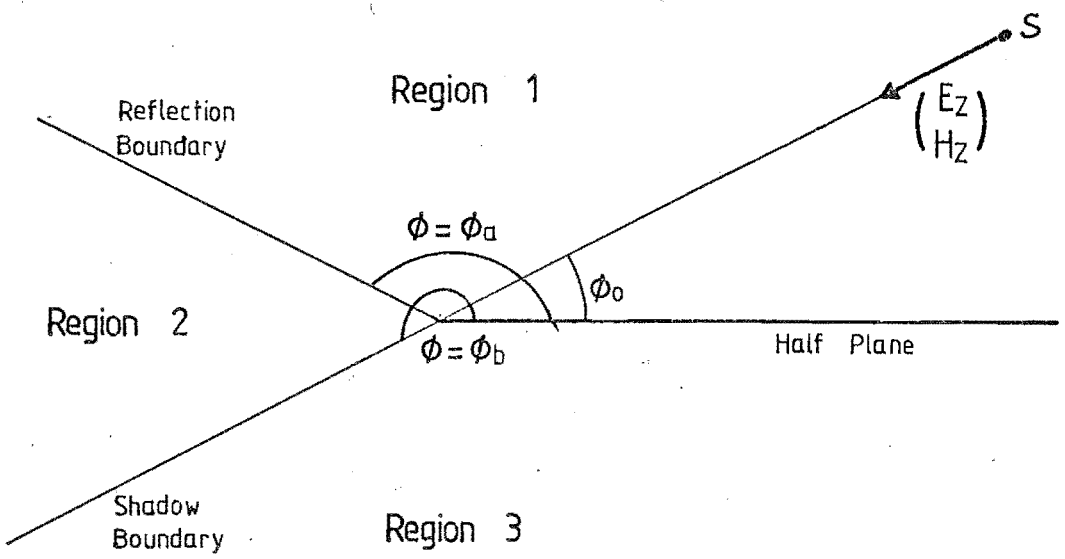

Figure 2.3 Half Plane Geometry.

Figure 2.3 shows a current line source near a perfectly conducting half plane. Both the edge of the half plane and the source are oriented parallel to the z - axis, and either the electric field or the magnetic field may be polarized in the z direction. Modifying Equation (2.9) for only one source gives,

$$\underline{A}(\underline{\rho}) = \underline{Je}(\underline{\rho}_o) \cdot \frac{e^{-jk\rho}}{(8\pi jk\rho)^{\frac{1}{2}}} \cdot e^{jk\cos\phi_o \ell_o}$$

$$\underline{F}(\underline{\rho}) = \underline{Jm}(\underline{\rho}_o) \cdot \frac{e^{-jk\rho}}{(8\pi jk\rho)^{\frac{1}{2}}} \cdot e^{jk\cos\phi_o \ell_o} \qquad (2.35)$$

where all vectors are aligned in the z direction, and ℓ and ℓ_o correspond to $|\rho'|$ and $|\rho|$ of Figure 2.2.

It is assumed that the field point is in the radiation zone of the source. Expanding in cylindrical coordinates about the source gives, using Equations (2.1) and (2.2),

$$\begin{aligned}
\underline{E}(\underline{\rho})_z &= -j\omega\mu\underline{A}(\underline{\rho})_z, \\
\underline{H}(\underline{\rho})_\phi &= -\sqrt{\frac{\varepsilon}{\mu}}\ \underline{E}(\underline{\rho})_z, \\
\underline{H}(\underline{\rho})_z &= -j\omega\varepsilon\underline{F}(\underline{\rho})_z, \\
\underline{E}(\underline{\rho})_\phi &= +\sqrt{\frac{\mu}{\varepsilon}}\ \underline{H}(\underline{\rho})_z,
\end{aligned} \tag{2.36}$$

which implies that in the radiation zone the field from a line current source is TEM.

2.5 HALF PLANE DIFFRACTION

2.5.1 EXACT

The separation of variables technique can be brought to bear upon this problem. The parabolic cylinder system is best suited to describe a half plane, Figure 2.4.

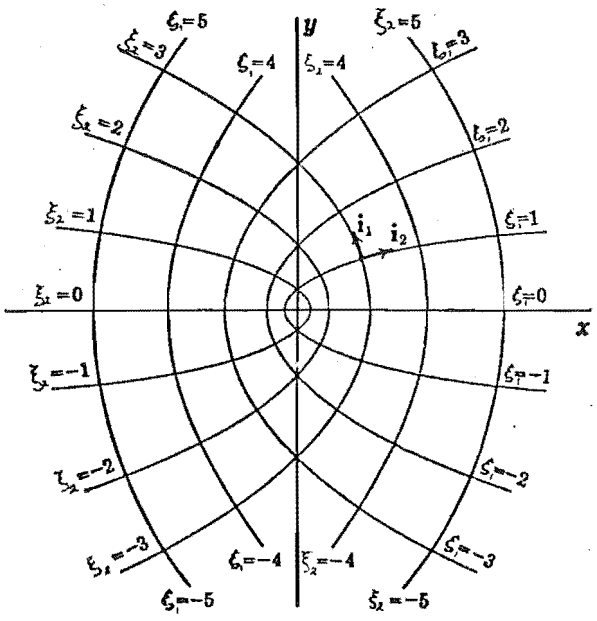

Figure 2.4 Parabolic Coordinate System, (Stratton, 1941).

The parabolic coordinates are related to rectangular cartesian coordinates by

$$\xi_1^2 = (x^2 + y^2)^{\frac{1}{2}} - x,$$

$$\xi_2^2 = (x^2 + y^2)^{\frac{1}{2}} + x,$$

$$Z = z. \tag{2.37}$$

The surface $\xi_1 = 0$ corresponds to a half plane for $x>0$ upon which either a Dirichlet or Neumann Boundary restriction may be applied.

In two dimensions, the Helmholtz Equation can be split into two ordinary differential equations, in parabolic coordinates, i.e.

$$\frac{d^2F}{d\xi_1^2} + (K^2 + k^2 \xi_1^2) F = 0, \tag{2.38}$$

$$\frac{d^2G}{d\xi_2^2} + (-K^2 + k^2 \xi_2^2) G = 0, \tag{2.39}$$

and the incident and scattered fields can be procured by looking at series of wave functions of the parabolic cylinder, and taking the boundary conditions at the half plane into account.

This procedure was used by Macdonald, (Macdonald 1915).

The eigenfunction solution, also due to Macdonald (Macdonald 1902) can be written as,

$$\begin{bmatrix} E_z \\ H_z \end{bmatrix} = \begin{cases} \dfrac{1}{4j}\sum_{n=o}^{\infty} \varepsilon_n \begin{Bmatrix} \sin(\frac{1}{2}n\phi)\sin(\frac{1}{2}n\phi_o) \\ \cos(\frac{1}{2}n\phi)\cos(\frac{1}{2}n\phi_o) \end{Bmatrix} J_{\frac{1}{2}n}(k\rho) \cdot H^{(2)}_{\frac{1}{2}n}(k\rho_o); & \rho<\rho_o \\ \dfrac{1}{4j}\sum_{n=o}^{\infty} \varepsilon_n \begin{Bmatrix} \sin(\frac{1}{2}n\phi)\sin(\frac{1}{2}n\phi_o) \\ \cos(\frac{1}{2}n\phi)\cos(\frac{1}{2}n\phi_o) \end{Bmatrix} \cdot J_{\frac{1}{2}n}(k\rho_o) \cdot H^{(2)}_{\frac{1}{2}n}(k\rho); & \rho_o<\rho \end{cases} \tag{2.40}$$

where $\varepsilon_n = 1$ for $n = 0$

$= 2$ for $n>0$

$J_{\frac{1}{2}n}$ is the $(n/2)$th order Bessel Function of the first kind and $H^{(2)}_{\frac{1}{2}n}$ is the $(n/2)$th order Hankel Function of the second kind and the upper (lower) line in the braces correspond to electric (magnetic) polarization in the z direction.

In the case of an incident plane wave, the eigenfunction solution reduces to

$$\begin{bmatrix} E_z \\ H_z \end{bmatrix} = \sum_{n=o}^{\infty} \varepsilon_n \, j^{\frac{1}{2}n} \, J_{\frac{1}{2}n}(k\rho) \begin{Bmatrix} \sin(\frac{1}{2}n\phi)\sin(\frac{1}{2}n\phi_o) \\ \cos(\frac{1}{2}n\phi)\cos(\frac{1}{2}n\phi_o) \end{Bmatrix}, \tag{2.41}$$

where the plane wave has been normalized to unit amplitude and the asymptotic expansion of the Hankel function for large argument has been taken, i.e.

$$H^{(2)}_{\nu}(\gamma) \approx \sqrt{\frac{2j}{\pi\gamma}} \, j^{\nu} \, e^{-jk\gamma} . \tag{2.42}$$

$(\gamma>>\nu)$

Sommerfeld, (Bouwkamp 1954), was able to solve the half plane diffraction problem solely in terms of Fresnel Integrals, in the case of plane wave incidence and is given as

$$\left.\begin{matrix} E_z \\ H_z \end{matrix}\right\}^{\gamma} = \frac{e^{j\pi/4}}{\sqrt{\pi}} \left[e^{jk\rho\cos(\phi-\phi_o)} \cdot F\left[\sqrt{2k\rho}\cos\tfrac{1}{2}(\phi-\phi_o)\right] \mp e^{jk\rho\cos(\phi+\phi_o)} \cdot F\left[-\sqrt{2k\rho}\cos\tfrac{1}{2}(\phi+\phi_o)\right] \right], \quad (2.43)$$

where $F[\gamma]$ is the Fresnel Integral

$$F[\gamma] = \int_{\gamma}^{\infty} e^{-j\mu^2}\, d\mu. \quad (2.44)$$

The incident plane wave is,

$$\left.\begin{matrix} E_z^{inc} \\ H_z^{inc} \end{matrix}\right\} = e^{jk\rho\cos(\phi-\phi_o)}. \quad (2.45)$$

It is tempting to try to pull out the plane wave like expressions from Equation (2.43).

The Fresnel Integral Expressions can be manipulated, for instance,

$$F[-\gamma] = \int_{-\gamma}^{\infty} e^{-j\mu^2}\, d\mu = \sqrt{\pi} \cdot e^{-j\pi/4} - F[\gamma], \quad (2.46)$$

is a useful property.

At various angles about the half plane edge, the signs of the arguments of the Fresnel Integrals change, allowing or precluding the use of (2.46).

Equation (2.43) then can be written as,

$$\left.\begin{matrix} E_z \\ H_z \end{matrix}\right\} = e^{jk\rho\cos(\phi-\phi_o)}\left[U(\pi-(\phi-\phi_o)) - \frac{e^{j\frac{1}{4}\pi}}{\sqrt{\pi}}\cdot\frac{\cos\frac{1}{2}(\phi-\phi_o)}{|\cos\frac{1}{2}(\phi-\phi_o)|}\cdot F\left[\sqrt{2k\rho}\,\cos\tfrac{1}{2}(\phi-\phi_o)\right]\right]$$

$$\mp\, e^{jk\rho\cos(\phi+\phi_o)}\left[U(\pi-(\phi+\phi_o)) - \frac{e^{j\frac{1}{4}\pi}}{\sqrt{\pi}}\cdot\frac{\cos\frac{1}{2}(\phi+\phi_o)}{|\cos\frac{1}{2}(\phi+\phi_o)|}\cdot F\left[\sqrt{2k\rho}\,\cos\tfrac{1}{2}(\phi+\phi_o)\right]\right] \qquad (2.47)$$

Incident and reflected plane waves are shown in Equation (2.47), i.e.,

$$\left.\begin{matrix} E_z \\ H_z \end{matrix}\right\} = e^{jk\rho\cos(\phi-\phi_o)}\cdot U(\pi-(\phi-\phi_o)) \mp e^{jk\rho\cos(\phi+\phi_o)}\cdot U(\pi-(\phi+\phi_o))$$

where $U(\gamma) = 1$ if $\gamma>o$

$= 0$ if $\gamma<o$. (2.48)

Where the step functions show the areas where the incident and reflected plane waves can be seen. In Equation (2.47), associated with the incident and reflected waves are diffracted waves,

$$\left.\begin{matrix} E_z^{diff} \\ H_z^{diff} \end{matrix}\right\} = \frac{-e^{j\pi/4}}{\sqrt{\pi}} \left\{ e^{jk\rho\cos(\phi-\phi_o)} \cdot \frac{\cos\frac{1}{2}(\phi-\phi_o)}{\left|\cos\frac{1}{2}(\phi-\phi_o)\right|} \cdot F\left[\sqrt{2k\rho}\,\cos\tfrac{1}{2}(\phi-\phi_o)\right] \right.$$

$$\left. \mp e^{jk\rho\cos(\phi+\phi_o)} \cdot \frac{\cos\frac{1}{2}(\phi+\phi_o)}{\left|\cos\frac{1}{2}(\phi+\phi_o)\right|} \cdot F\left[\sqrt{2k\rho}\,\cos\tfrac{1}{2}(\phi+\phi_o)\right] \right\}. \tag{2.49}$$

Equations (2.48) and (2.49) can be brought together to produce a total field,

$$\phi_{total} = (\phi_{inc} + \phi_{inc}^{diff}) \mp (\phi_{refl} + \phi_{refl}^{diff}), \tag{2.50}$$

where ϕ can stand for either E or H and the top sign applies in the case of electric polarization and the lower sign applies for the magnetic field polarization.

Simplifications can be made to the Fresnel Integrals. In the case of large ρ and $\cos\frac{1}{2}(\phi\pm\phi_o) \neq 0$ a large argument expansion of the Fresnel Integral may be used, (i.e. (James, 1973)),

$$F[\gamma] \approx \frac{e^{-j\gamma^2}}{2j\gamma} \sum_{m=o}^{\infty} j^m (\tfrac{1}{2})_m \gamma^{-2m}, \tag{2.51}$$

where

$$(\tfrac{1}{2})_o = 1; \quad (\tfrac{1}{2})_m = \tfrac{1}{2}(\tfrac{1}{2}+1) \ldots\ldots (\tfrac{1}{2}+m-1).$$

Only the first term of the series of Equation (2.51) need be used when $\cos\frac{1}{2}(\phi\pm\phi_o)\neq 0$ hence,

$$F[\gamma] \approx \frac{e^{-j\gamma^2}}{2j\gamma} \quad . \tag{2.52}$$

This asymptotic value may be substituted into (2.49) to give

$$\left.\begin{matrix} E_z^{diff} \\ H_z^{diff} \end{matrix}\right\} = -\frac{e^{-jk\rho}}{\sqrt{8\pi jk\rho}} \left(\frac{1}{\cos\frac{1}{2}(\phi-\phi_o)} \mp \frac{1}{\cos\frac{1}{2}(\phi+\phi_o)} \right) \tag{2.53}$$

Equation (2.53) is a description of a cylindrical source with a pattern factor [*], placed at the edge of the half plane. This is the passive source referred to at the beginning of this section. It will be noted that the $\frac{1}{\sqrt{j}}$ implies that a phase change of $-\pi/4$ occurs on diffraction, although this is a gradual effect which occurs over a number of wavelengths away from the edge (Sommerfeld, 1954)*. Note that when $(\phi\pm\phi_o) = \pi$ the expression becomes undefined.

In this situation recourse must be made to the Fresnal Integral solution of Equation (2.49). From the definitions of incident and reflected wave it is possible to define various regions about a half plane, as in Figure 2.3. In the case $(\phi+\phi_o) = \pi$ the argument of the second Fresnel integral in Equation (2.47) becomes zero.

The Fresnel Integral value is

$$F[o] = \int_o^\infty e^{-j\mu^2} d\mu = \frac{\sqrt{\pi}}{2} \; e^{-j\pi/4}. \tag{2.54}$$

---

* Equation (2.53) is a far field description.

This subtracts from the reflected wave, and as $(\phi+\phi_o)$ increases beyond π the Fresnel Integral contribution will increase until it cancels the reflected wave. Where $(\phi+\phi_o) = \pi$ we can define as the reflection boundary. ~~The same is true for the angles $(\phi-\phi_o)$.~~ At $(\phi-\phi_o) = \pi$ is the shadow boundary, where the effects of the incident wave are exactly halved. Beyond the shadow boundary in Region 3 the incident wave is cancelled out by the Fresnel Integral associated wave.

The reflection and shadow boundaries gain a greater significance when geometrical optic considerations are applied. On the shadow and reflection boundaries the associated Fresnel Integral waves show plane wave dependence.

The solution of Equation (2.50) is exact only when a plane wave is incident. In the case of an incident cylindrical wave, if the relations in Equation (2.36) apply in the radiation zone of the input wave, then it is possible to normalize the amplitude of the plane wave solution. In this case Equation (2.50) can be modified to give,

$$\Psi^{cyl}_{total} = \frac{e^{-jk\rho_o}}{\sqrt{8\pi jk\rho_o}} \left[(\Psi_{inc} + \Psi^{diff}_{inc}) \mp (\Psi_{refl} + \Psi^{diff}_{refl}) \right], \qquad (2.55)$$

where ρ_o - source-edge distance.

This representation will be accurate for either source or field point many wavelengths away from the diffracting edge of the half plane. If the ρ_o in Equation (2.55) is substituted by $\rho_>$, the greater distance from the half plane edge to the source or the probe*, the smaller distance $\rho_<$ will be placed in the Fresnel integral formulation. Equation (2.55) will be most accurate when $\rho_> >> \rho_<$, approximating the plane wave diffraction description.

---

* field point.

2.5.2 HIGH FREQUENCY METHODS

Ray tracing comes directly from optics, where a wave front is modelled as a ray which obeys Fermat's Principle. Fermat's Principle states that the optical path length between two points is the shortest possible. Fermat's Principle can also be used where there is a reflection or refraction boundary between two points. In a homogenous medium the optical pathlength is proportional to the geometrical path length, and under such circumstances the optical path length between two points will be a straight line.

In the radiation zone of a source, referring to Equation (2.36) in the case of a 2-d source, the transverse electric and magnetic fields can be described as,

$$\underline{E} = \underline{E}(\underline{R}) \cdot e^{-jk\Psi(\underline{R})},$$

$$\underline{H} = \underline{H}(\underline{R}) \cdot e^{-jk\Psi(\underline{R})}, \tag{2.56}$$

where $\underline{E}(\underline{R})$, $\underline{H}(\underline{R})$ are the field strengths at position $\underline{R}$ and where $\Psi(\underline{R})$ satisfies the eikonal equation,

$$|\nabla\psi(\underline{R})|^2 = n^2, \tag{2.57}$$

where n is the refractive index of the medium of propagation (Kouyoumjian, 1975). The unit vector $\hat{S}$ can be defined as,

$$\hat{S} = \frac{\nabla\psi(\underline{R})}{n}, \tag{2.58}$$

which is in the direction of the wave path and is normal to the wavefront when n is position independent.

A tube of rays must obey the conservation of energy principle. The energy flux through the cross-sectional area of the tube of rays

at one point must be the same at all points on the tube. Figure 2.5 shows a tube of rays with areas A and B representing wavefronts a distance S apart.

ρ_1 and ρ_2 are the principal radii of curvature of the wavefront through area A.

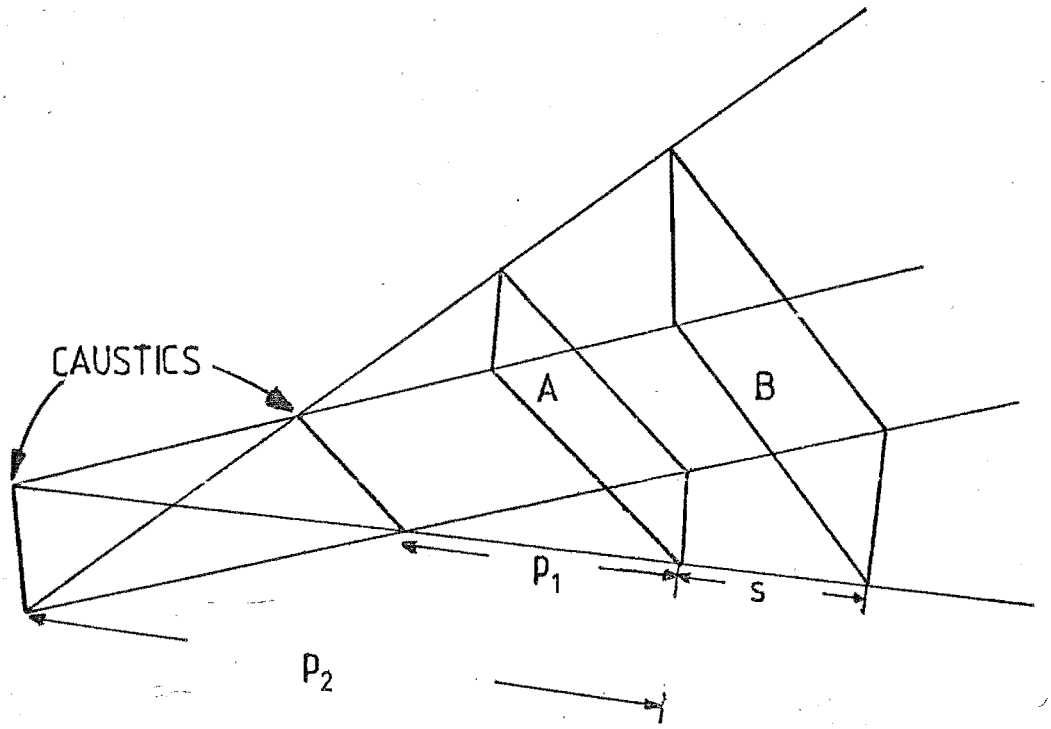

Figure 2.5 Geometrical Optics Tube of Rays.

The field at B, with respect to the field at A is,

$$\begin{pmatrix} \underline{E}_B \\ \underline{H}_B \end{pmatrix} = \begin{pmatrix} \underline{E}_A \\ \underline{H}_A \end{pmatrix} \cdot \left[\frac{\rho_1 \rho_2}{(\rho_1+s)(\rho_2+s)} \right]^{\frac{1}{2}} e^{-jk\psi(A)} \quad e^{-jks}. \tag{2.59}$$

From Equation (2.59) the following statements can be made:

(a) $s \to \infty$, the field decays as s^{-1}, as in a spherical wave.

(b) ρ_1 or $\rho_2 \to \infty$ the field decays as $s^{-\frac{1}{2}}$, as for a cylindrical wave.

(c) ρ_1 and $\rho_2 \to \infty$ the field remains of constant amplitude, behaving like a plane wave.

(d) $s = -\rho_1$ or $-\rho_2$, Equation (2.59) becomes infinite and is invalid. Such points are termed as caustics, and separate considerations must be made to evaluate the field at the caustic.

On either side of the caustic the field remains finite, but a phase shift of $\pi/2$ in Equation (2.59) is introduced by a change in sign of either ρ_1 or ρ_2. This phase shift was initially observed by Guoy, (Rubinowicz, 1938).

2.5.3 GEOMETRICAL THEORY OF DIFFRACTION

Geometrical optics fails to account properly for the electromagnetic properties of interference, polarization and diffraction. At a shadow boundary Geometrical Optics predicts no leakage into the dark region. In an attempt to overcome this shortcoming, while still trying to retain the basic simplicity of Geometrical Optics, Keller (Keller, 1962) extended Fermat's Principle to take into account diffraction at edges.

The three major extensions of geometrical optics that Keller proposed were:

1.) That diffracted rays emerge tangentially from convex surfaces.

2.) That diffracted rays emerge radially from tips and edges.

3.) That diffracted rays themselves obey rules 1 and 2 at any further diffractions.

Figure 2.6 pictures diffraction under such circumstances.

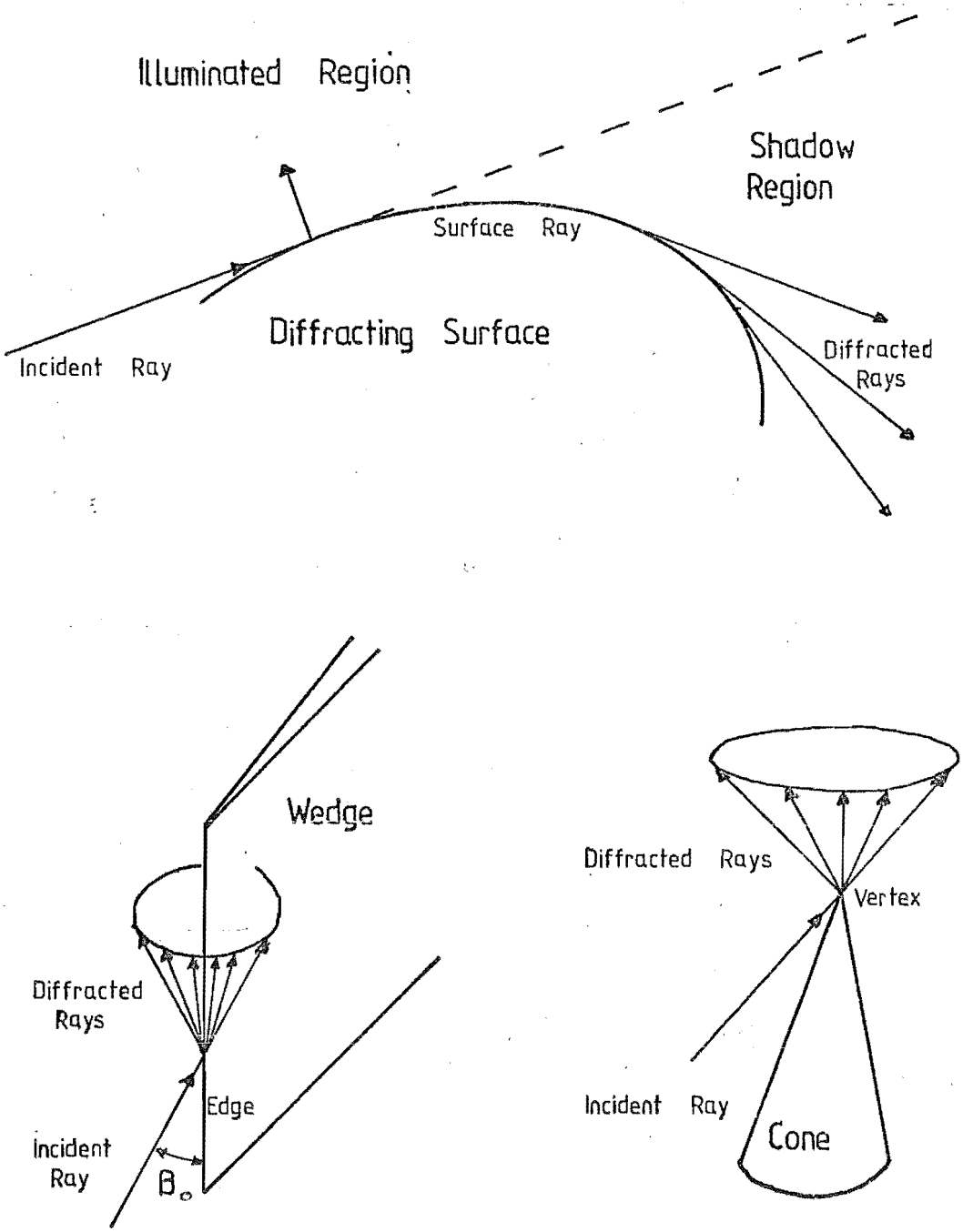

Figure 2.6 Diffraction Mechanisms, Curved Surface, Edge, Vertex.

A diffracted ray may be described, following the rules above, as

$$U^d(s) = U^d(0) \left[\frac{\rho_1 \rho_2}{(\rho_1+s)(\rho_2+s)} \right]^{\frac{1}{2}} e^{-jks}, \qquad (2.60)$$

where U^d represents either E^d or H^d. Naturally, Equation (2.60) is of the same form as Equation (2.59), where the reference point 0 is at the diffracting edge or a smooth line on a curved surface. Looking at the

half plane diffraction formulae of Equation (2.50) it can be seen that there is a phase variation of $\pi/4$.* This is a property of a caustic, hence a caustic exists at the diffracting edge.

Assuming that ρ_2 corresponds to the distance from where diffraction occurs to the field point, and knowing that $U^d(s)$ must be independent of the reference point, and $E^d(0)$ will 'blow up' on a caustic in proportion to $\frac{1}{\rho}$ as $\rho \to 0$ it is necessary to state that,

$$\lim_{\rho_2 \to 0} U^d(0) \sqrt{\rho_2} = C. \tag{2.61}$$

Hence,

$$U^d(s) = C \sqrt{\frac{\rho_1}{s(\rho_1+s)}}\, e^{-jks}, \tag{2.62}$$

where ρ_1 is the distance between the caustic of the surface and the second caustic of the diffracted ray, which is away from the surface, in analogy to Figure 2.5.

In the case of a tip or vertex, both caustic points coincide at the diffracting surface. Repeating the application of Equation (2.61), this time to Equation (2.62) we obtain,

$$U^d(s) = B \frac{e^{-jks}}{s}, \tag{2.63}$$

which is spherical in nature and would be weak any reasonable distance away from the diffracting point, ie. in the Far Field.

Also in the case of a two dimensional problem, $\rho_1 \to \infty$ thus, Equation (2.62) is altered to,

$$U^d(s) = C \frac{e^{-jks}}{\sqrt{s}}. \tag{2.64}$$

---

* with respect to the incident wave.

The multiplication factors B and C are proportional to the incident field strength, depend upon the boundary conditions, polarization, angle of incidence and the angle of diffraction. B and C for the general three dimensional case are dyadics.

Following a well trodden path (Keller 1962) we can study the diffraction of a plane wave by a half plane. The diffracted field will be of the form Equation (2.64), hence we may compare (2.64) with our known solution Equations (2.49) or (2.53). In the case of Dirichlet boundary conditions

$$C = \frac{-E^{inc}}{\sqrt{8\pi jk}} \left(\frac{1}{\cos\frac{1}{2}(\phi-\phi_o)} - \frac{1}{\cos\frac{1}{2}(\phi+\phi_o)} \right), \tag{2.65}$$

away from shadow boundaries. Fresnel integrals must be used near and on reflection boundaries. C in Equation (2.65) is a diffraction constant under two dimensional circumstances.

In the case of an incident ray at angle β_o as in Figure 2.6, the fact that it is non-normal can be taken into account, provided the edge is continuous about the point of diffraction. Once again, in the case of Dirichlet conditions, the diffracted field can be described by,

$$E^d(s) = E^{inc} \; D_d(\psi,\psi_o;\; \beta_o) \; \frac{\rho}{\sqrt{s(\rho+s)}} \; e^{-jks}, \tag{2.66}$$

where $D_d(\psi,\psi_o;\; \beta_o)$ is the Dirichlet edge diffraction coefficient, and is, using Keller's (Keller, 1962) results.

$$D_d(\psi,\psi_o;\; \beta_o) = \frac{1}{\sqrt{8\pi jk}\;\sin\beta_o} \left(\frac{1}{\cos\frac{1}{2}(\phi-\phi_o)} \mp \frac{1}{\cos\frac{1}{2}(\phi+\phi_o)} \right). \tag{2.67}$$

In the case of Neumann boundary conditions, use the lower sign inside the braces.* Equation (2.67) can be modified to describe diffraction at

* and $D_n(\ldots)$.

shadow and reflection boundaries, but the case of grazing incidence requires further insight.

Consider the case when $\phi_o \to o$. Equation (2.67) describing the Dirichlet boundary condition becomes zero, which is to be expected because of the boundary conditions themselves. The half plane edge is not seen by the incident wave. However, at the edge there is a discontinuity, which affects the normal derivative of the incident ray. (Karp and Keller, 1961).

Hence for $\psi_o = 0$

$$E^d(s) = \left[\frac{1}{2} \frac{\partial E^{inc}}{\partial n} \cdot \frac{1}{jk\sin\beta_o} \frac{\partial}{\partial \phi_o} D_d(\phi, \phi_o; \beta) \Big|_{\phi_o=0} \right] \cdot \sqrt{\frac{\rho}{s(\rho+s)}} \cdot e^{-jks} \tag{2.68}$$

For Neumman boundary conditions we can appeal to the concept of image sources. As $\phi_o \to 0$ the image source will coincide with the incident source. Under the boundary conditions the image source is exactly the same as the incident source and the sources will sum. With the + sign in Equation (2.67), the diffraction coefficient will need to be halved to give useful results.

2.6 CURVED WEDGE EXAMPLE

Figure 2.7 depicts a curved wedge. Under such circumstances Equation (2.67) is modified to

$$D_{\substack{d \\ n}}(\psi, \psi_o; \beta_o) = \frac{\sin(\pi/N)}{N\sqrt{2\pi jk}\,\sin\beta o} \left[\frac{1}{\cos\frac{\pi}{N} - \cos\frac{\phi-\phi_o}{N}} \mp \frac{1}{\cos\frac{\pi}{N} - \cos\frac{\phi+\phi_o}{N}} \right] \tag{2.69}$$

where $N\pi$ is the outside angle of the tangents of the wedge faces at the edge.

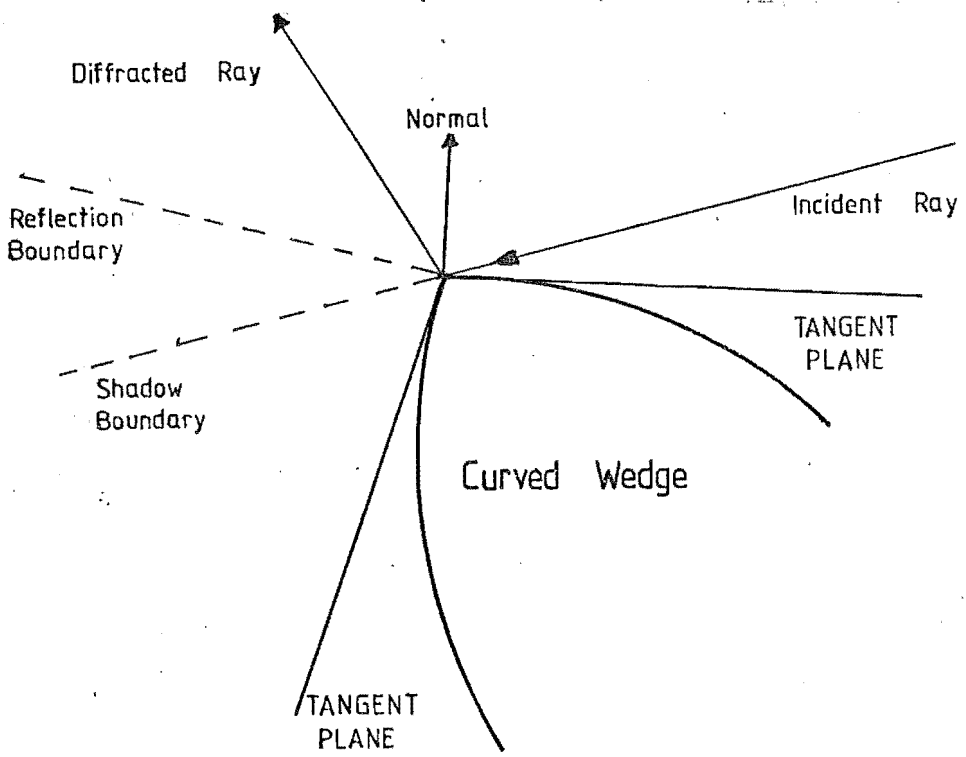

Figure 2.7 Curved Wedge

Equation (2.69) is also the result for a plane wedge of exterior angle $N\pi$. This formulation is a good approximation to diffraction from a curved wedge (Kouyoumjian, 1975), as high frequency diffraction is a purely local phenomenon, allowing planes to be straightened over the (small) region of interest. The simplicity of (2.69) is lost if further manipulations are undertaken to account for the curve in the wedge. A first order improvement changes the reflected rays. Instead of reflection being taken off the tangent planes the actual planes are used. At a curved reflector the radius of curvature ρ_{inc} of the incident wave will be changed, although the law of reflection from a plane will be obeyed at the reflection point. This in turn will affect the caustic distances of the reflected and diffracted rays, (Kouyoumjian, 1975).

Not many treatments of the curved wedge looks into the diffracted field along the surface of the wedge, i.e. (James 1976). Many other

workers mention that surface rays are produced but state that the field is essentially a very high frequency effect involving complicated analyses for very little return, i.e. (Rusch, 1975). We shall first look at diffraction off a convex surface.

In the case of a convex surface GTD produces a diffracted wave for a general case of non-constant curvature, (Keller and Levy, 1959). Figure 2.8 shows how a wave is diffracted by a curved surface. A ray strikes the surface at grazing incidence at P_1, is diffracted around the surface and leaves at Q_1.

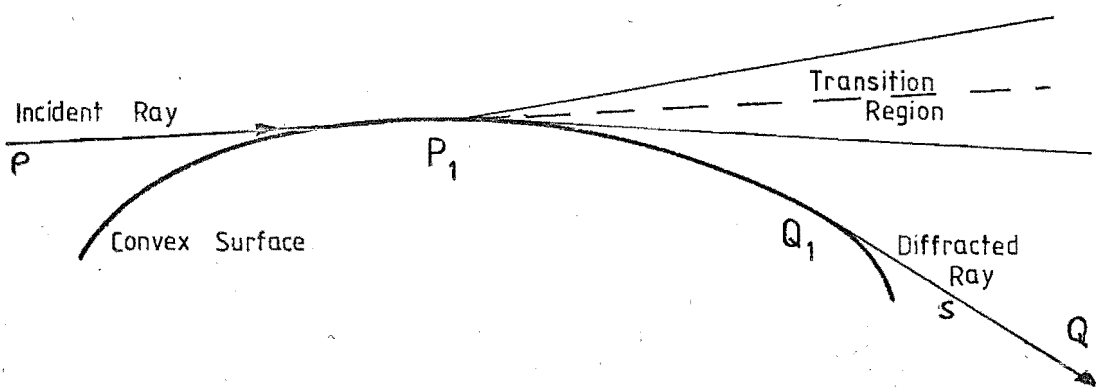

Figure 2.8 Regions in Convex Surface Diffraction.

The GTD approach enumerates the following arguments:

i. There is a constant shedding of tangent rays between P_1 and Q_1, in proportion to the energy of the surface rays. The amplitude a(t) of the surface ray will then attenuate in an exponential fashion, thus

$$\frac{da(t)}{dt} = -\alpha(t)\, a(t),$$

$$\therefore \quad a(t) = a(0) \exp\left(-\int_0^t \alpha(\tau)\, d\tau\right), \tag{2.70}$$

where $-\alpha(\tau)$ is the decay factor, and t is distance along a geodesic on the curved surface. The Geodesic Path is found by the application of Fermat's Principle along the surface.

ii. The phase change of a ray which undergoes surface diffraction between P and S is proportional to the pathlength,

$$\Delta_{phase} = k(\rho_1+t+s). \tag{2.71}$$

iii. In the case of scalar diffraction where the incident wave is cylindrical, i.e. of the form $\frac{1}{\sqrt{\rho_1}}$ as it grazes the surface it undergoes a diffraction. The surface wave has to be multiplied by a diffraction coefficient $C(P_1)$ where C depends upon the local geometry and boundary conditions at P_1. When the surface wave becomes a tangent wave at Q_1, another diffraction occurs, hence the surface wave must be multiplied by a second diffraction coefficient, $C(Q_1)$ where again Q_1 depends upon the local geometry and boundary conditions.

iv. Following the same argument to reach Equation (2.64), the diffracted ray will exhibit cylindrical properties.

Collecting results i. to iv., a representation of the diffracted field will be

$$U_{diff} \sim \frac{U_{inc}C(P_1)C(Q_1)}{\sqrt{\rho_1 s}}.\exp\left[-\int_o^t \alpha(\tau)\,d\tau - jk(\rho_1+t+s)\right]. \tag{2.72}$$

Equation (2.72) shows that the diffracted surface ray will attenuate rapidly for any reasonable pathlength on the convex surface. For a specified convex surface the canonical problem has to be solved to put values on $C(x)$ and $\alpha(\tau)$.

For a reasonably short pathlength it may be assumed that there is a reasonable amount of 'throw off', especially if the radius of curvature

at P_1 is quite small. Figure 2.8 shows a transition region between a reflection region and a shadow region. The shadow boundary has become 'fuzzy' under such circumstances and a resultant shadow boundary can be presumed to occur at the bottom of the transition region near the deep shadow region.

To solve for curved wedge geometry, James (James 1976) initially studied the problem of a current source on the surface of a cylinder. He then took the results of this and modelled the passive source as a current at the diffracting edge.

Another solution may be obtained by looking at the reciprocal problem (Cashman, Kouyoumjian, Pathak, 1977) replacing the field point by the source and the initial source point by a field point. The initial diffracted surface field would be provided by a modification of Equation (2.72), that is

$$U_{P_1}^{surf} \sim \frac{U'_{inc} C(Q_1)}{\sqrt{s}} \cdot \exp\left[-\int_o^t \alpha(\tau)\, d\tau - jk(s+t)\right] \qquad (2.73)$$

where again the actual value of Equation (2.73) would depend upon the surface geometry amplitude and polarization of the incident ray from Q to Q_1 and P_1 would be at the edge of the wedge. Assuming that curvature of a surface is a global effect, and that on a local scale the surface is plane, then the diffraction coefficients for a straight wedge for grazing incidence may be used to further multiply Equation (2.73) along with a cylindrical field dependence, $\frac{1}{\sqrt{\rho}}$, from the edge to the field point, at P.

The straight edge diffraction coefficients would be either the part of Equation (2.68) in braces in the case of Dirichlet boundary conditions, or one half of Equation (2.67) in the case of Neumann boundary conditions.

For a concave surface, surface diffracted waves are produced and would be similar in form to Equation (2.72). The Geometrical Optics component of incident and reflected rays will swamp these diffracted rays, hence no benefit would be gained by characterising the surface rays, unless a 'whispering gallery' effect is set up.

2.7 ASYMPTOTIC THEORIES OF DIFFRACTION

2.7.1 HALF PLANE DIFFRACTION

Once again take the diffraction of a half plane by a cylindrical source field. GTD, in its modified state is of the form,

$$\psi_{tot} = \frac{e^{-jk\rho_>}}{\sqrt{8\pi jk\rho_>}} \left[e^{jk\rho_< \cos(\phi-\phi_o)} \cdot \left[U(\pi-(\phi-\phi_o)) - \frac{e^{j\frac{1}{4}\pi}}{\sqrt{\pi}} \cdot \frac{\cos\frac{1}{2}(\phi-\phi_o)}{\left|\cos\frac{1}{2}(\phi-\phi_o)\right|} \right.\right.$$

$$\left.\left. \cdot F\left[\sqrt{2k\rho_<}\cos\tfrac{1}{2}(\phi-\phi_o)\right] \right] \mp e^{jk\rho_< \cos(\phi+\phi_o)} \left[U(\pi-(\phi+\phi_o)) \right.\right.$$

$$\left.\left. - \frac{e^{j\frac{1}{4}\pi}}{\sqrt{\pi}} \cdot \frac{\cos\frac{1}{2}(\phi+\phi_o)}{\left|\cos\frac{1}{2}(\phi+\phi_o)\right|} \cdot F\left[\sqrt{2k\rho_<}\cos\tfrac{1}{2}(\phi+\phi_o)\right] \right] \right] \qquad (2.74)$$

where $\rho_>$ is the radial distance to the source or field point, whichever is further from the edge of the half plane,

$\rho_<$ is the radial distance to the source or field point, whichever is nearer to the edge of the half plane,

ϕ_o is the source incident angle

ϕ is the field point angle

U(x) is a step function; U=1, $x \geq o$; U=0, $x<o$

and the top sign is in the case of Dirichlet boundary conditions and the lower sign under Neumann boundary conditions.

Equation (2.74) will provide an accurate assessment of half plane diffraction provided $\rho_> >> \rho_<$. When $\rho_> \to \rho_<$ and $\rho_> \to$ a small value, then Equation (2.74) will tend to provide step discontinuities at shadow and reflection boundaries, ie. Menendez and Lee, (1977).

Under such circumstances it is necessary to improve upon Equation (2.74), but away from boundaries (2.74) is a good description of the field.

2.7.2 CLEMMOW DIFFRACTION

The asymptotic description of diffraction described below is attributed to Clemmow (Clemmow, 1966), (Born and Wolf, 1959) who has championed the use of Plane Wave Spectra. In the case of Half Plane diffraction of a line source field, Clemmow produces an angular spectrum of plane waves to describe the field of a line source. He then uses Sommerfeld's plane wave solution for the half plane diffraction, Equation (2.43) to diffract each one of spectrum of the plane waves, leaving him with an integral formulation for the total field which is very similar to a representation produced by Macdonald, (Macdonald, 1915).

To set the scene, the half plane geometry is given as Figure 2.9, and the resultant field is given as,

$$\left.\begin{matrix} E_z \\ H_z \end{matrix}\right\} = \frac{1}{\sqrt{8\pi j}} \left\{ e^{-jkR} \int_m^\infty \frac{e^{-j\mu^2}}{\sqrt{\mu^2+2kR}}\, d\mu \mp e^{-jkR'} \int_{m'}^\infty \frac{e^{-j\mu^2}}{\sqrt{\mu^2+2kR'}}\, d\mu \right\},$$

where

$$m = \sqrt{k(r_o+r-R)}\, \frac{\cos\tfrac{1}{2}(\phi-\phi_o)}{|\cos\tfrac{1}{2}(\phi-\phi_o)|}$$

$$m' = \sqrt{k(r_o+r-R')}\, \frac{\cos\tfrac{1}{2}(\phi+\phi_o)}{|\cos\tfrac{1}{2}(\phi+\phi_o)|}. \qquad (2.75)$$

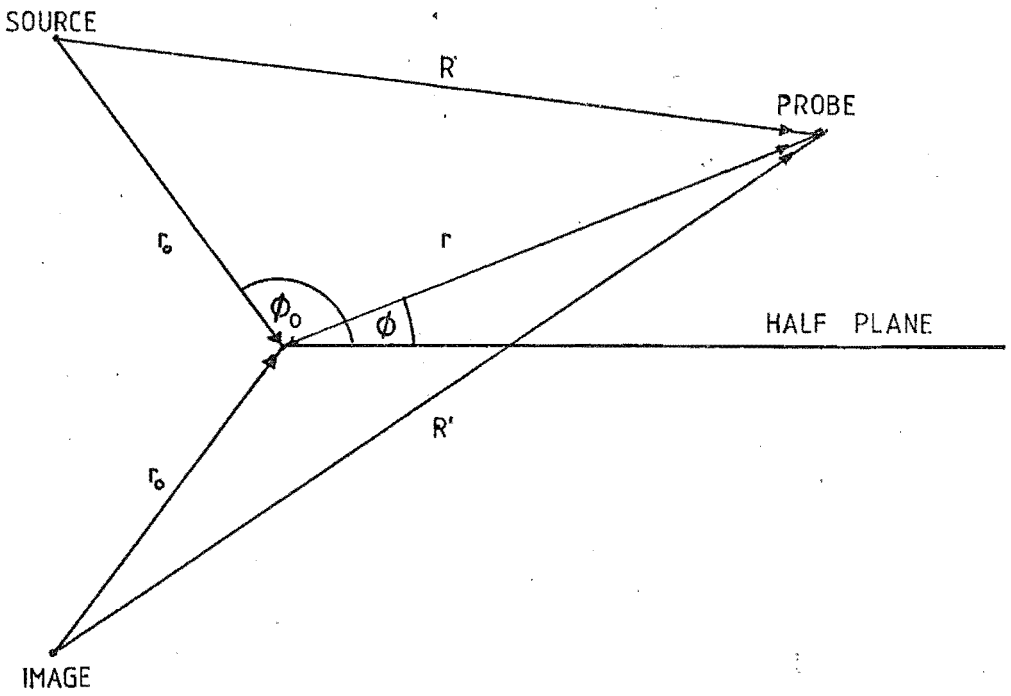

Figure 2.9 Line Source Near a Diffracting Half Plane.

Now the incident field can be written as a spectral function,

$$\left.\begin{matrix} E_z^{inc} \\ H_z^{inc} \end{matrix}\right\} = \frac{1}{\sqrt{8\pi j}} \cdot e^{-jkR} \cdot \int_{-\infty}^{\infty} \frac{e^{-j\mu^2}}{\sqrt{\mu^2+2kR}}\, d\mu \tag{2.76}$$

Following a similar argument as used in diffraction of a plane wave, we find a diffracted field, which is the total field minus the Geometrical Optics incident and reflected field.

Thus,

$$\left.\begin{matrix} E_z^{diff} \\ H_z^{diff} \end{matrix}\right\} = \frac{1}{\sqrt{8\pi j}} \left[\frac{\cos\frac{1}{2}(\phi-\phi_o)}{|\cos\frac{1}{2}(\phi-\phi_o)|} e^{-jkR} \int_q^{\infty} \frac{e^{-j\mu 2}}{\sqrt{\mu^2+2kR}}\, d\mu \right.$$

$$\left. \mp \frac{\cos\frac{1}{2}(\phi+\phi_o)}{|\cos\frac{1}{2}(\phi+\phi_o)|} e^{-jkR'} \int_{q'}^{\infty} \frac{e^{-j\mu 2}}{\sqrt{\mu^2+2kR'}}\, d\mu \right] \tag{2.77}$$

where

$$q = \sqrt{k(r+r_o-R)}$$

$$q' = \sqrt{k(r+r_o-R')},$$

describes the diffracted field. Equation (2.77) is still an exact representation of the diffracted field. The integrals can be transformed to Fresnel Integrals if the assumption $k(r_o+r) \gg 1$ can be adhered to. This limit requires that the source and field observation point be more than a wavelength away from the half plane edge, but can still be accurate if either point is within a wavelength distant from the edge. The effect of the approximation on Equation (2.77) is,

$$\left.\begin{matrix} E_z^{diff} \\ H_z^{diff} \end{matrix}\right\} = \frac{1}{\sqrt{8\pi j}} \left(\frac{\cos\frac{1}{2}(\phi-\phi_o)}{|\cos\frac{1}{2}(\phi-\phi_o)|} \frac{e^{-jkR}}{\sqrt{k(r_o+r+R)}} \cdot F\left[\sqrt{k(r_o+r-R)}\right] \right.$$

$$\left. \mp \frac{\cos\frac{1}{2}(\phi+\phi_o)}{|\cos\frac{1}{2}(\phi+\phi_o)|} \frac{e^{-jkR}}{\sqrt{k(r_o+r+R')}} \cdot F\left[\sqrt{k(r_o+r-R')}\right] \right). \tag{2.78}$$

The associated geometrical optics fields can also be written.

$$\left.\begin{matrix} E_z^{go} \\ H_z^{go} \end{matrix}\right\} = U(\pi-(\phi-\phi_o)) \frac{e^{-jkR}}{\sqrt{8\pi jkR}} \mp$$

$$U(\pi-(\phi+\phi_o)) \frac{e^{-jkR'}}{\sqrt{8\pi jkR'}}, \tag{2.79}$$

where $U(x)$ is a step function. When R or R' are small a Hankel Function description of the field may be used.

Equations (2.78) and (2.79) were the standard forms used for GTD like calculations in this project.

The Clemmow formulation, hereinafter referred to as Clemmow Diffraction, is an asymptotic form of GTD. Several other kinds have been produced in the literature, all closely related and all using some form of Fresnel Integral.

The two major asymptotic diffraction theories are called KP theory introduced by Kouyoumjian and his associates (Kouyoumjian and Pathak 1974) and Uniform Asymptotic Theory - (UAT), introduced by Lee and his associates, (Lee and Deschamps, 1976).

The KP theory overcomes infinities at boundaries by the introduction of a multiplicative transition function, while UAT gives a finite value to the GTD solution at shadow boundaries by the inclusion of an additive transition function (Rahmat-Samii and Mittra, 1977).

As an example, the diffraction coefficient for a normal cylindrical wave is reproduced (Kouyoumjian and Pathak, 1974) when diffracted by a halfplane.

$$\left.\begin{matrix} E_z^{diff} \\ H_z^{diff} \end{matrix}\right\} = \frac{e^{-jk(r_o+r)}}{\sqrt{8\pi k(r+r_o)}} \left\{ F\left[\sqrt{2kL}\,\middle|\,\cos\tfrac{1}{2}(\phi-\phi_o)\right] e^{jk2L\cos^2\frac{1}{2}(\phi-\phi_o)} \cdot \mathrm{sgn}(\pi-(\phi-\phi_o)) \right.$$
$$\left. \mp F\left[\sqrt{2kL}\,\middle|\,\cos\tfrac{1}{2}(\phi+\phi_o)\right] e^{jk2L\cos^2\frac{1}{2}(\phi+\phi_o)} \cdot \mathrm{sgn}(\pi-(\phi_o+\phi)) \right\}, \tag{2.80}$$

where $L = \dfrac{r \cdot r_o}{r+r_o}$,

$\mathrm{sgn}(x) = +1$ if $x \geq o$

-1 if $x < o$,

and $F[\gamma]$ is the Fresnel Integral form given in Equation (2.44).

It is clear that there are similarities between Equations (2.80) and (2.79), but also a close similarity to Equation (2.74).

L in Equation (2.80) can be changed, depending upon the type of illumination, i.e.,

$$L = \begin{cases} s\sin^2\beta_o & \text{for plane wave illumination,} \\ \dfrac{r.r_o}{r+r_o} & \text{for cylindrical wave illumination,} \\ \dfrac{s.s_o}{s+s_o}\sin^2\beta_o & \text{for conical and spherical wave illumination.} \end{cases} \tag{2.81}$$

where s_o = source - edge point distance, at oblique angle β_o

s = edgepoint - field point distance, at oblique angle β_o.

L can be determined for an arbitrary wavefront or for a curved edge, where the spreading of the wave reflected from a curved surface is different from that of the incident wave.

In many cases, where the radius of curvature of the diffracting object is large, the inclusion of new distance parameters will not be worth the loss of simplicity.

2.7.3 UNIFORM ASYMPTOTIC THEORY

Unlike the KP Diffraction, the UAT formulation begins with the total field rather than with a modified Geometrical optics field.

The UAT (Lee and Deschamps, 1976) is based on an Ansatz (Ahluwalia, Lewis and Boersma 1968) which was suggested by Sommerfeld's half plane solution.

The total field E^t is related by the sum of two parts, one related to the incident field, the other to the reflected field. To each part there is a geometrical optics type field and a diffracted field. The geometrical optics type field is given as (Menendez and Lee, 1977),

$$\begin{pmatrix} E^{G.O.} \\ H^{G.O.} \end{pmatrix} = \left[F(\xi^i) - \hat{F}(\xi^i)\right] \begin{pmatrix} E^{inc} \\ H^{inc} \end{pmatrix} + \left[F(\xi^r) - \hat{F}(\xi^r)\right] \begin{pmatrix} E^{refl} \\ H^{refl} \end{pmatrix}, \tag{2.82}$$

where,

$$F(\gamma) = \frac{e^{j\pi/4}}{\sqrt{\pi}} \int_{\gamma}^{\infty} e^{-jt^2} \, dt \,, \tag{2.83}$$

$$\hat{F}(\gamma) = \frac{1}{2\gamma\sqrt{\pi}} \, e^{-j(\gamma^2 + \pi/4)}, \tag{2.84}$$

Equation (2.84) is related to (2.83) by the large asymptotic expansion,

$$F(\xi) = U(-\xi) + \hat{F}(\xi), \qquad |\xi| \to \infty. \tag{2.85}$$

ξ is called the detour parameter. In the case of half plane diffraction of a cylindrical wave

$$\xi^{i,r} = \varepsilon^{i,r} \left| \sqrt{k(r_o + r - R^{i,r})} \right|, \tag{2.86}$$

where

$$\varepsilon^{i,r} = \begin{cases} +1 & \text{if observation point is in the shadow region of incident (reflected) wave,} \\ -1 & \text{if observation point is in the lit region of incident (reflected) wave,} \end{cases}$$

$R^i = R$

$R^r = R'$

referring to Figure 2.9.

The diffraction coefficient is of the same form as Keller Plane Wave GTD diffraction, given in Equation (2.69) but with $\beta_o = \pi/2$ and $N = 2$.

The detour parameter is defined as the difference of the direct distance between source and observation point and the distance via the edge. This definition can be applied to a plane wave, and any arbitrary incident wave from a known source distribution.

2.7.4 NON UNIFORM FIELD DIFFRACTION

If the incident field is non-uniform, there will be higher order terms in the asymptotic solution. The first order higher term is proportional to the derivative of the incident field with respect to angle. For this reason this diffraction is called Slope Wave Diffraction (Ahluwalia et al, 1968).

In the case where the variation of the field is slow, it is possible to characterise it by a summation of uniform sources. The diffracted field in the non-uniform case is then just the sum of diffractions of the uniform constituent sources.

2.8 PHYSICAL OPTICS

Physical optics is a frequency dependent extension of Geometrical optics, where the field scattered by an object is determined by induced currents on the surface of the scatterer caused by the geometrical optics incident field. On the illuminated side of the body, scattering is assumed to take place as if from a plane targent at each point, while on the shadow side of the body there are no allowed surface currents.

The current distribution is,

$$\underline{J}_s = \begin{cases} 2\underline{n} \times \underline{H}_{inc} & \text{on the lit side} \\ 0 & \text{on the shadow side} \end{cases} \qquad (2.87)$$

and the scattered field can be found by the use of vector potentials using Equations (2.6) and (2.8).

Take the case of a plane conducting sheet with a parallel line current source situated nearby, as in Figure 2.10. Define the origin of a polar coordinate system at the source. Assume also that the plane conducting sheet is removed enough from the source to be in the radiation zone of the source. Under such circumstances, the line source field would be described by Equations (2.35) and (2.36), showing TEM type transmission. For the purpose of this example, let the line source consist of electric currents.

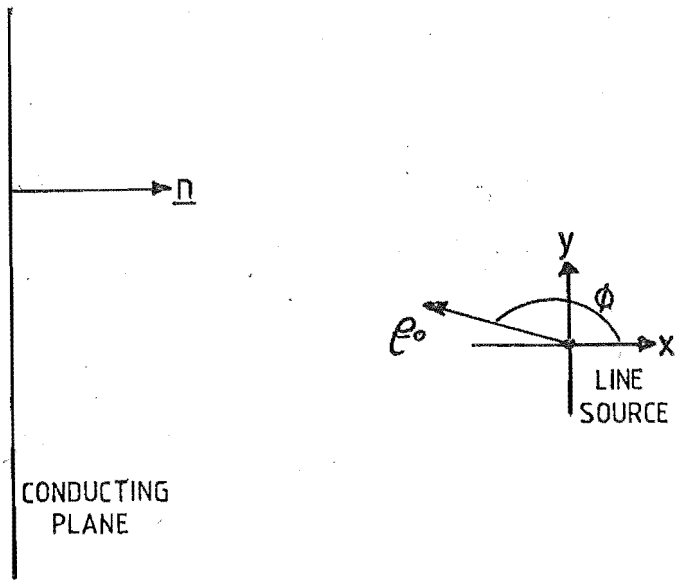

2.10 Plane Conducting Sheet with Line Source Nearby.

In the radiation zone, the relationship between $\underline{E}$ and $\underline{H}$ fields is

$$\underline{H}_{inc} = \sqrt{\frac{\varepsilon}{\mu}} \; (\underline{\rho}_o \times \underline{E}_{inc}), \tag{2.88}$$

where $\underline{\rho}_o$ is a radial unit vector from the source.

Substituting (2.88) into (2.87) we see that,

$$\underline{J}_{es} = \sqrt{\frac{\varepsilon}{\mu}} \; (\underline{n} \times (\underline{\rho}_o \times \underline{E}_{inc})) \tag{2.89}$$

$$= \sqrt{\frac{\varepsilon}{\mu}} \left[(\underline{n} \cdot \underline{E}_{inc}) \underline{\rho}_o - (\underline{\rho}_o \cdot \underline{n}) \; \underline{E}_{inc} \right] .$$

From Figure 2.10 we see that

$$\underline{E}_{inc} = \hat{z} \; E_{inc},$$

$$\underline{n} = \hat{x},$$

$$\underline{\rho}_o = \hat{x} \cos \phi + \hat{y} \sin \phi. \tag{2.90}$$

where $\hat{x}$, $\hat{y}$, $\hat{z}$ are unit vectors in a Rectangular Coordinate System. Thus,

$$\underline{J}_{es} = -2 \sqrt{\frac{\varepsilon}{\mu}} \cos \phi \; \underline{E}_{inc} \tag{2.91}$$

This expression for $\underline{J}_{es}$ may be substituted into Equations (2.10) and (2.36) to obtain the field from the physical optics currents on the plane.

The simplicity of this analysis relies upon the assumption that the plane is in the far field of the source and that the probe is well away from the plane.

If the source is placed very close to the plane, then for a region about the source the assumption of TEM transmission will not stand. Over a very large part of the plane, however, the source will be well removed, hence near field currents will appear on the plane only close to the source. These near field currents are the result of effects

which decay rapidly over a short distance. The total current on the plane in the near zone of the source can be considered as a sum of the Physical Optics Current and a difference current attributable to the near field. The near field of a source is transient in nature, hence it is to be expected that the difference currents produced by the near field will be transient and small, in comparison to the effects of the physical optics currents over the whole plane. If the probe is removed from the source and plane, the greatest effect will come from the physical optics currents, thus the near field difference currents can safely be ignored under the circumstances which we will use the physical optics currents.

Another problem arises from the evaluation of the scattering field. The Vector Potential, found by Equation (2.10) involves an integral from $-\infty$ to $+\infty$. When the conducting plane is illuminated by a plane wave, or a cylindrical wave the integral becomes infinite. This problem can be overcome by assuming that the transmission space is slightly lossy, introducing a small attenuation, and bounding the effective limits of the integration. Under practical circumstances, especially under cylindrical wave illumination, if the field about an edge is being studied, then contributions from physical optics currents more than 100λ distant can be ignored, without recourse to inclusion of attenuations.

Geometrical optics can only provide scattering in specular directions, while physical optics is capable of providing an estimate of the scattered field in non-specular directions.

Near the edge of the scatterer Equation (2.87) will provide erroneous surface currents. There will also be a leakage of currents into the shadow region. Physical optics cannot predict these currents without modification, hence the theory is limited in use to large

equivalent apertures and radar cross section analyses of large objects. In an attempt to gauge these currents not predicted by physical optics Ufimtsev (Ufimtsev, 1962) produced a Physical Theory of Diffraction (PTD). The non-uniform component of current near an edge is caused by a sudden change in curvature, hence if a field is known by some other method, the non-uniform currents can be calculated. Ufimtsev solved for these currents in the case of a half plane using Sommerfeld's solution, producing the same diffraction coefficients as Keller. In many cases, in contrast to the uniform current found by Physical Optics the solution of the non-uniform current is very difficult to obtain, and usually has to be found by indirect considerations. Despite the problems of PTD, it is capable of producing the correct fields over the transition boundaries, while GTD has a correct asymptotic form. (Plonus et al, 1978). This immediately complicates the theory to the point where a modified GTD is the only reasonably simple direct method of calculation.

Consider, as an example, the Physical Optics Field scattered from a half plane, with a cylindrical source at (ρ_o, ϕ_o). Under the circumstances depicted in Figure 2.11, the field found at the probe is plotted in Figure 2.12 for a Physical Optics Formulation. As a comparison the Clemmow type GTD results are also on Figure 2.12. It can be seen that the Physical Optics field is not attenuated to the same extent as the GTD field in the shadow region. The ripples on the Physical Optics Field is due to the wide current positioning on the half plane and the fact that the probe is relatively near to the half plane.

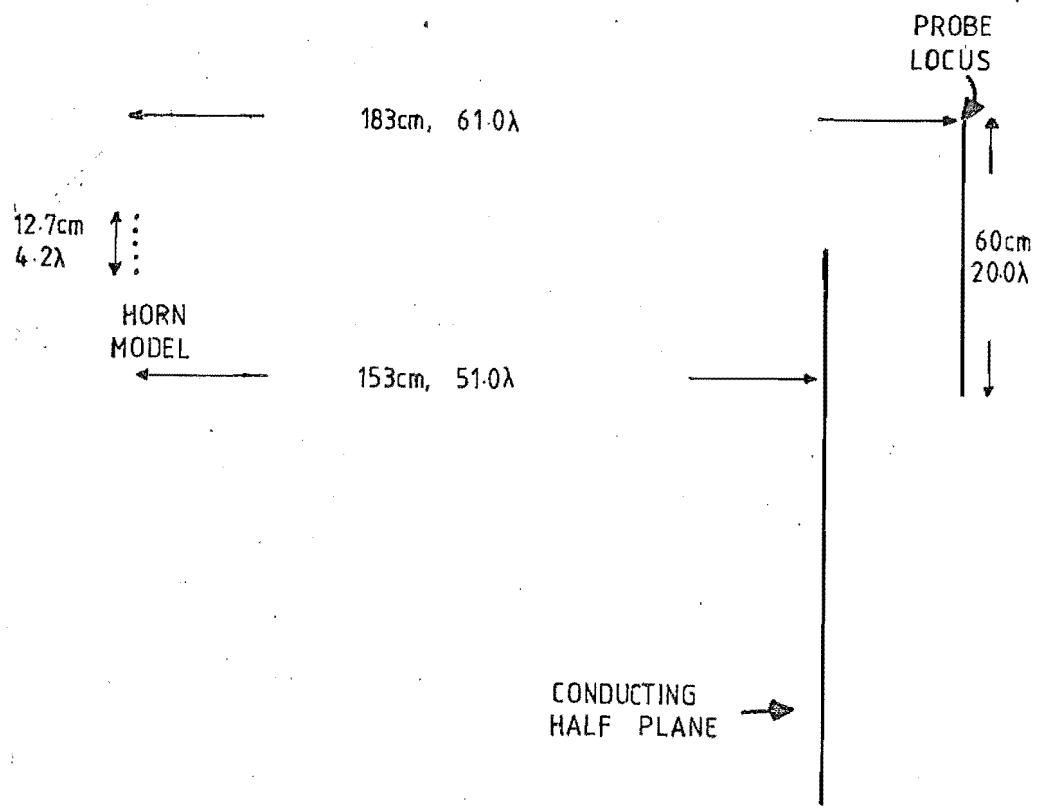

Figure 2.11 Half Plane Geometry Example.

The total Physical Optics field may be split up into a Geometrical Optics component and a Diffracted component. The P.O. Diffraction Coefficient is (James, 1976), (Knop and Osterlag, 1977),

$$D_d^{p.o.} = + \frac{2\sin\phi_o}{\cos\phi_o + \cos\phi}$$

$$D_n^{p.o.} = - \frac{2\sin\phi}{\cos\phi_o - \cos\phi} \qquad (2.92)$$

The corresponding GTD coefficients are,

$$D_d^{GTD} = \frac{4\sin\phi/2 . \sin\phi_o/2}{\cos\phi_o + \cos\phi}.$$

$$D_n^{GTD} = \frac{4\cos\phi/2 \cos\phi_o/2}{\cos\phi_o + \cos\phi}. \qquad (2.93)$$

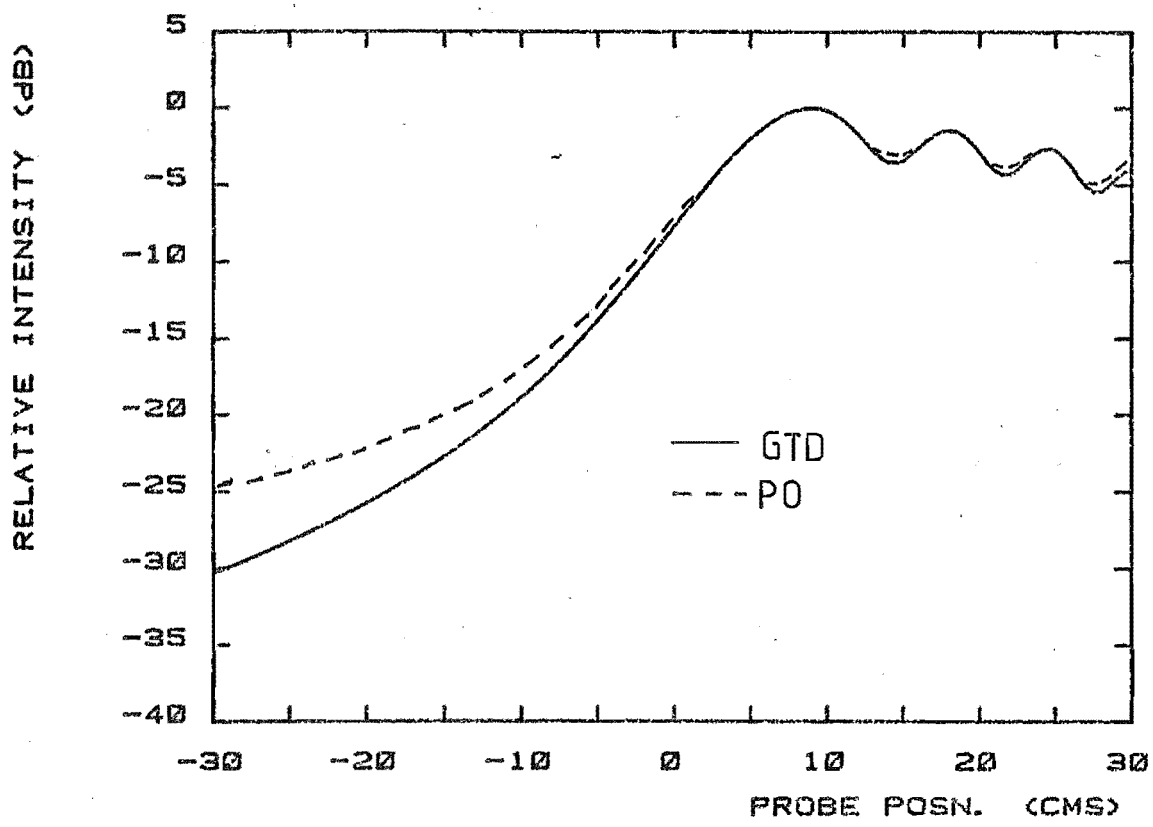

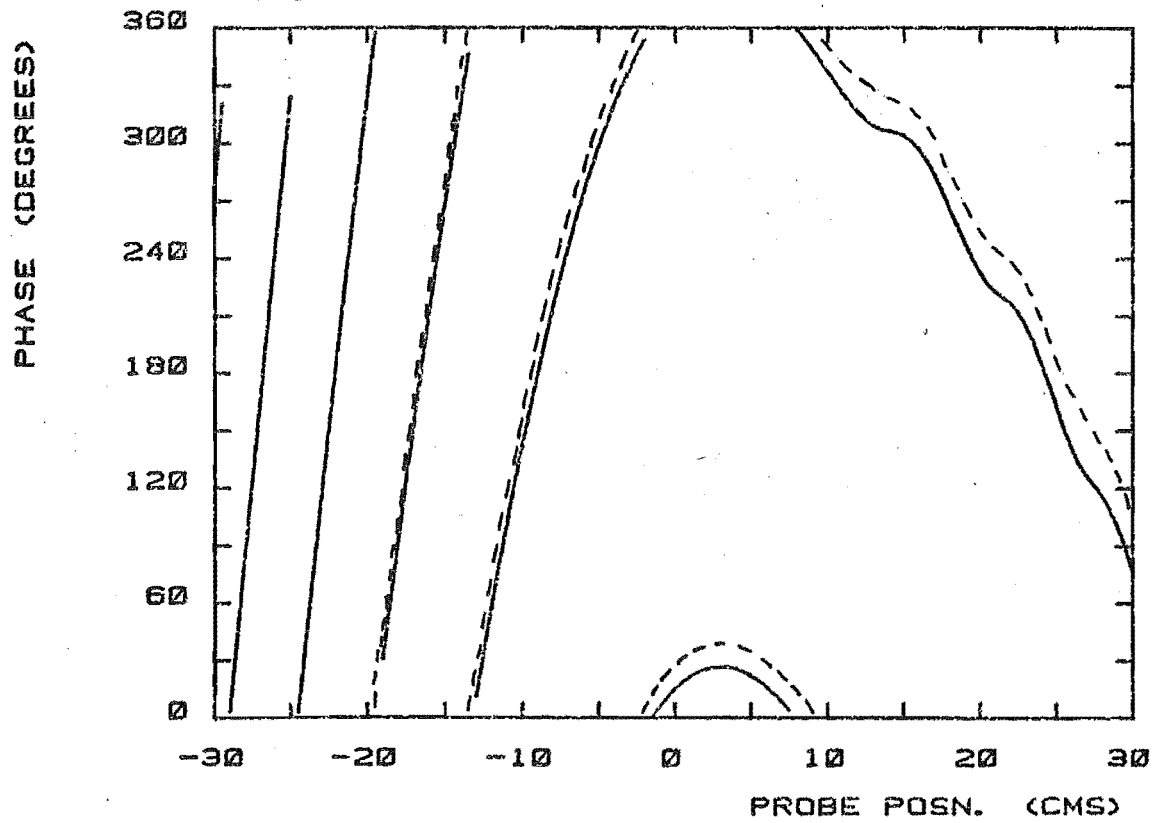

Figure 2.12 Comparison of GTD and PO field in the presence of a Conducting half plane.

Equations (2.88) and (2.89) apply away from shadow and reflection boundaries.

A comparison of (2.88) with (2.89) yields multiplicative correction factors for the Physical Optics field description which will improve results, i.e.

$$C_d = \sin \phi/2 \ \sec \phi_o/2$$
$$C_n = \cos \phi_o/2 \ \csc \phi/2 \qquad (2.94)$$

Figure (2.13) compares the Diffracted Field Strengths of Physical Optics and Exact GTD, showing the regions where differences occur. The reason behind these differences lies in the poor estimation of the surface current near the edge of the half plane. Figure (2.14) shows the current distributions under both Neumann and Dirichlet Boundary Conditions. Close to the edge the errors are the greatest. Away from the edge, the current under Dirichlet boundary conditions approaches the Physical Optics value more quickly than the current affected by Neumann Boundary Conditions. The field from a current distribution is found by a summation or integration. Under such an operation the oscillatory effects of the current distribution will cancel out in a similar manner to stationary phase integration. Under such circumstances, the Physical Optics current is a reasonable average to a point close to the edge, where the actual current sinks to zero.

A theory related to PTD is the Spectral Theory of Diffraction (STD) introduced by Rahmat-Samii and Mittra,(1977). In their formulation they study the scattered field found by convolving the induced currents and the Greens function in the space domain. They also characterize the currents induced in a half plane, reproducing the results of Ufimtsev.

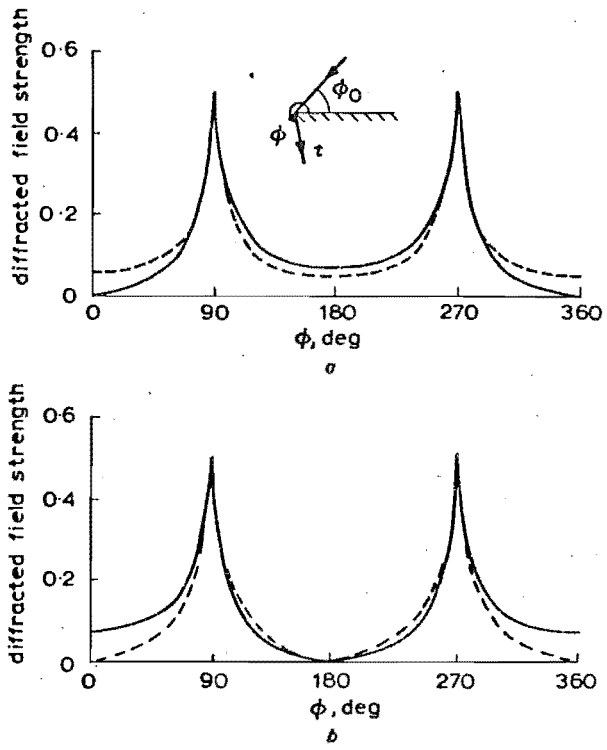

Physical optics and exact solution for diffraction at a half-plane
($\tau = 10\lambda, \phi_0 = 90$ deg.)
a Electric polarisation
b Magnetic polarisation
——— exact
– – – asymptotic physical optics

Figure 2.13 Diffracted Field Strengths from a Half Plane, Comparing Polarizations and Theories. (James, 1976)

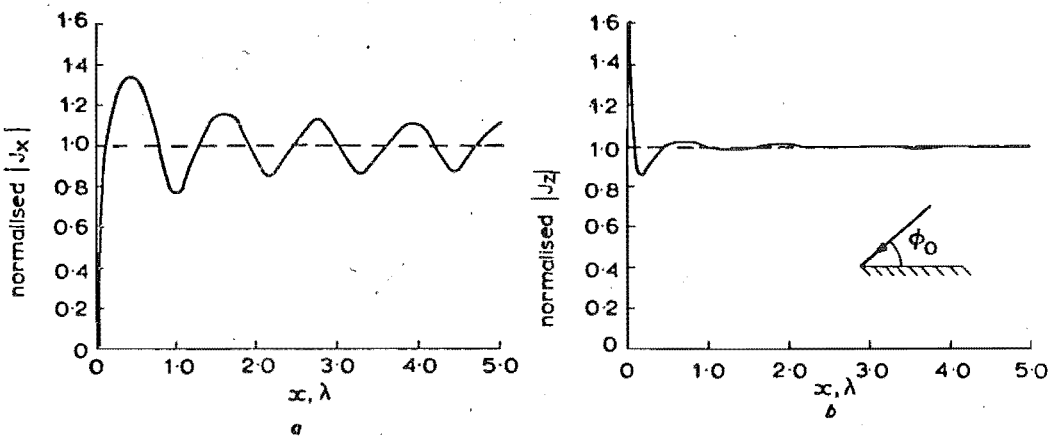

Currents on the half-plane for plane wave incidence at $\phi_0 = 30$ deg.
——— exact
– – – – physical optics

Figure 2.14 Currents Near the Edge of a Half Plane, Comparing Polarizations and Theories. (James, 1976)

The theory is simpler to use in the transformed domain, and can be applied to many situations. A major disadvantage is that the conceptually simple ray theory has to be abandoned.

2.9 EQUIVALENT CURRENT TECHNIQUES

The following is a short summary on equivalent edge currents. About the time that Keller introduced the GTD, Ufimtsev brought forward his PTD and Millar (1955),(1956a), (1956b), theorised on currents about apertures in planes.

In the case of applying GTD to a paraboloidal antenna, or through a circular aperture, a caustic in the diffracted rays will appear in the rear axial direction, when many diffracted rays meet. GTD will predict an infinity at this point. Similarly non-asymptotic GTD predicts infinities at boundaries. In a situation like this other methods need to be applied. To overcome this problem, equivalent sources can be placed at the diffracting edges which can be used in the caustic region.

Consider the far field from an infinite z- directed electric (magnetic) line current source, (James 1976),

$$\underline{E}_z = -j\omega\mu\, \underline{J}e_z \frac{e^{-jk\rho}}{\sqrt{8\pi jk\rho}},$$

$$\underline{E}_\phi = -jk\, \underline{J}m_z \frac{e^{-jk\rho}}{\sqrt{8\pi jk\rho}}. \qquad (2.95)$$

Now taking the case of a half plane, it is possible to reconcile the diffracted field found with GTD, as in Equation (2.66) and (2.67), in a similar manner to the correction of the P.O. diffracted field, to give,

$$\underline{J}_{ez} = \frac{-\underline{E}^{inc}_z}{j\omega\mu} \cdot \frac{4\sin^2\!\tfrac{1}{2}\phi\, \sin\tfrac{1}{2}\phi}{\cos\phi_o+\cos\phi},$$

$$\underline{J}_{mz} = \frac{\underline{E}^{inc}_\phi}{jk} \cdot \frac{4\cos^2\!\tfrac{1}{2}\phi\, \cos\tfrac{1}{2}\phi}{\cos\phi_o+\cos\phi}. \qquad (2.96)$$

These fictitious currents can then be used in the integral solutions i.e. Equation (2.11) to produce a finite field in the caustic directions. The equivalent currents depend upon ϕ, the angle of observation, hence $\underline{Je}_z$ ($\underline{Jm}_z$) will vary, unlike real currents. It can be assumed, however, that over a small variation of ϕ through the transition region, that the effect of the variation of ϕ on $\underline{Je}_z$ or $\underline{Jm}_z$ is very small. In this way the currents do not need to be continuously re-evaluated, considerably simplifying calculations. (James, 1976), (James and Kerdemelidis, 1973).

Moullin (1949), (1954), and Moullin and Phillips, (1952), have attempted to find the actual currents produced by the discontinuities at the edge of a half plane and a strip from an evaluation of the total field at $\phi = 0$ and $\phi = 2\pi$ using Equation (2.40), producing in phase currents and quadrature currents. Changes in currents attributed to the edge are calculated. In their work Moullin and Phillips state that the perturbed currents die out in about $\lambda/10$ away from the edge, in the case of sources very near to the planes and strips. Some doubt has been cast upon the accuracy of computed results of Moullin (1954), (Bowman et al, 1969).

For a curved structure, where the radius of curvature is large, it may be possible to place the same currents near the edge as if it was a half plane, (Plonsey, 1958). This procedure should provide similar results to the asymptotic GTD's and would have the advantage over the ficticious equivalent current method due to the fact that the currents are constant with respect to observation angle.

2.10 MOMENT METHODS

The Moment Method is a procedure used to solve field integration equations which are formulated to find the induced current distributions on scatterers and antennas. The integral equation is reduced to an

algebraic matrix equation, sometimes involving some form of approximation of the Helmholtz Equation or Maxwell's Equations. The matrix equation is inverted to produce a set of multiplicative coefficients for currents arbitrarily distributed about or within the circumference of the scatterer/antenna, (Tsai et al, 1972).

The first definitive text on the subject was produced by Harrington (1968), but many articles in the literature have dealt with this highly numerical form of computation. See for example Mei and Van Bladel, (1963a, 1963b); Andreasen, (1964); Waterman, (1965); Rusch (1975). These workers have extended moment methods from small interior waveguide problems to large two dimensional reflector arrays.

2.10.1 APPLICATION

In this section we will eventually look at the two dimensional case of scattering of a plane wave by an infinite strip. Both Dirichlet and Neumann boundary conditions will be considered simultaneously in the derivation, but the example will consist only of the Dirichlet Boundary Condition.

Looking first at the top relation in Equation (2.10), the top relation in Equation (2.36) and the Greens Function of (2.19), the Electric far field for a collection of electric current line sources can be described as,

$$\underline{E}_z(\underline{\rho}) = \tfrac{1}{4}k\sqrt{\frac{\mu}{\epsilon}}\cdot\frac{1}{J}\int_{S'}\int \underline{Je}_z\,(\underline{\rho}_o)\; H_o^{(2)}\;(k|\underline{\rho}-\underline{\rho}_o|)\; dS', \qquad (2.97)$$

where the integration is over the cross section of the currents.

For Neumann conditions, where the electric vector potential $\underline{F}$ is used for fictitious magnetic line sources,

$$\underline{H}_z(\underline{\rho}) = \tfrac{1}{4}k\sqrt{\frac{\varepsilon}{\mu}}\frac{1}{j}\int_{S'}\int \underline{\rho m}_z\,(\underline{\rho}_o)\,H_o^{(2)}\,(k|\underline{\rho}-\underline{\rho}_o|)\;dS'. \qquad (2.98)$$

In the case of electric line sources only, the magnetic vector potential $\underline{A}$ only is available. In this case the lower relationship in Equation (2.1) with $\underline{F} = 0$ is used, along with the top relationship is Equation (2.10) and the associated Greens Function of (2.18) are used to give,

$$\underline{H}_z(\underline{\rho}) = \frac{1}{4j}\,\hat{z}.\;\nabla \times \int_{\ell'} \underline{J}_{ex}(\underline{\rho}_o)\,H_o^{(2)}\,(k|\underline{\rho}-\underline{\rho}_o|)\;d\ell'. \qquad (2.99)$$

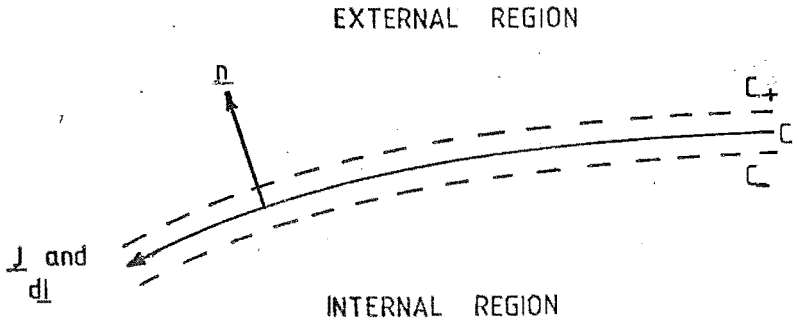

Figure 2.15 Section of a Cylindrical Boundary, Magnetic Polarization.

The boundary condition in the Dirichlet case is,

$$E_z = E_z^i + E_z^s = 0 \qquad \text{on C,} \qquad (2.100)$$

hence E_z^i is the negative of Equation (2.97) on the surface. The Neumann boundary condition is specified by the fact that the field external to C in Figure 2.15 is finite, and zero internal to C. The field discontinuity on C is proportional to the surface current density. Using the right hand rule, if the interior C is on the inside of $d\underline{\ell}'$ then,

$$\underline{J}_{ex} = - \left[\underline{H}_z\right]_{C+} \tag{2.101}$$

as $\underline{J}_s$ is transverse to $\underline{H}_z$, and the relation $\underline{J}_s = \underline{n} \times \underline{H}$ holds on the surface.

The total field $\underline{H}_z$ is the sum of the incident field and the scattered field, hence,

$$\underline{J}_{ex} = - \left[\underline{H}_z^{inc} + \underline{H}_z^{scatt}\right]_{C+}$$

$$= - \left[\underline{H}_z^{inc} + \frac{1}{4j} \hat{z} \cdot \nabla \times \int_{\ell'} \underline{J}_{ex} \cdot H_o^{(2)} (k|\underline{\rho}-\underline{\rho}_o|) d\underline{\ell}'\right]_{C+}. \tag{2.102}$$

In the case of a dielectric scatterer, polarization current sources are spaced throughout the volume rather than upon the surface. The scattered field $\underline{E}^s$ is related to the source current density by Equation (2.97). The total field is the sum of the scattered and the incident field, and within the dielectric the current is related to the total field by,

$$\underline{J}_{ez} = j\omega(\varepsilon-\varepsilon_o)\ \underline{E}_z^{total}, \tag{2.103}$$

$$= j\omega(\varepsilon-\varepsilon_o)\ (\underline{E}_z^i + \underline{E}_z^s),$$

where ε is the permittivity of the dielectric.

Combining Equation (2.97) with (2.103) produces,

$$\underline{E}_z^i = -\frac{k}{4j}\sqrt{\frac{\mu}{\varepsilon_o}}\iint_{S'} \underline{J}_{ez}(\underline{\rho}_o)\, H_o^{(2)}\,(k|\underline{\rho}-\underline{\rho}_o|)\,dS' + \frac{\underline{Jez}}{j\omega(\varepsilon-\varepsilon_o)}\,,$$

$$= -\frac{k^2}{4}\iint_{S'} (\varepsilon_r-1)\,\underline{E}_z^{tot}(\underline{\rho}_o)\,.\,H_o^{(2)}\,(k|\underline{\rho}-\underline{\rho}_o|)\,dS' + E_z^{tot}(\underline{\rho}_o)\,, \qquad (2.104)$$

where ε_r is the relative permittivity, and the result is voltage dependent. Either form of (2.104) is useable.

The method of moments can be applied to Equations (2.97), (2.102) and (2.104) to provide an estimate the surface currents in the case of conductors and the polarization source current or induced voltage in the case of a dielectric.

The method of moments derivation is in an Appendix.

2.10.2 STRIP EXAMPLE

The method of moments was applied to a 2λ strip under Dirichlet conditions. In order to find the currents on the back of such a strip, the strip was given a width of $\lambda/20$. It is known that the current on a strip has a $y^{-\frac{1}{2}}$ singularity away from the edges where y is measured from an edge, hence in one case the currents were positioned together about the edges as shown in Figure 2.16a, (Tsai et al, 1972).

Evenly spaced currents were tried, as shown in Figure 2.16b-d. The current densities were calculated and their plot is shown Figure 2.17a-d. The current density in Figure 2.17a will follow the real current density as it varies more accurately than in Figure 2.17b-d.

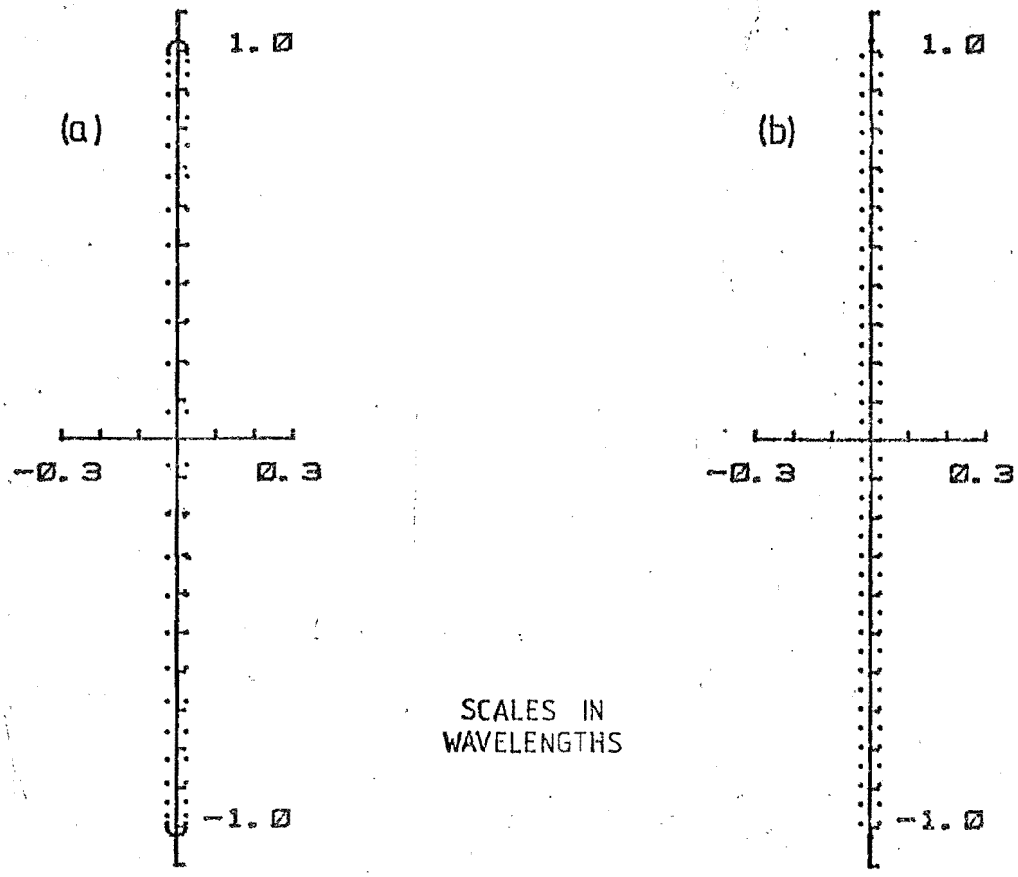

a) 68 unevenly spaced currents

b) 84 evenly spaced currents

c) 42 evenly spaced currents

d) 21 evenly spaced currents

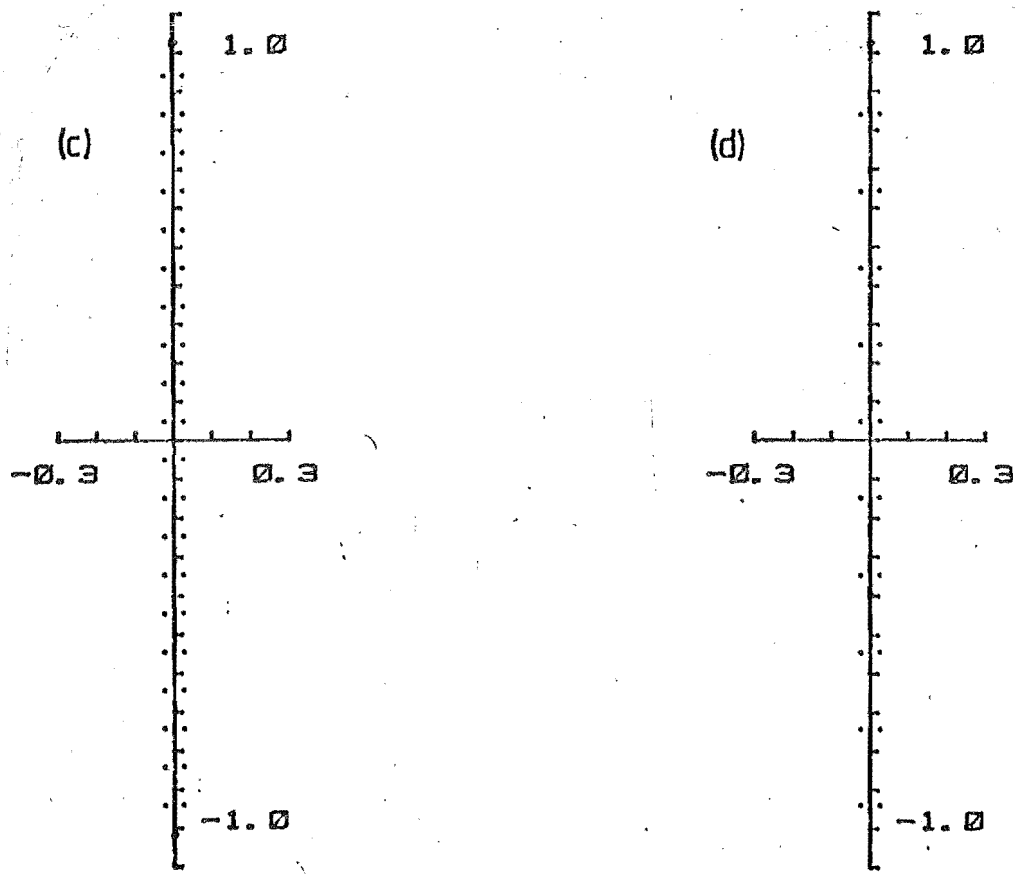

Figure 2.16 Placement of Moments currents on a 2λ slit.

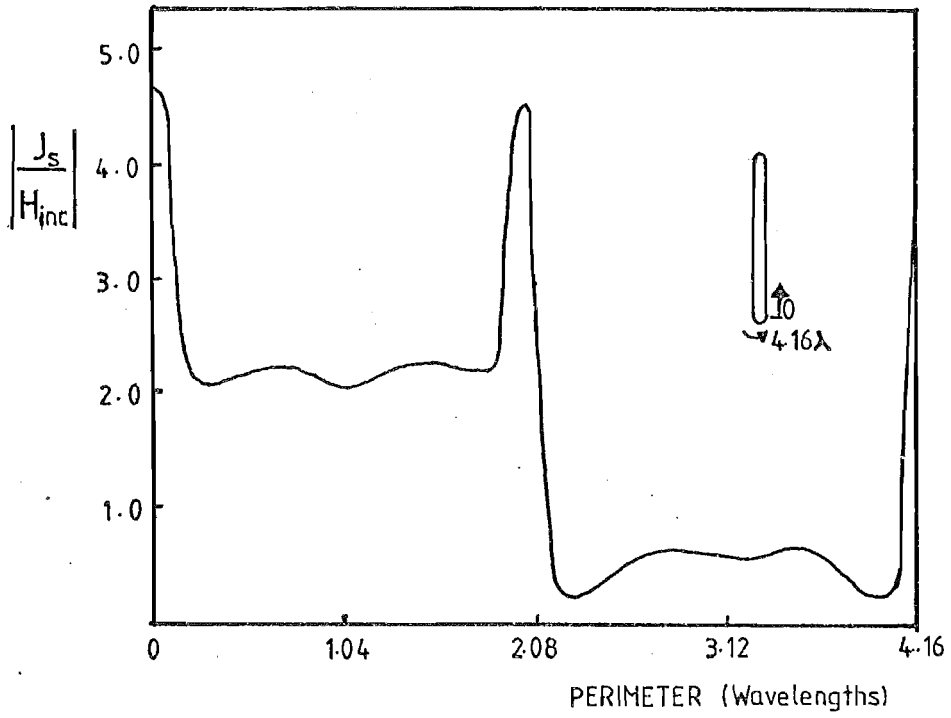

a) 68 current case

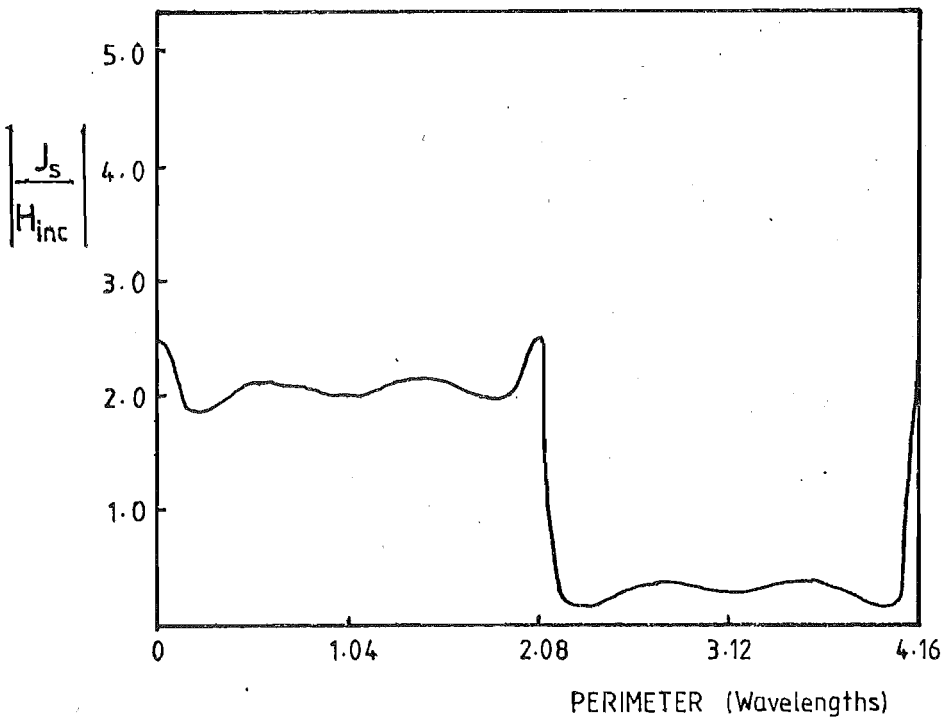

b) 84 current case

Figure 2.17 Moments Current Densities on a 2λ Conducting Strip.

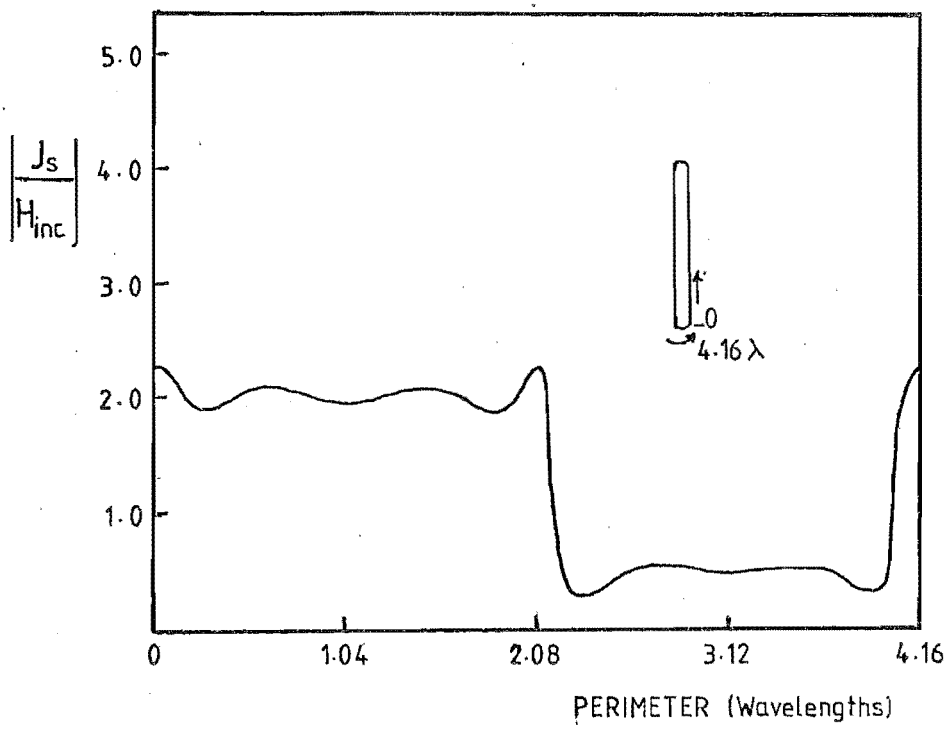

c) 42 current case

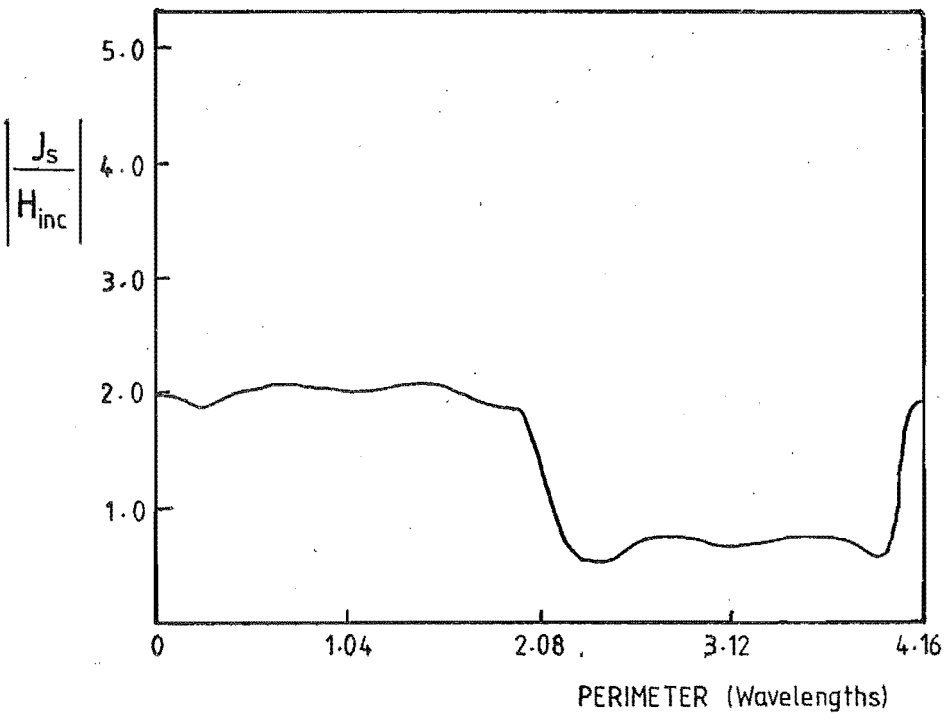

d) 21 current case

Figure 2.17 (Continued).

The non-symmetry in Figure 2.17d is a result in the non-symmetrical placement of currents shown in Figure 2.16d. Figure 2.18a-d are the scattered far fieldsof the currents when the strip is under plane wave illumination. For such a variation in current densities for the cases of evenly spaced currents the far fields are very similar. The accuracy of the estimate can be compared with the scattered fields calculated by Clemmow GTD. (Figure 2.18e) and the exact representation which will be studied in Chapter 3 (Figure 2.18f). The phase at 0^{o} and 180^{o} varies by 18^{o} for the moments calculated scattering. This corresponds to the $\lambda/20$ thickness of the strip.

For this example, the GTD solution was the quickest to calculate, while the moment method solutions took the greatest C.P.U. time. Not surprisingly then the time taken was dependent upon the number of currents to be matched, and it became clear that there was a feasible upper limit of 250 currents before the computer, a Vax 11-780, spent too much time transferring data between disk and core. The biggest time factor involved the inversion of the scatterer matrix, which was done by the Gauss-Jordan method using a modified version of a DECSSP routine called MINV to take complex variables.

The number of currents severely limits the scatterer size, especially as it is generally suggested that the distance between surface currents be less than $\lambda/10$, hence in the case of a 3 dimensional surface to give 3 dimensional radiation the surface is limited to a few wavelengths. In the case where a surface variation is slow with a large radius of curvature, it may be possible to define surface areas where Physical Optics can be used and edges where equivalent or moment method edge currents may be utilised.

In the case where a problem is being run with only minor changes, once the currents far away from the area being changed have been

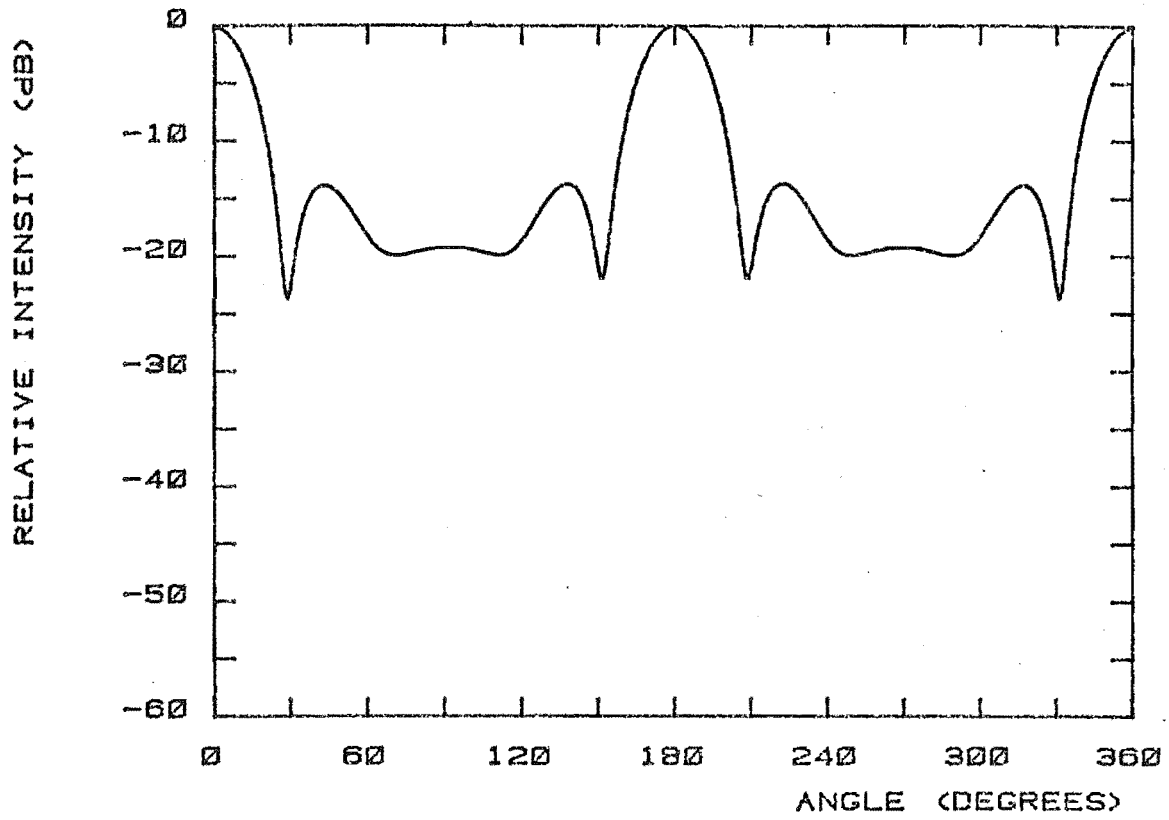

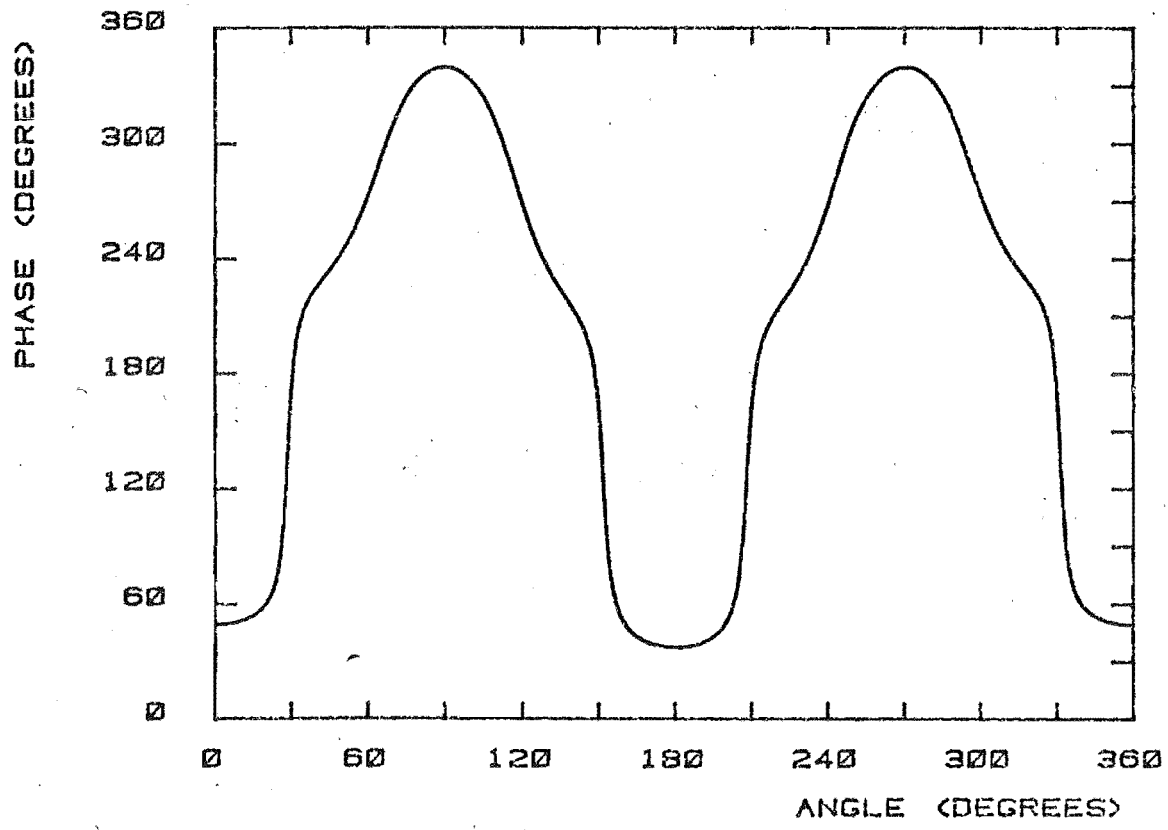

a) Moments method, 68 unevenly spaced currents case.

Figure 2.18 Scattered Fields off a 2λ Conducting Strip, a comparison of Theories.

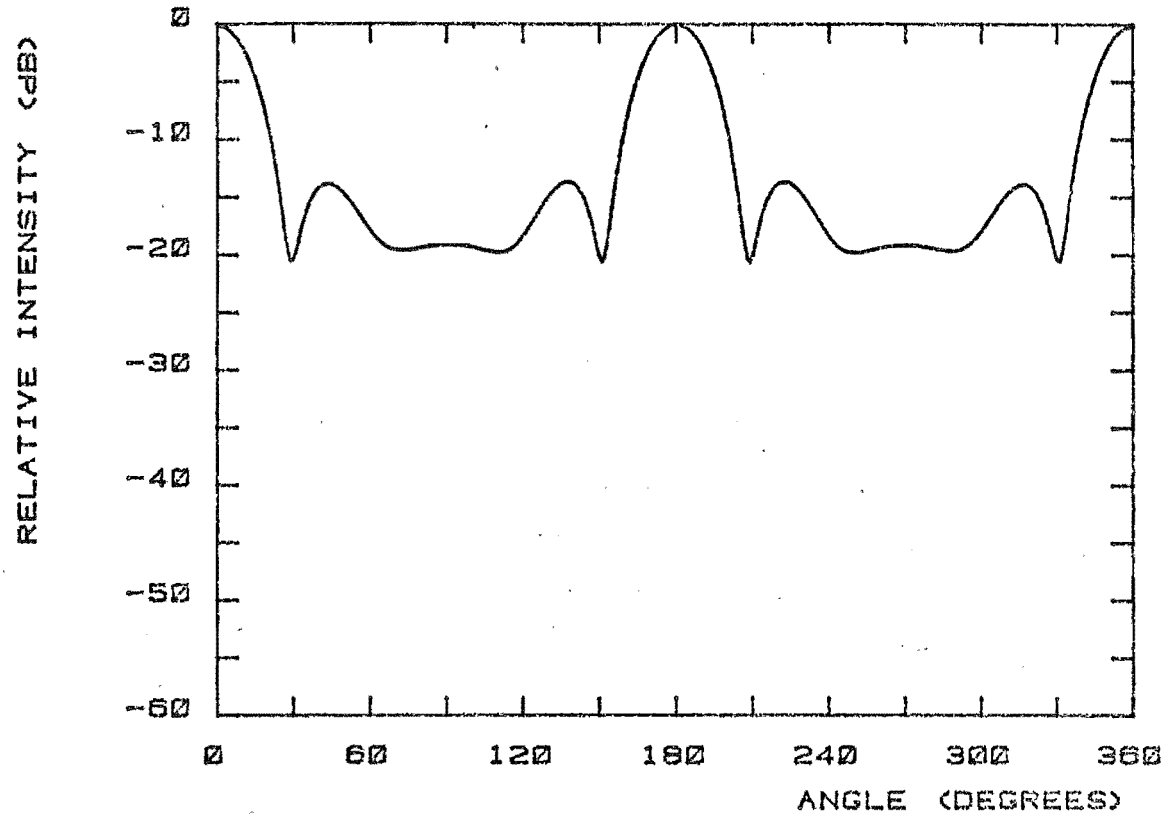

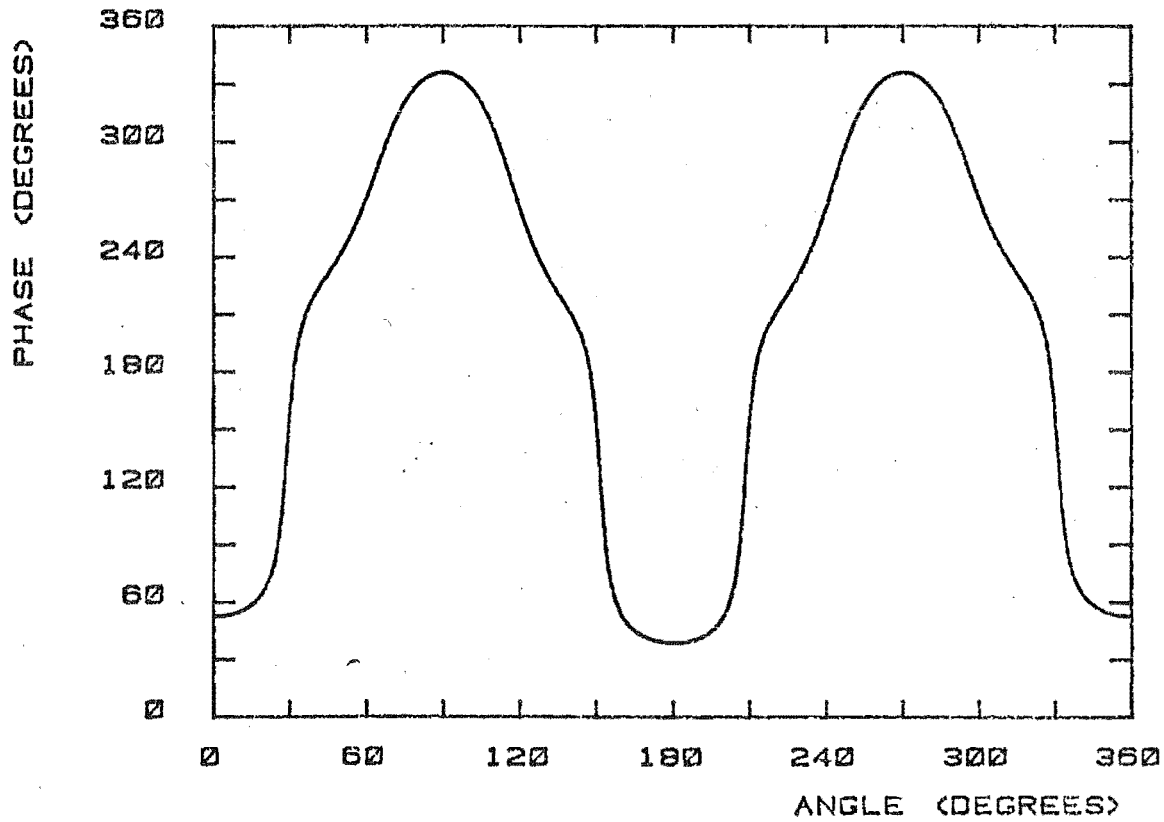

b) Moments Method, 84 evenly spaced currents case.

Figure 2.18 (Continued).

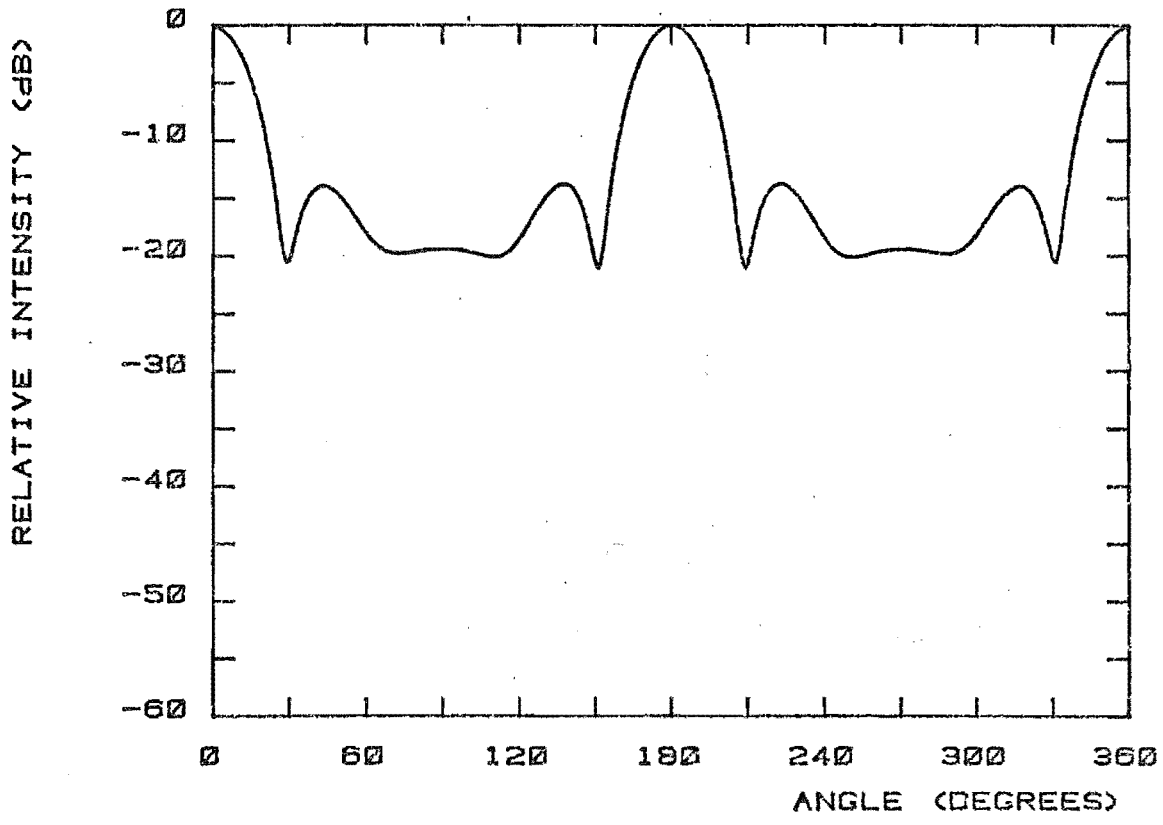

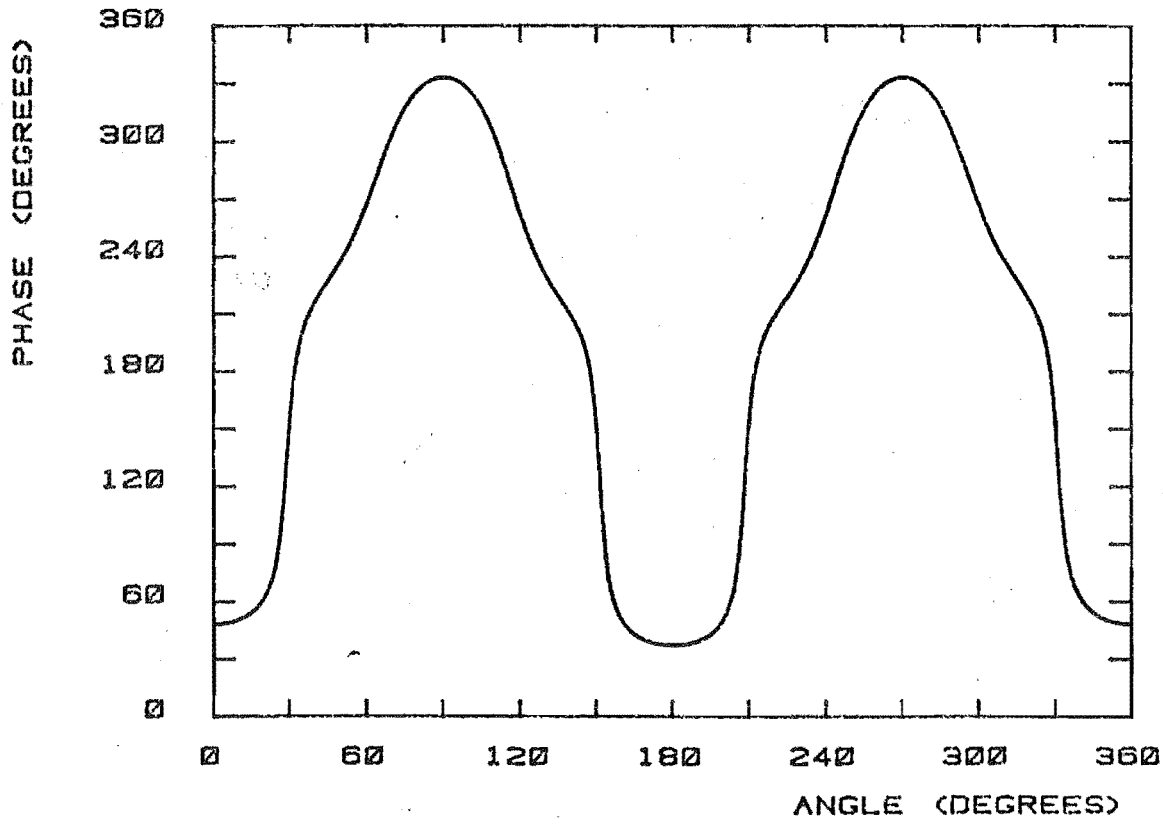

c) Moments Method, 42 evenly spaced currents case.

Figure 2.18 (Continued).

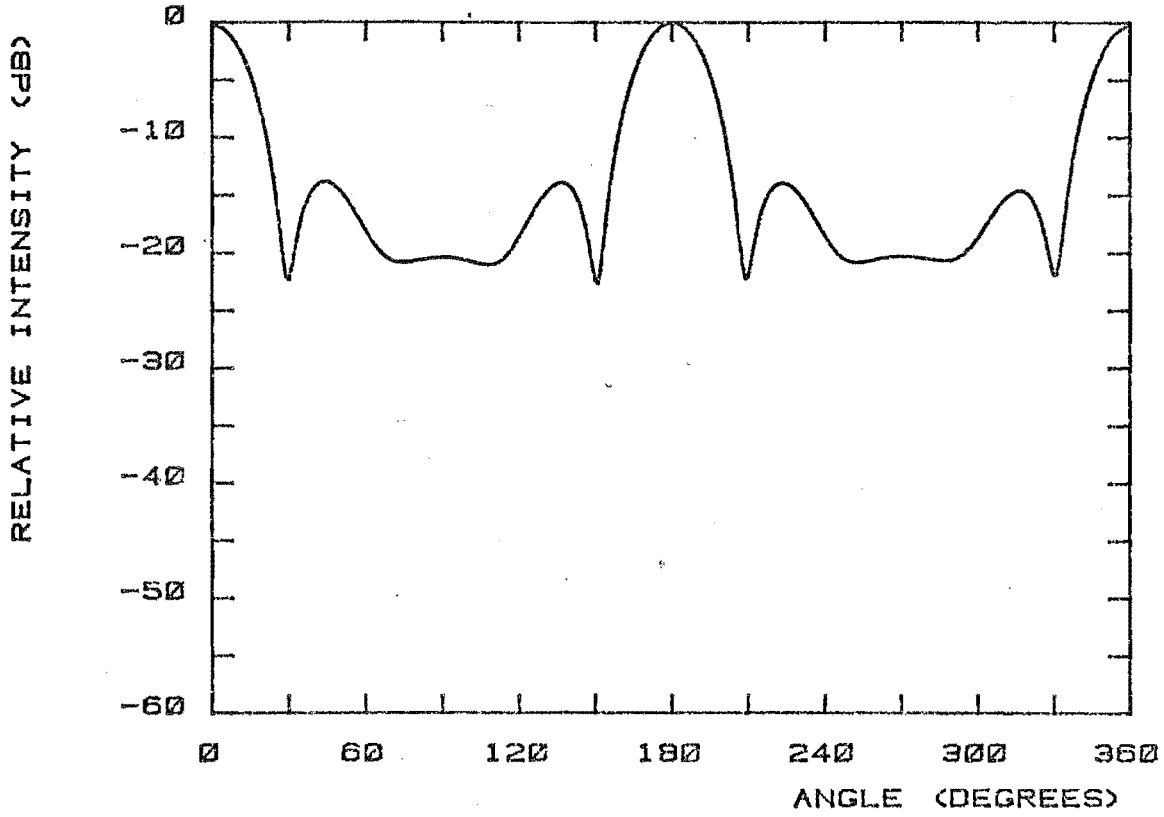

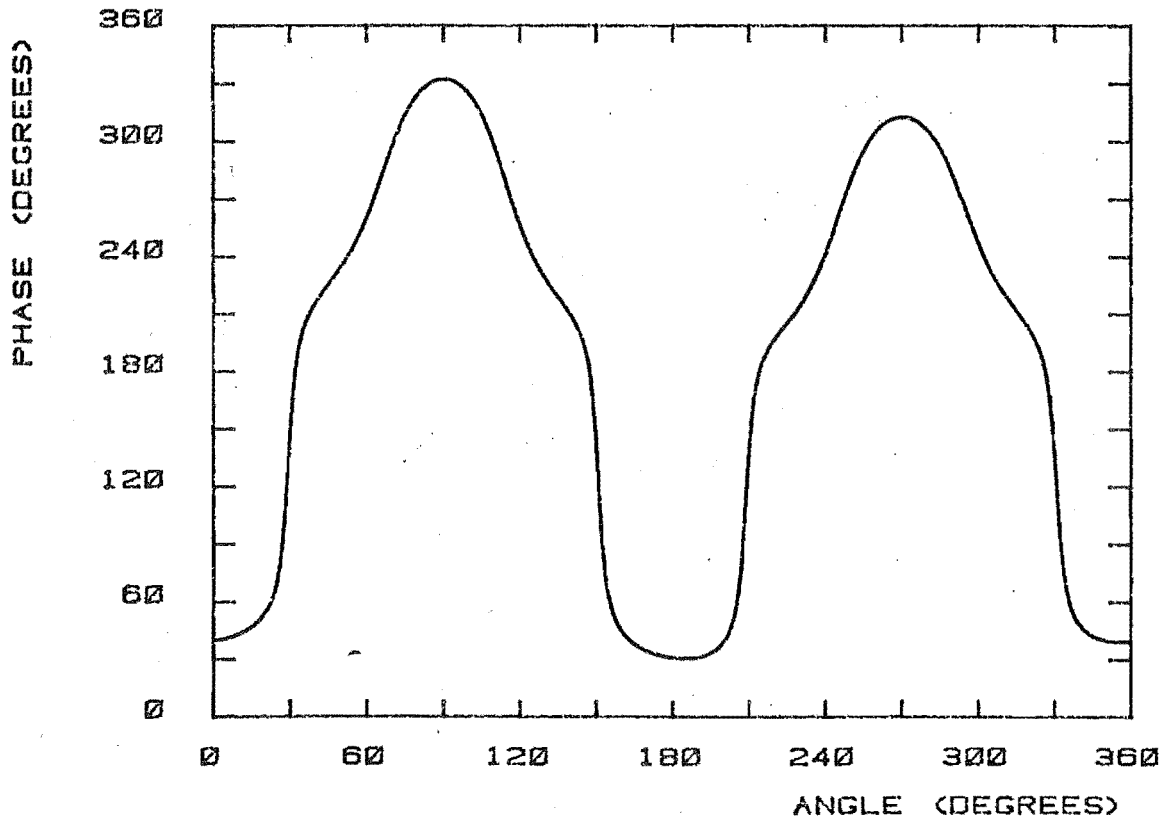

d) Moments Method, 21 evenly spaced currents case.

Figure 2.18 (Continued).

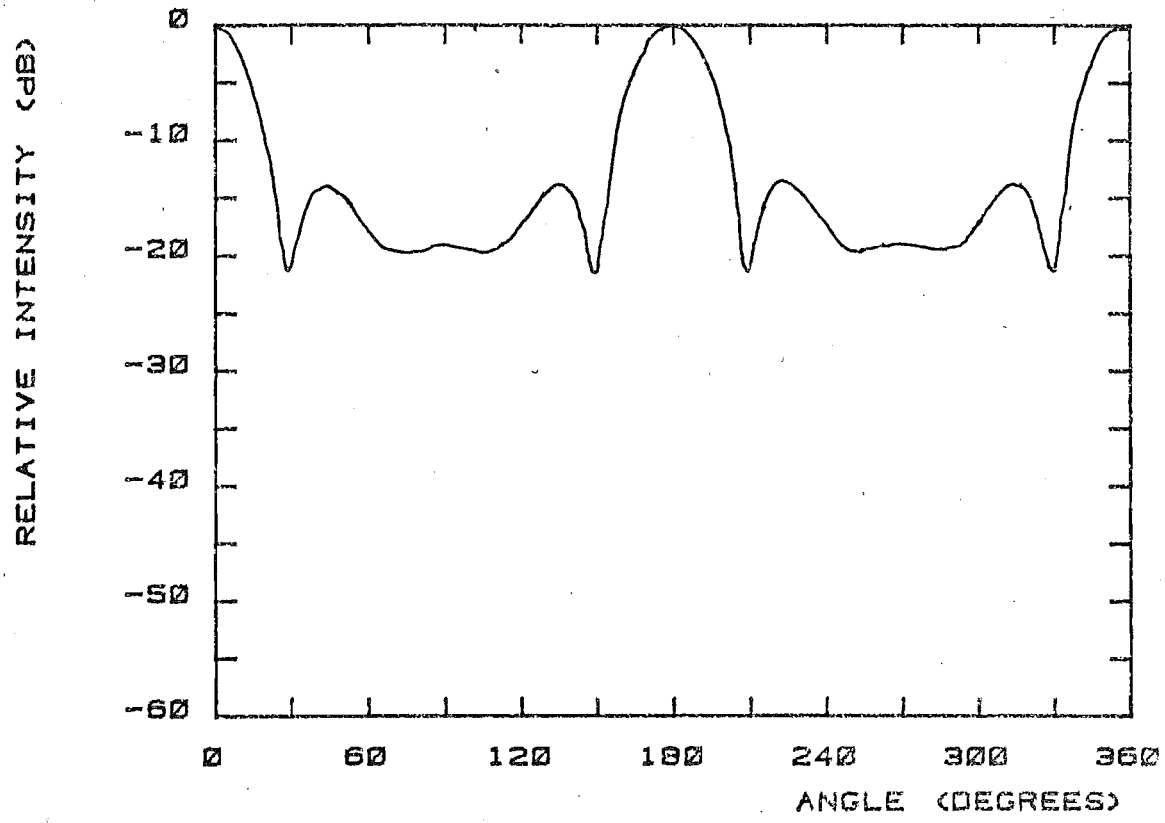

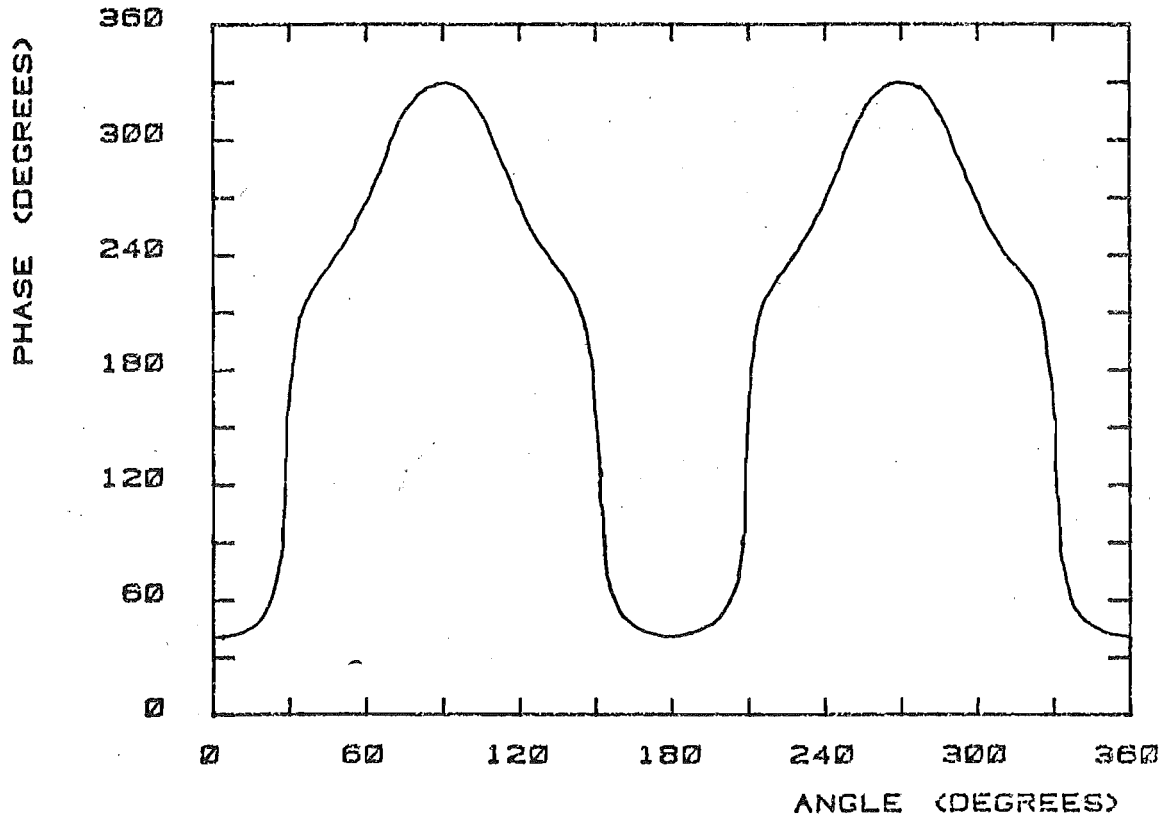

e) GTD result (Equation, (2.66)).

Figure 2.18 (Continued).

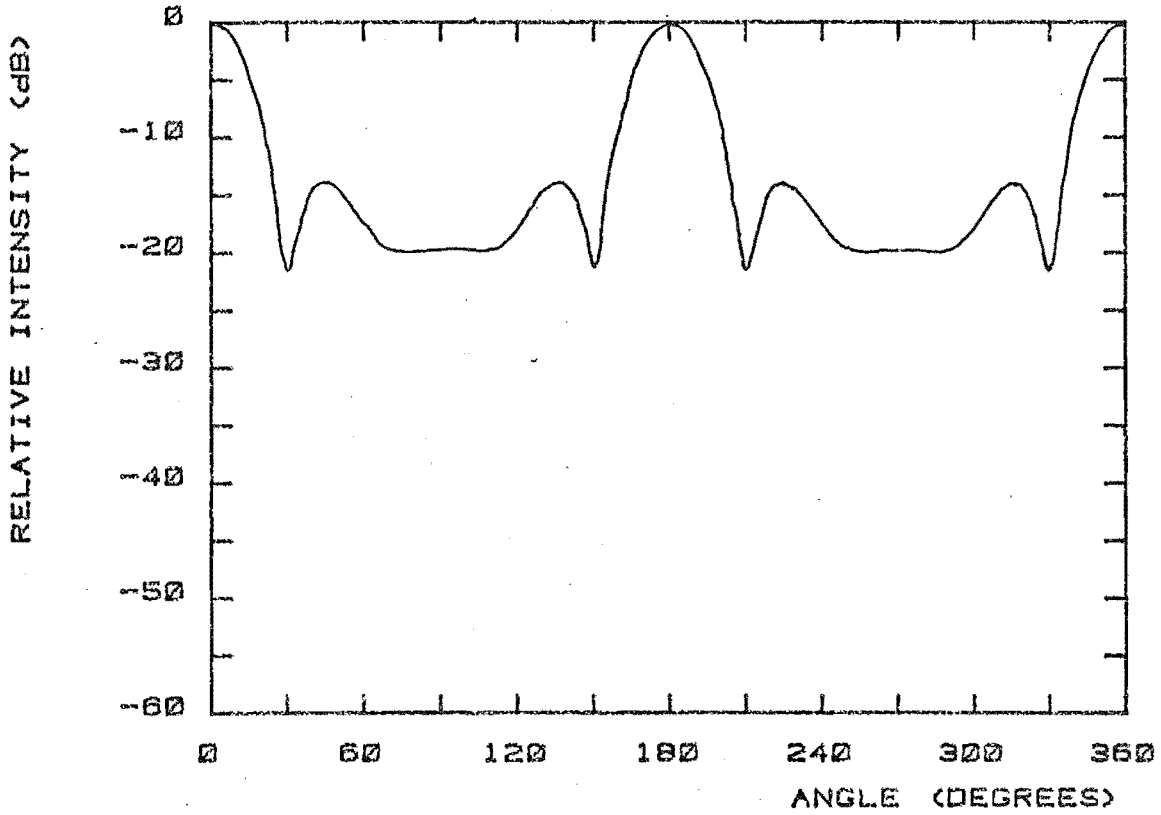

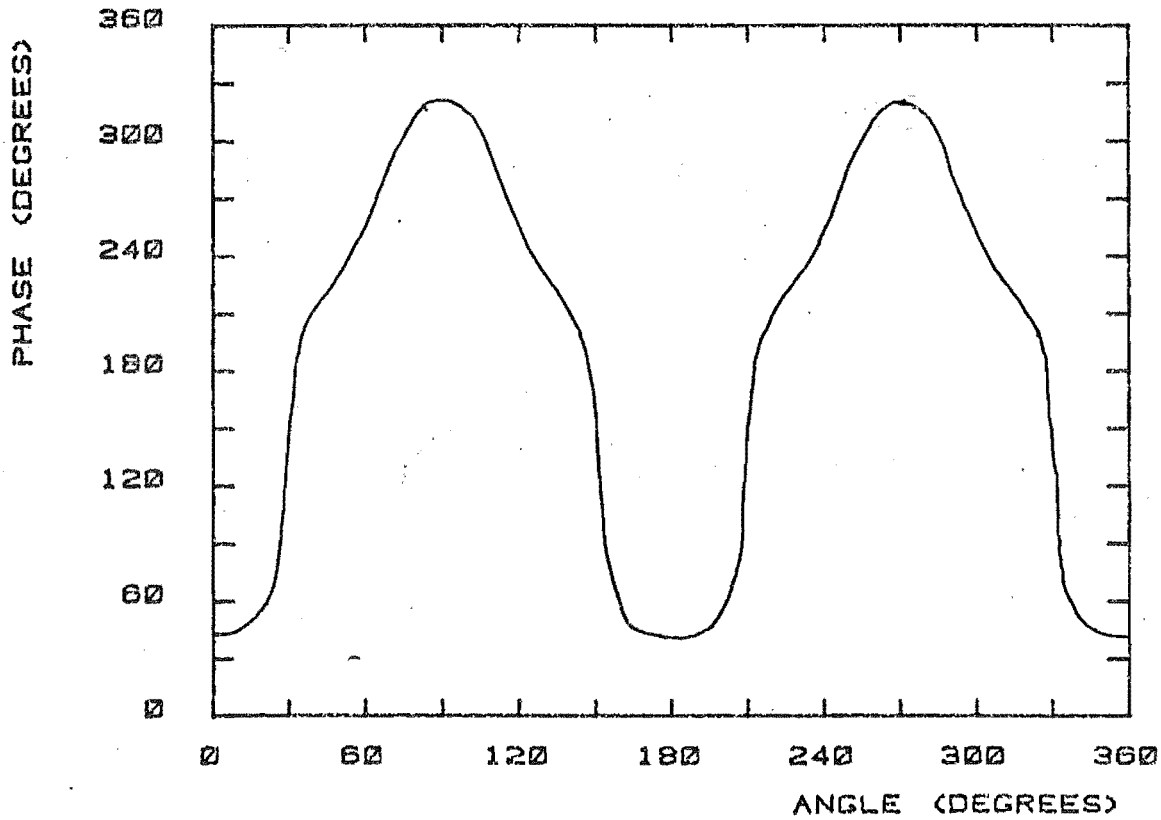

f) Exact, Mathieu Theory, (Appendix C).

Figure 2.18 (Continued).

determined, they can then be included as sources and be used in the source matrix. This will reduce the size of the scatterer matrix to be inverted with a consequent faster solution time. This concept will be studied in Chapter 4.

In an attempt to study half plane diffraction using moment methods we try to approximate the currents away from the diffracting edge by physical optics and calculate the currents about the edge by moment methods, (Azarbar and Shafai, 1978).

Azarbar and Shafai assume Physical optics currents up to the edge, and add difference currents to account for the effect of the edge. At each point, under this method, there will be a summed Physical Optics current and a difference current. The difference currents are found by the Method of Moments. A problem associated with this method is the evaluation of logarithmic singularities caused by the Physical Optics source currents. This can be alleviated by assuming Physical Optics currents are a good description of the surface currents more than 1λ away from the edge. About the edge may be placed moments currents, where the spatial oscillatory currents occur, as in Figure 2.14.

The number of moments currents will be reduced in comparison to those of Azarbar and Shafai resulting in a smaller scatterer matrix to invert. Figure 2.19 shows the resultant field for half plane diffraction using the combination of Physical Optics and Method of Moments using 56 edge currents. Results compare very closely to those of GTD, and Experiment also shown in Figure 2.19.

Another hybrid form of the Method of Moments involves the use of Geometrical Optics and GTD to produce modified Moments Currents and GTD induced currents. (Thiele and Newhouse, 1975), (Burnside et al, 1975), (Ekelman and Thiele, 1980).

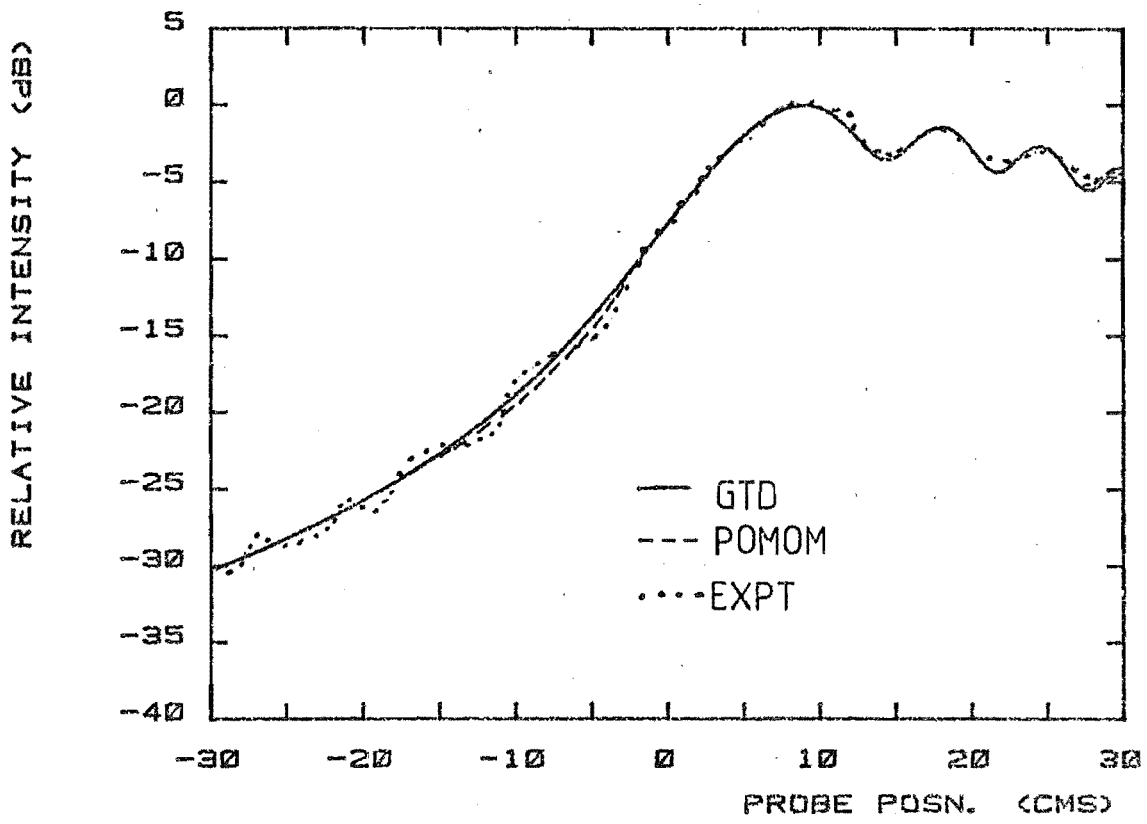

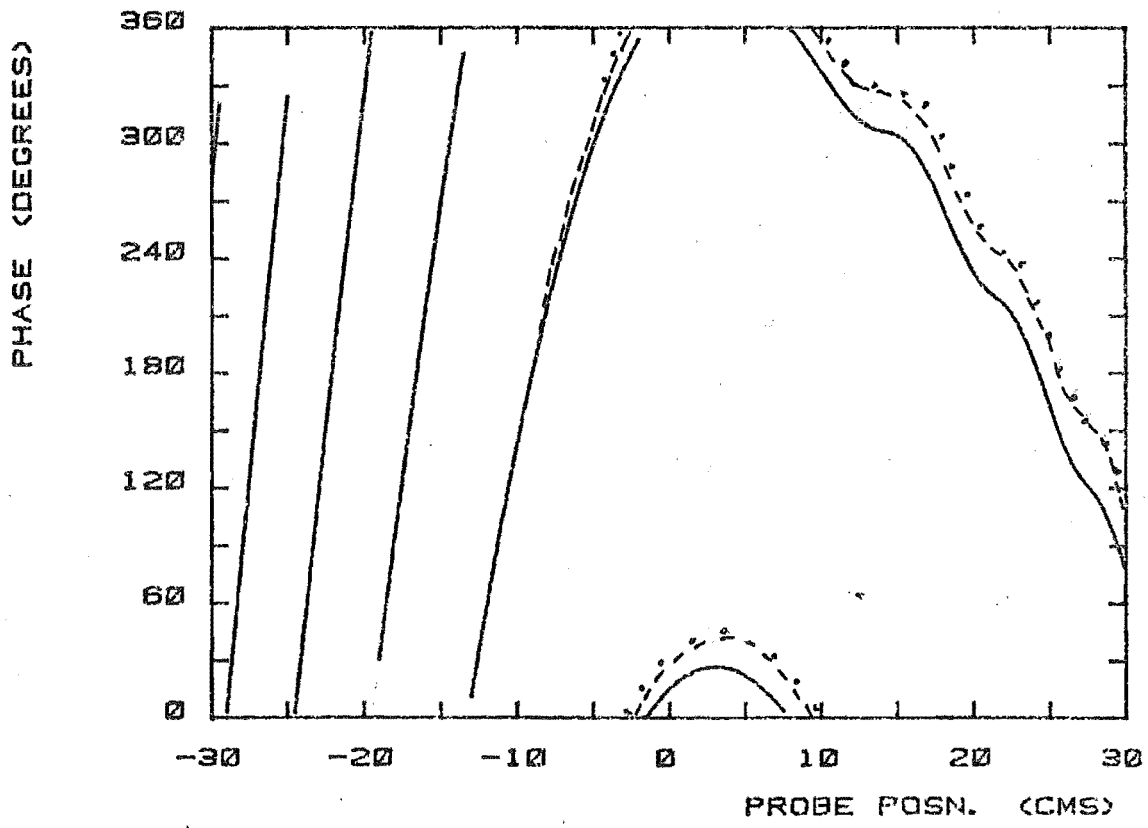

Figure 2.19 A comparison of the field at the probe in the Geometry of Figure 2.11, GTD; Physical Optics cum Method of Moments; Experiment.

CHAPTER 3

SLIT DIFFRACTION

'Curiouser and curiouser!', cried Alice.

Lewis Carroll

3.1 SLIT DESCRIPTION

The simplest two edge diffraction problem, is that of either the infinite slit or the infinite strip. The slit and strip are related by Babinet's Principle (Bouwkamp 1954), hence if it is possible to characterize the properties of one, the behaviour of the other is available. In this chapter we will study the slit with a view to placing one in the reflector of a parabolic cylinder antenna. A major difference between a slit in a parabolic reflector and theoretical infinite slit is that the conducting planes no longer share the same plane as the slit gap. The slits are shown in Figure 3.1.

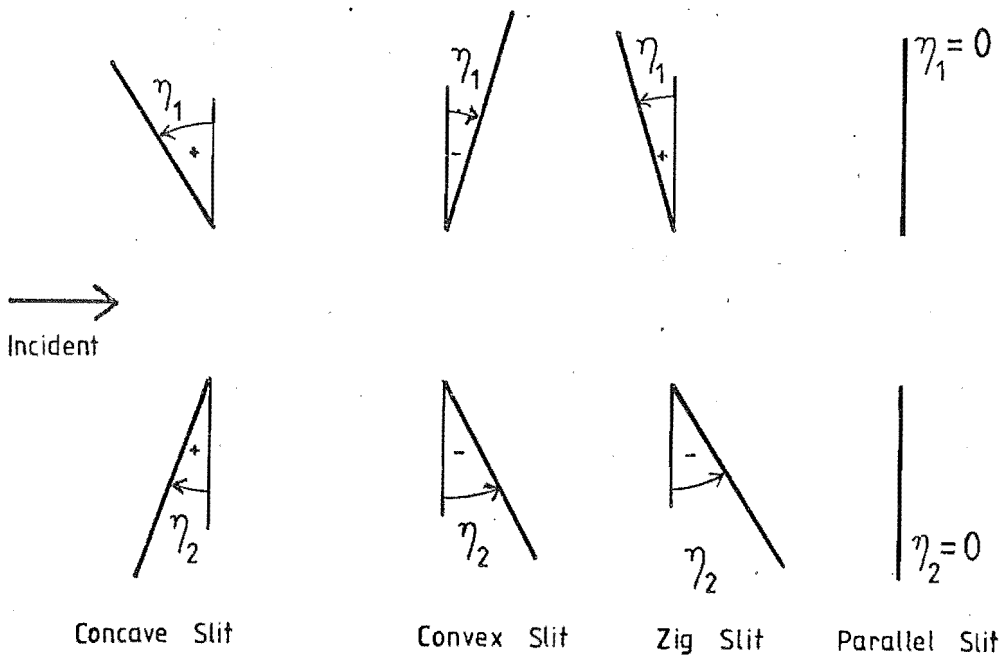

Figure 3.1 Inclined Plane Slits.

In Figure 3.1, η_1 and η_2 are the angles of inclination of planes Σ_1 and Σ_2 with respect to the aperture plane in the slit. η_1 and η_2 are positive when the planes are inclined towards the source and are negative when the conducting planes are inclined away from the source. The slits have been named as follows:

a) Parallel slit, when $\eta_1 = \eta_2 = 0$,

b) Concave slit, when $\eta_1 > 0$ and $\eta_2 > 0$,

c) Zig slit, when $\eta_1 > 0$ and $\eta_2 < 0$, or $\eta_1 < 0$ and $\eta_2 > 0$,

d) Convex slit, when $\eta_1 < 0$ and $\eta_2 < 0$,

No conducting strips related to the non-parallel slits can satisfy Babinet's Principle.

In this chapter we will study and compare the electromagnetic transmission of such slits, utilising the theories introduced in chapter 2.

3.2 SEPARATION OF VARIABLES TECHNIQUE APPLIED TO A PARALLEL SLIT

Following the procedures of Section 2.2 the Helmholtz Wave Equation can be separated into two independent ordinary differential equations in the Elliptic Cylinder coordinate system, (Figure 3.2).

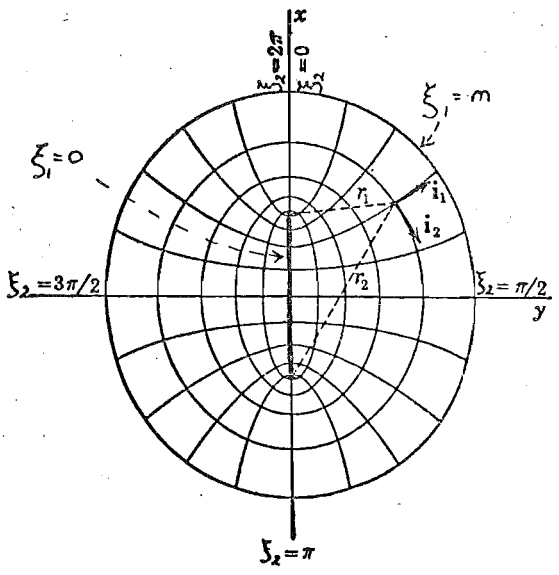

Figure 3.2 Elliptic Cylinder Coordinate System.

The elliptic cylinder $\xi_1 = 0$ is a strip of width 2d, the interfocal length.

In the two dimensional case, where there is no z-dependence, the scalar source-free Helmholtz Equation, Equation (2.5) can be written in the form (Morse and Feshbach 1953, Chapter 5).

$$\frac{\delta^2\psi}{\delta\xi_1^2} + \frac{\delta^2\psi}{\delta\xi_2^2} + d^2k^2 (\cosh^2\xi_1 - \cos^2\xi_2)\ \psi = 0 , \tag{3.1}$$

where,

$$x = d \cosh (\xi_1) \cos (\xi_2),$$
$$y = d \sinh (\xi_1) \sin (\xi_2), \tag{3.2}$$

Now the ψ can be formulated as a product of two factors,

$$\psi = F(\xi_1).\ G(\xi_2) , \tag{3.3}$$

where,

$$-\frac{d^2F}{d\xi_1^2} + (b - d^2k^2 \cosh^2\xi_1)F = 0, \tag{3.4}$$

and,

$$\frac{d^2G}{d\xi_2^2} - (b - d^2k^2 \cos^2\xi_2)\ G = 0, \tag{3.5}$$

where b is a constant, d is half the interfocal distance of the ellipses in Figure 3.2 and k is the wave number, $\frac{2\pi}{\lambda}$.

Equation (3.5) is Mathieu's Equation for real arguments, while (3.4) is Mathieu's Equation for imaginary arguments.

Equations (3.4) and (3.5) can be solved in terms of Mathieu Functions, (Morse and Feshbach, 1953). The Mathieu Functions are found by a slowly convergent infinite series. (Blanch 1966, Clemm 1969).

The slit or strip is the ellipse $\xi_1 = 0$ which is a straight line of length 2d. The slit can be varied in width by altering d, but care must be taken as the Mathieu Functions become increasingly more difficult to handle as d is increased. The boundary conditions are set at the slit, and an outward travelling wave in terms of a series of Mathieu Functions is formulated with its source being the slit.

The amplitude and phase of the outward wave is adjusted to cancel the effects of the source (also a series of Mathieu functions) giving a resultant total field.

This field may be split into an incident field and a scattered field. The details may be found in an Appendix.

Repeating results from the Appendix, the field transmission by a slit, under excitation from a cylindrical source with Dirichlet Boundary Conditions at the conducting planes may be written as,

$$\psi_{trans}^{cyl} = 4 \sum_{m=1}^{\infty} \frac{1}{M_m^{o}(h)} \cdot So_m(h,\cos\xi_2^{o}) \cdot So_m(h,\cos\xi_2^{p}) \cdot \frac{Jo_m'(h,1)}{Ho_m'(h,1)} Ho_m(h,\cosh\xi_1^{o}) Ho_m(h,\cosh\xi_1^{p}), \qquad (3.6)$$

where $h^2 = d^2k^2$,

$M_m^{o}(h)$ is a normalizing constant associated with Mathieu Functions.

$So_m(a,b)$ is an odd Angular Mathieu Function of the mth order.

$Ho_m(a,b)$ is an odd Radial Mathieu Function of the fourth kind, mth order.

$Jo_m'(h,1)$ is $\left.\frac{dJo_m(h,\cosh\xi_1)}{d\xi_1}\right|_{\xi_1 = 0}$,

$Jo_m(a,b)$ is an odd Radial Mathieu Function of the first kind, order m and,

$$Ho_m'(h,1) \text{ is } \left.\frac{d\, Ho_m(h,\cosh\xi_1)}{d\xi_1}\right|_{\xi_1 = 0},$$

and the source is located at (ξ_1^o,ξ_2^o) with the observation point at (ξ_1^p,ξ_2^p).

For plane wave illumination, a large argument expansion of $Ho_m(h,\cosh\xi_1^o)$ similar to that of a Hankel Function, may be used (Morse and Feshbach, 1953). Thus as $\cosh\xi_1^o \to \infty$, i.e. the source point is removed an infinite distance from the slit,

$$Ho_m(h,\ \cosh\xi_1^o) \xrightarrow{\xi_1 \to \infty} \frac{1}{\sqrt{h\cosh\xi_1^o}} \exp\left(j\left(-h.\cosh\xi_1^o + \frac{\pi}{2}(m+\tfrac{1}{2})\right)\right). \qquad (3.7)$$

Normalising Equation (3.7) and substituting into Equation (3.6) gives,

$$\psi_{trans}^{plane} = \sqrt{8\pi} \sum_{n=1}^{\infty} j^m \frac{1}{M_m^o(h)}\ So_m(h,\cos\xi_2^o).\ So_m(h,\cos\xi_2^p).$$

$$\cdot \left(\frac{Jo_m'(h,1)}{Ho_m'(h,1)}\right).\ Ho_m(h,\cosh\xi_2^p). \qquad (3.8)$$

The Equations (3.7) amd (3.8) can be programmed using Mathieu Function generation routines by Clemm, (1969), which will provide results for slits up to two wavelengths wide without too long computations.

For wider slits an excessively large number of terms have to be employed and the precision of results is suspect.

The production of the Mathieu Functions rely upon finding the Eigenvalues of Mathieu's Equation in Equations (3.4) and (3.5). The actual Functions are then determined by the appropriate addition of Eigenfunctions, depending upon normalization used and whether radial or angular functions are required. Blanch (1966), produced an algorithm, to give the Eigenvalues of Mathieu's Equation by the evaluation of continued

fractions. Clemm (1969) used Blanch's algorithm to provide a Fortran Code routine to calculate the Eigenvalues and to then find the Eigenfunctions using either Ince, Stratton or Neutral normalization (Blanch, 1966), (Ince, 1932), (Stratton et al, 1941). The Stratton normalization was used in this thesis, mainly because most of the applied material using Mathieu Functions did so, i.e. (Morse and Feshbach, 1953), (Stratton, 1951), (Bowman et al, 1969). At a test, Equation (3.6) was evaluated for various slits up to 2λ wide using each kind of normalization available in Clemm's program. Results showed negligible differences, although Blanch recommends that the Stratton normalization be avoided as there can be a loss of significance.

Under Neumann boundary conditions at the slit planes a formulation involving even Mathieu Functions is used, see Appendix.

From the Appendix it can be seen that the solution of diffraction off a strip is found, and is applied to the slit by Babinets principle, hence referring to the argument earlier on, the Separation of Variables Technique cannot be applied to non-parallel slits.

The exact form, using the separation of variables technique is limited to 11 coordinate systems (Morse and Feshbach, 1953). Conformal transformation of the boundaries cannot be performed for the Helmholtz equation, but are only applicable to potential problems involving the Laplace Equation, (Kraus, 1953), i.e.

$$\nabla^2\psi = 0 \tag{3.9}$$

Note that the $k^2\psi$ term is missing in this equation, allowing time and distance to be independent of each other. Under these circumstances we are forced to abandon the Mathieu representation, having to rely upon approximate formulations to describe transmitted fields through slits with variable inclined planes.

3.3 EDGE DIFFRACTION THEORIES APPLIED TO THE PARALLEL PLANE SLIT

Keller, (Keller, 1962), reasoned that a slit could be thought of as a pair of half planes brought close together. Thus diffraction by a slit can be described as the independent superposition of the two independent diffractions by each of the half planes to a first approximation.

Keller was able to apply his 'diffraction coefficient', Equation (2.67), to the problem of slit diffraction by treating each edge independently. The geometry of the problem is found in Figure 3.3.

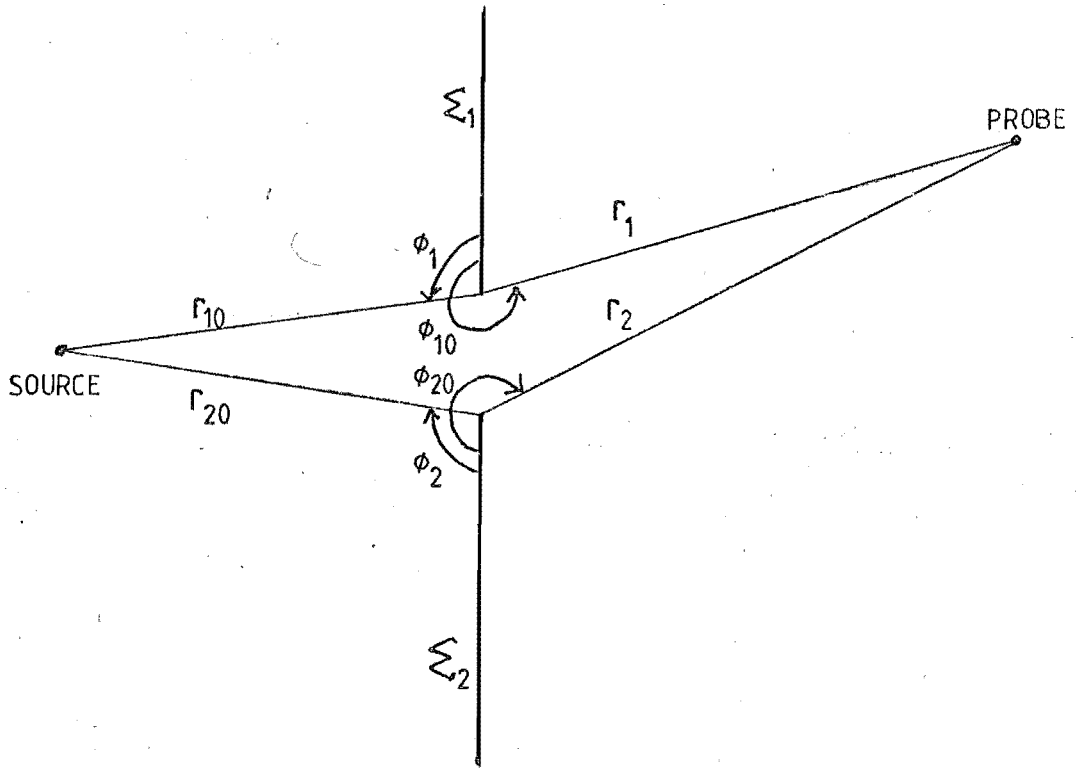

Figure 3.3 Diffraction Geometry for Parallel Plane Slit.

$$\left.\begin{matrix} E_2^{diff} \\ H_z^{diff} \end{matrix}\right\} = \frac{-e^{jk(r_{10}+r_1)}}{8\pi jk\sqrt{r_1 r_{10}}} \left[\frac{1}{\cos\frac{1}{2}(\phi_1-\phi_{10})} \mp \frac{1}{\cos\frac{1}{2}(\phi_1+\phi_{10})}\right]$$

$$- \frac{e^{jk(r_{20}+r_2)}}{8\pi jk\sqrt{r_2 r_{20}}} \left[\frac{1}{\cos\frac{1}{2}(\phi_2-\phi_{20})} \mp \frac{1}{\cos\frac{1}{2}(\phi_2+\phi_{20})}\right] \qquad (3.10)$$

If Equation (3.10) is to be used successfully, an important condition must be fulfilled, that is, r_1 and r_2, the distances of the edges to the observation point, must be extremely large. Ideally this would place the observation point nearly at infinity. Under such circumstances, the rays from the edges to the observation point would be parallel and the shadow boundaries associated with each edge would occur at the same observation angle. Both expressions in brackets in Equation (3.10) exhibit singularities at their shadow boundaries.

In the situation above, however, when both singularities are at the same observation angle, the infinities will cancel, giving a smooth transition in the diffracted field amplitude across the shadow boundary.

In situations where r_1 and r_2 have specified lengths, the singularities occur at different probe positions. To overcome this, the Fresnel integral representation, Equation (2.74), will be required, and a geometrical optics component to satisfy direct incident radiation will then be included for observation angles between the shadow boundaries, (Menendez and Lee, 1977).

'Clemmow' type diffraction can be applied to the slit problem in a similar manner to Keller GTD, (Hamilton and Kerdemelidis, 1981). Figure (3.4) shows a parallel slit geometry for source and observation point a finite distance away from the slit.

For this analysis we shall assume Dirichlet boundary conditions at the slit planes, although Neumann boundary conditions are easily taken care of by the sign changes as shown in Equations (2.78) and (2.79). The source has an image placed directly opposite on the other side of the slit. Three regions are defined on the transmission side of the slit. Region E is the shadow region of plane Σ_1, Region G is the shadow region of plane Σ_2, while Region H is the geometrically lit

Region between Regions E and G. The boundaries between the regions are the shadow boundaries associated with each plane.

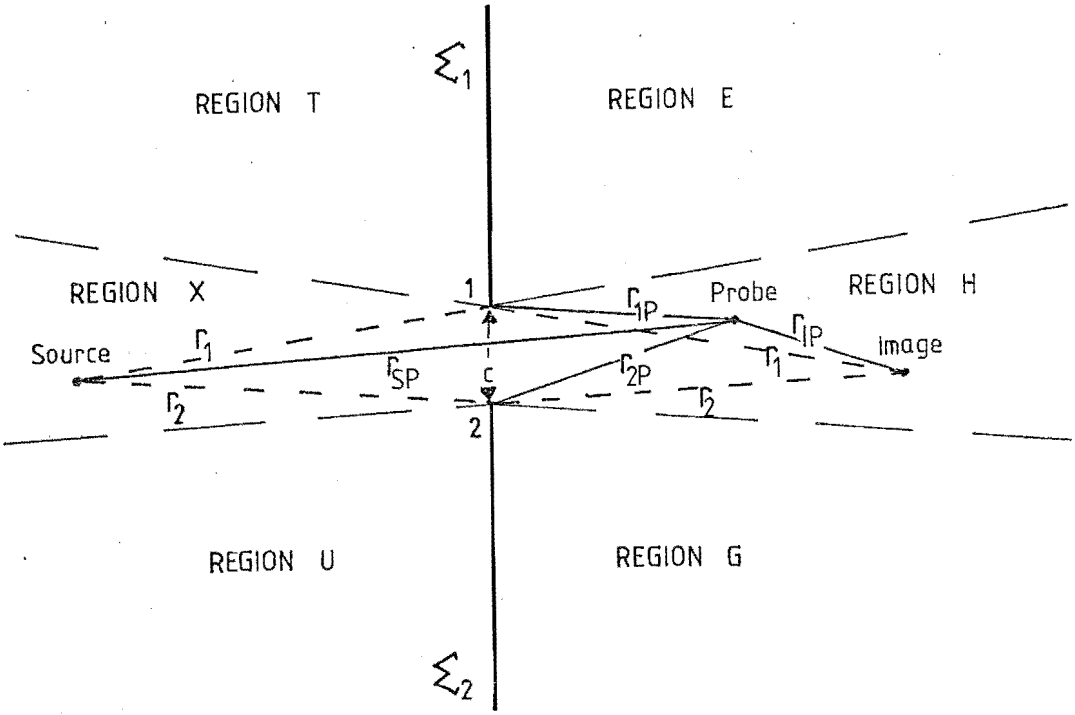

Figure 3.4 Clemmow Geometry for Parallel Plane Slit.

On the lit side of the slit, three further regions are defined. Region T is the reflection region of conducting plane Σ_1, and Region U is similarly the reflection region of Σ_2. In Region X, no reflections occur. The boundaries between Regions T, X and U are the reflection boundaries.

Following Keller's reasoning, the field on the far side of the slit is the addition of the effects of the two half-plane diffracted fields, Equation (2.89), i.e.

$$E_t = E_s + D_1 + D_2, \tag{3.11}$$

where E_s is the direct source field, i.e.,

$$E_s = \frac{e^{-jkr_{sp}}}{(8\pi jkr_{sp})^{\frac{1}{2}}} \text{ in Region H}$$

$$= 0 \text{ in Regions E and G.} \qquad (3,12)$$

and is the geometrical optics far field representation of the cylindrical source, and

D_1 is the diffracted field from the edge of half plane Σ_1

D_2 is the diffracted field from the edge of half plane Σ_2

where D_1 and D_2 are defined as,

$$D_1 = -Q(r_{IP},r_1,r_{1P}) \cdot F\left[k(r_1+r_{1P}-r_{IP})\right]$$

$$-B_1 \cdot Q(r_{SP},r_1,r_{1P}) \cdot F\left[k(r_1+r_{1P}-r_{SP})\right] , \qquad (3.13)$$

where

$$Q(a,b,c) = \frac{e^{-j(ka-\pi/4)}}{(8\pi jk(a+b+c))^{\frac{1}{2}}} ,$$

$B_1 = -1$ for P in Region E,

$= +1$ for P in Regions H, G,

also similarly,

$$D_2 = -Q(r_{IP},r_2,r_{2P}) \cdot F\left[k(r_2+r_{2P}-r_{IP})\right]$$

$$-B_2 \cdot Q(r_{SP},r_2,r_{2P}) \cdot F\left[k(r_2+r_{2P}-r_{SP})\right] , \qquad (3.14)$$

$B_2 = -1$ for P in Region G,

$= +1$ for P in Region E, H,

and $$F\left[\gamma\right] = \int_{\gamma}^{\infty} \frac{e^{-jt}}{\sqrt{t}}\, dt, \qquad (3.15)$$

is a Fresnel Integral.

Unlike Equation (3.10), Equation (3.11) can be applied for any position of the observation point and source, providing of course that they are on opposite sides of the slit. When both observation point and source are on the same side of the slit, Equation (3.11) would require modification to the form.

$$E_t = E_s + E_r + D_1{}^r + D_2{}^r, \tag{3.16}$$

where E_s is the source incident field, i.e.,

$$E_s = \frac{e^{-jkr_{SP}}}{(8\pi jkr_{SP})^{\frac{1}{2}}} \tag{3.17}$$

in any of the Regions T, U or X. Now,

$$E_r = \frac{-e^{-jkr_{IP}}}{(8\pi jkr_{IP})^{\frac{1}{2}}} \quad \text{in Regions T, U,} \tag{3.18}$$

$$= 0 \quad \text{in Region X.}$$

E_r is the reflection term associated with reflections from planes Σ_1 or Σ_2. The diffraction terms differ slightly from those defined in Equations (3.13) and (3.14) and are now given as,

$$D_1{}^r = B_3 . D_1, \tag{3.19}$$

where $B_3 = 1$, $B_1 = 1$ in Regions X, U,

$B_3 = 1$, $B_1 = -1$ in Region T.

where B_1 is shown in Equation (3.13). Also,

$$D_2{}^r = B_4 . D_2, \tag{3.20}$$

where,

$B_4 = 1$, $B_2 = 1$ in Regions T, X,

$B_4 = 1$, $B_2 = -1$ in Region U.

An improvement to the diffraction by a slit involves the inclusion of multiple diffractions (Keller, 1962). In the case of half-plane diffraction, the edge can be modelled as a cylindrical source with a pattern factor given by Equation (2.78). This passive source may then be used as a source which could diffract off another edge. Similarly multiple diffractions using the same model can continue ad infinitum.

We shall apply 'Clemmow' type diffraction to the multidiffraction in a slit. If the passive sources at the edges of the half planes are defined as S_1 for Σ_1 and S_2 for Σ_2 from Figure 3.5, it can be seen that in the case of a parallel slit that the Image sources I_1 and I_2 coincide with S_1 and S_2.

Using Figure 3.5, define:

R_1 as the source strength of S_1 on edge 1 towards edge 2, caused by source S.

R_2 as the source strength of S_2 on edge 2 towards edge 1, caused by source S.

C_1 as the field at the observation point P from S_2 on edge 2 which is diffracted off edge 1.

C_2 as the field at the observation point P from S_1 on edge 1 which is diffracted off edge 2.

V_1 as the source strength from edge 1 diffracted towards edge 2, caused by source S_2 on edge 2.

V_2 as the source strength from edge 2 diffracted towards edge 1, caused by source S_1 on edge 1.

From the above definitions, a ray which travels a path from the source via edge 1, then edge 2 to the observation point would be described as R_1C_2.

Multiple diffraction can be described using the visualization of Figure 3.5. In Figure 3.5, an inclined arrow represents a diffracted output ray, portrayed as D_x or C_x, (Smith, 1974).

The vertical arrows depict the directions in which the source strengths are calculated, and are symbolised by R_x or C_x.

For a parallel slit, since the sources coincide with their images, the cross-slit source strengths V_1 and V_2 will be the same.

From Figure 3.5 the field diffracted off edge 1 will be,

$$E_1^{diff} = D_1 + R_2C_1 + R_1VC_1 + R_2V^2C_1 + R_1V^3C_1 + \ldots\ldots, \qquad (3.21)$$

where $V = V_1 = V_2$.

Similarly, the field diffracted off edge 2 will be,

$$E_2^{diff} = D_2 + R_1C_2 + R_2VC_2 + R_1V^2C_2 + R_2V^3C_2 + \ldots\ldots \qquad (3.22)$$

Summing Equations (3.21) and (3.22), and rearranging terms produces two geometric series, which can be summed to produce,

$$E_1^{Diff} + E_2^{Diff} = D_1 + D_2 + \frac{C_1(R_2+R_1V)}{(1-V^2)} + \frac{C_2(R_1+R_2V)}{(1-V^2)} \quad . \qquad (3.23)$$

Now

$$R_1 = \left[-2.Q(r_{SY}, r_{1Y}, r_1) \cdot F\left[k(r_{1Y}+r_1-r_{SY})\right]\right] \exp(jkr_{1Y})(8\pi jkr_{1Y})^{\frac{1}{2}}, \qquad (3.24)$$

where Y is an arbitrary point on the same plane as the aperture shown in Figure 3.5. The singly diffracted field of edge 1 is evaluated at Y, and then the source field strength is found, assuming that the diffracted field has cylindrical dependence. The portion in braces of Equation (3.24) is derived from Equation (3.13), but in this case $r_{SY} = r_{IY}$ and $B_1 = +1$ as Y is in the lit region.

The point Z, the arbitrary point opposite to Y is also shown in Figure 3.5.

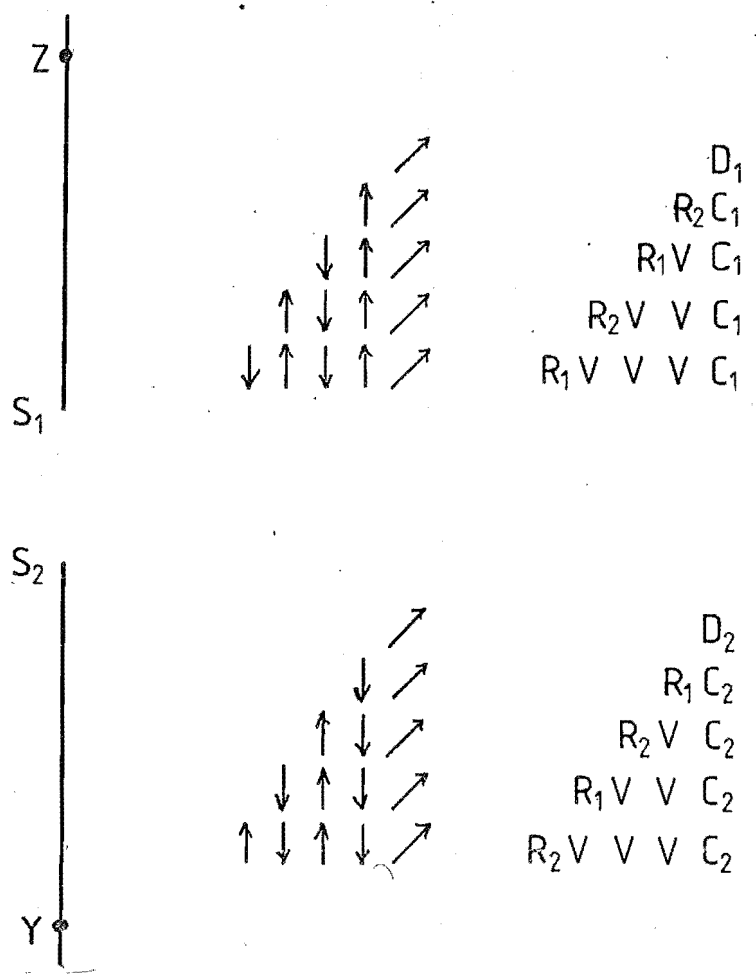

Figure 3.5 Multiple Diffraction Geometry, Parallel Slit

For computations it has been assumed that the points Y and Z are about six wavelengths from the slit centre.

Also,

$$R_2 = \left[-2.Q(r_{SZ}, r_{2Z}, r_2) \cdot F\left[k(r_{2Z}+r_2-r_{SZ})\right]\right] \exp(jkr_{2Z}).(8\pi jkr_{2Z})^{\frac{1}{2}} \quad (3.25)$$

and

$$C_1 = -2.Q(r_{2P}, C, r_{1P}) \cdot F\left[k(r_{1P}+C-r_{2P})\right] , \quad (3.26)$$

$$C_2 = -2.Q(r_{1P},C,r_{2P}) . \quad F\left[k(r_{2P}+C-r_{1P})\right] \quad , \tag{3.27}$$

$$V = \left[-2.Q(r_{2Y},C,r_{1Y}) . \quad F\left[k(r_{1Y}+C-r_{2Y})\right]\right]\exp(jkr_{1Y})(8\pi jkr_{1Y})^{\frac{1}{2}}, \tag{3.28}$$

and $V_1 = V_2 = V$ if $r_{2Y} = r_{1Z}$ and $r_{1Y} = r_{2Z}$.

Equations (3.24) to (3.28) can be used to evaluate Equation (3.23) which with the geometrical optics field in Equation (3.12) will produce the multidiffracted field transmitted through a slit.

In the case of the observation point and the source being on the same side of the slit, the multidiffraction terms will remain untouched. For a parallel slit the shadow and reflection boundaries will coincide on the conducting planes, hence every observation point away from the conducting half planes will be in a lit region from the passive source on the edge of the opposite half plane. Reflection effects, in this case, only have to be taken into account for the geometric optics reflection regions, U and T. The total field, including multidiffraction, when the source and probe are on the same side of the slit can be written as,

$$E_t = E_s + E_r + D_1{}^r + D_2{}^r + \frac{C_1(R_2+R_1V)}{(1-V^2)} + \frac{C_2(R_1+R_2V)}{(1-V^2)} \quad . \tag{3.29}$$

In the case of Neumann boundary conditions on the conducting planes C_1, C_2 and V will be zero. In this case, higher order diffraction effects will require investigation. The situation under study is the reciprocal problem of a source on a half plane under Dirichlet Boundary conditions. The same solution, Equation (2.79), can be applied. This will produce a diffracted ray proportional to $k^{-3/2}$. In many high frequency analyses it is not necessary to go beyond $k^{-1/2}$ terms as this complicates analysis with little gain, following a law of diminishing returns.

To investigate the theories a single cylindrical line source was placed 47λ away from the slit centre and on observation point was run along a line parallel to the slit plane 9.15λ beyond the slit and 9.15λ either side of the slit axis. This geometry is shown in Figure 3.6.

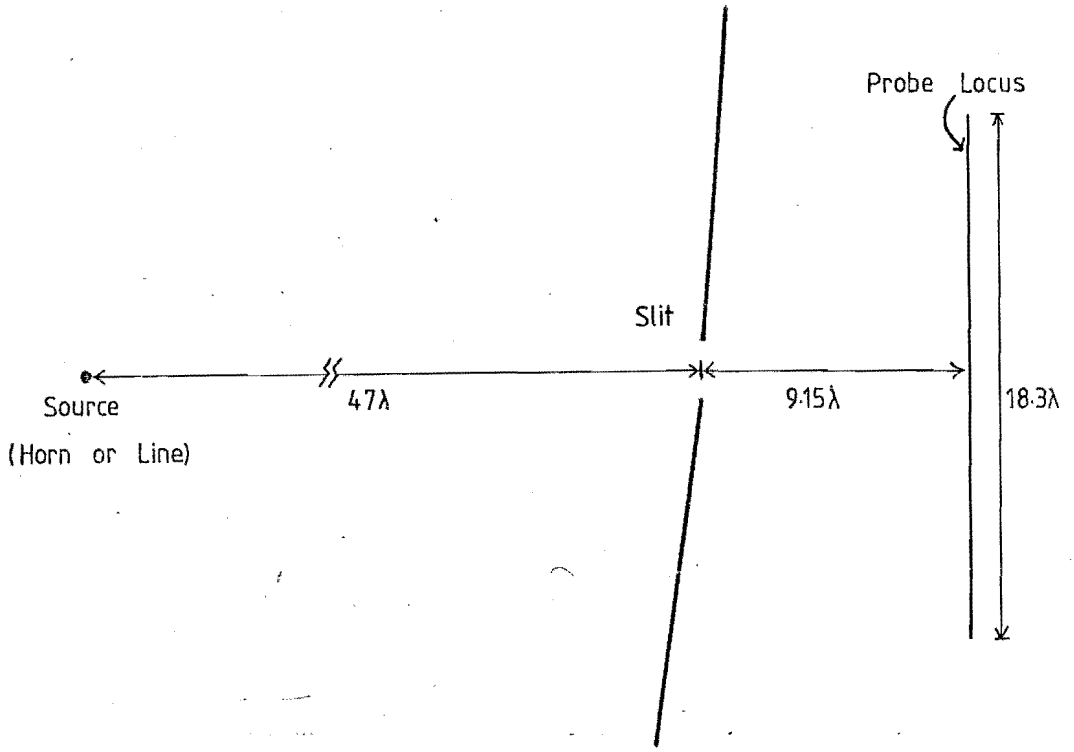

Figure 3.6 Slit Geometry used for Examples.

Figure 3.7 compares the intensity and phase distributions of the transmitted fields for Mathieu, single 'Clemmow' diffraction and multiple 'Clemmow' Diffraction for a half wavelength slit for various ϕ_{inc}. Figure 3.8, compares intensity and phase distributions of the fields transmitted through λ/2, λ and 2λ slits for normal incidence using the Mathieu representation and multiple 'Clemmow' representation. Figure 3.9 is a comparison of calculated normal transmissions for slits to 2λ in width. From these diagrams it is clear over which ranges the various approximate formulae are applicable. For slit widths greater than 1½λ multiple diffraction appears unnecessary. (Ryan, 1968).

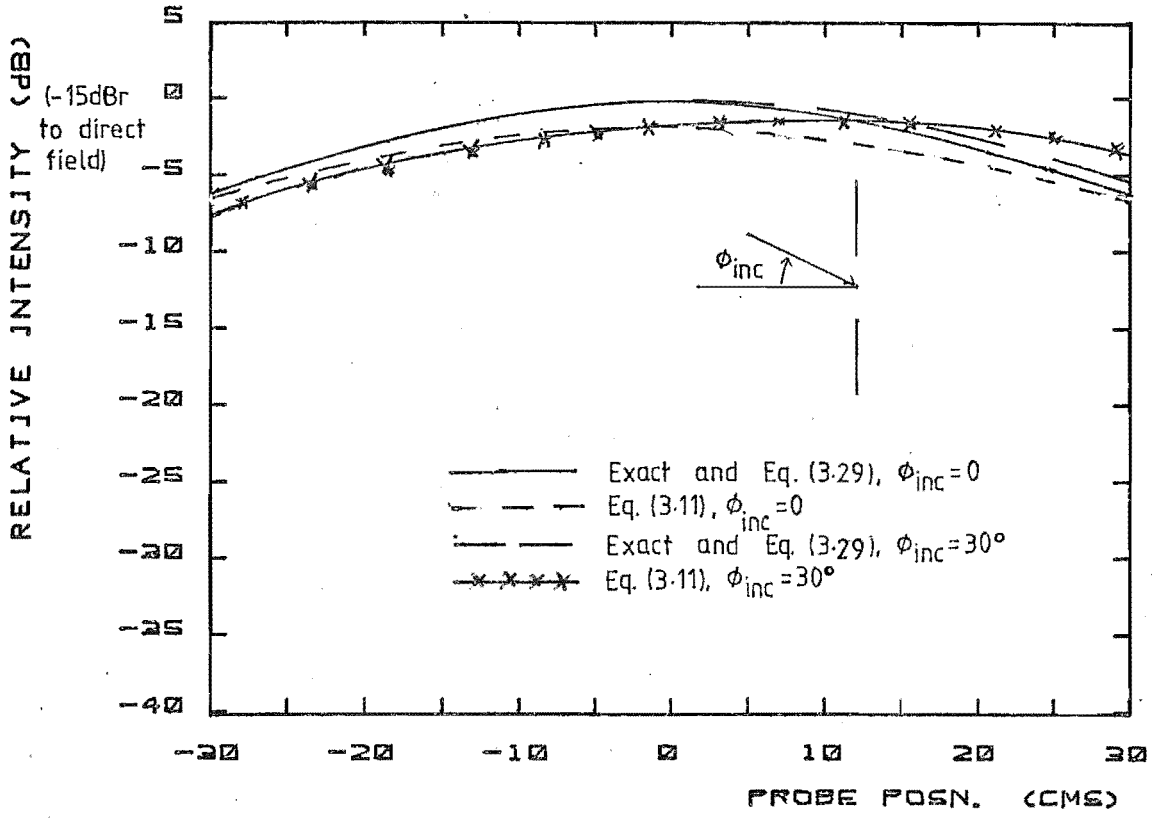

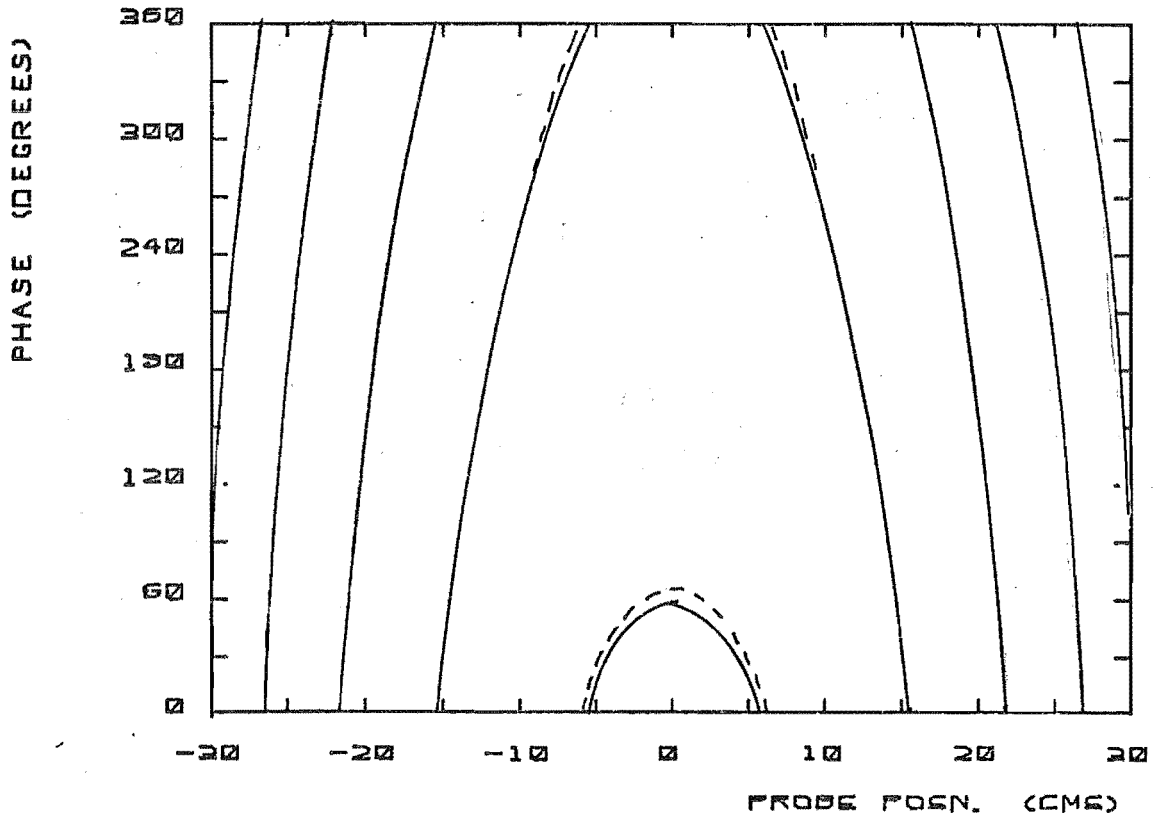

Phases unaffected by incident angle.

Figure 3.7 Comparison of field beyond a $\lambda/2$ slit for various incident angles and theories.

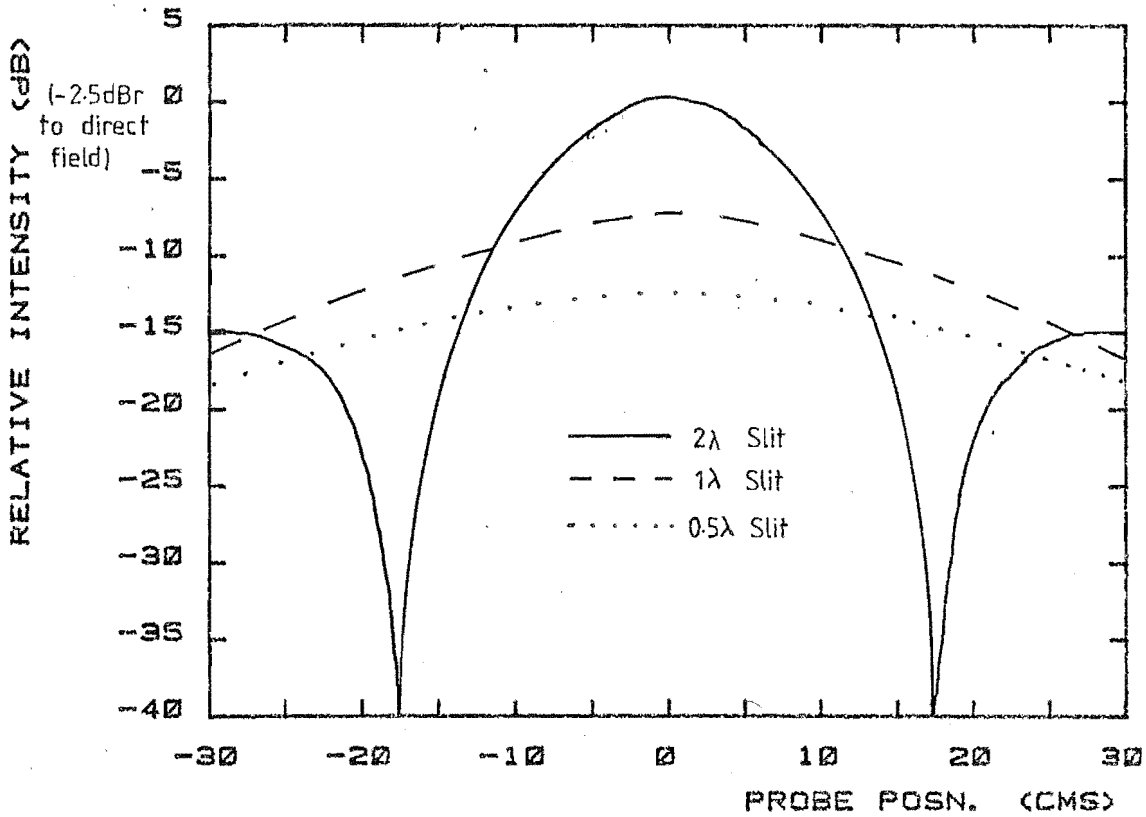

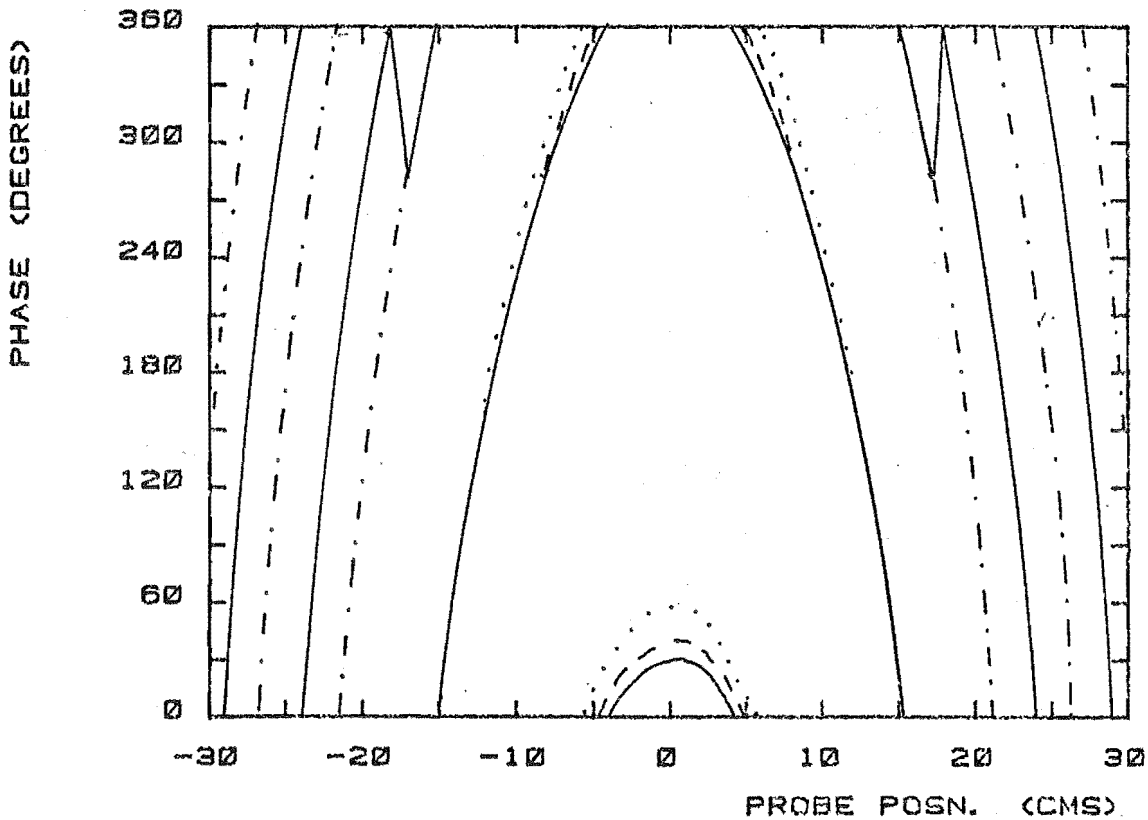

Figure 3.8 Comparison of field through slits of various width.

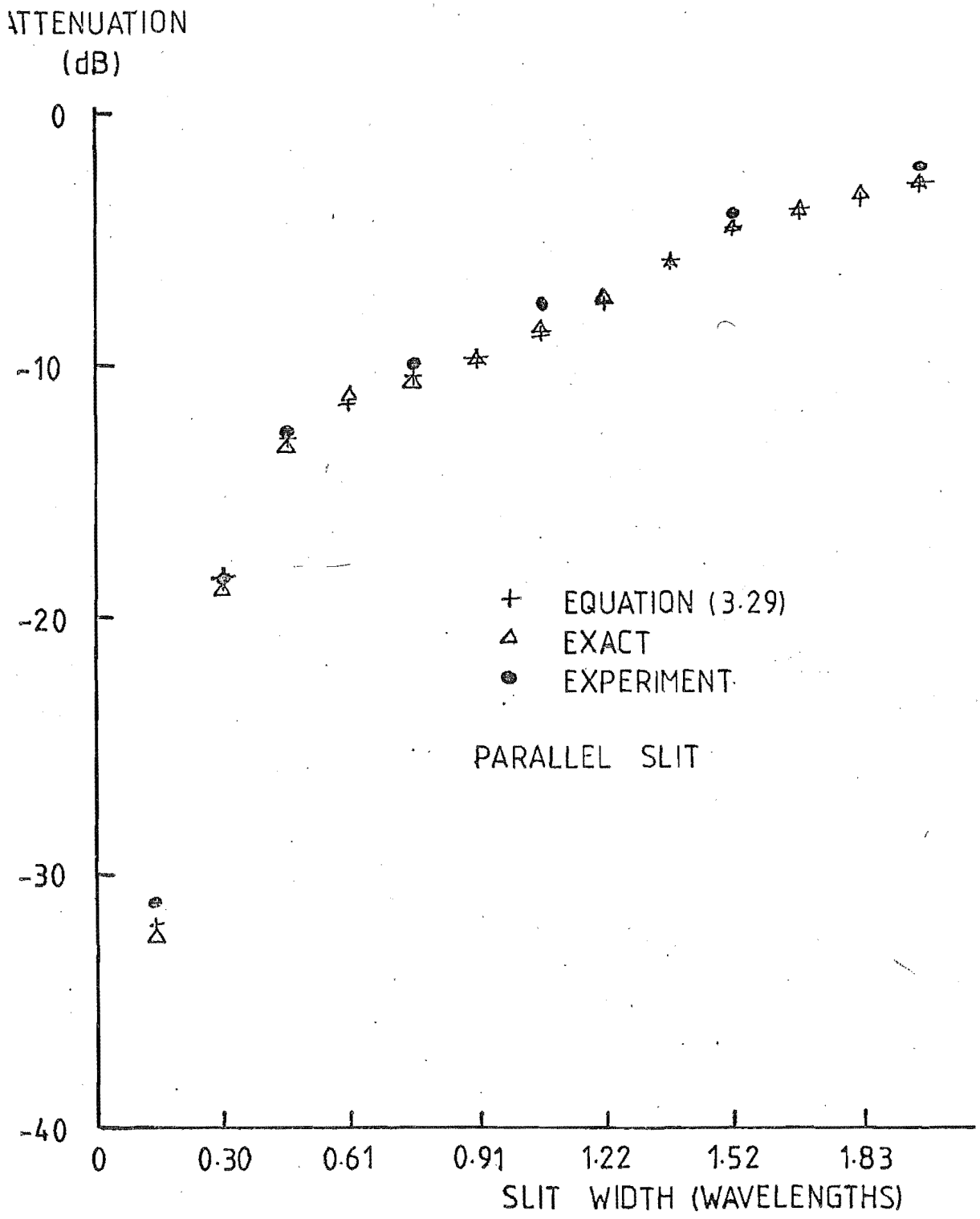

Figure 3.9a Comparison of transmissions through parallel slits (Intensity).

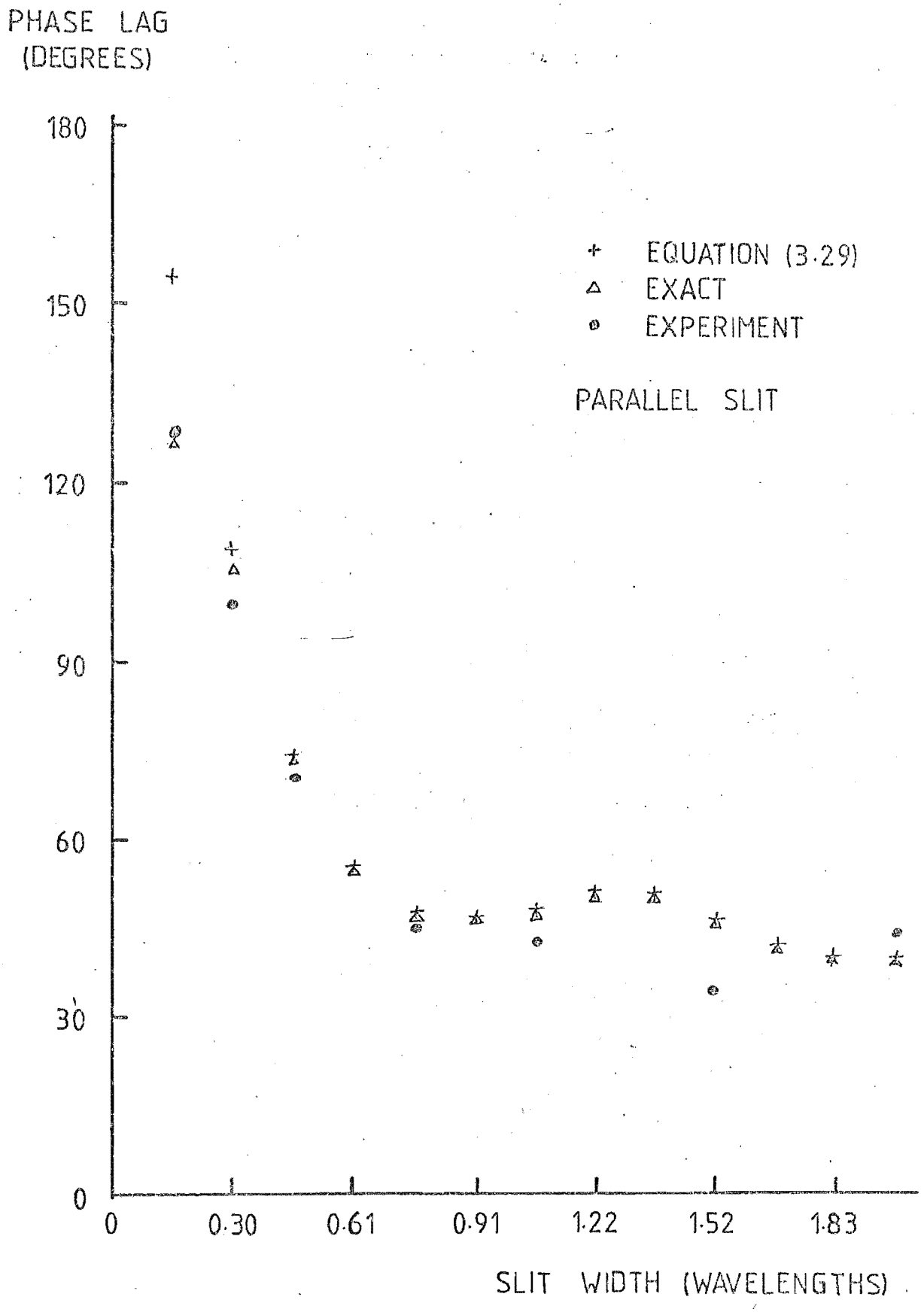

Figure 3.9b Comparison of transmissions through parallel slits, (Phase).

3.4 SLITS WITH INCLINED PLANES

We shall now focus our attention onto slits where the conducting half planes are inclined away from the slit plane. Running to an argument parallel to that of the previous section, we look first at single diffraction. For inclined planes, the geometry is slightly different, as depicted in Figure 3.10.

The main difference between Figures 3.4 and 3.10 is that the conducting planes have individual image sources.

For single diffraction, Equation (3.11) will still hold, but D_1 and D_2 will be changed to D_1' and D_2' to account for the repositioning of image sources. Referring to the geometry of Figure 3.10, we see that,

$$D_1' = -Q(r_{Q1P}, r_1, r_{1P}) \cdot F\left[k(r_1+r_{1P}-r_{Q1P})\right]$$

$$-B_1 \cdot Q(r_{SP}, r_1, r_{1P}) \cdot F\left[k(r_1+r_{1P}-r_{SP})\right], \tag{3.30}$$

and

$$D_2' = -Q(r_{Q2P}, r_2, r_{2P}) \cdot F\left[k(r_2+r_{2P}-r_{Q2P})\right]$$

$$-B_2 \cdot Q(r_{SP}, r_2, r_{2P}) \cdot F\left[k(r_2+r_{2P}-r_{SP})\right], \tag{3.31}$$

where B_1 and B_2 remain as defined below Equations (3.13) and (3.14).

When $\eta_x \neq 0$, x = 1 or 2, there occurs two regions for any slit where only one half plane has any effect. In Figure 3.11a these are shown as areas M and N. In region M, $D_2' = 0$, and diffraction of source R_2 off edge 1 must be used to give a smooth transition over the shadow boundary between regions E and M. Similar care must be taken at the shadow boundary between regions H and N.

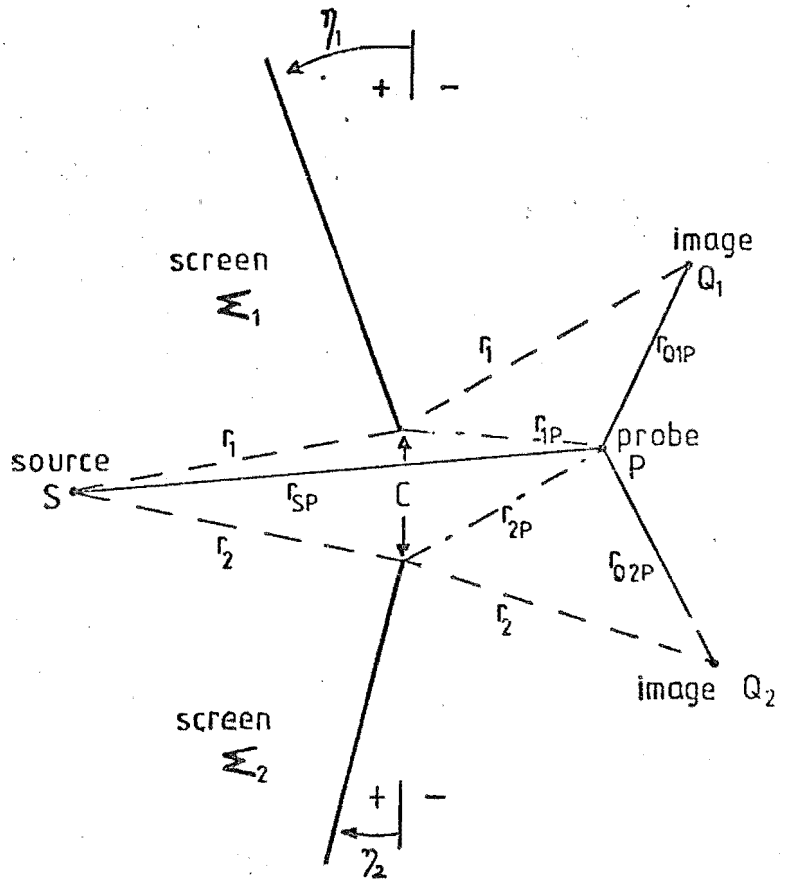

Figure 3.10 Clemmow Diffraction Geometry for a Slit with inclined planes.

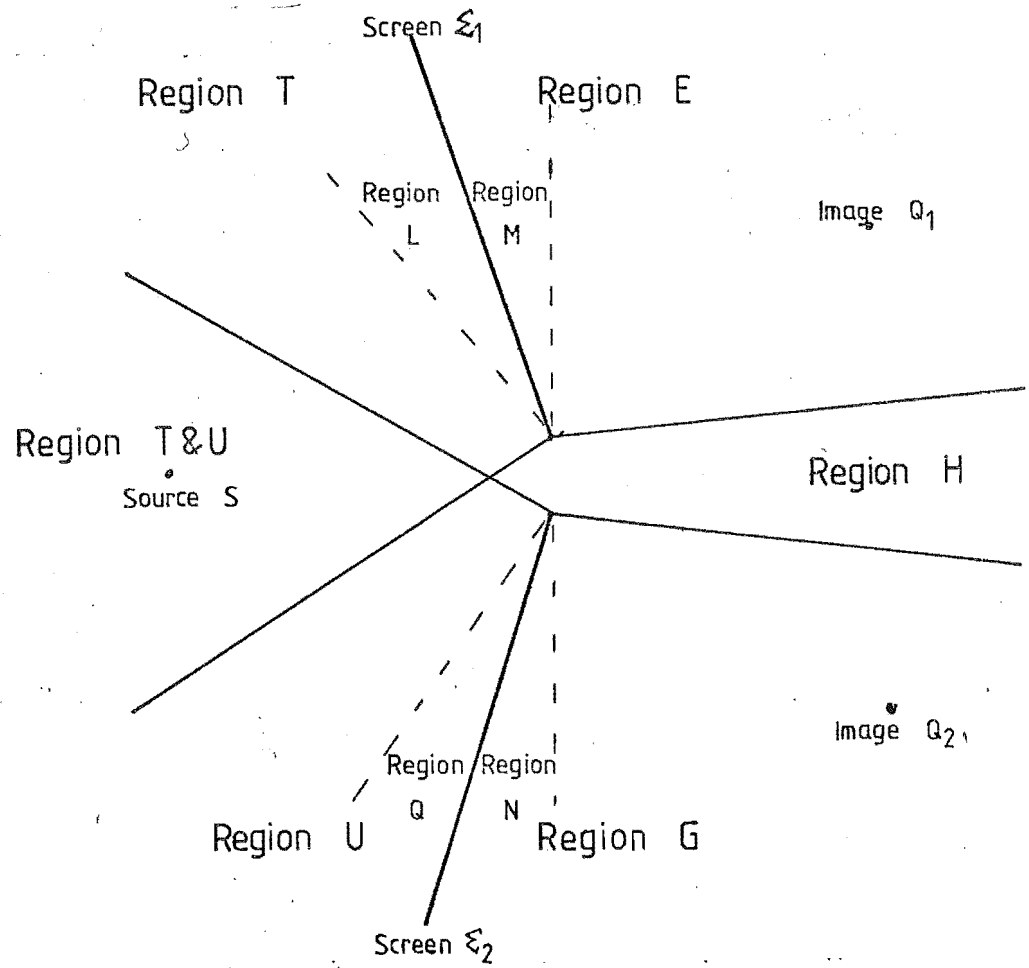

Figure 3.11a Regions around a concave slit.

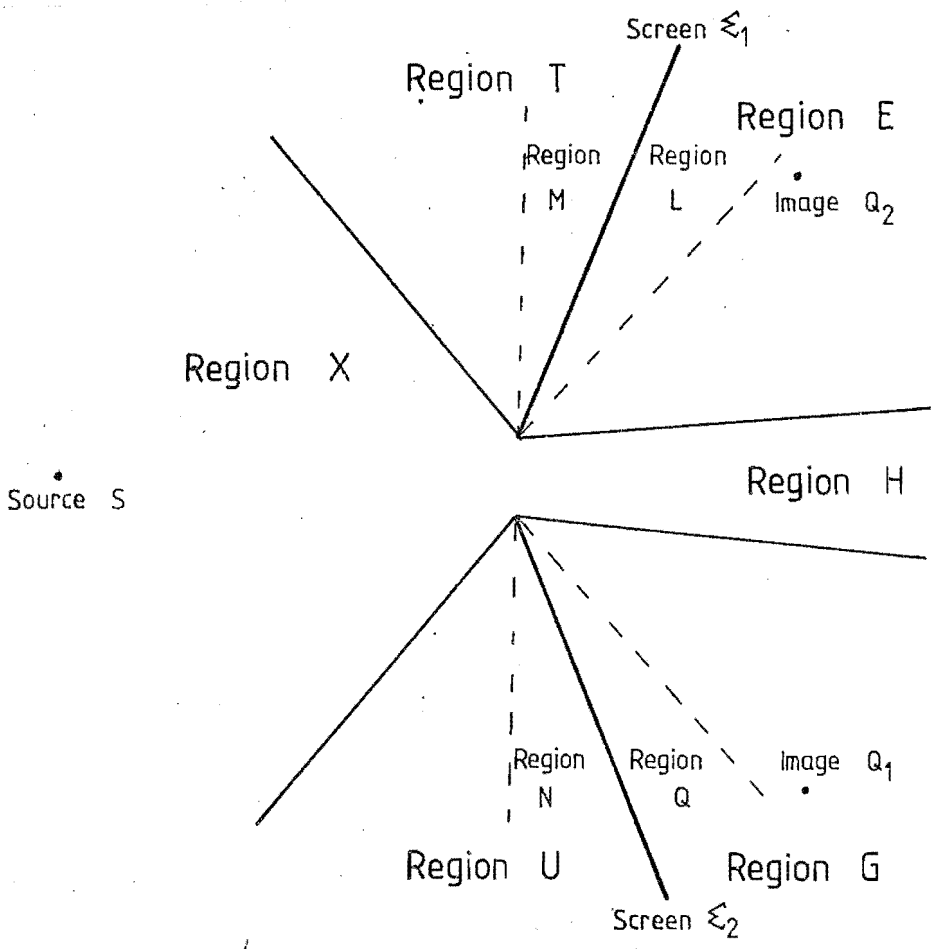

Figure 3.11b Regions about a convex slit.

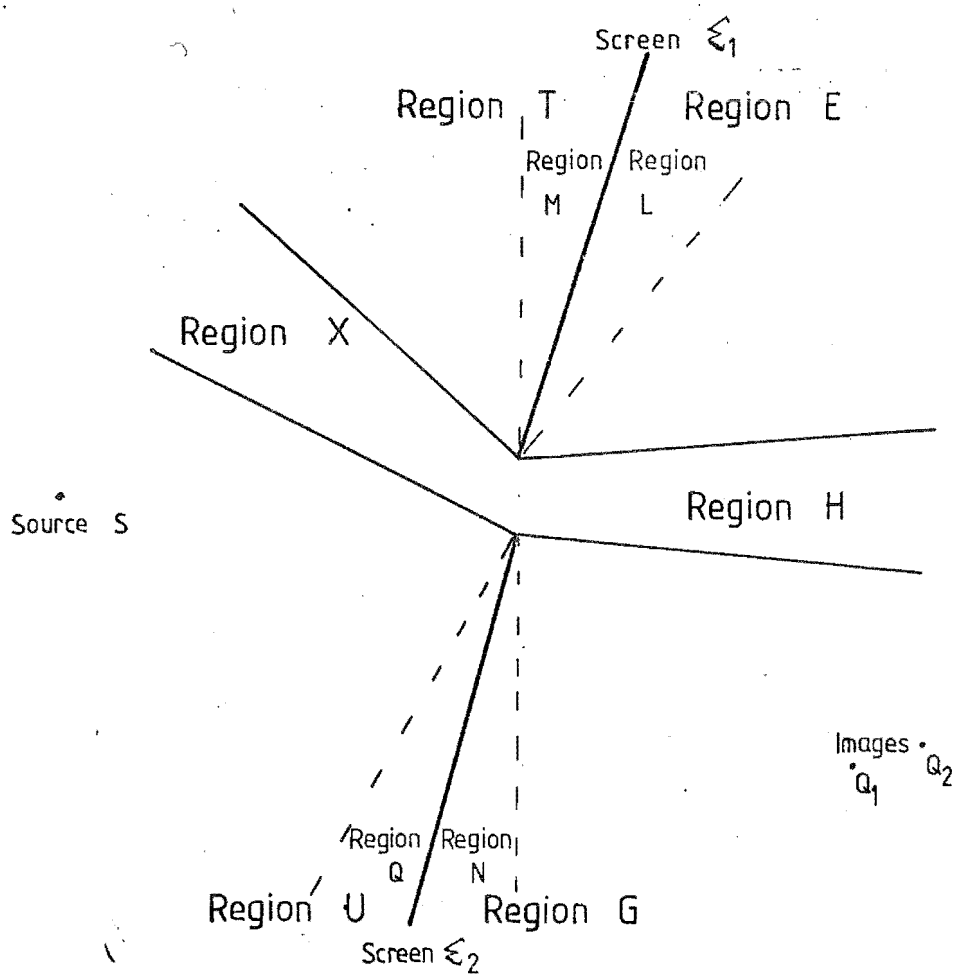

Figure 3.11c Regions about a zig slit.

When the observation point is on the same side of the slit as the source, it is possible, as shown in Figure 3.11a, that the reflection regions U and T may overlap, leaving a small triangular region where no reflections occur.

Regions Q and L are areas where second order reflection occurs off the opposite plane. Figures 3.11b and 3.11c show the regions defined above for a convex slit and zig slit. In order to find a smooth representation for the total field over all of the regions, multiple diffractions will be required.

Using the definitions in Section 3.3 , and referring to Figure 3.12, we find that the edge source images no longer coincide with the edge sources.

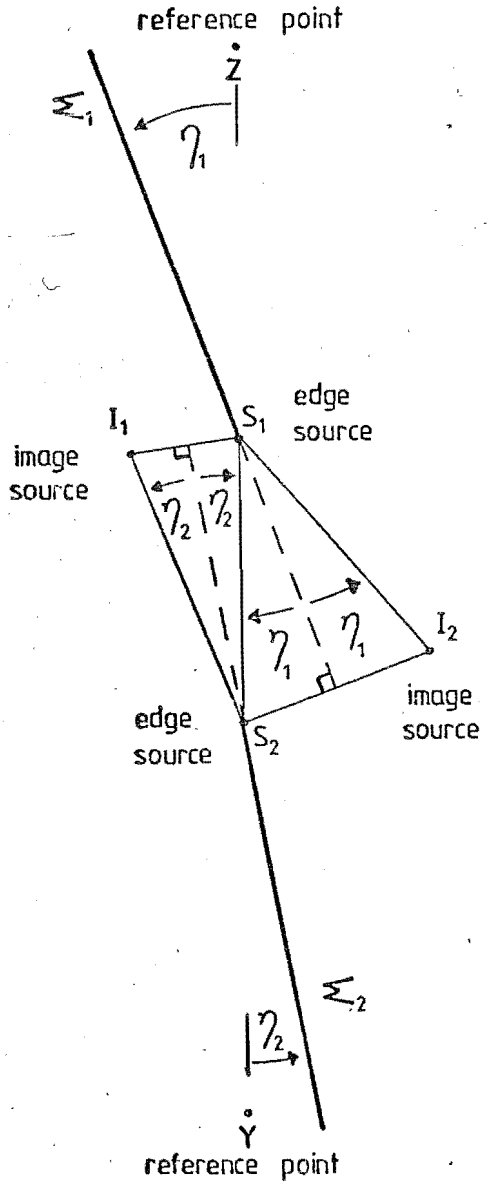

Figure 3.12 Edge Sources and Images for an Inclined Plane Slit.

In this situation the cross slit source strengths V_1 and V_2 will not be the same.

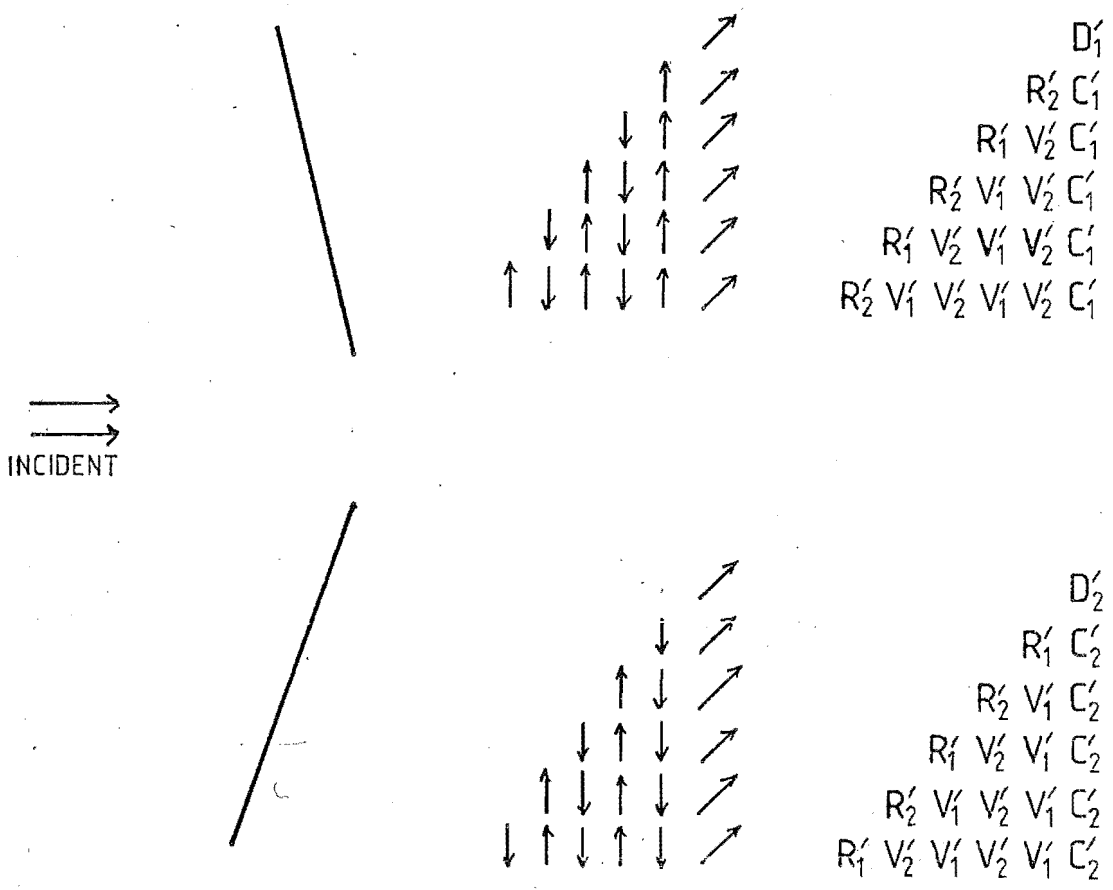

Figure 3.13 Multidiffracted Field Representation from an Inclined Plane Slit.

From Figure 3.13, for inclined slits, the field diffracted off edge 1, will be,

$$E_1^{Diff} = D_1' + R_2' C_1' + R_1' V_2' C_1' + R_2' V_1' V_2' C_1' + \ldots\ldots, \qquad (3.32)$$

where the dashes imply an inclined plane slit.

The field diffracted off edge 2 will be,

$$E_2^{Diff} = D_2' + R_1' C_2' + R_2' V_1' C_2' + R_1' V_2' C_2' + \ldots\ldots, \qquad (3.33)$$

and summing Equations (3.32) and (3.33) gives

$$E_1^{Diff} + E_2^{Diff} = D_1' + D_2' + \frac{C_1'(R_2'+R_1'V_2')}{(1-V_1' V_2')} + \frac{C_2'(R_1'+R_2'V_1')}{(1-V_1' V_2')} \qquad (3.34)$$

We now need to define R_1', R_2', V_1', V_2', C_1', and C_2'. Reference points Y and Z are at the same positions as shown in Figure 3.5.

$$R_1' = \left(-Q(r_{Q1Y}, r_{1Y}, r_1) \cdot F\left[k(r_{1Y}+r_1-r_{Q1Y})\right] - Q(r_{SY}, r_{1Y}, r_1) \cdot F\left[k(r_{1Y}+r_1-r_{SY})\right] \right)$$

$$\cdot (8\pi jkr_{1Y})^{\frac{1}{2}} \cdot \exp(jkr_{1Y}) \qquad (3.35)$$

$$R_2' = \left(-Q(r_{Q2Z}, r_{2Z}, r_2) \cdot F\left[k(r_{2Z}+r_2-r_{Q2Z})\right] \right.$$

$$\left. -Q(r_{SZ}, r_{2Z}, r_2) \cdot F\left[k(r_{2Z}+r_2-r_{SZ})\right] \right) \cdot (8\pi jkr_{2Z})^{\frac{1}{2}} \cdot \exp(jkr_{2Z}) \qquad (3.36)$$

$$C_1' = -\Delta_1 Q(r_{I2P}, C, r_{1P}) \cdot F\left[k(r_{1P}+C-r_{I2P})\right]$$

$$-\Delta_2 \cdot Q(r_{2P}, C, r_{1P}) \cdot F\left[k(r_{1P}+C-r_{2P})\right], \qquad (3.37)$$

$$C_2' = -\Delta_3 \cdot Q(r_{I1P}, C, r_{2P}) \cdot F\left[k(r_{2P}+C-r_{I1P})\right]$$

$$-\Delta_4 \cdot Q(r_{1P}, C, r_{2P}) \cdot F\left[k(r_{2P}+C-r_{1P})\right], \qquad (3.38)$$

$\Delta_1 = +1$ in Regions other than Q.

$\Delta_1 = -1$ in Region Q.

Δ_2 = +1 in Regions other than M

= -1 in Region M

Δ_3 = +1 in Regions other than L

= -1 in Region L

Δ_4 = +1 in Regions other than N

= -1 in Region N

$$V_1' = \left\{ -Q(r_{I2Y}, C, r_{1Y}) \cdot F\left[k(r_{1Y}+C-r_{I2Y})\right] - Q(r_{2Y}, C, r_{1Y}) \cdot F\left[k(r_{1}+C-r_{2Y})\right] \right\} \cdot (8\pi jkr_{2Y})^{\frac{1}{2}} \exp(jkr_{2Y}) \quad (3.39)$$

$$V_2' = \left\{ -Q(r_{I1Z}, C, r_{2Z}) \cdot F\left[k(r_{2Z}+C-r_{I1Z})\right] - Q(r_{IZ}, C, r_{2Z}) \cdot F\left[k(r_{2Z}+C-r_{1Z})\right] \right\} \cdot (8\pi jkr_{1Z})^{\frac{1}{2}} \exp(jkr_{1Z}) \quad (3.40)$$

The Δ_x factors take into account diffractions into secondary reflection and shadow regions.

In the reflection regions L and Q, and the shadow regions M and N (c.f. Figure 3.11a to 3.11c) additional source terms must be included to take into account reflections off or shadowing by a conducting plane.

In the case of reflection, a source at the opposite edge and its image must be used to find the 'direct' field at an observation point.

Hence, in region L, the ray that reaches the observation point off conducting plane Σ_2 is included. The field strength at the observation

point under Dirichlet conditions via the plane is just the negative of the field strength at an image observation point J if the conducting plane is removed as in Figure 3.14. Where Neumann boundary conditions are being obeyed there is no negation of the field strength at J. For the rest of this derivation it is assumed that Dirichlet boundary conditions will hold, but it is a relatively simple extension to include Neumann boundary conditions.

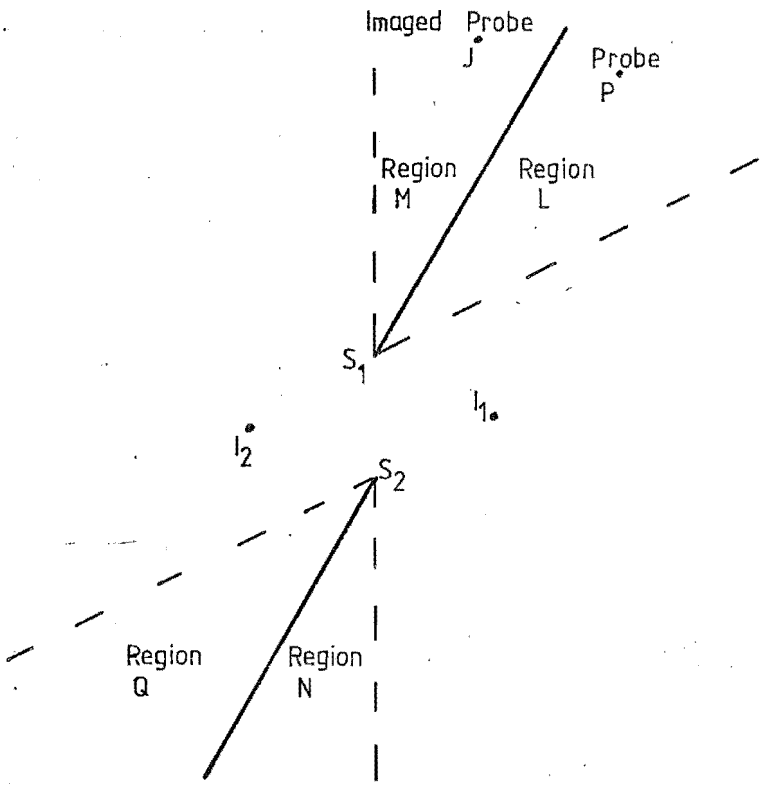

Figure 3.14 Diffraction-Reflection Geometry for an Inclined Plane Slit.

Thus, including reflections, off Edge 1,

$$E'_{1Refl} = D_1'^R + R_2'C_1'^R + R_1'V_2'C_1'^R + R_2'V_1'V_2'C_1'^R + \ldots\ldots, \qquad (3.41)$$

and off Edge 2

$$E'_{2Refl} = D_2'^R + R_1'C_2'^R + R_2'V_1'C_2'^R + R_1'V_2'V_1'C_2'^R + \ldots\ldots \qquad (3.42)$$

Equations (3.41) and (3.42) can be summed

$$E'_{1Refl} + E'_{2Refl} = E'_{Refl} = D_1'^R + D_2'^R + \frac{C_1'^R(R_2'+R_1'V_2')}{(1-V_1'V_2')} + \frac{C_2'^R(R_1'+R_2'V_1')}{(1-V_1'V_2')} \quad (3.43)$$

Now

$$D_1'^R = Q(r_{Q1J}, r_1, r_{1J}) \cdot F\left[k(r_1+r_{1J}-r_{Q1J})\right] + B_1 \cdot Q(r_{SJ}, r_1, r_{IJ}) \cdot F\left[k(r_1+r_{1J}-r_{SJ})\right], \quad (3.44)$$

where B_1 = -1 for P in Region Q

= +1 for P elsewhere.

$D_1'^R = -D_1'$ for P in region N,

= 0 for P elsewhere.

$$D_2'^R = Q(r_{Q2J}, r_2, r_{2J}) \cdot F\left[k(r_2+r_{2J}-r_{Q2J})\right] + B_2 \cdot Q(r_{SJ}, r_2, r_{2J}) \cdot F\left[k(r_2+r_{2J}-r_{SJ})\right], \quad (3.45)$$

where B_2 = -1 for P in Region L,

= +1 for P elsewhere.

$D_2'^R = -D_2'$ for P in Region M,

= 0 for P elsewhere.

Also, $C_1'^R = -C_1'$ for P in region N, and

$$C_1^{1R} = Q(r_{I2J}, C, r_{1J}) \cdot F\left[k(r_{1J}+C-r_{I2J})\right]$$

$$+ Q(r_{2J}, C, r_{1J}) \cdot F\left[k(r_{1J}+C-r_{2J})\right] \qquad (3.46)$$

For J in Region N,

= 0 elsewhere

$$C_2^{'R} = -C_2^{'} \quad \text{for P in region M}$$

$$= Q(r_{I1J}, C, r_{2J}) \cdot F\left[k(r_{2J}+C-r_{I1J})\right]$$

$$+Q(r_{1J}, C, r_{2J}) \cdot F\left[k(r_{2J}+C-r_{1J})\right] \qquad (3.47)$$

For J in Region M

= 0 elsewhere

Thus, the total field about the slit can now be read as

$$E_T^{'} = E_{Refl}^{'} + E^{Diff} + E_R + E_S, \qquad (3.48)$$

using Equations (3.43), (3.34), (3.18) and (3.12).

For the purposes of the examples, using the geometry of Figure 3.6, the reflection term in $E_{Refl}^{'}$ will not be required provided η_1 and η_2 remain reasonably small, and E_R will not be required.

Experiments were performed to study the effects of plane incination on the slit transmission. The experimental set up using a parallel plate range is described in Chapter 5. The source was a horn, with the aperture distribution as shown in Figure 3.15 as calculated from Collin and Zucker, (1969). The 'Clemmow' type diffraction, as it stands, does not describe diffraction with a non-uniform source, such as a horn source. The

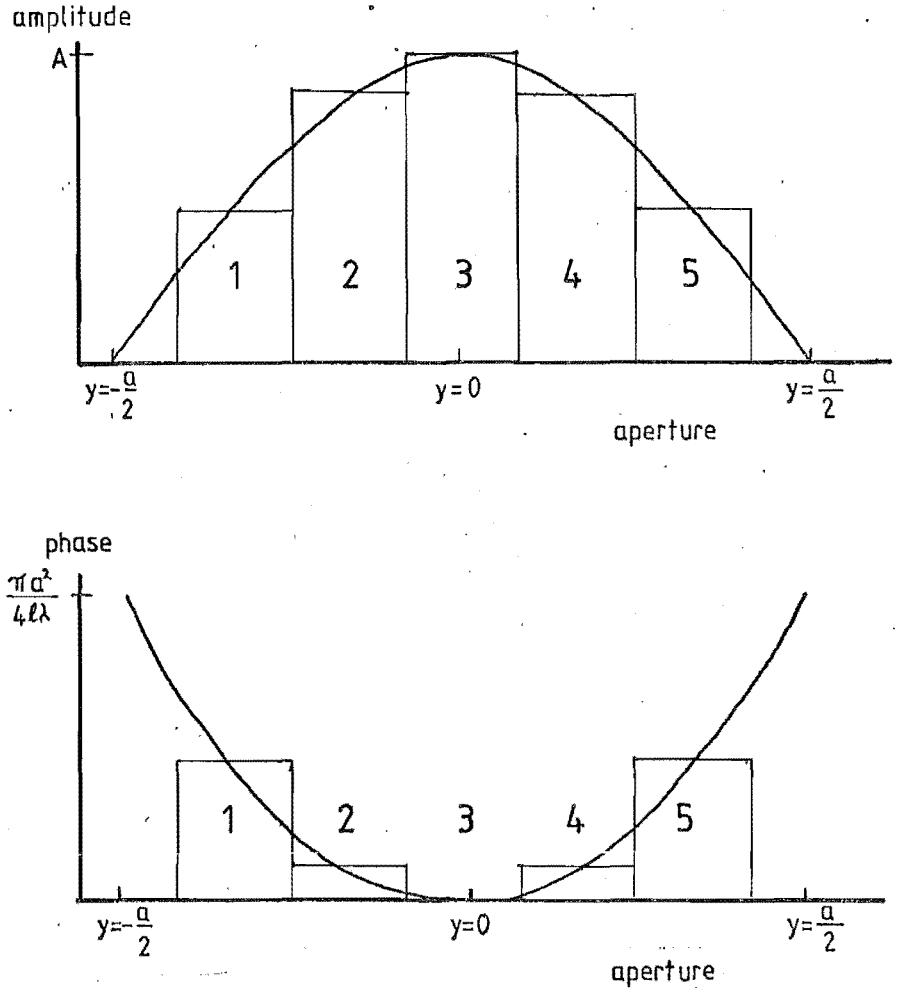

Figure 3.15 5 line source approximation of Horn Aperture Distribution.

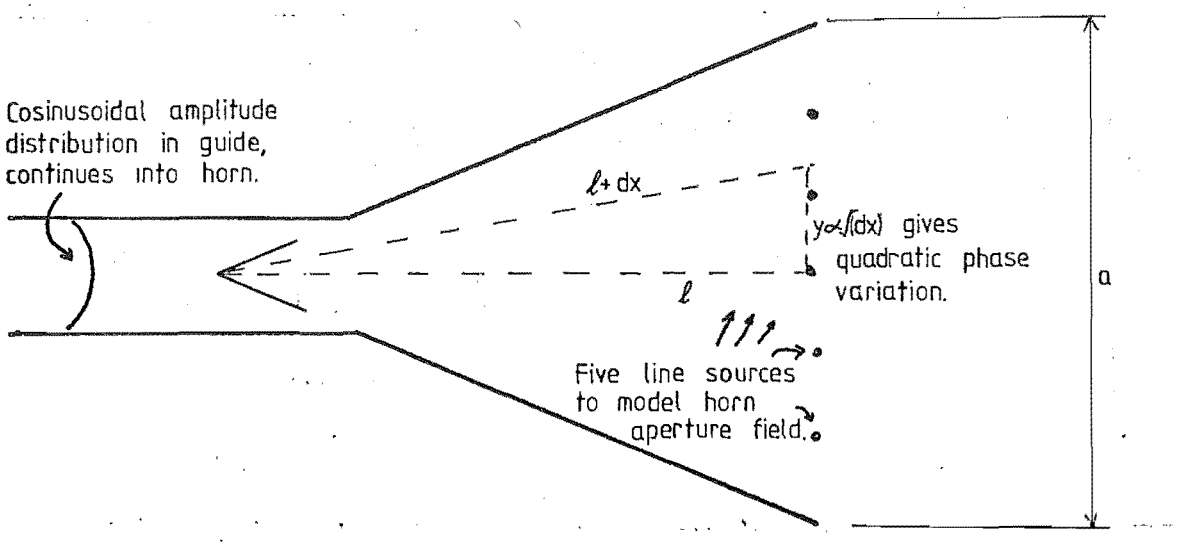

Figure 3.16 Modelling of Aperture Field of a Horn.

Uniform Asymptotic Theory, (Menendez and Lee, 1977) does look into this possibility and overcomes the problem by defining different detour parameters for different non-uniform sources, and the K.P. theory (Kouyoumjian and Pathak, 1974) uses a slope-wave diffraction term as noted in Chapter 2. The non-uniform horn source can be modelled as an array of line sources. Figure 3.16 shows how the horn in question can be considered as a collection of 5 cylindrical sources with a cosinusoidal amplitude distribution and a quadratic phase distribution. The field distribution of this collection of line sources is compared to the theoretical distribution, in Figure 3.17 which is a Fourier Transform of the aperture distribution of Figure 3.15.

The resultant diffraction is the sum of the individual diffractions of each source.

The Electric Field in the aperture of the horn used in the experiment was assumed to be,

$$E_{Horn} = A \cos\left(\frac{\pi y}{a}\right) \cdot \exp(-jky^2/2\ell), \tag{3.49}$$

where A - arbitrary constant

a - is the aperture width of the horn in the H-Plane

y - is a cartesian axis across the width of the horn

and y=0 is the centre

ℓ - is the length of the sectoral horn.

Each source strength, in the case of five sources, is given by

$$E^N_{Horn} = A \cos\left(\frac{\pi(N-3)}{6}\right) \cdot \exp(-jk(a.(N-3)/6)^2/2\ell), \tag{3.50}$$

for N = 1, 2, 3, 4, 5.

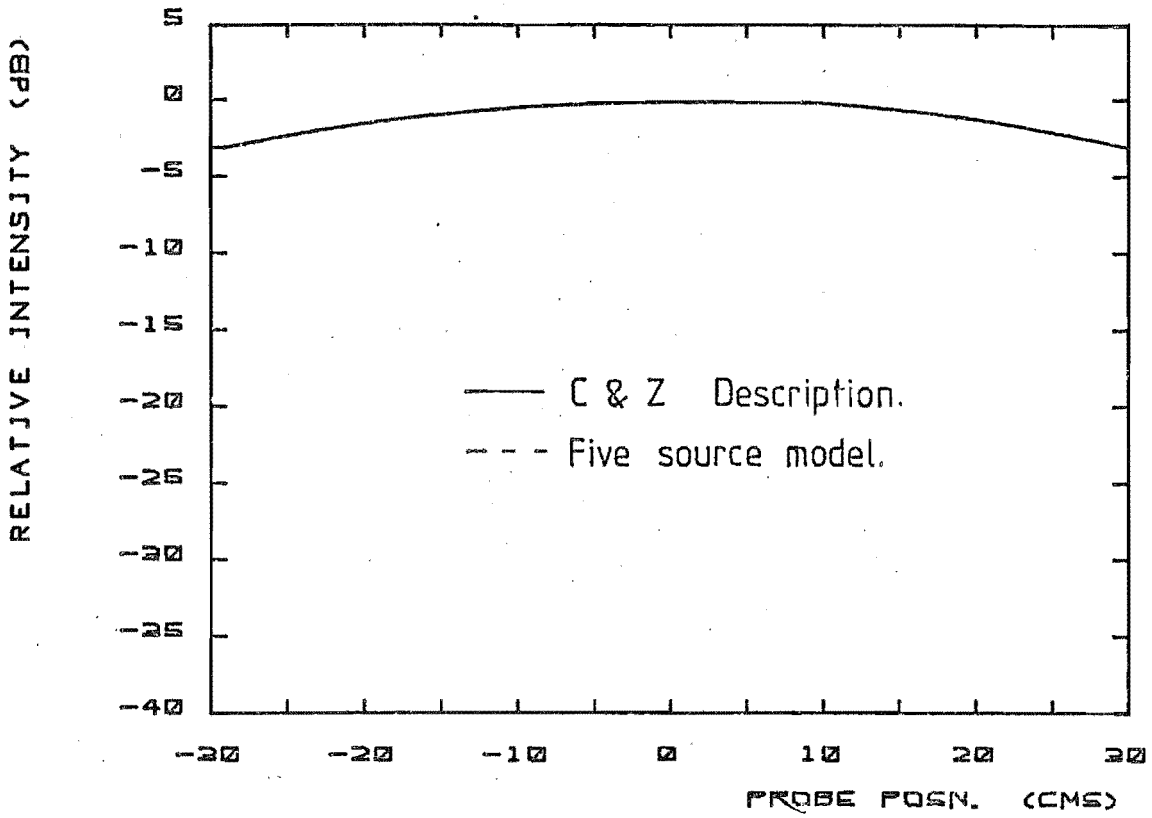

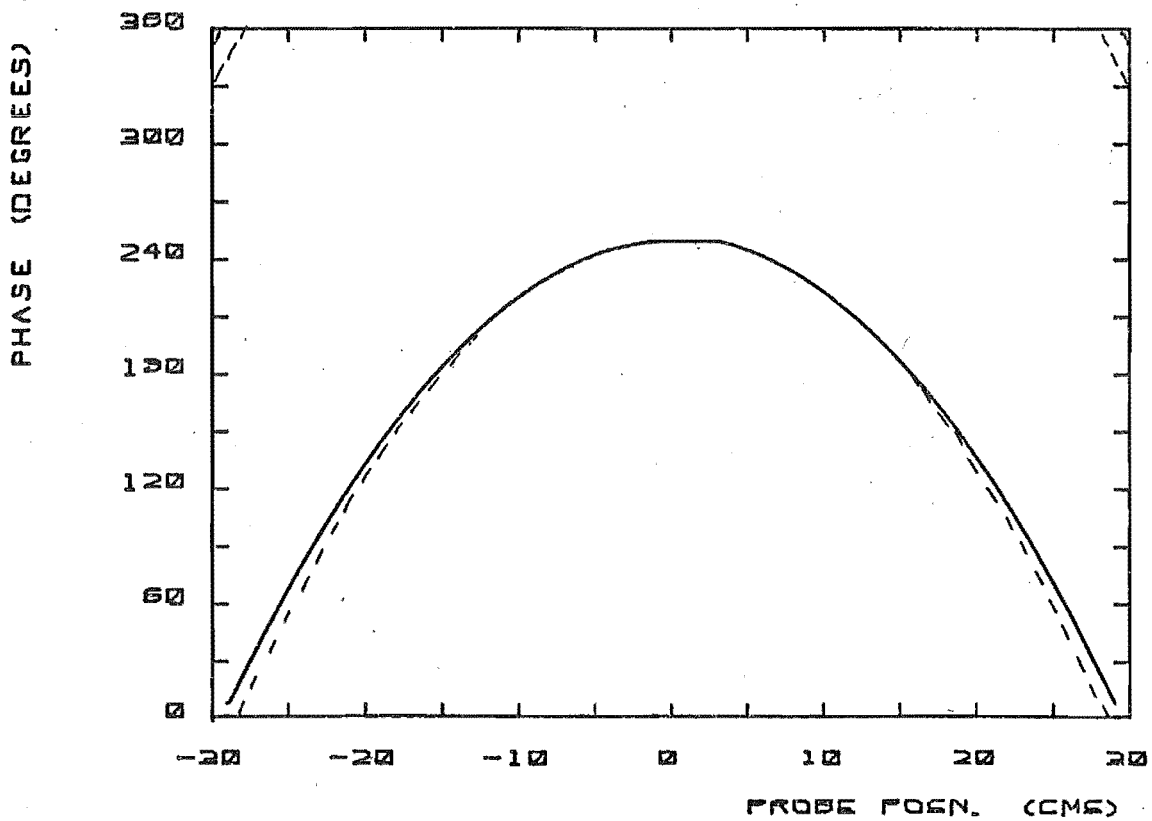

Figure 3.17 Comparison of Far Fields for Horn Aperture Descriptions.

Modifying the cylindrical description into a horn description requires the summation of the diffracted fields caused by the sources described in Equation (3.50) i.e., for the example, where reflection terms are ignored,

$$E_T^{Horn} = \sum_{N=1}^{5} E_{Horn}^{N} \left[E_S^N + D_1^N + D_2^N + \frac{C_1^N (R_2^N + R_1^N V_2^N)}{(1 - V_1^N V_2^N)} + \frac{C_2^N (R_1^N + R_2^N V_1^N)}{(1 - V_1^N V_2^N)} \right], \tag{3.51}$$

where the superscript N implies that the distances associated with each source need to be calculated individually.

The horn source diffraction was applied only to the situation where the observation point was away from reflection regions and secondary shadow regions.

The horn source approximation is essentially a Physical Optics interpretation. Edge pertubations from the horn have been ignored, hence the far field of the horn is only accurate in the forward region, and close to the forward axis. A better collection of sources would be required to properly define the horn field where the observation point is on the same side of the slit as the source, but over the locus of the probe movement in the experiment, the Physical Optics approximation is an accurate interpretation of the Horn far field.

Figures 3.18 to 3.20 compare the measured and theoretical transmissions through concave and convex slits for normal incidence. Figure 3.21 shows the diffracted field distributions for three zig slits of different widths with the same plane inclinations.

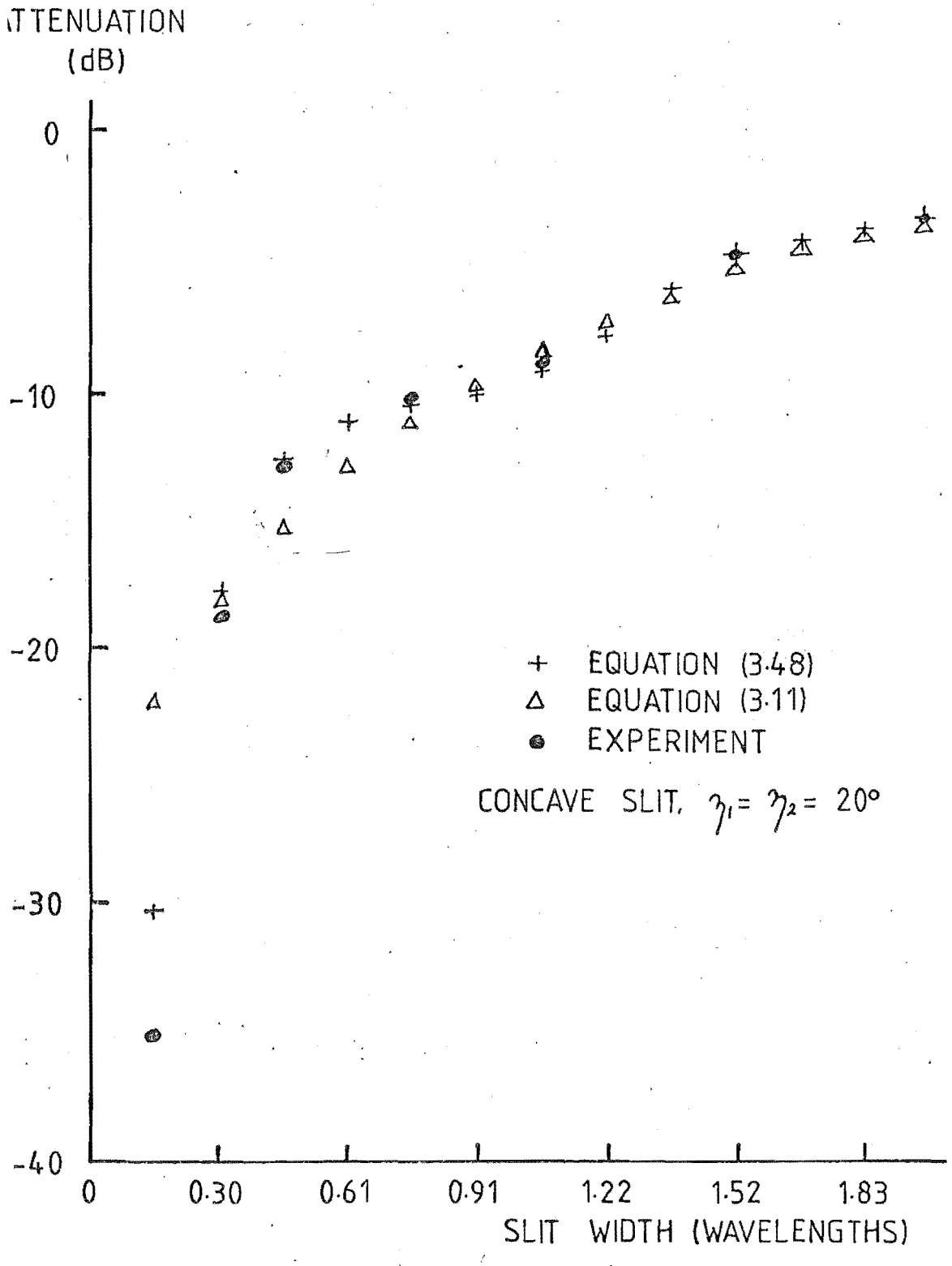

Figure 3.18a Comparison of Transmissions through concave slits (Intensity).

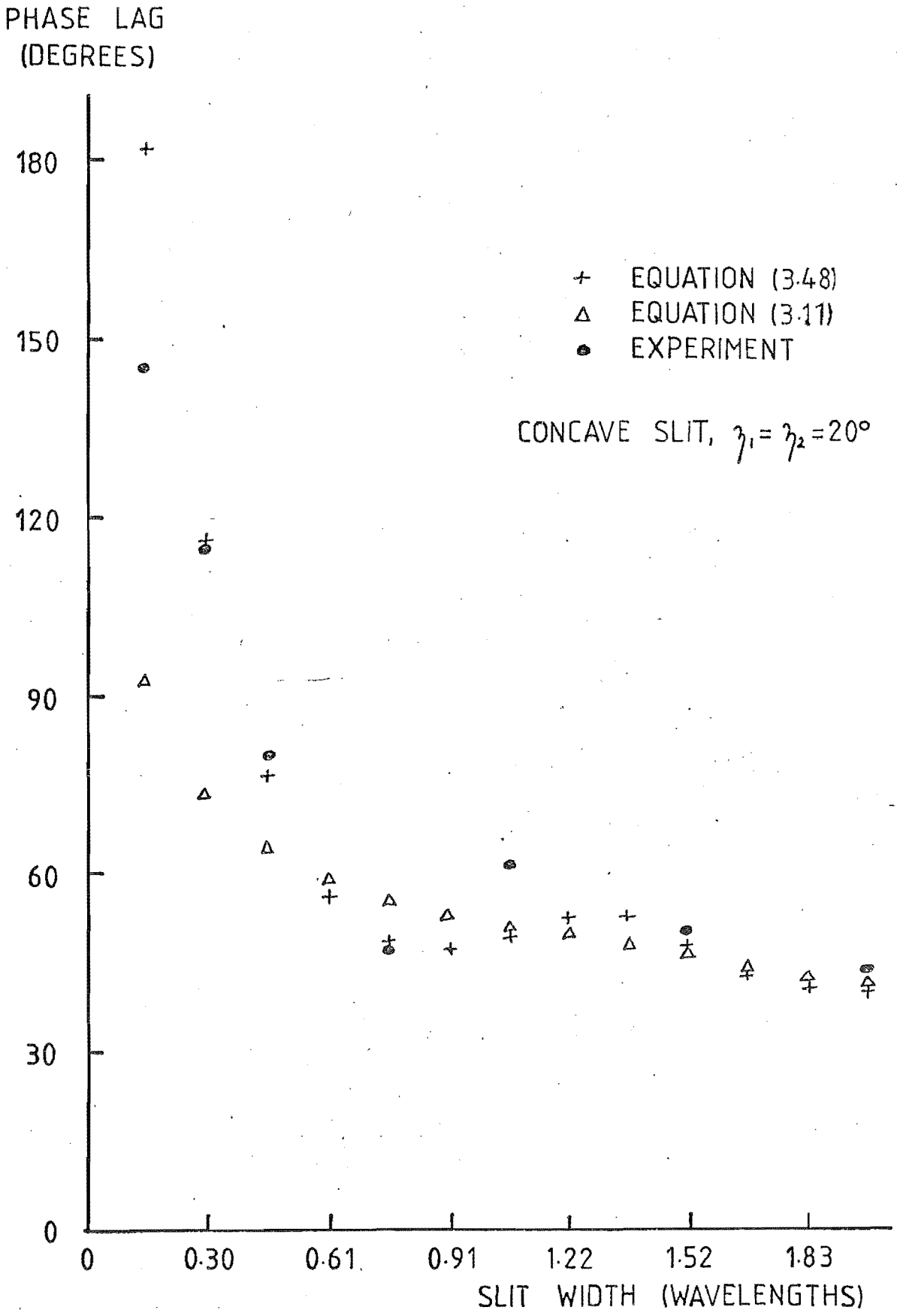

Figure 3.18b Comparison of Transmissions through concave slits (Phase).

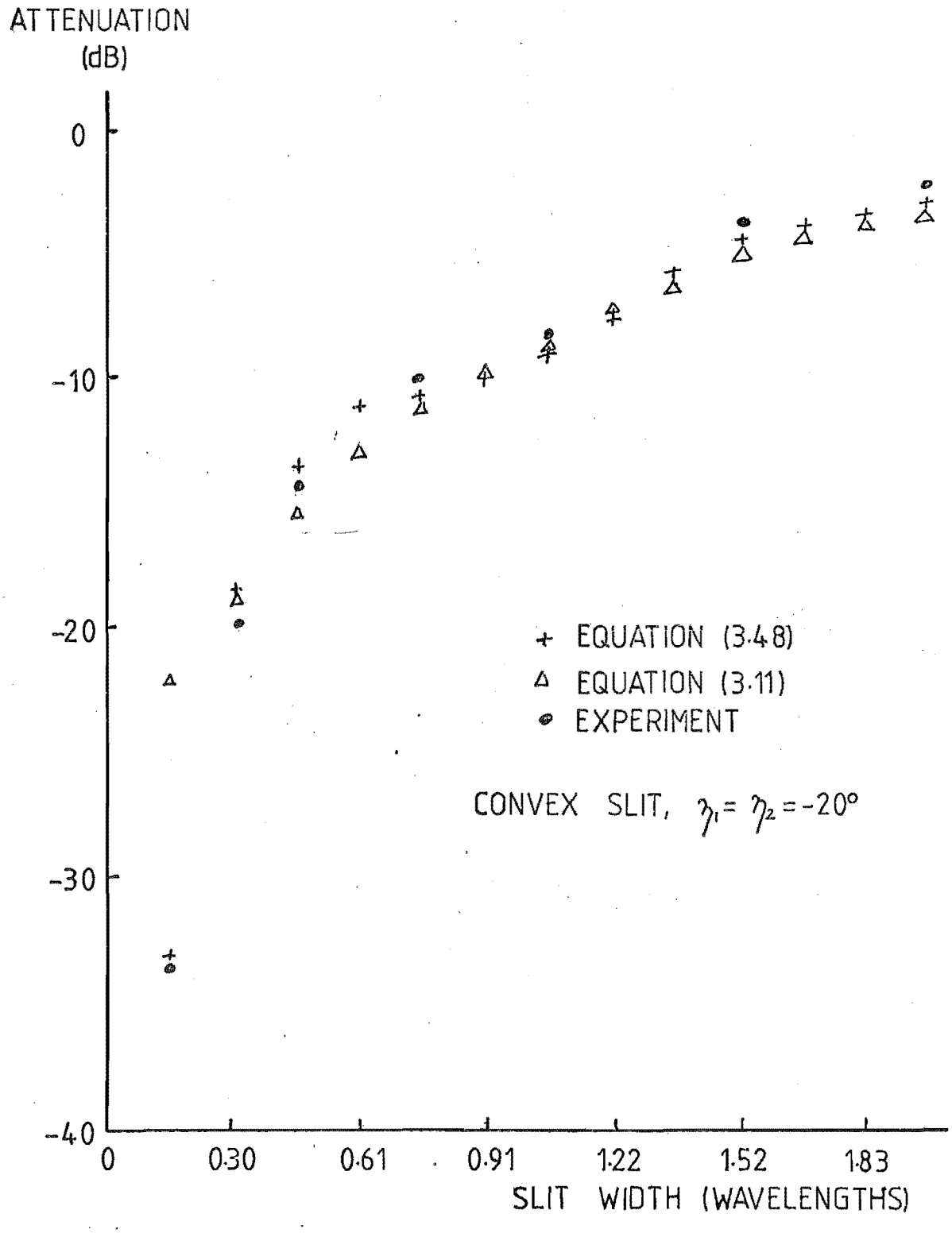

Figure 3.19a Comparison of Transmissions through convex slits, (Intensity).

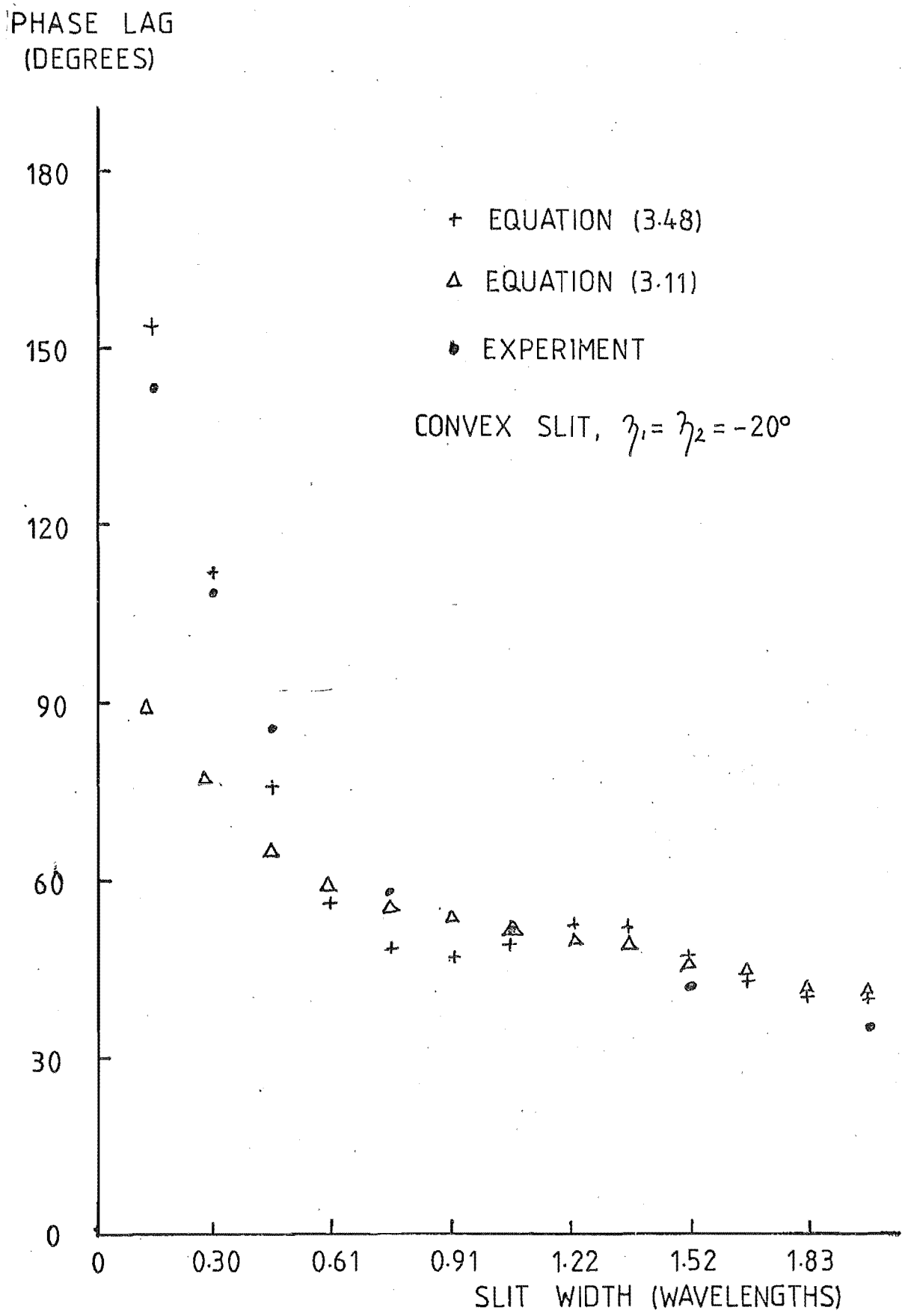

Figure 3.19b Comparisons of Transmissions through convex slits, (Phase).

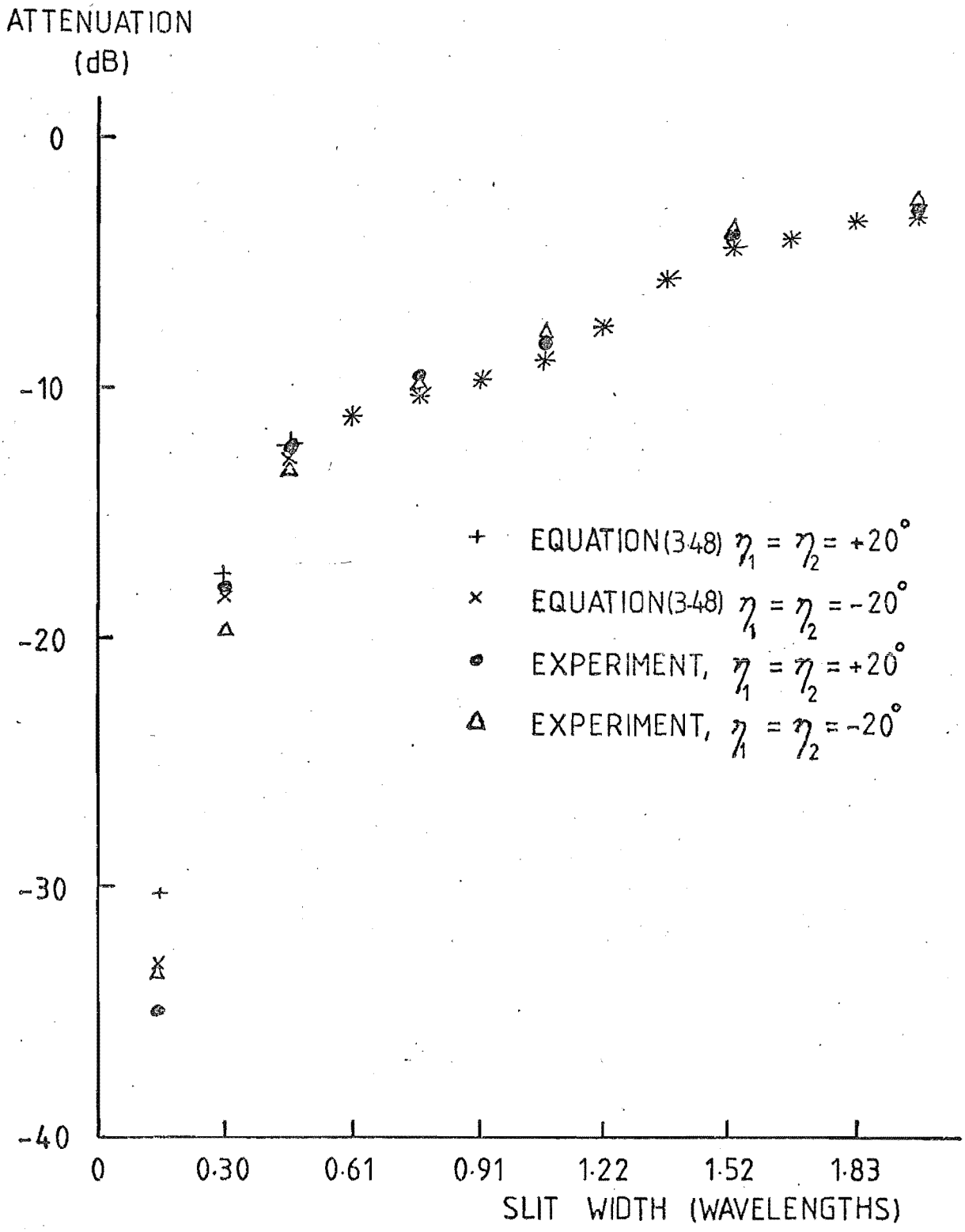

Figure 3.20a Comparison of Transmissions through concave and convex slits, (Intensity).

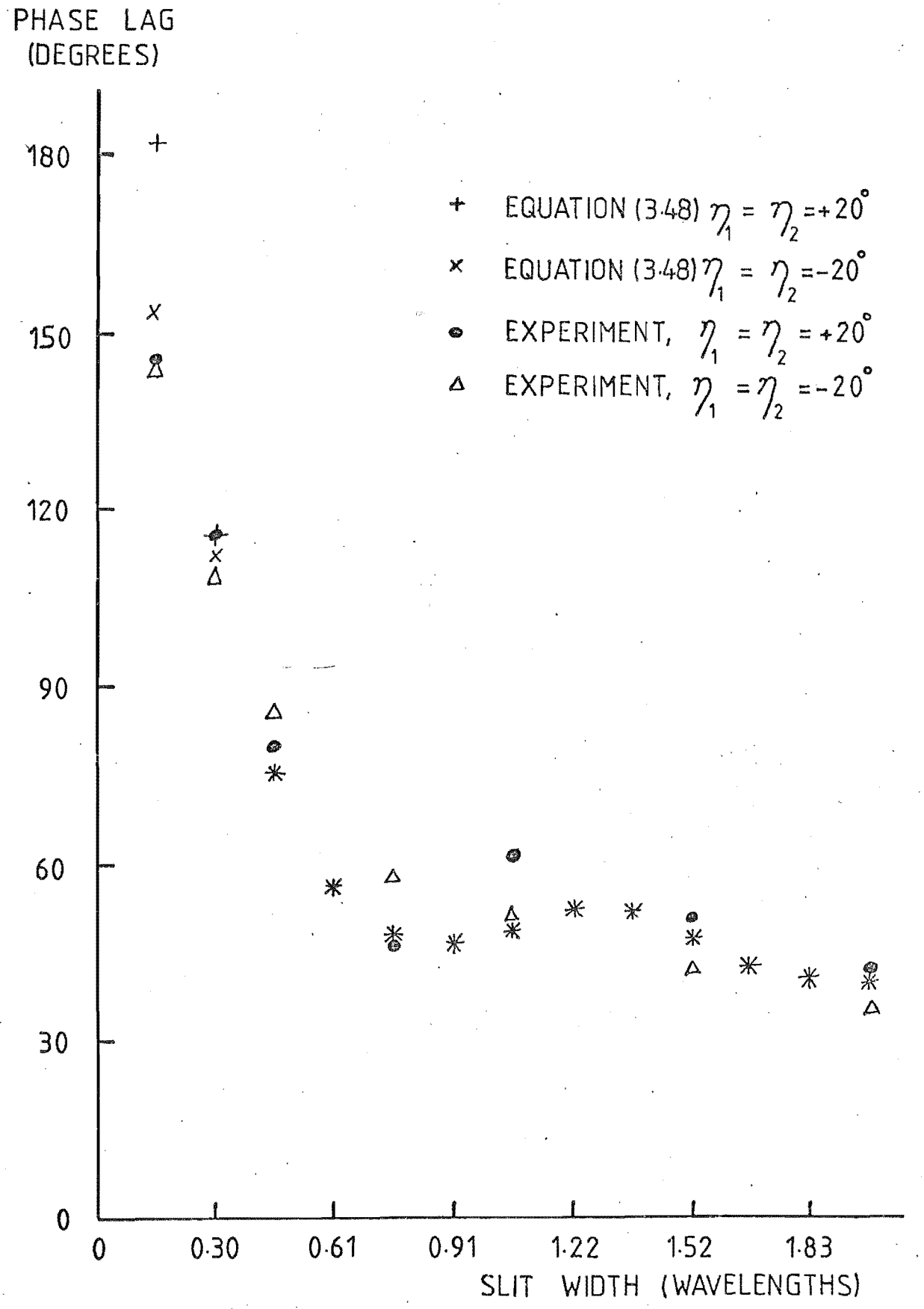

Figure 3.20b Comparison of Transmission through concave and convex slits, (Phase).

From the results presented in Figures 3.18 to 3.21, we see that the Clemmow type GTD approximation loses validity for slits less than a sixth of a wavelength wide although distribution shape remains well behaved. At such a small width, experimental values tend to show differences. This suggests that plane inclination becomes more important for narrow slits, where the aperture field distribution is more affected by currents on the conducting plane. It is conceivable that in the case of a narrow slit, an analogy between field strength and fluid velocity can be made. A concave shaped aperture might be expected to force more fluid through at a greater velocity than through a convex shaped aperture. From this crude anaology, for a very small slit, we would expect a greater field strength with a concave slit. This is not completely borne out by experiment, in Figure 3.20, for the smallest slit width, although the expected pattern is shown for all other small slit measurements.

Distributions for a number of concave, convex and zig slits were found by experiment and compared with theory. Agreement was found between theory and experiment for all slits except the most narrow ones where the theoretical phase tended to be incorrect and experimental results were degraded slightly by noise. Several example distributions are shown in Figure 3.21, a full list of which are found in Section 5.4.4.

3.5 METHOD OF MOMENTS

Another approach to the small slit problem can be through the method of moments.

The half plane solution technique involving the combination of Physical Optics and the Method of Moments in Chapter 2 can be applied to slits of any plane inclination. Physical optics currents can be placed on the front surfaces of the planes away from the edges, and moments method currents can be arranged about the edges. Higher order cross slit

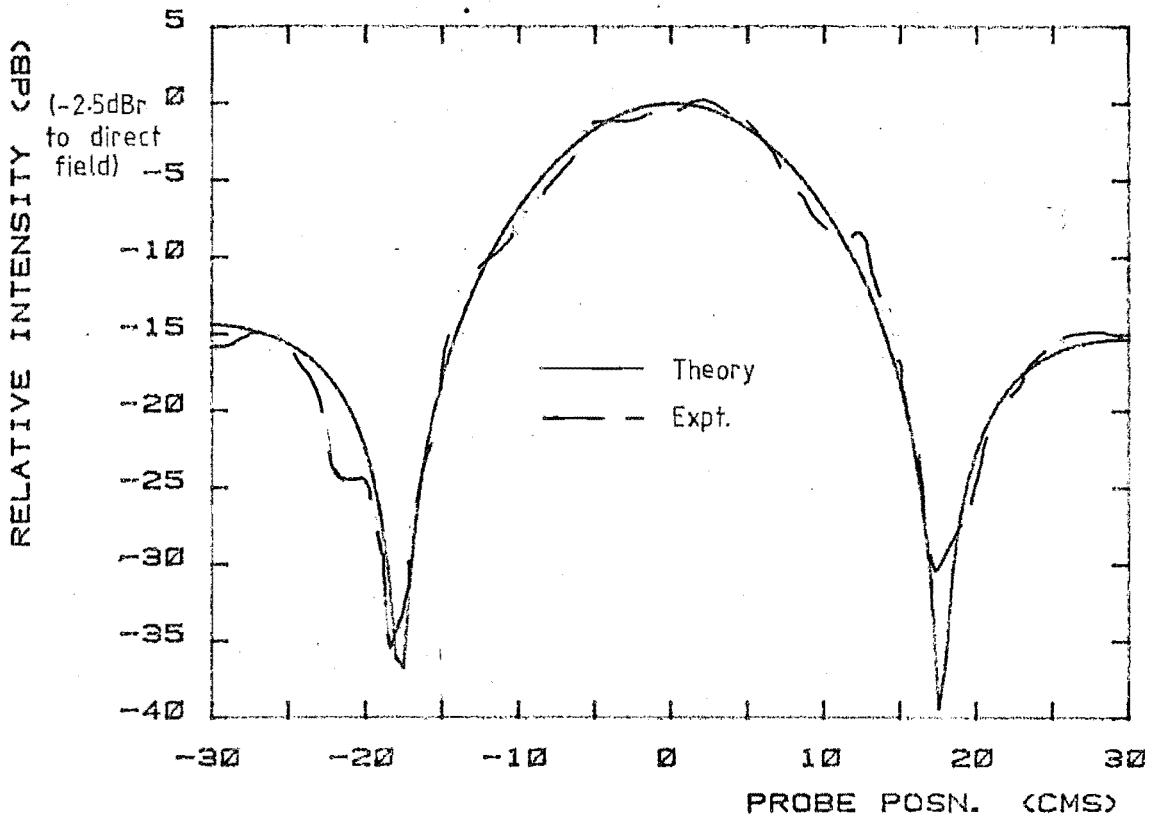

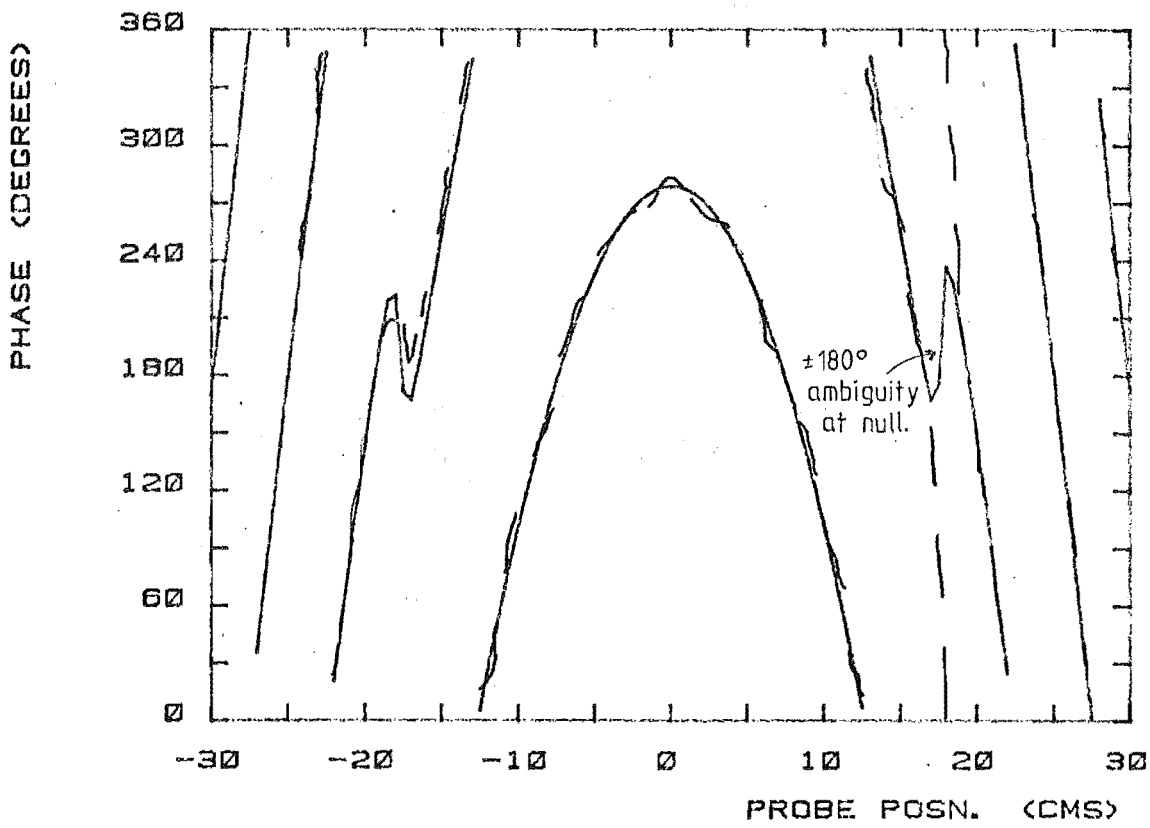

Figure 3.21a) $\eta_1 = 0$, $\eta_2 = 20^\circ$ 2λ wide Zig Slit, Comparison of Experiment and Theory.

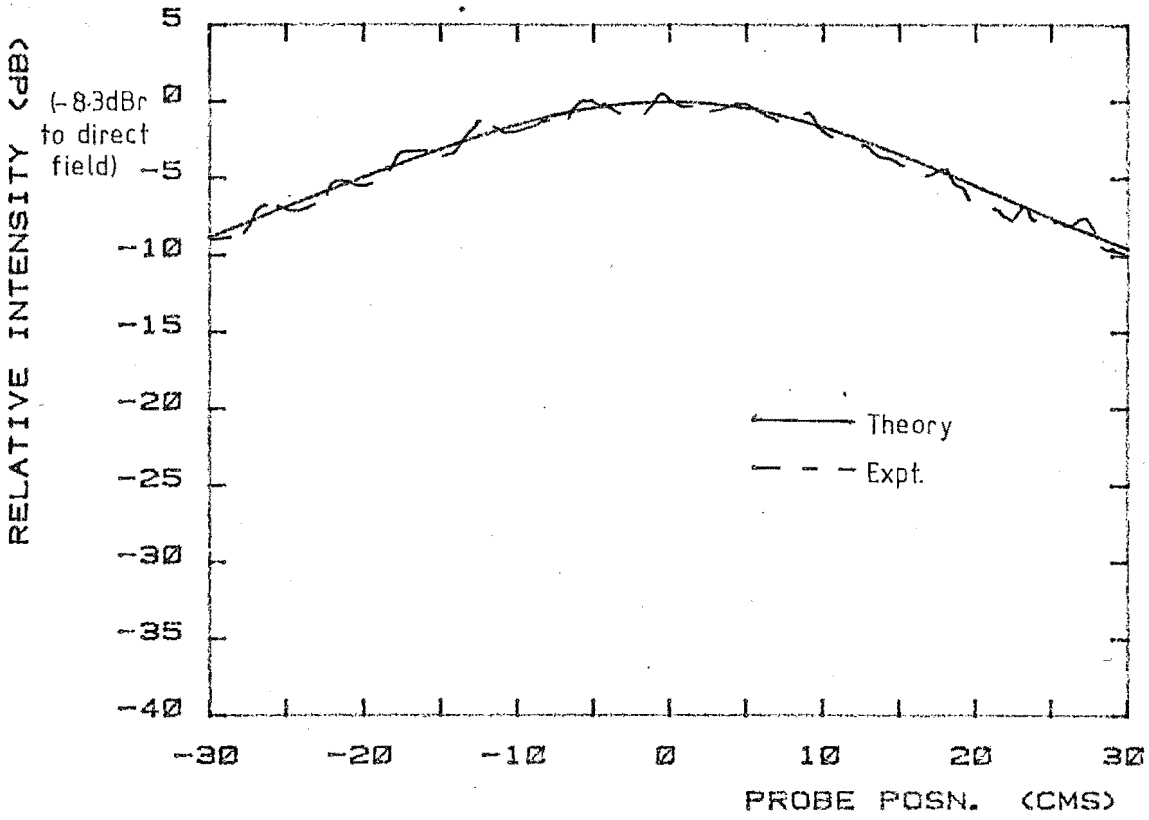

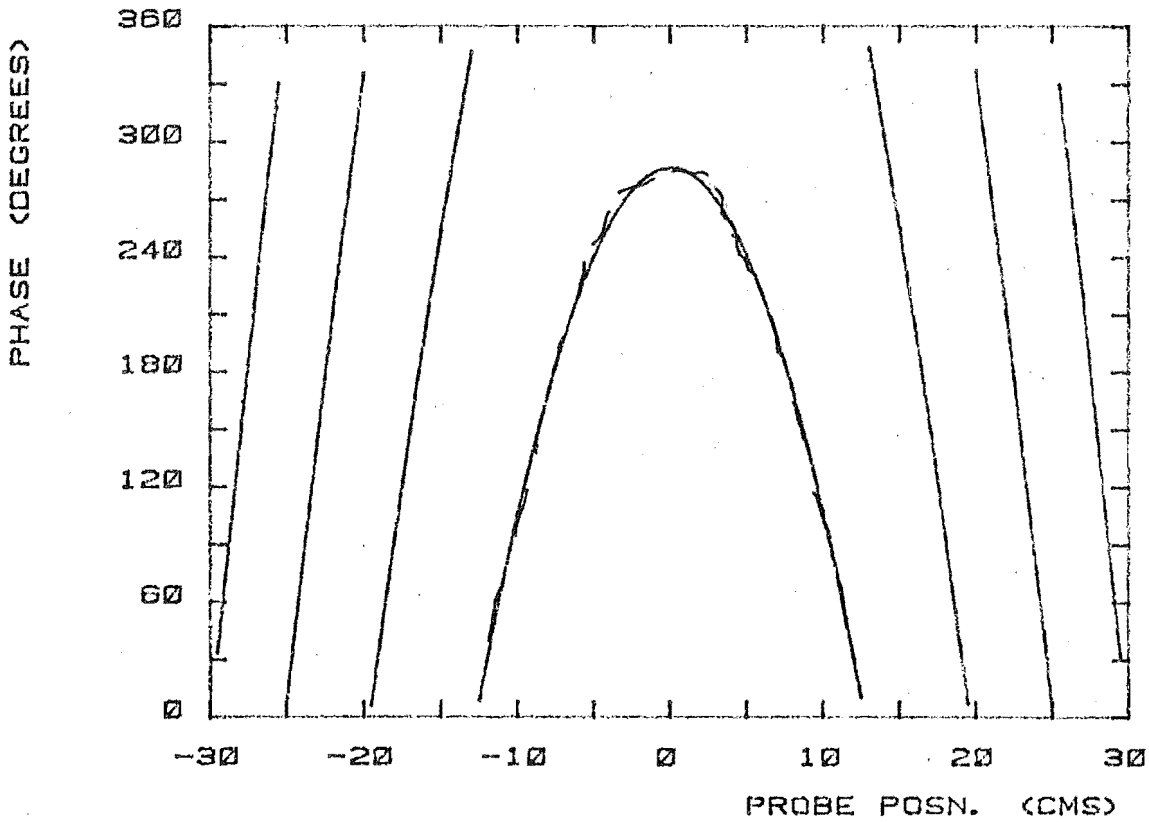

Figure 3.21b) $\eta_1 = o$, $\eta_2 = 20^o$ 1λ Wide Slit, Comparison of Experiment and Theory.

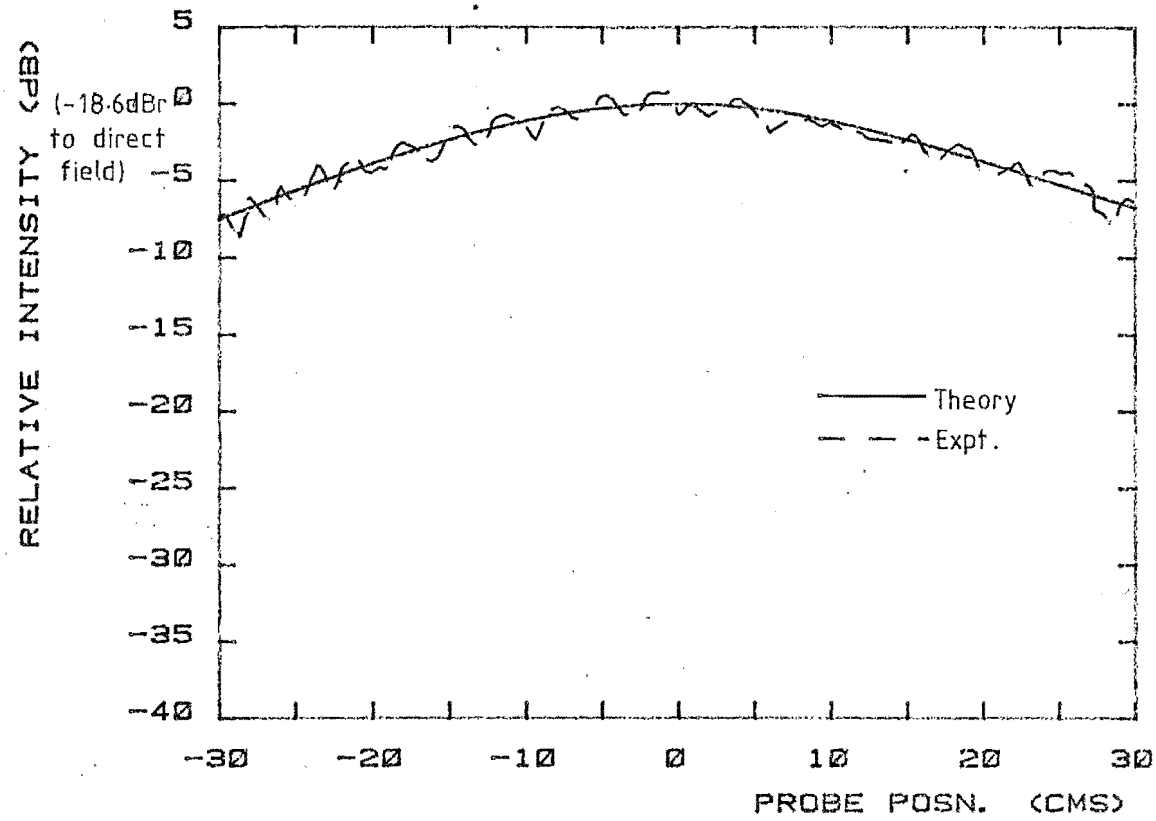

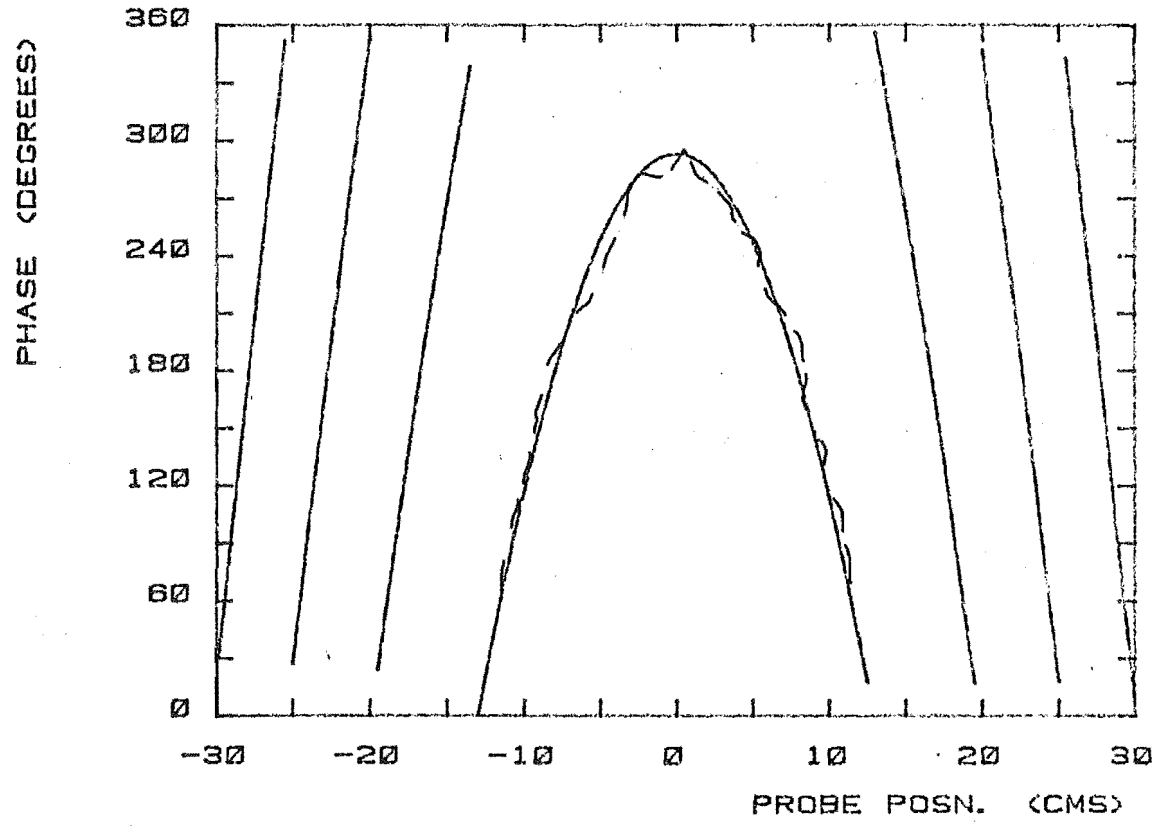

Figure 3.21c) $\eta_1 = 0$, $\eta_2 = 20^\circ$ $\lambda/3$ Slit, Comparison of Experiment and Theory.

couplings should be taken care of automatically by the production of the scatterer matrix. Naturally, with the inversion of a 110 x 110 scatterer matrix and the evaluation of a large number of physical optics currents away from the edges the time of solution is very much larger than that of the equivalent GTD solution, and will be of use mainly in situations where GTD results are incorrect.

This method was applied to various slits, and results are presented for narrow 20° concave and 20° convex slits to supplement the questionable GTD results. ~~(The transmitted intensities and phases are included in Figures 3.18 to 3.20 and)~~ A specimen field distribution for a 20° convex slit of width one third of a wavelength is presented in Figure 3.22. Extra wiggles on the intensity distribution are evident, and can be attributed to the leakage between the physical optics currents reaching a value comparable to the leakage through the slit.

This points out a major shortcoming of the method of calculation of the Physical Optics associated currents and field. A formulation involving a more complicated integration procedure would need to be used where physical optics currents extend over a wide range, 'blocking out' the incident field more completely.

The moments method gives an opportunity for study of the edge currents and for guaging the effects of screen inclination. Figure 3.23 pictures the currents on an isolated half plane, and on corresponding conducting planes of slits of various inclinations.

In all cases there are changes to the rear currents, behind the slit, in comparison with the currents behind an isolated half plane. It is apparent that the forward currents are affected most in the concave slit case. This might be expected as the larger forward plane currents will be closer to each other. From the results it looks as if these

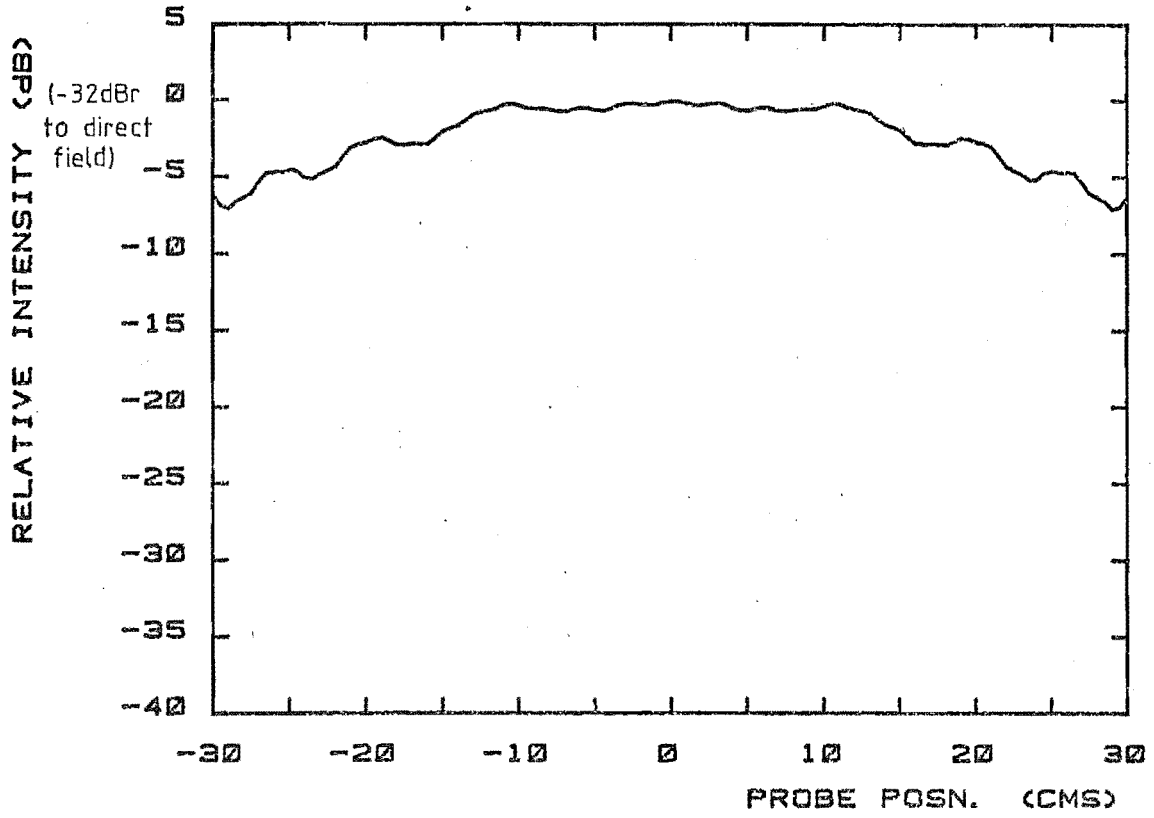

0·16λ SLIT.

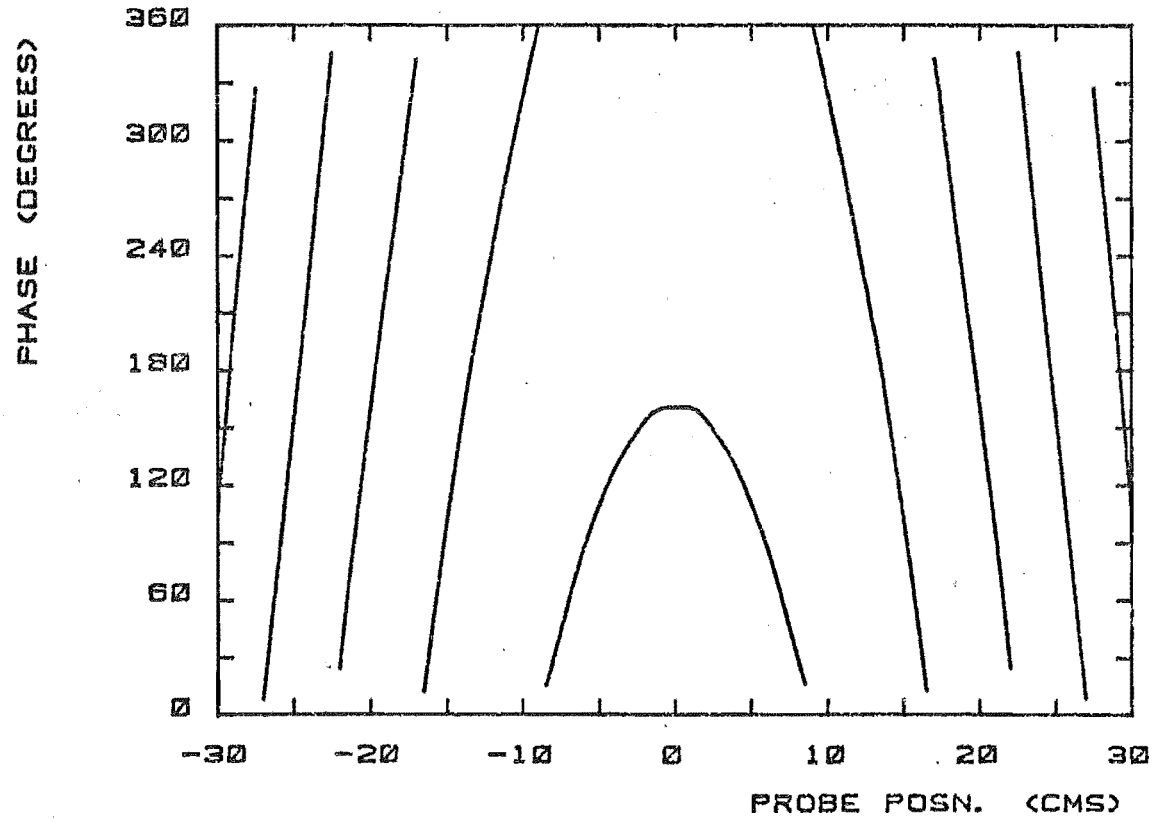

Figure 3.22, Field Diffraction by a Narrow Slit,

Physical Optics cum Method of Moments.

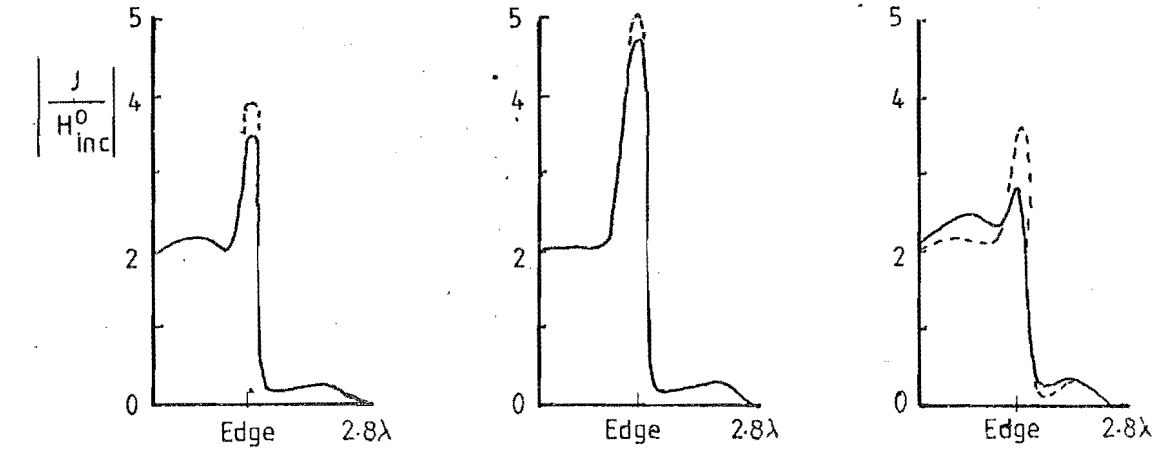

(a) 2λ Slit Case

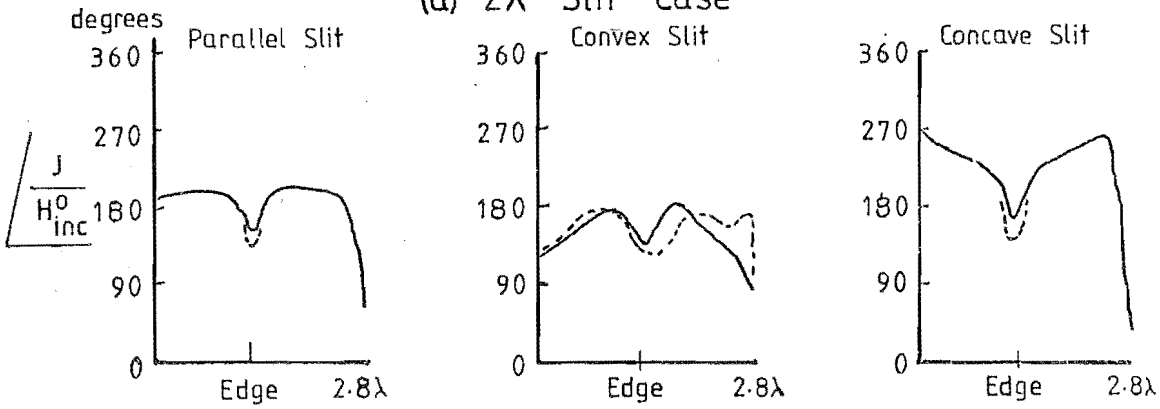

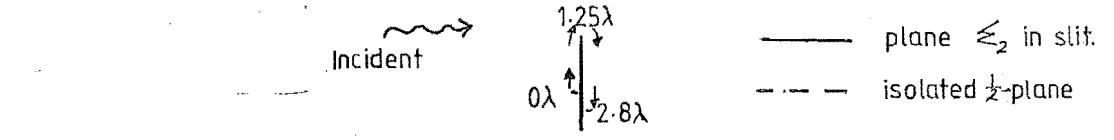

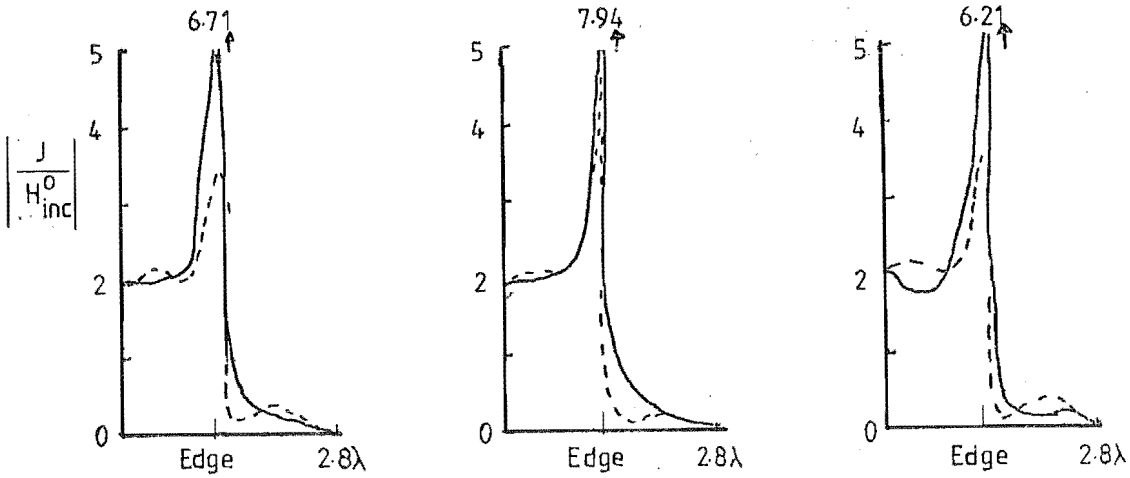

(b) 0·3λ Slit Case

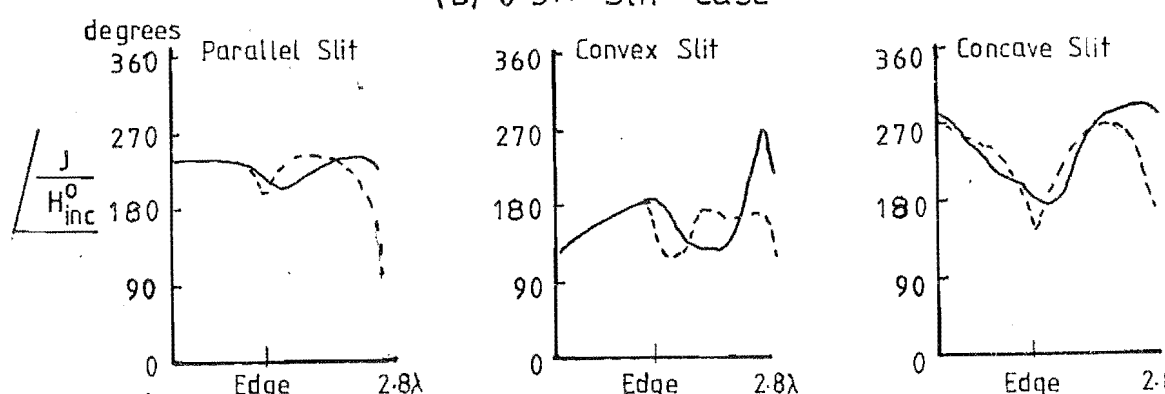

Figure 3.23 Moments Currents near the edges of Conducting Screens.

large currents have little effect upon the fields transmitted through slits.

In a situation where a large number of moments currents are clustered about an edge, with another large group of currents nearby, the total scatterer matrix may be very large. Under such circumstances, an iteration scheme may be utilised, as follows:

a). Assume P.O. currents on one plane, up to the edge. Use these currents and the P.O. currents on the other plane as sources to find the moments currents on the second edge using moment methods.

b). Use the found moments current and P.O. currents of the second plane in concert with the P.O. currents of the first plane to find the moments currents on the first plane. Stop if criteria met.

c). Use the moments currents and P.O. currents on the first plane along with the P.O. currents on the second plane to calculate a new set of second plane moments currents. Stop if criteria met.

d). Go to step b).

The finishing criterion can be either a small difference in the moments currents of the previous iteration or a small difference in the field. Such a calculation was carried out for a $\frac{1}{2}\lambda$ parallel plane slit and is presented in Figure 3.24. When step b) of the above scheme was run for the second time, the stopping criterion was met. The same solution could be obtained using the GTD theory in a much shorter time, but this example proves that the iteration scheme works, especially if it is considered that the Physical Optics edge currents are very inaccurate.

From the results in Figures 3.18 to 3.20 we have seen that the transmitted wave phase change in a slit is controllable over the region 40° to 140°, but the price is a large variation of the transmitted field

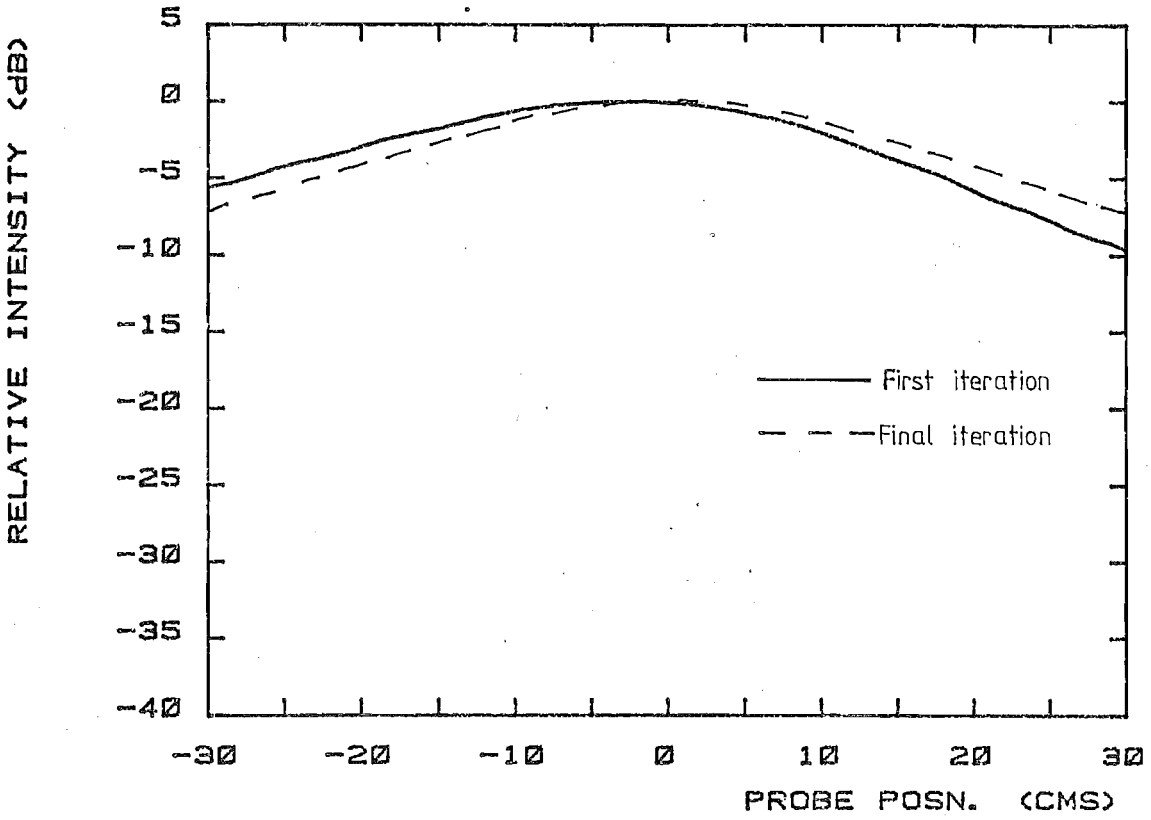

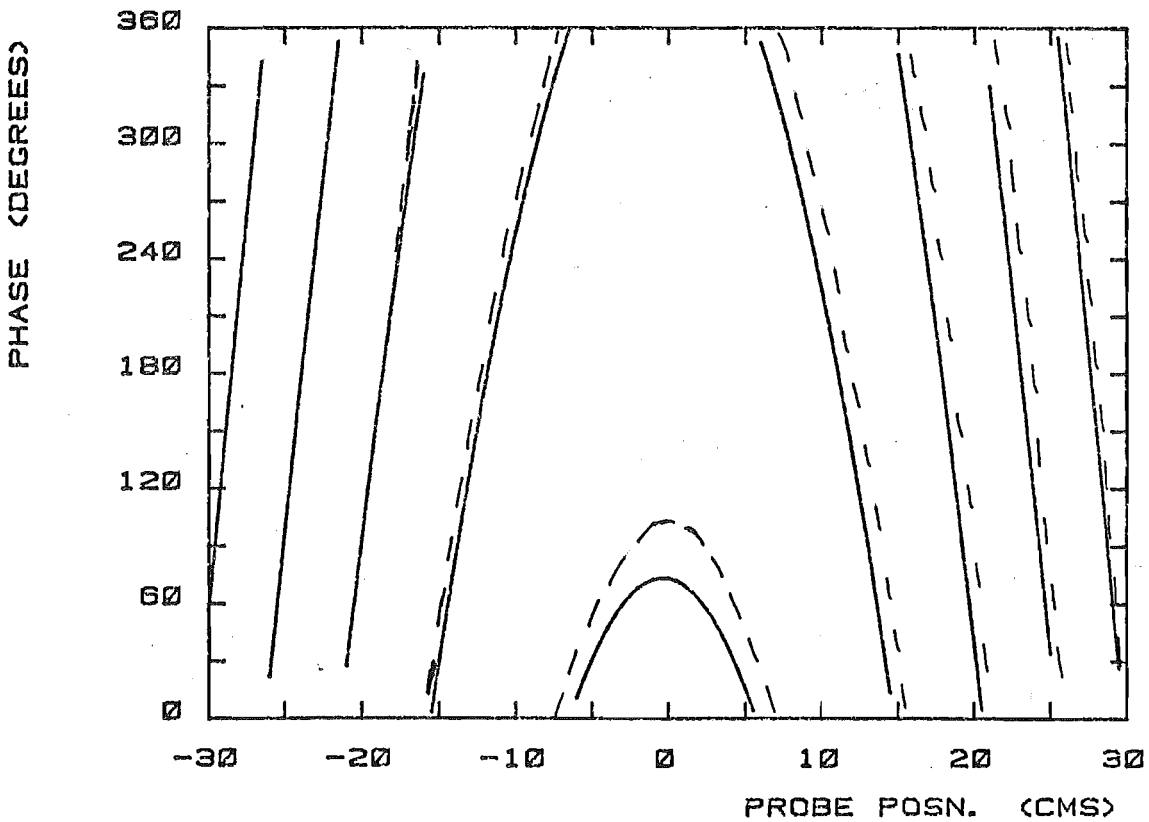

Figure 3.24 Comparison of the field through a $\lambda/2$ slit, iterated solutions of the Moments Method.

intensity. It may be possible to control the intensity independently of phase by the use of a pattern of relatively closely-spaced slits, which may be positioned to give the required intensity and phase leakage in a pre-determined direction.

A large number of identical slits placed apart at regular intervals is a diffraction grating. If the slits are far enough apart it can be assumed that the only interactions come from across slits rather than across the strips between the slits. In this case the diffraction pattern of a grating is just the sum of individual diffraction patterns of the slits. (Keller, 1957). When the strips between the slits are small in comparison to a wavelength (probably less than half a wavelength), the higher order differential term can be taken into account to provide an indication of the coupling between slits.

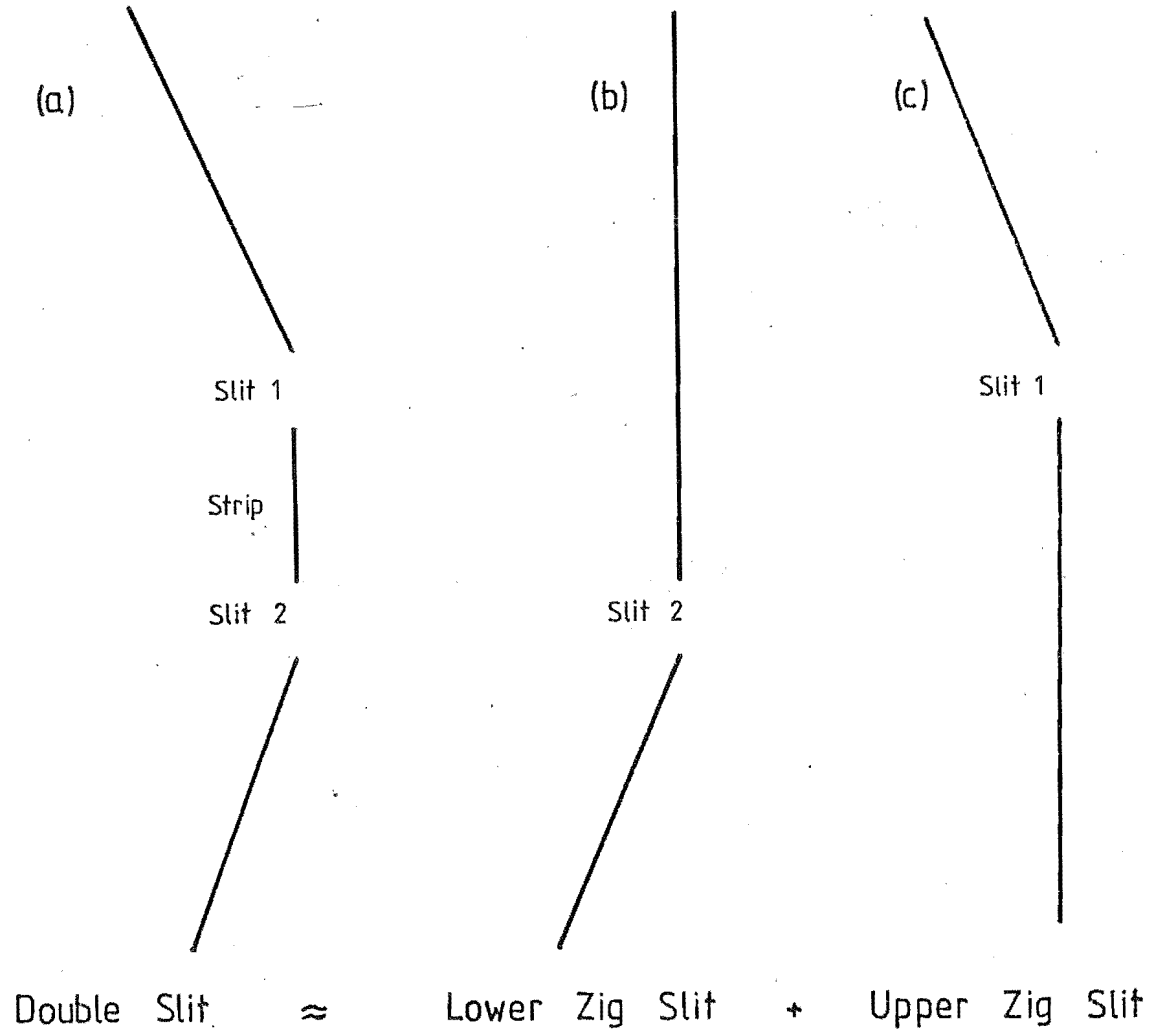

Figure 3.25 Double Slit Geometries.

For such small spacings, however, GTD is of questionable value, as shown by experimental results.

Take for example, the geometry shown in Figure 3.25(a).

In a case, where the slits, and the centre strip are small, GTD will be of little use. A result which, at best, can be considered only as a first approximation is the simple addition of the diffractions through the slits, considered independently of each other, i.e.,

$$E_{TOT} = E_T^{\text{Slit 1}} + E_T^{\text{Slit 2}}. \tag{3.52}$$

where $E_T^{\text{Slit 1}}$ is found using Equations (3.12) and (3.34) assuming that no reflection boundaries or secondary shadow boundaries are crossed, and using the zig slit geometry in Figure 3.25(b). Similarly, $E_T^{\text{Slit 2}}$ is found with the help of Figure 3.25(c) and Equations (3.12) and (3.34).

As an example we can study a double slit combination, where the slits are $\lambda/2$ wide with a 1λ wide strip, and the conducting planes and strip share the same plane.

The result of Equation (3.52), shown in Figure 3.26 needs confirmation, hence some other method of calculation must be used. Recourse can be made to the Method of Moments, by placing a total of 150 currents on the strip and round the half plane edges, and assuming Physical Optics Currents away from the edges. We assume that, the strip and conducting planes are $\lambda/40$ wide.

Figure 3.27 shows the transmitted field distribution for the doubleslit example geometry with the conducting planes sharing the same plane as the strip.

There are differences between Figures 3.26 and 3.27, probably because the strip is not wide enough to isolate the slits as implied in Equation (3.52).

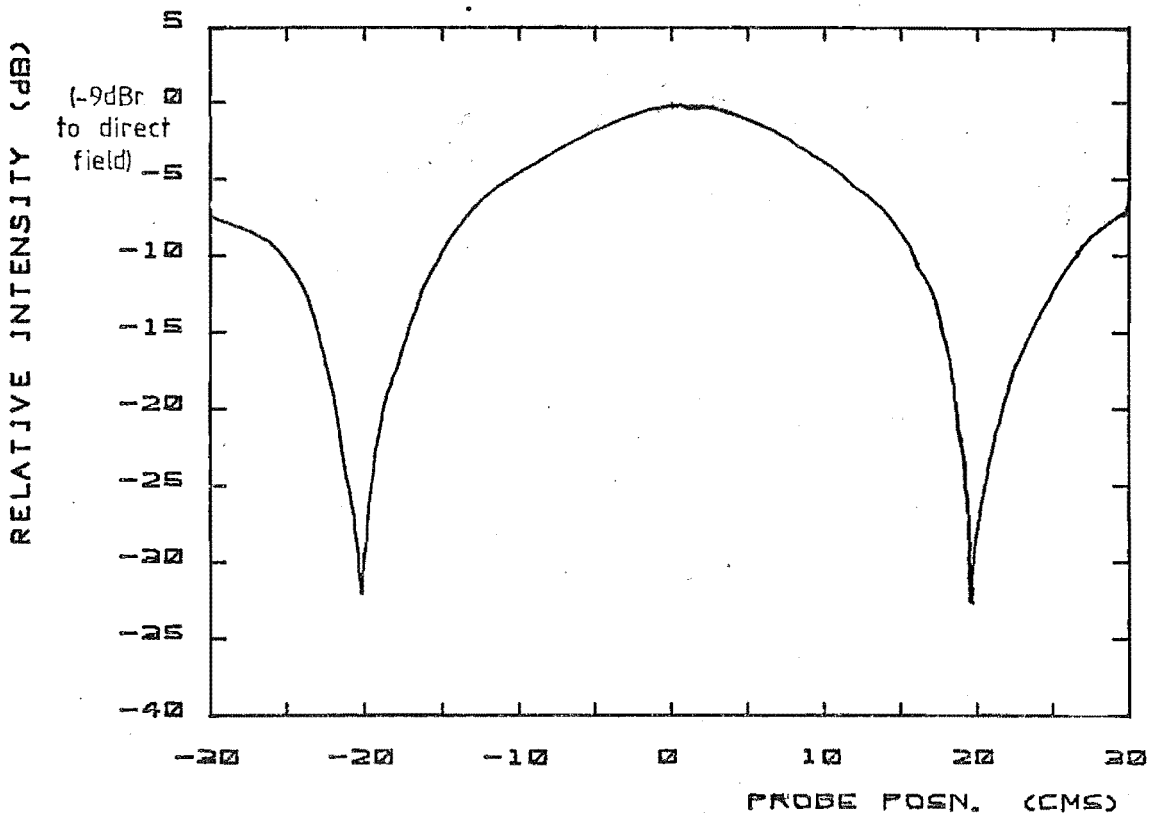

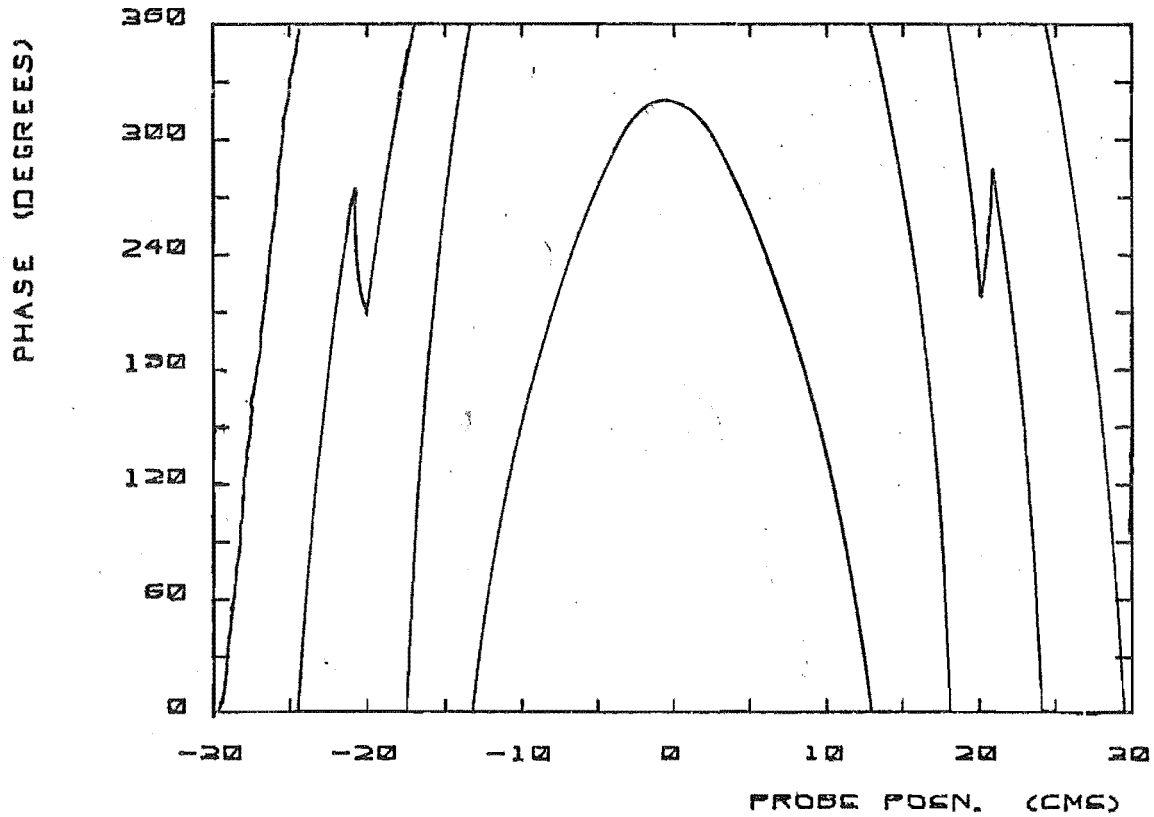

Figure 3.26 Field through a Double Slit, GTD Description.

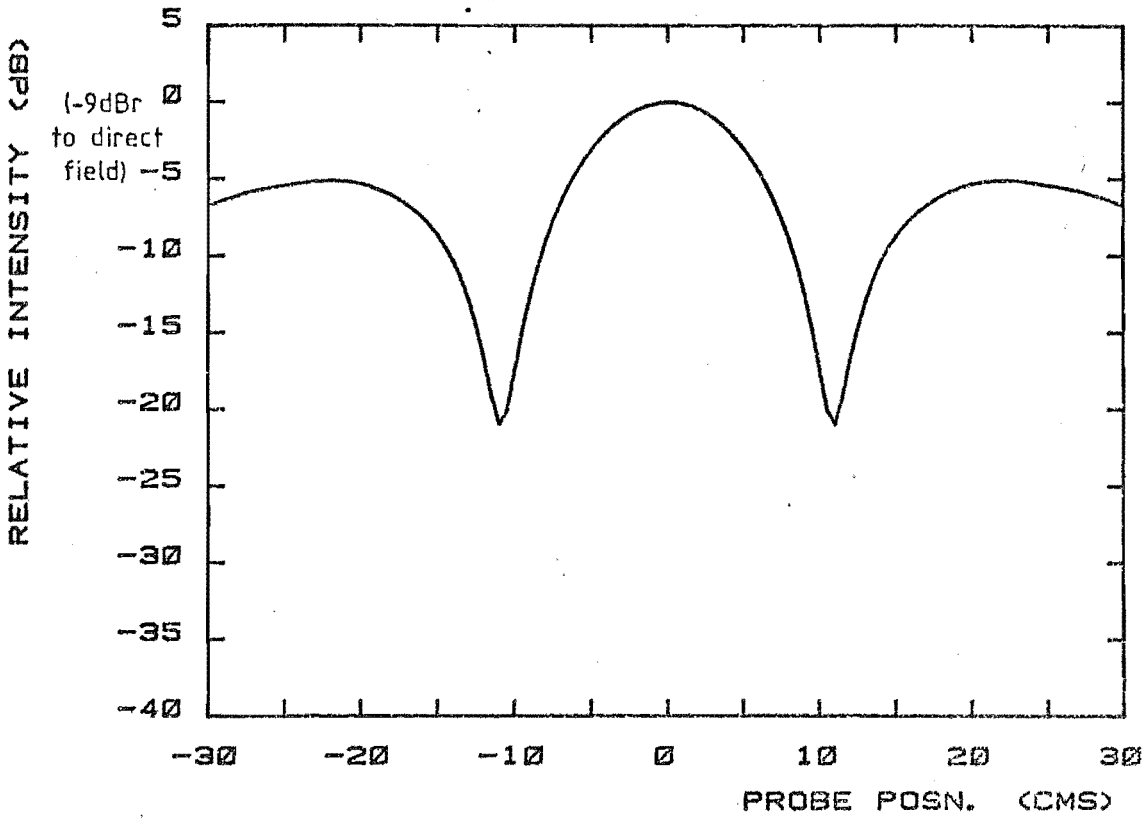

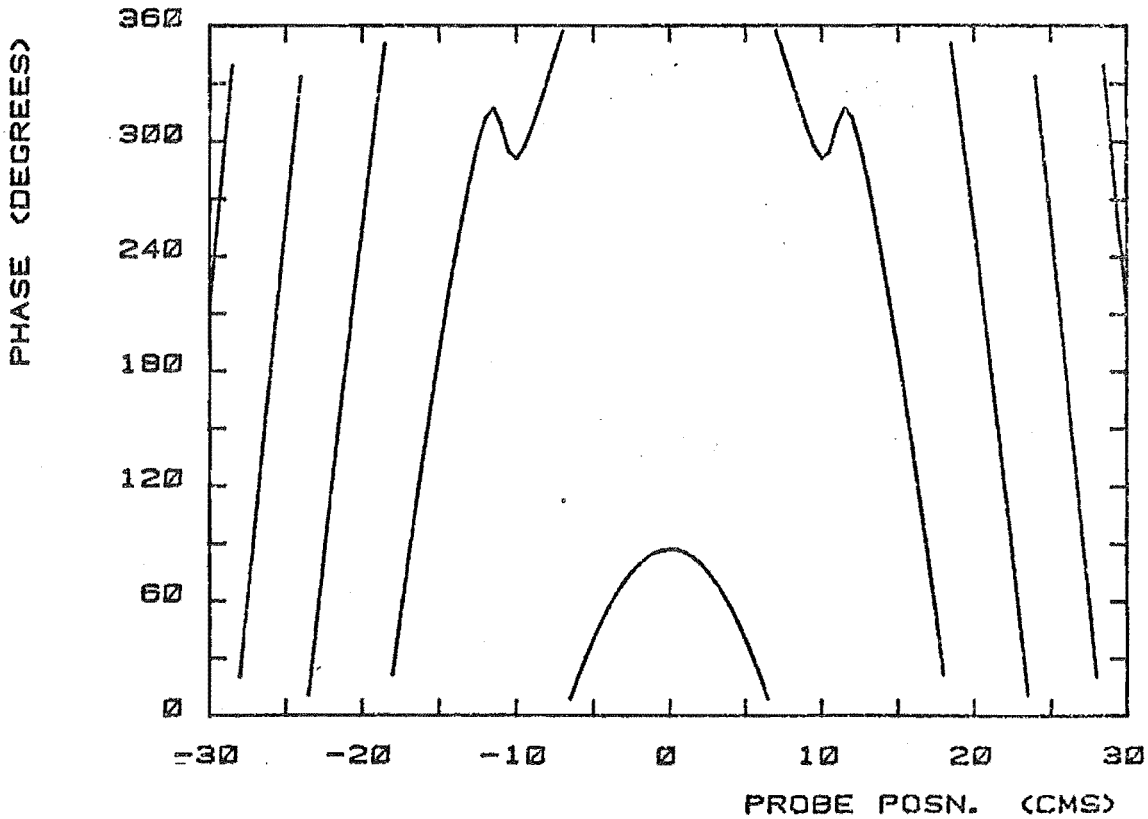

Figure 3.27 Field through a Double Slit, Moments Description.

Method of Moments result shows a null placed about 10cm along the probe locus from the direct transmission axis. This can be compared to the 18cm distance to a null in the case of a 2λ parallel plane slit. The GTD result shows no close nulls, but does show that a cross-strip diffraction term is of consequence if the Moment Method results are correct.

It is expected that the induced current method will be the most accurate representation as results from GTD methods are essentially for far fields while the small width current filaments in the method of moments have a far field extending almost immediately from their boundaries, hence small apertures can be accounted for by the method of moments. The assumed width of the planes and the strip (λ/40) may affect results for such width slits, (Row, 1954).

The moment method is limited by the size of problem to about 250 current elements. This in turn will limit the number of strip/slit combinations.

3.6 OTHER WORK ON INCLINED PLANE SLITS

Tan (1967a), (1967b), (1968) studied the transmitted fields through symmetrical convex slits. His work used the variational principle employing the Kirchoff's descriptions of the aperture field as the starting field. He also took into account some cross-aperture interaction by introducing a 'reflection-interaction' term.

Tan's 'reflection-interaction' comes from considering induced line currents near the edges which act as sources diffracting off the opposite edge to the observation point. Higher order cross-slit diffractions are disregarded, although an iteration scheme is introduced to alter these induced edge currents to incorporate the effects of the proximity of the opposite slit edge. It is interesting to note than Tan applies Clemmow's

half plane diffraction formulation (Equation (2.75)) to each slit plane. Equation (2.75) is used to describe the initial diffraction of the incident wave by each inclined half plane and is also applied to the 'reflection-interaction' by using the induced line currents as sources.

The 'reflection-interaction' interpretation works only for convex slits, and in the case of concave no such interaction can occur. Tan's later work (Tan, 1968), is related to the work of Millar (1956a), (1956b) and James and Kerdermelidis (1973) in that he uses edge currents to better define the slit transmitted field. Tan's work is less related to the GTD high frequency form but more closely associated to the PO-MOM iterated-slit work carried out in this Chapter.

Tan has studied wide slits, i.e. 3λ wide or greater, and his experimental results have little in common with our experimental work. The formulation given here can be applied at any probe point about the slit, i.e. on either side of the aperture

3.7 DISCUSSION

To a first approximation, a slit in the reflector of a parabolic cylinder antenna can be modelled as a slit with inclined conducting half planes. For such a slit, exact results from the Separation of Variables technique cannot be obtained, and unless the slit is extremely small, quasi static techniques cannot be used. A Rayleigh scatterer, with an aperture extremely small in terms of a wavelength appears to produce a far field which is relatively independent of the shape of the aperture, (Van Bladel, 1977). This implies that for small slit widths the inclination of the planes has no significant effect upon the transmitted far field. From experimental results, the opposite appears to be true. The only explanation that can be offered to explain this apparent difference is to assume that the Quasi-static interpretation can only be

used where the aperture is less than a small width and where the source field is uniform. A larger aperture will allow a greater sensitivity for the plane inclinations, while for a very wide aperture the induced currents on the far side of the conducting planes will have a diminished effect upon the transmitted field through the aperture. It appears that slit planes inclination will cause variations over a range of small slit widths in what could best be described as a 'sub-resonance' region, i.e., in the case of transmission measurements, where the direct field is present, the edge-diffracted fields are of the order of $1/ka$ or $1/(ka)^{\frac{1}{2}}$ (See Equation (3.7))* smaller than the incident field. In this case any change in the diffracted field will have a relatively small effect on the measured transmitted field. Study of Figure (3.20), where transmission measurements of slits with $\eta_1 = \eta_2 = +20^{\circ}$ and $\eta_1 = \eta_2 = -20^{\circ}$ are compared, shows that measured differences do not occur until the incident direct field is attenuated by a slit of less than a third of a wavelength width.

G.T.D. relies upon a single edge passive source to model the disturbances caused by an edge. This source is not properly useable in the near-zone regions within half a wavelength of the edge, hence for narrow slits even where multiple-diffraction is taken into account, it must be expected that the GTD interpretation of the far field will fail. For a more accurate representation the actual currents induced about the edges must be found. This is done in the Method of Moments. These currents are affected by other edges in proximity and will give a more accurate rendition of the far field for smaller slits.

A diffraction grating will provide a greater leaked intensity, but it must be noted that its size is limited for two reasons:

---

* where a is the distance from the diffracting edge to the field point.

1. The field transmitted through the grating will exhibit many peaks and nulls. These peaks will vary in position with any slight movements of the parabolic reflector.

2. The total aperture size will be too big, causing unwanted specular lobes and nulls in the forward direction of the reflector antenna.

For these reasons a diffraction grating would be of little use in the reflector of a parabolic reflector.

CHAPTER 4: PARABOLIC REFLECTOR

'My way of joking is to tell the truth.

Its the funniest joke in the world'

George Bernard Shaw, 1850-1950

In this chapter we will use the tools developed in Chapter 2 and modified in Chapter 3 to study the field properties of a Parabolic Reflector antenna, with and without slits in the reflector. Figure 4.1 is a two-dimensional cross section of the parabolic reflector antenna with the forward aperture in the focal plane. The dipole is at the focal point. For the purposes of the derivations and calculations it will be assumed that the Dirichlet boundary conditions are satisfied. If the antenna is modelled at the z = 0 plane as in Figure 4.1, a two-dimensional description of the antenna is adequate, if the dipole is replaced by an E-plane polarized line source.

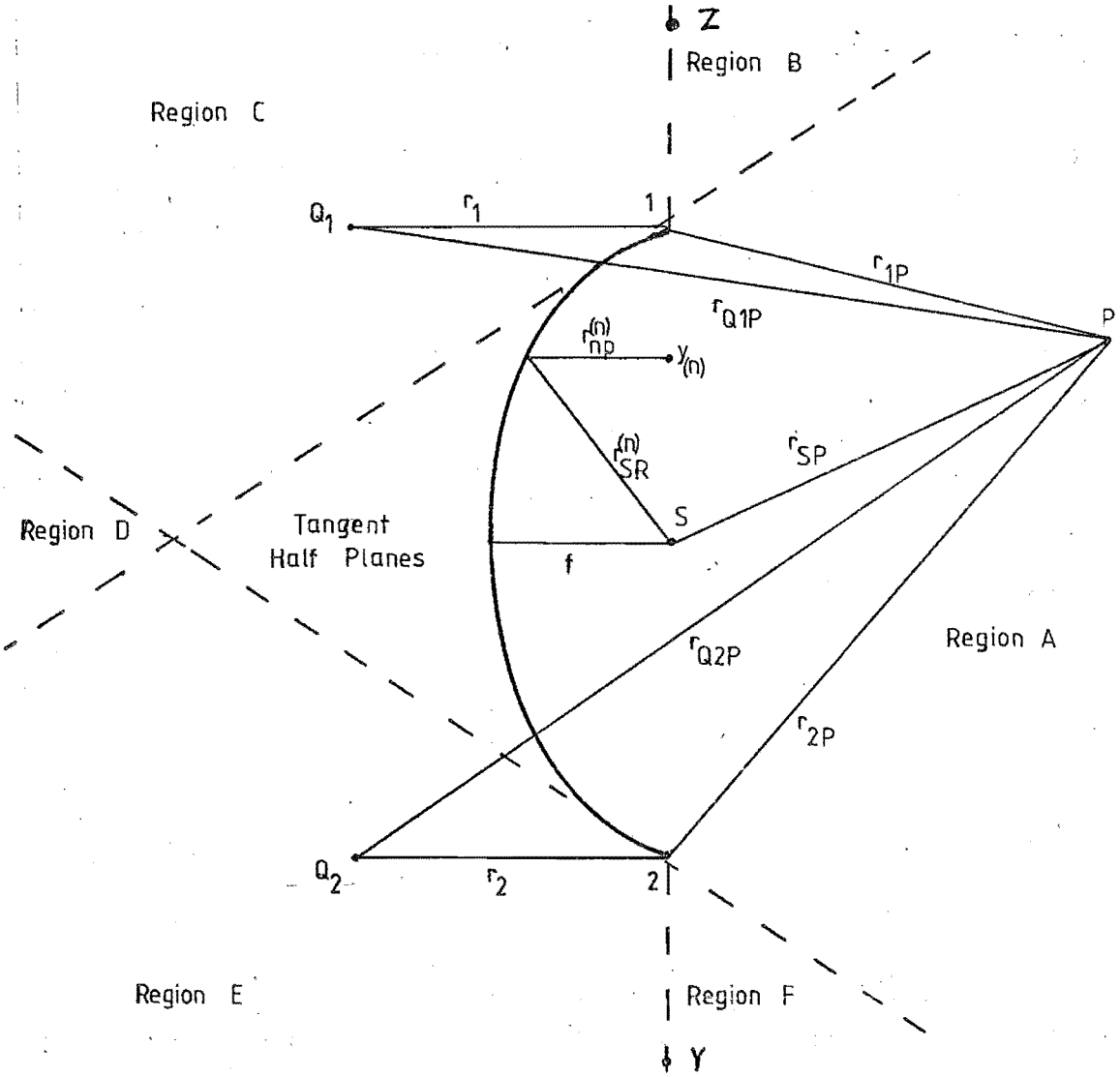

Figure 4.1 Parabolic Reflector Antenna, aperture 10λ.

4.1 UNPERTURBED PARABOLA

4.1.1 GTD DESCRIPTION

As a first approximation the diffracting edges of the reflector in Figure 4.1 can be placed on tangent half planes. Applying the Clemmow type GTD formulae for the half plane given in Chapter 2, Equation (2.78) to the tangent half planes, we arrive at the expression,

$$E^{diff}_{par} = D_1 + D_2 \tag{4.1}$$

where D_x, (x=1,2), describes the diffracted field off edge X.

Now,

$$D_1 = \Delta_1 \frac{e^{-j(kr_{Q1P}-\pi/4)}}{(8\pi jk(r_{Q1P}+r_{1P}+r_1))^{\frac{1}{2}}} F\left[k(r_1+r_{1P}-r_{Q1P})\right]$$

$$- \Delta_2 \frac{e^{-j(kr_{SP}-\pi/4)}}{(8\pi jk(r_{SP}+r_{1P}+r_1))^{\frac{1}{2}}} F\left[k(r_1+r_{1P}-r_{SP})\right], \tag{4.2}$$

$$= -\Delta_1 \cdot Q(r_{Q1P}, r_{1P}, r_1) \cdot F\left[k(r_1+r_{1P}-r_{Q1P})\right]$$

$$- \Delta_2 \cdot Q(r_{SP}, r_{1P}, r_1) \cdot F\left[k(r_1+r_{1P}-r_{SP})\right] ,$$

where Δ_1 = -1 in Regions A and F,

= 0 in Region E,

= +1 Elsewhere.

Δ_2 = -1 in Regions C and D,

= 0 in Region E,

= +1 Elsewhere.

The shortened Q function formulations defined in Chapter 3 may be used to shorten the lengths of the equations in this Chapter.

$$D_2 = \Delta_3 \cdot Q(r_{Q2P}, r_{2P}, r_2) \cdot F\left[k(r_2+r_{2P}-r_{Q2P})\right] - \Delta_4 \cdot Q(r_{SP}, r_{2P}, r_2) \cdot F\left[k(r_2+r_{2P}-r_{SP})\right] , \tag{4.3}$$

where Δ_3 = -1 in Regions A and B,

= 0 in Region C,

= +1 Elsewhere.

Δ_4 = -1 in Regions D and E,

= 0 in Region C,

= +1 Elsewhere.

The total field of the parabolic reflector includes the source, hence,

$$E_{par}^{tot} = E_{par}^{source} + E_{par}^{diff}, \tag{4.4}$$

where

$$E_{par}^{source} = \frac{e^{-jkr_{sp}}}{\sqrt{8\pi jkr_{sp}}} \text{ in Regions A, B, F,} \tag{4.5}$$

and = 0 Elsewhere.

The GTD result is shown as Figure 4.2. Three points which arise from inspection of the intensity distribution in Figure 4.2a are,

a) there is no main lobe in the forward direction,

b) there are no interference effects in the angular regions 90-135 degrees and 225 to 270 degrees where the angle is measured from the source to the probe according to Figure 4.1,

c) there are discontinuities at 90° and 270°.

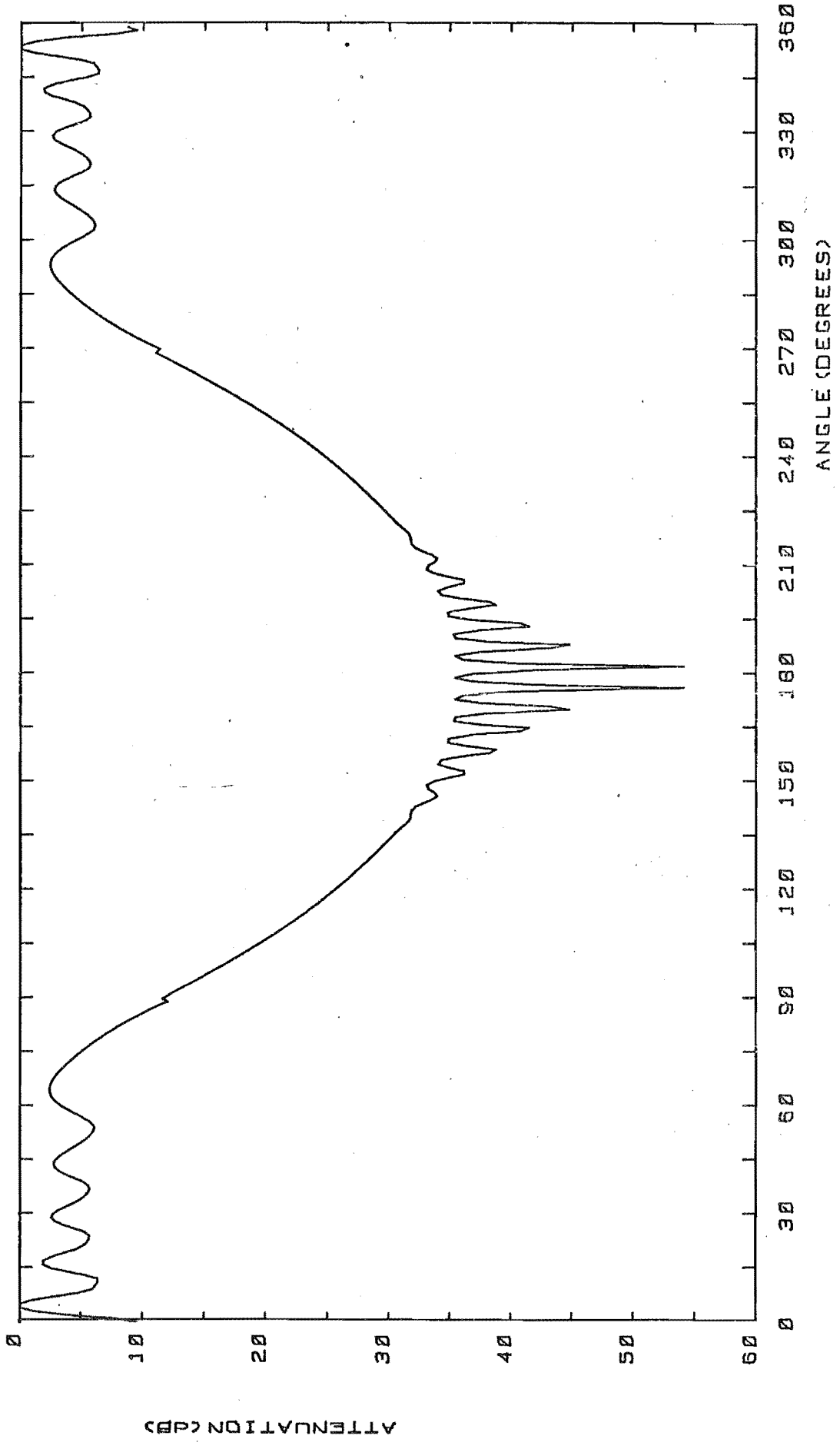

Figure 4.2a) Reflector Field Distribution, Initial GTD Description, (Intensity).

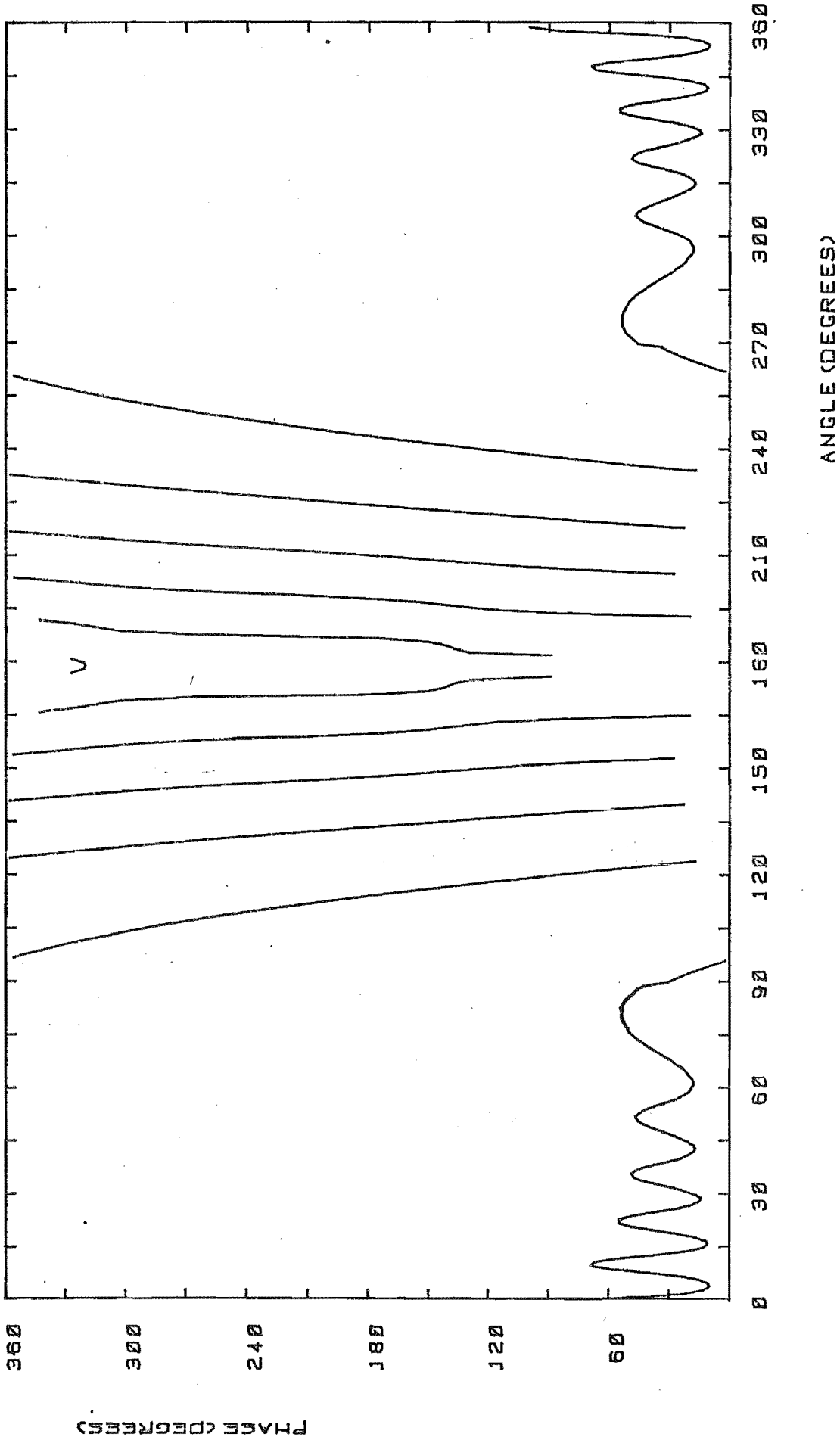

Figure 4.2b) Reflector Field Distribution, Initial GTD Description, (Phase).

Studying point a) we find that the rim sources are cylindrical in nature, hence the field found from the summation of the focus source and the rim sources will have cylindrical dependence. The GTD representation is reasonably accurate to within 10^{o} of the forward axis (Kouyoumjian, 1975), but closer to the forward axis plane wave transmission is found. In the forward region a line of aperture sources between edges 1 and 2 can be included as sources to account for the larger forward field strength.

Hence for the GTD description of the reflector in Figure 4.1, an additional forward axial source field must be included, which will be the spatial Fourier transform of the reflector aperture distribution shown in Figure 4.3.

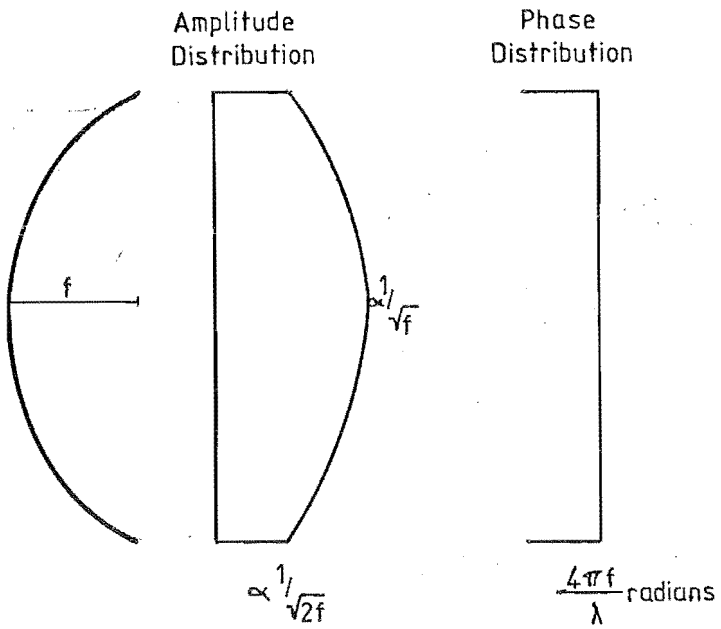

Figure 4.3 Parabolic Reflector Aperture Distribution.

The aperture distribution has an approximate quadratic amplitude variation and a linear phase distribution, which is found by using ray tracing from the source which has a cylindrical dependence until

reflection at the parabolic reflector where it becomes a plane wave. On reflection the ray passes through a caustic where there is a 'π' phase change. Rather than going through the process of obtaining the Fourier Transform of the aperture distribution, it can be assumed that the distribution is a Physical Optics (P.O.) approximation of the actual distribution. At the edges the currents on the aperture will not exhibit the discontinuity as shown in Figure 4.1, but have amplitude and phase variations about and beyond the edges (Kritikos, 1963).

The P.O. approximation is only properly useable in the near axial direction, about 30° off axis (Ross, 1966). The field from the P.O. aperture is found by integrating the surface currents over the aperture, but the integration may be avoided by replacing the continuous aperture distribution with an array of in-phase cylindrical line sources with amplitudes dependent upon source positions.

Hence,

$$E_{par}^{for} = \frac{e^{-jk(2f+\pi)}}{\sqrt{8\pi jk}} \sum_{n=1}^{N} \frac{1}{\sqrt{r_{SR}^{(n)}}} \frac{e^{-jkr_{np}}}{\sqrt{8\pi jkr_{np}}} \cdot \Delta C_n \qquad (4.6)$$

$$= 0 \qquad 10^{\circ} \ll \theta < 350^{\circ},$$

Where $r_{SR}^{(n)}$ is the distance from the focal source to the reflector on the ray which connects the focal source and the n^{th} source via the reflector, as shown in Figure 4.1,

r_{np} is the distance from the n^{th} source to the probe,

ΔC_n is the nqrmalised width of source n,

f is the focal distance of the reflector.

For the geometry of Figure 4.1, we find

$$r_{SR}^{(n)} = \left(\frac{Y_{(n)}^4}{16f^2} + \frac{Y_{(n)}^2}{2} + f^2\right)^{\frac{1}{2}}, \tag{4.7}$$

assuming that the focal source is at the origin of a rectangular coordinate system and that $Y_{(n)}$ is the predetermined position of the n^{th} line source on the aperture.

Ten line sources placed 3cm apart are used to give the field in the forward direction.

Turning our attention to point (b) of the GTD approach we find that there is no interference in Regions C and E in Figure 4.1. The only place behind the reflector where interference of the diffracted rays from the edges will occur is in Region D. This corresponds to the rather narrow region 135° to 225° in Figure 4.2a where there are peaks and nulls. This effect is a direct consequence of assuming tangential half planes at the edges and treating the edges as such. In this way, false boundary conditions will apply at the antenna angles 135° and 225°, forcing one diffracted ray to zero. This problem can only be circumvented by assuming diffraction off a convex surface with a source at the edge. This problem was studied in Chapter 2, and the conclusion reached was that under Dirichlet boundary conditions the diffracted rays into the deep shadow region (beyond 225° for edge 1 and less than 135° for edge 2) would suffer a large amount of attenuation, due to the long surface path length and also the normal differential diffraction coefficient in Equation (2.79). Thus it appears reasonable to disregard the effects of convex surface diffraction, (Rusch and Sørensen, 1975).

The discontinuities noted in the GTD approach point (c) arise from the arbitrary nulling of the cross aperture diffracted field at the opposite edge. To overcome this, higher order diffractions can be taken into account. Edge to edge multidiffraction, analogous to multiple

cross slit diffractions, can be included, but are of little real consequence beyond the second order, due to their greater attenuation with distance. Such high order diffractions will however cut out the discontinuities. Multiple diffractions are only important in apertures less than two wavelengths in size but for completeness we shall include second order diffraction (Ryan, 1968).

Reflections of diffracted rays off the concave surface of the parabolic from the edge sources can also be included in the analyais.

The geometry for second order diffraction is shown as Figure 4.4., and

$$E_{par}^{2diff} = R_1 C_2 + R_2 C_1, \qquad (4.8)$$

where E_{par}^{2diff} is the field from second order diffractions, and $R_X (X=1,2)$, are the cross aperture edge source strengths. C_X are the diffracted fields off edge X from the source situated on the opposite edge.

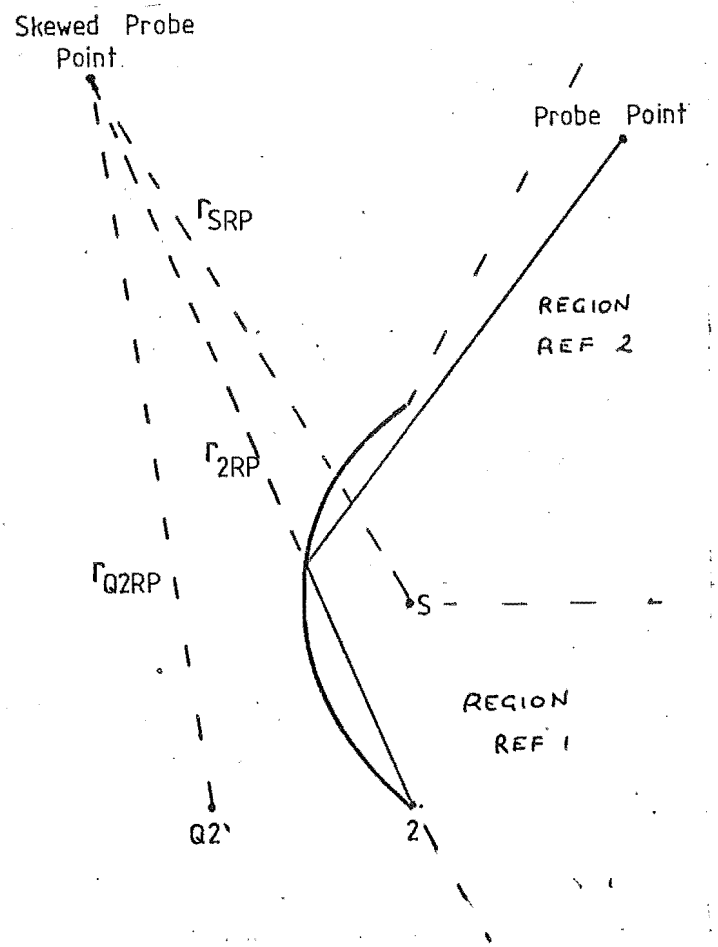

Figure 4.4 Higher Order Diffractions and Reflections associated with a Parabolic Reflector.

Now,

$$R_1 = \Big[Q(r_{Q1Y}', d/2, r_{1Y}) \cdot F\left[k(r_{1Y} + \frac{d}{2} - r_{Q1Y})\right] - Q(r_{sY}', d/2, r_{1Y}) \cdot F\left[k(r_{1Y} + \frac{d}{2} - r_{sY})\right] \Big] e^{jkr_{1Y}} \cdot (8\pi jkr_{1Y})^{\frac{1}{2}} \tag{4.9}$$

$$R_2 = \Big[Q(r_{Q2Z}', d/2, r_{2Z}) \cdot F\left[k(r_{2Z} + \frac{d}{2} - r_{Q2Z})\right] - Q(r_{sZ}', d/2, r_{2Z}) \cdot F\left[k(r_{2Z} + \frac{d}{2} - r_{sZ})\right] \Big] e^{jkr_{2Z}} \cdot (8\pi jkr_{2Z})^{\frac{1}{2}} \tag{4.10}$$

$$C_1 = -\Delta_1 \cdot Q(r_{I2P}', r_{1P}, d) \cdot F\left[k(r_{1P} + d - r_{I2P})\right] - \Delta_2 \cdot Q(r_{2P}', r_{1P}, d) \cdot F\left[k(r_{1P} + d - r_{2P})\right] \tag{4.11}$$

$$C_2 = -\Delta_3 \cdot Q(r_{I1P}', r_{2P}, d) \cdot F\left[k(r_{2P} + d - r_{I1P})\right] - \Delta_4 \cdot Q(r_{1P}', r_{2P}, d) \cdot F\left[k(r_{2P} + d - r_{1P})\right] \tag{4.12}$$

Where d is the reflector aperture width, and

where $\Delta_1 \rightarrow \Delta_4$ have the same values as in Equations (4.2) and (4.3).

Only those rays that undergo one reflection are considered. Rays that suffer two reflections or more on the concave surface of the reflector experience a whispering gallery effect which is usually swamped by the Geometrical Optics term and the first order reflections.

Consider diffraction from the lower edge, Number 2 in Figure 4.4. Only those rays diffracted from edge 2 which strike the upper concave side of the reflector will escape from the front aperture in one reflection. For each value of antenna angle, Θ, studied, those between

approximately angles 0^{o} and 63^{o} will have a 'diffracted-reflected' ray present. The actual reflection point on the reflector is found using the laws of geometrical reflection and a bisection routine on the computer.

The 'diffracted-reflected' rays would then be,

$$E_{par}^{dr1} = Q(r_{Q1RP}, d/2, r_{1RP}) \cdot F\left[k(r_{1RP} + \frac{d}{2} - r_{Q1RP})\right]$$

$$+ Q(r_{SRP}, d/2, r_{1RP}) \cdot F\left[k(r_{1RP} + \frac{d}{2} - r_{SRP})\right] \qquad (4.13)$$

For P in Region Ref. 1.,

$= 0$ Elsewhere,

$$E_{par}^{dr2} = Q(r_{Q2RP}, d/2, r_{2RP}) \cdot F\left[k(r_{2RP} + \frac{d}{2} - r_{Q2RP})\right]$$

$$+ Q(r_{SRP}, d/2, r_{2RP}) \cdot F\left[k(r_{2RP} + \frac{d}{2} - r_{SRP})\right] \qquad (4.14)$$

For P in Region Ref. 2.,

$= 0$ Elsewhere,

r_{QXRP} (X = 1,2), is the distance between the image source and the probe if the path between the reflector and the probe is skewed in line with the path from the edge X to the reflector as shown in Figure 4.4

The distances r_{XRP} (X = 1,2) are found in a similar manner.

The inclusion of these higher order GTD rays will modify Equation (4.4) to,

$$E_{par}^{tot} = E_{par}^{S} + E_{par}^{diff} + E_{par}^{2diff} + E_{par}^{dr1} + E_{par}^{dr2}. \qquad (4.15)$$

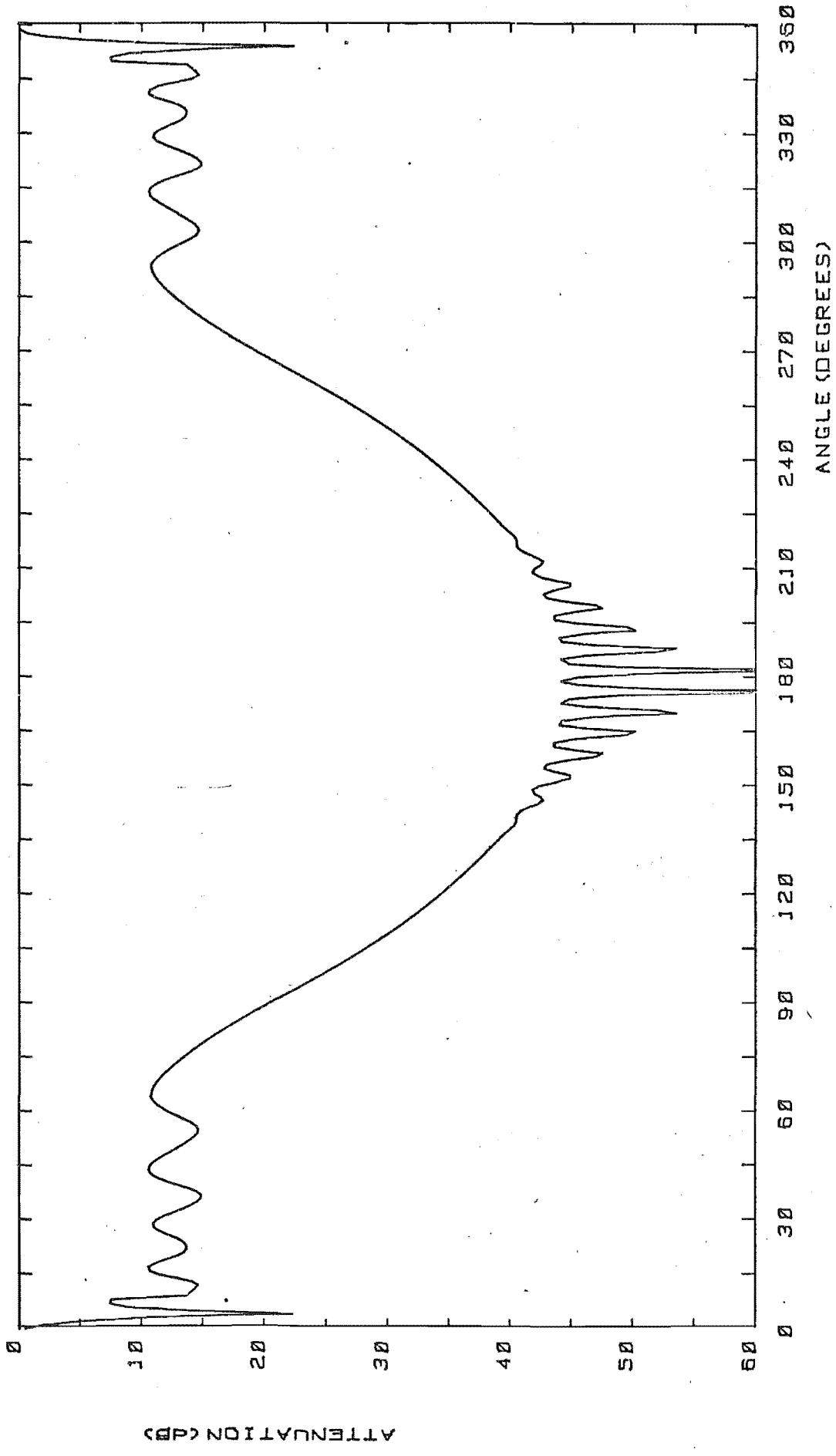

Figure 4.5a) Reflector Field Distribution, Final GTD Description, (Intensity).

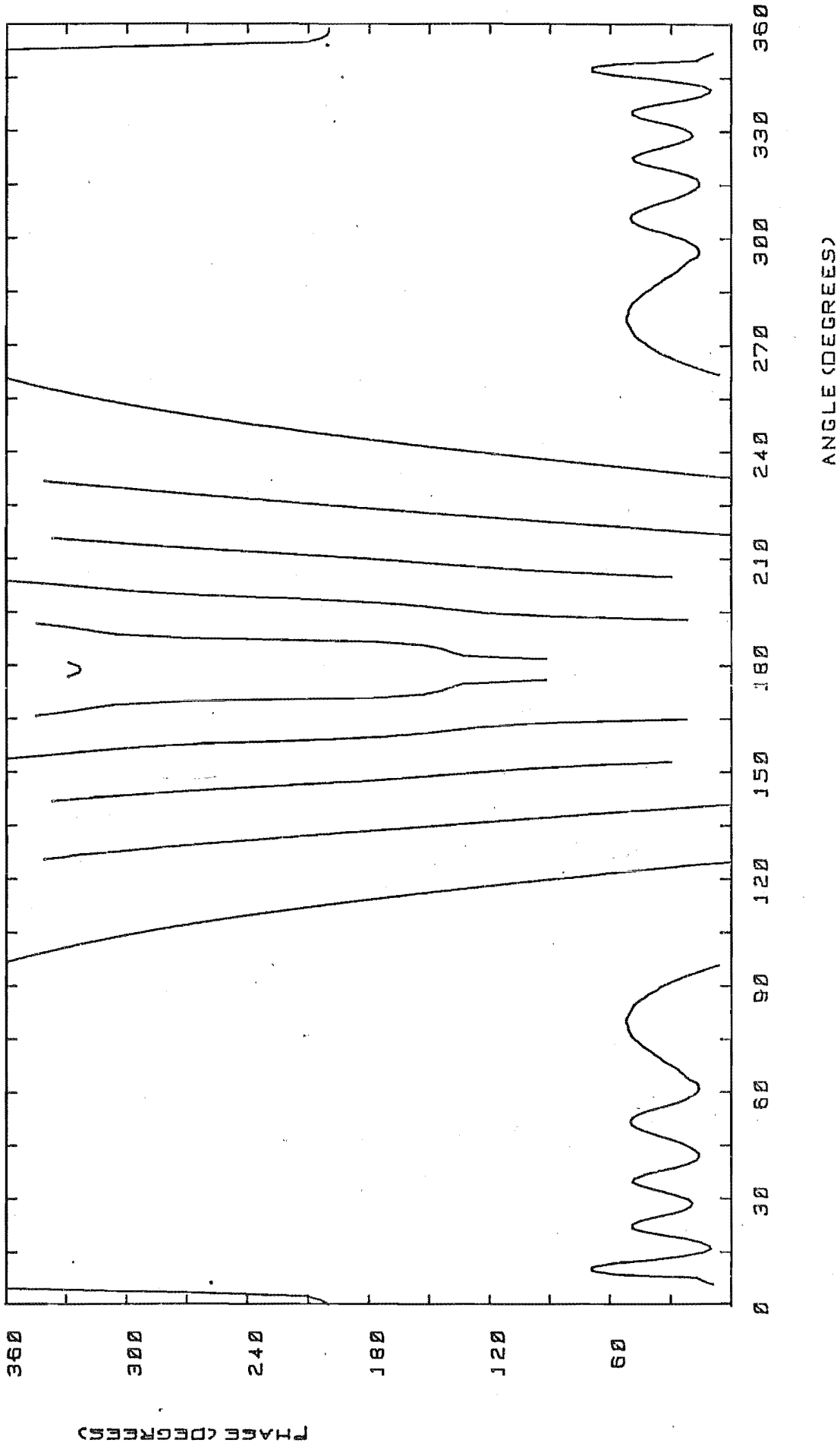

Figure 4.5b) Reflector Field Distribution, Final GTD Description, (Phase).

The results of these modifications are shown in Figure (4.5). A main lobe in the forward direction is now found, but it appears that second order diffraction and 'diffraction-reflection' has little consequence, other than to smooth the pattern about 90° and 270°.

4.1.2 PHYSICAL OPTICS DESCRIPTION

For a large scatterer, as in this case, a good approximation to the surface currents can be made by using Physical Optics, (P.O.). Repeating Equation (2.87) we see that,

$$\underline{J}_{po}^{e} = 2\hat{n} \times \underline{H}_{inc}, \tag{4.16a}$$

on the front surface of the reflector, and,

$$\underline{J}_{po}^{e} = 0, \tag{4.16b}$$

on the rear surface. The geometry is shown in Figure 4.6.

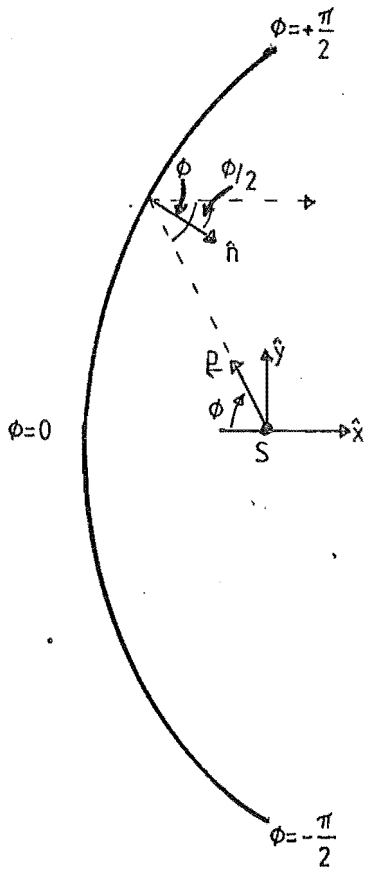

Figure 4.6 Geometry of Parabolic Reflector, Physical Optics Formulation.

If we assume that the reflector is in the far field of the line source, then Equation (4.16a) may be simplified by using the procedure adopted in Section 2.8 to form,

$$\underline{J}^{e}_{po} = -2(\hat{n}.\underline{\rho}).\sqrt{\frac{\varepsilon}{\mu}}.\underline{E}_{inc},$$

i.e.

$$\hat{z}J^{e}_{po} = -2(\hat{n}.\underline{\rho}).\sqrt{\frac{\varepsilon}{\mu}}.E_{inc}\ \hat{z}. \tag{4.17}$$

Appealing to Figure 4.6, Equation (4.17) can be simplified to produce,

$$J^{e}_{po} = -2\sqrt{\frac{\varepsilon}{\mu}}.\ \ \text{Sin}\ (\phi/2).\ \ E_{inc} \tag{4.18}$$

The scattered field from this collection of Physical Optics currents is found by an application of Equation (2.11), thus producing,

$$\underline{E}_{scat} = \frac{1}{4j}\int_{-\pi/2}^{\pi/2} \underline{J}^{e}_{po}\ H_o^{(2)}\ (k|\underline{\rho}_r-\underline{\rho}|)\ d\phi\ , \tag{4.19}$$

and the total field is,

$$\underline{E}_{total} = \frac{1}{4j}\ \hat{z}.\ H_o^{(2)}\ (k|\underline{\rho}_s-\underline{\rho}|)\ +\ \underline{E}_{scat}. \tag{4.20}$$

In Equations (4.19) and (4.20) the Hankel Functions may be replaced by the far field approximation with small loss in accuracy, if the probe point is far off from the source and the reflector.

The P.O. current distribution for this case is depicted in Figure 4.7, and the resultant far field, found from Equation (4.20) is shown in Figure 4.8. Comparing the far fields of the GTD result with the P.O. formulation, the following points may be made.

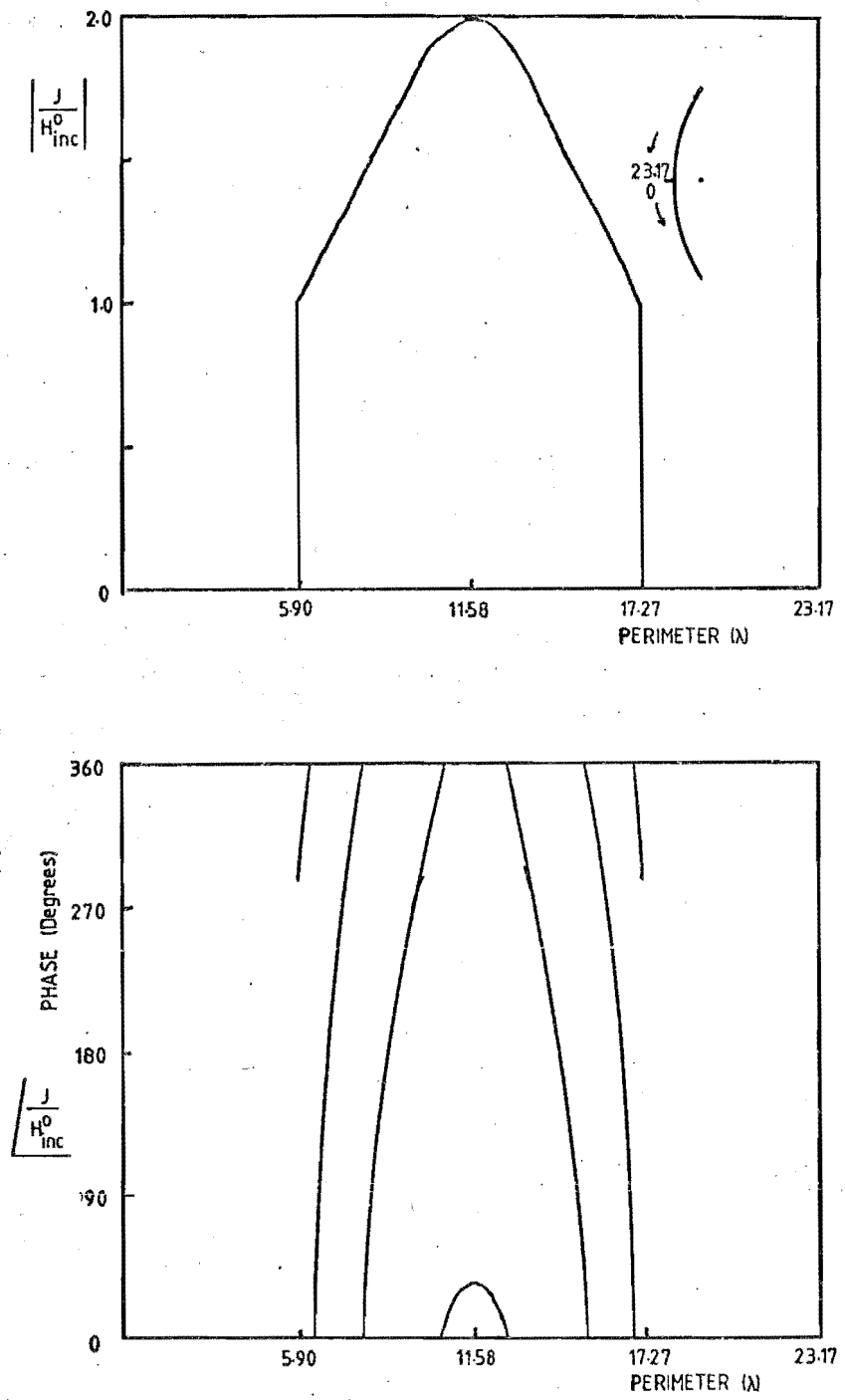

Figure 4.7 Parabolic Reflector, Physical Optics Currents.

1. The P.O. result predicts interference over most of the rear region behind the reflector, and there are a greater number of interference fringes in comparison to GTD.

2. The diffracted field suffers less attenuation than the GTD result, as would be expected from the half plane example of Section 2.8.

3. The spatial frequency of the interferences is the same as that of GTD, implying a ten wavelength wide aperture.

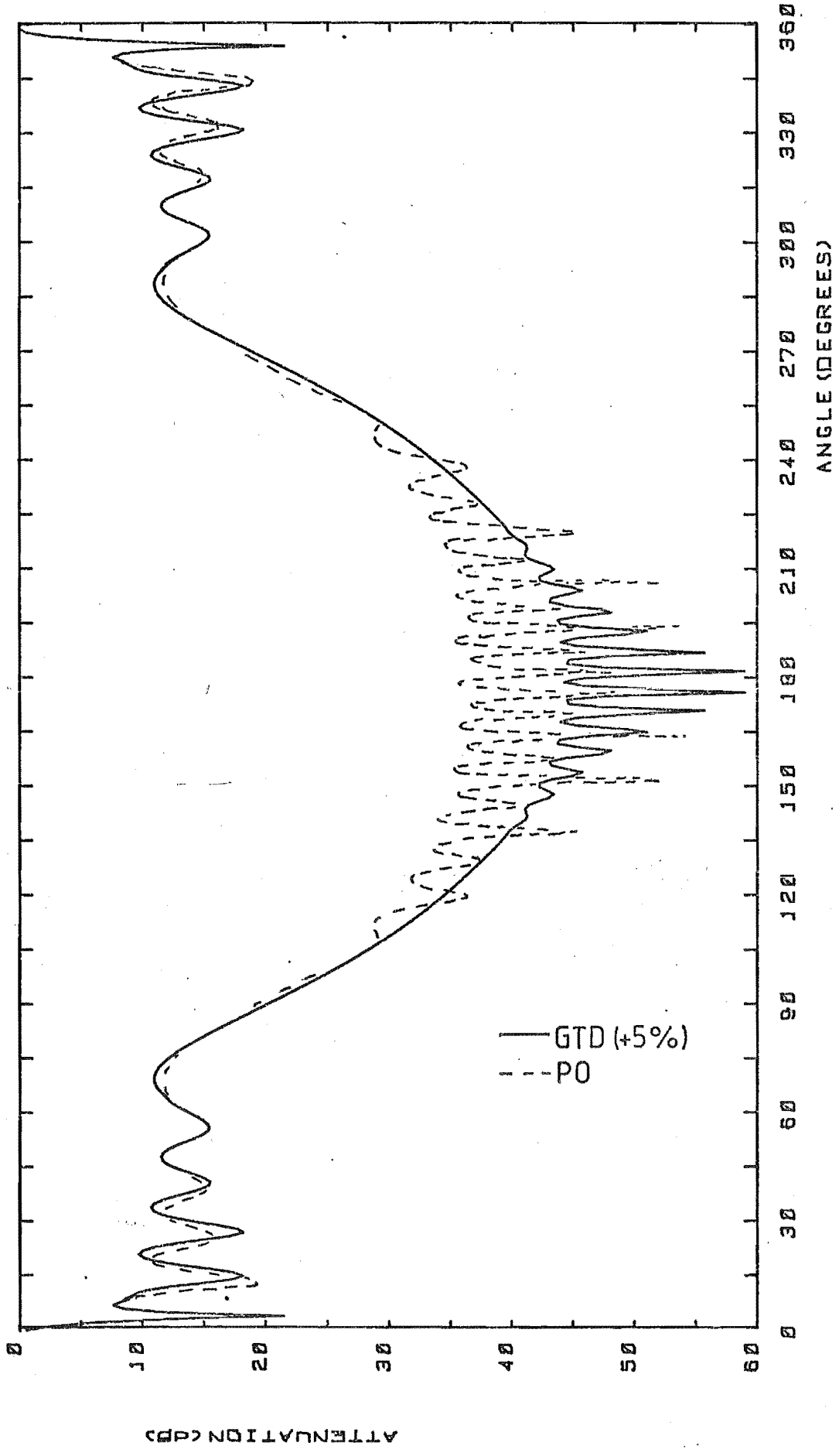

Figure 4.8a) Reflector Field Distribution, Physical Optics, and GTD with a 5% increase in frequency.

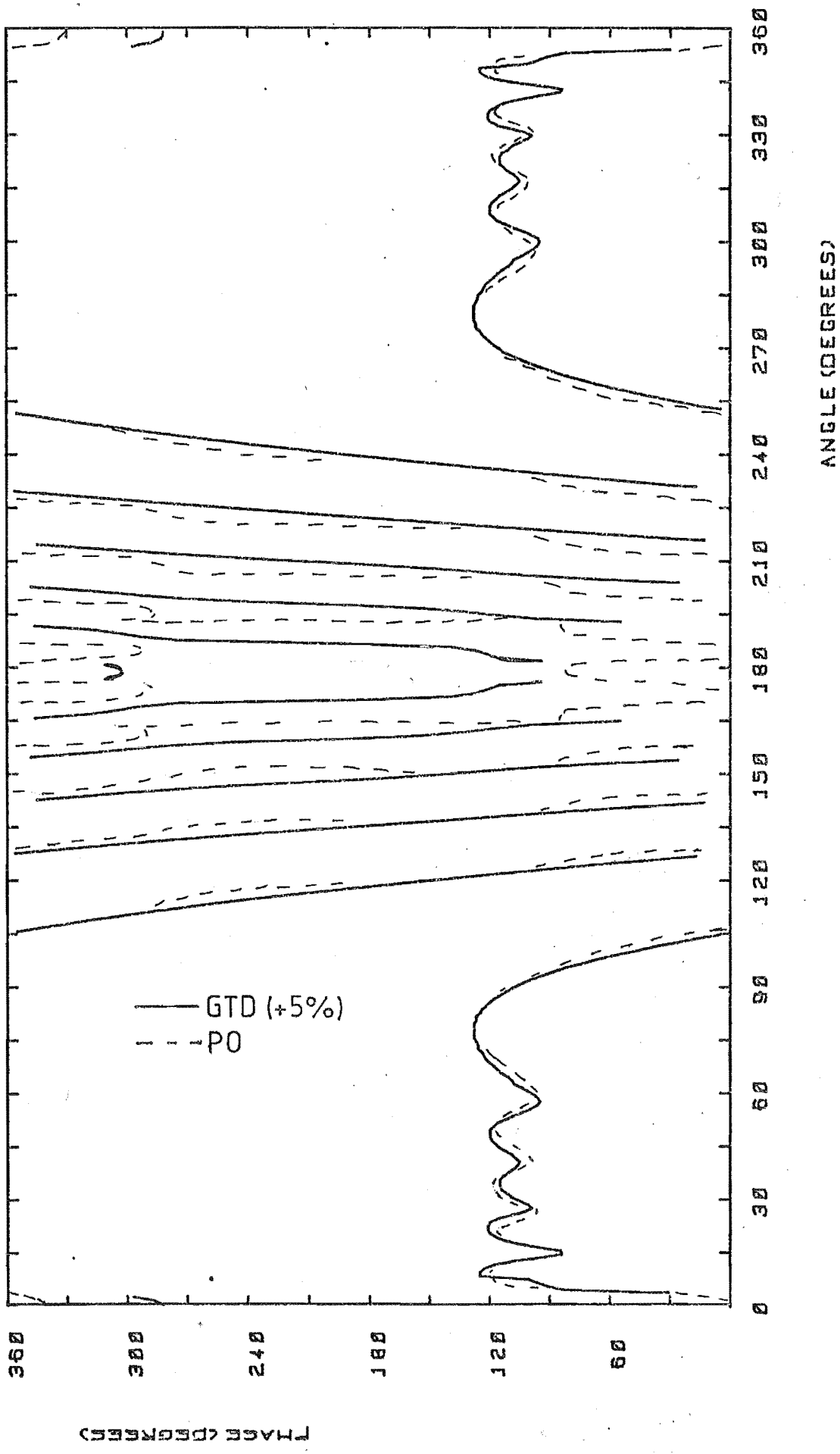

Figure 4.8b) Reflector Field Distribution, Physical Optics and GTD with a 5% increase in frequency.

4. The forward directed side lobes of the P.O. result, other than the three mainlobes in the forward direction, are shifted about 3^{o} from the same lobes in the GTD result. This implies that the temporal frequencies of the methods are at some variance. Kouyoumjian (Kouyoumjian, 1975), has found that the GTD results in comparison to experimental results (Affifi, 1966), show better agreement when the wavelength used in the GTD description is modified by a few percent. The GTD formulation was rerun with a 5% increase in frequency, and is plotted in Figure 4.8. Comparing with the P.O. result, it is clear that a 5% increase in frequency gives a GTD representation which compares well with the P.O. forward field. The P.O. approximation is reasonable when used in the forward direction (Rusch and Ludwig, 1973), hence this suggests that the GTD result requires a slightly larger effective aperture.

Another explanation is the assumption that the reflector edges are on tangent half planes. The GTD* representation, (where the diffracted-reflected rays are of little consequence) could easily be that of a V-shaped reflector. Physical Optics makes no such assumption, actually approximating the boundary conditions on the parabolic reflecting surface, (Beckmann, 1968). This exhibits the limitations of basing theories on Geometrical Optics i.e., assuming global properties on a local scale.

5. The phase of the Physical Optics result is very similar to the GTD result, except near the rear axis. Small lobes appear, and it is hard to resolve exactly what is happening. Large phase changes occur over a very small spatial angle near 165^{o} and 195^{o}. The apparent change in direction of phase variation suggests that there is not a proper cancellation of the scattered field by the source. In such a case the subtraction of the reflector field from the source field may be inaccurate in the same way that the relative error of a result of

* diffracted field

subtraction is much greater than the relative errors of the numbers in the actual calculation.

The main shortcoming of Physical Optics is it's inability to 'see around corners' by not specifying leakage currents around the rear of the reflector. In the forward direction, especially for large apertures the P.O. interpretation gives a reasonable interpretation of the reflector field. In the rear direction, Physical Optics is not constrained by the existence of tangent boundaries, and interference effects are found over most of the back direction. It is known that the back field is not correct, and half plane correction factors can be used as in Section 2.8. This immediately implies a Geometrical Optics interpretation of the rear field, resulting in no interference outside of the spatial range 135^{o} to 225^{o}.

4.1.3 MOMENT METHODS DESCRIPTION

The parabolic reflector was modelled with a thickness of one twentieth of a wavelength, upon which currents were evenly spaced. The total length around the outside of such a reflector is approximately 23.2 wavelengths. Applying the precept that in modelling currents on surfaces they should be about one tenth of a wavelength apart, 220 current filaments were placed on the reflector surface. Their positioning is shown in Figure 4.9a. Point Matching was used to find the induced surface currents, which in association with the source were employed to find the resultant field of the antenna. The current densities are indicated in Figure 4.10 , while the antenna field is shown in Figure 4.11. The gaps between the currents were doubled as in Figure 4.9b, resulting in induced current densities in Figure 4.10 and the far field in Figure 4.11.

A comparison of the far fields in Figure 4.11 shows close similarities in the forward field, but in the rear direction there are

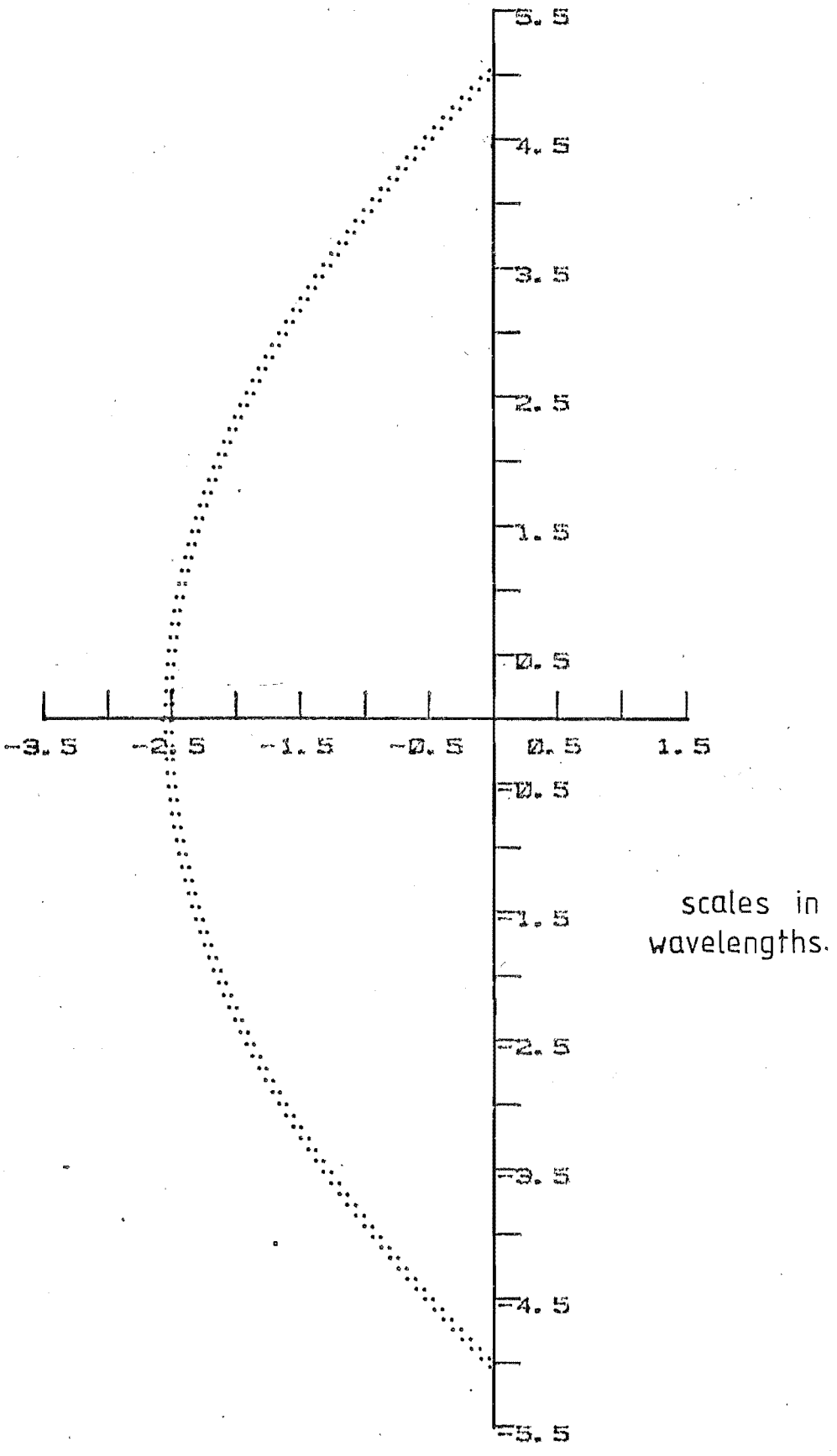

Figure 4.9a) Current Distributions on Reflector, 220pt Case.

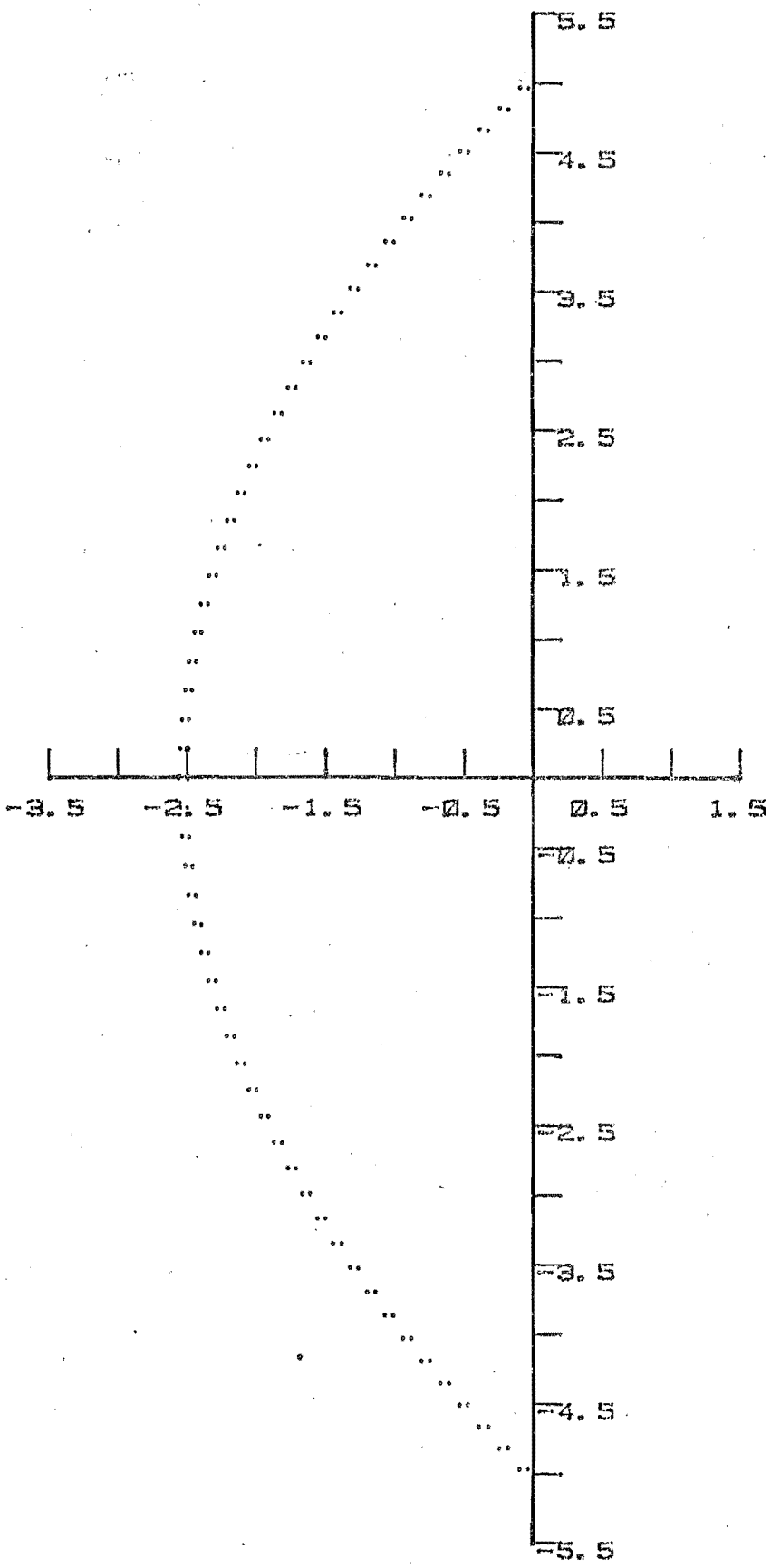

Figure 4.9b Current Distribution on a Parabolic Reflector
110 pt case.

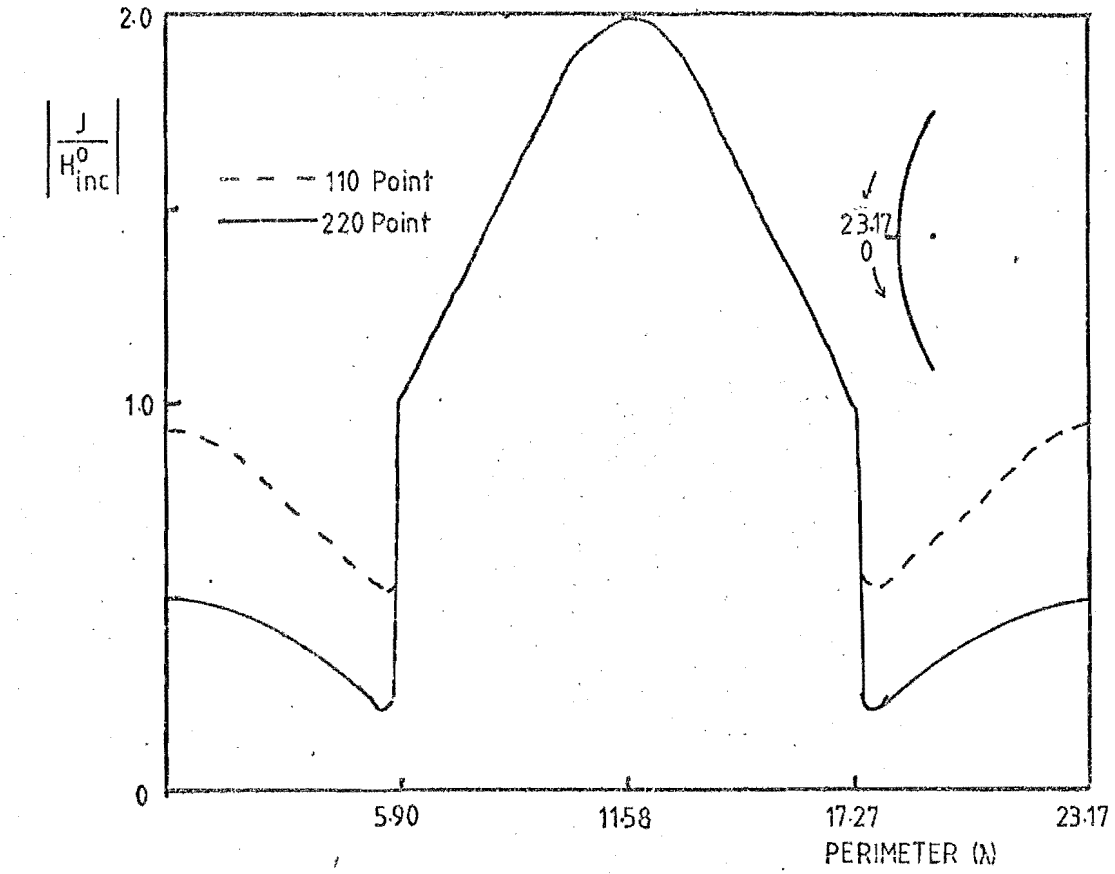

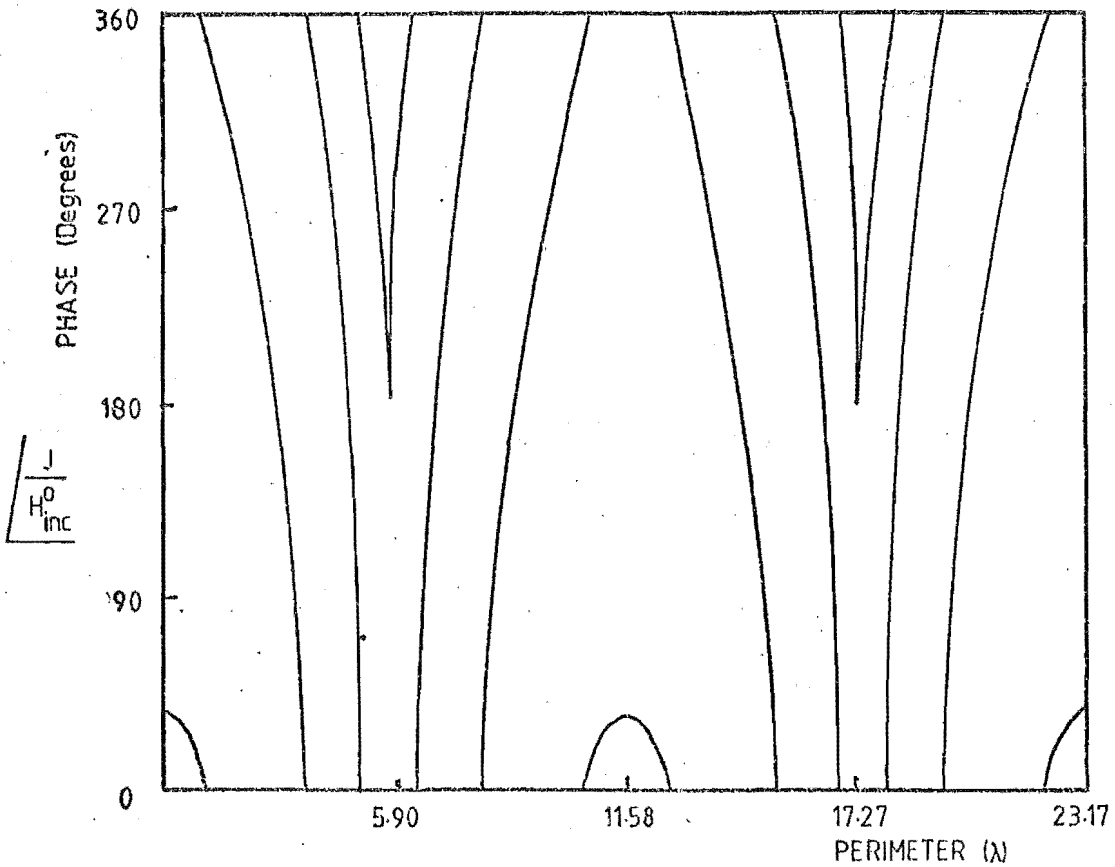

Figure 4.10 Moments current Densities on a Parabolic Reflector.

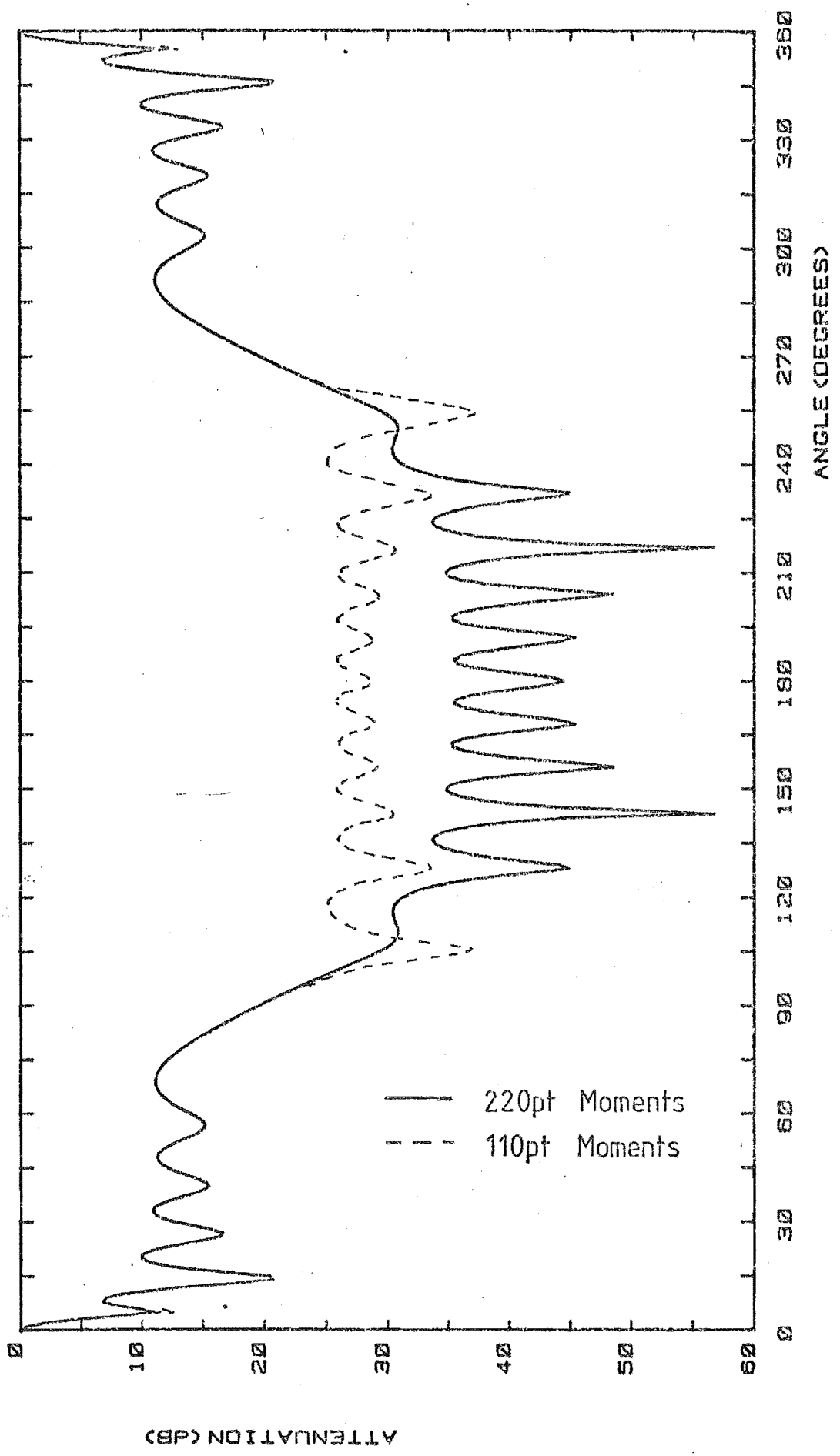

Figure 4.11a) Reflector Field Distribution, Moments Descriptions, (Intensity).

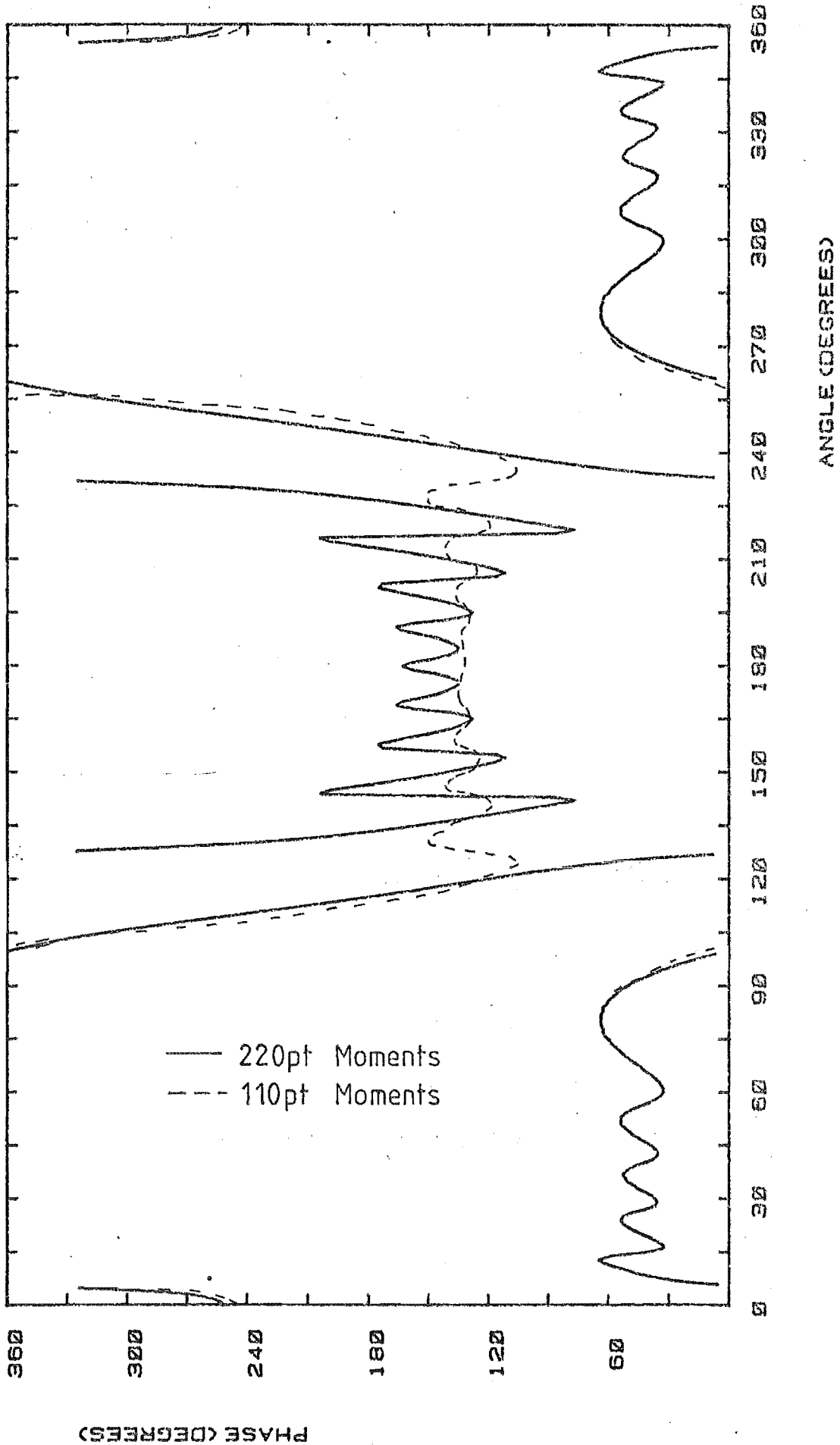

Figure 4.11b) Reflector Field Distribution, Moments Descriptions, (Phase).

differences in the sizes of the peaks and nulls. This variation can be attributed to the different current densities. The densities in the forward direction are very similar, but in the rear direction the current in the 110-point model reaches a greater value than in the 220-point case. The larger rear currents do little to provide a reasonable rear field radiation pattern, especially in the case of the phase. The phase should vary rapidly in this region, being a result of interference by two sources far apart, but due to the currents being so large in the rear of the reflector, the effective aperture of the reflector is reduced, resulting in an apparent slow variation of phase. It is noticeable that the angular distance between lobes of the sinusoidal phase variation corresponds to a 360^{o} phase variation in the case of GTD or PO. The rear field attenuation is about the same as that of Physical Optics, and is not quite enough. The strength of the rear field in this case can be attributed to the anomalous currents on the rear of the reflector as well as inaccuracies in cancellation of the front currents field and the source field. Interference effects occur over roughly the same region in the rear as for the Physical Optics case, but the angular distance between lobes is roughly twice that of both GTD and PO. This is explained by the assumption of a source near the centre of the rearwards looking aperture, giving a lower angular spatial frequency in the rear radiation pattern. The source at the centre of the rearwards aperture is the distribution of currents found by the Method of Moments.

The forward field in the case of Physical Optics, GTD and Method of Moments is virtually the same, showing that in the forward direction the combination of source and front currents swamp any inaccuracy in rear currents.

The shape of the reflector is such that current positions specified on the rear are very close to the currents placed on the front of the reflector. This means that in the generation and the inversion of the scatterer matrix, which is defined in an Appendix, the probability of large errors being found on the reflector rear currents is high due to the large currents being nearby on reflector front. It is clear from Figure 4.10 that the currents in the centre rear are too large and come directly from errors proportional to current amplitude on the front of the reflector. It appears that if the number of currents on the reflector are increased the currents on the rear may produce more reasonable behaviour.

The currents on the front in Figure 4.10 may be compared directly with the Physical Optics currents of Figure 4.7. In the case of this reflector no harm would be done by specifying Physical Optics currents on the front of the reflector away from the edges.

The major limitation of the Moment calculations is the amount of computer time required to find current densities. The rapidly changing radius of curvature at the reflector edges required the employment of point matching. This resulted in the large scatterer matrices and long CPU times. A Gauss-Jordan routine was used to invert the matrices, requiring about 3 hours for a 220 point problem, but only 22 minutes for a 110 point problem. The CPU time limited problem sizes to 220 currents. In the case of a symmetric problem like the unperturbed parabolic reflector, the problem could be split up into two 110 point problems, reducing the solution time substantially. Results were the same as in the 220 point case.

In a non-symmetrical case, the problem cannot be split and under such circumstances the original method will have to be applied.

The long times required on the computer using this method indicated that improved methods were needed. Such an approach is discussed next...

4.1.4 IMPROVED MOMENT METHODS

Obvious improvements present themselves. They are;

a) specify a new current on the reflector, being the sum of the expected Physical Optics current and an unknown difference current (Azarbar and Shafai, 1978), i.e. for Dirichlet Boundary Conditions,

$$\underline{J}_s^e = \underline{J}_{po}^e + \underline{J}_{diff}^e \tag{4.21}$$

where $\underline{J}_{po}^e$ is specified in Equation (4.16) and $\underline{J}_{diff}^e$ is found by Moment Methods;

b) split the problem into various regions and define the currents as,

$$\underline{J}_s^e = \underline{J}_{po}^e, \quad \text{away from surface discontinuities,}$$

$$\underline{J}_s^e = \underline{J}_{mom}^e, \quad \text{about surface discontinuities,} \tag{4.22}$$

where $\underline{J}_{po}^e$ is specified in Equation (4.16) and $\underline{J}_{mom}^e$ is found by Moment Methods using the specified Physical Optics reflector currents as extra sources.

Looking first at suggestion a) we find that in most cases, especially away from the surface discontinuities, the difference currents will be small. If these currents are small, the matrix inversion involved in the Method of Moments will be more accurate, and the rear direction currents will also be more reasonable. The problem still exists in that there is a large matrix to invert, and consequent long CPU times.

In cases where the difference currents can be expected to be negligible, they may be disregarded, resulting in a smaller matrix to invert. This implies suggestion b)

The smaller scatterer matrix would be the same size in both cases if the negligible difference currents are disregarded. In a case where difference currents are large near the edge, as for Dirichlet Boundary Conditions, the inclusion of Physical Optics currents up to the edge would make little difference. For H-plane polarization and Neumann Boundary Conditions, the currents are $\underline{x}$ polarized. Working from the known current distributions about a half plane, c.f. Section 2.9 , the $\underline{x}$ polarized currents do not die out rapidly but have a transient oscillatory behaviour which carries over a number of wavelengths away from the edge. The far field of a scatterer is relatively decoupled from transient current effects, (Harrington, 1968), (Tan, 1968). As long as the first couple of oscillations of $\underline{x}$ polarized currents are retained near the edge, the effects of the smaller decayed oscillations will tend to cancel in the far field, and can be disregarded.

The source vector will be different for each suggestion, and in the case a) considerable care must be taken in the evaluation of the source vector at each element, remembering that there is a logarithmic singularity for a zero argument of a Hankel function.

This difficulty is circumverted if the procedure in suggestion b) is used, where all source currents are removed from the moments currents. Another minor benefit of case b) allows variation in the number and placing of moments currents near the edges without having to recalculate the associated Physical Optics currents.

The problem of the unperturbed parabolic reflector was solved using the method of b). Physical Optics currents were placed on the reflector front to within 1.3 wavelengths, and moments currents from the Physical Optics currents to the edge and 1.6 wavelengths around the rear. No currents were specified on the rear other than about the edges, fulfilling a Physical Optics interpretation. This method allows close spacing of many currents near the edge without problems of matrix size limitations, as 'moments' currents can be restricted to arbitrarily small surface areas.

For the unperturbed parabolic reflector 110 Moment edge current filaments were specified, 55 at each edge, and in the other regions Physical Optics currents were placed in the same positions as the Moments currents of Section 4.1.3. The currents and the far field for this method are given in Figure 4.12 and 4.13 respectively.

Looking at the far field intensity pattern in Figure 4.13 it is clear that the forward field is very similar to the P.O., GTD and the Moment Method results. The rear field exhibits greater attenuation than the P.O. and Moment Method results, but not as much as GTD. Two bumps appear in the rear field pattern near 180°. It should be noted that they are about 6° away from the rear axis, in the position where a lobe might be expected, if a ten wavelength wide aperture is used. The major lobes in the rear direction are spaced approximately 12° apart, about double the spatial distance of the GTD and PO results. The Moment Method lobes do not match, and in fact the Moment Method result shows a minimum at the rear axis, where a maximum might be expected.

Interference fringes in Figure 4.13 extend from about 120° to 240°, a wider range than GTD but not as wide as that of Physical Optics. The interference lobes are further apart near the edge of the pattern. This implies that at an angle far off the rear axis, in the far field, both

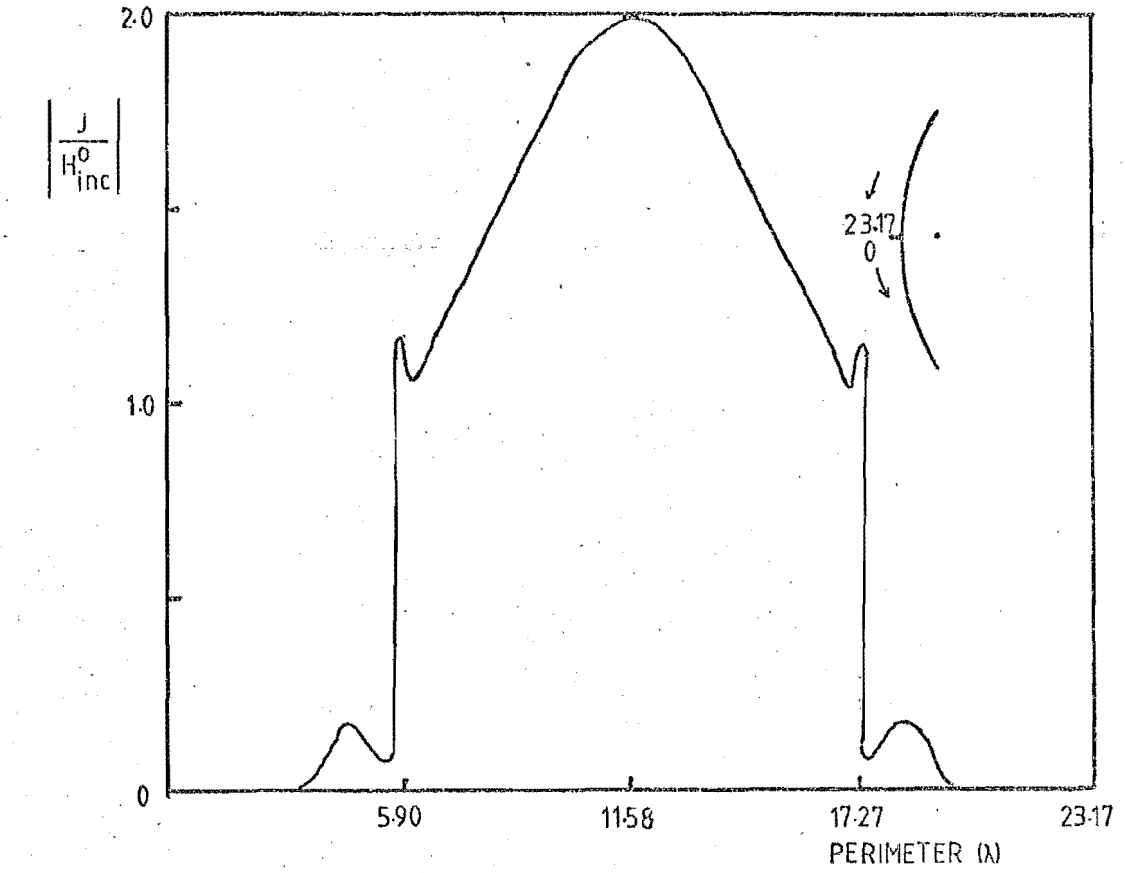

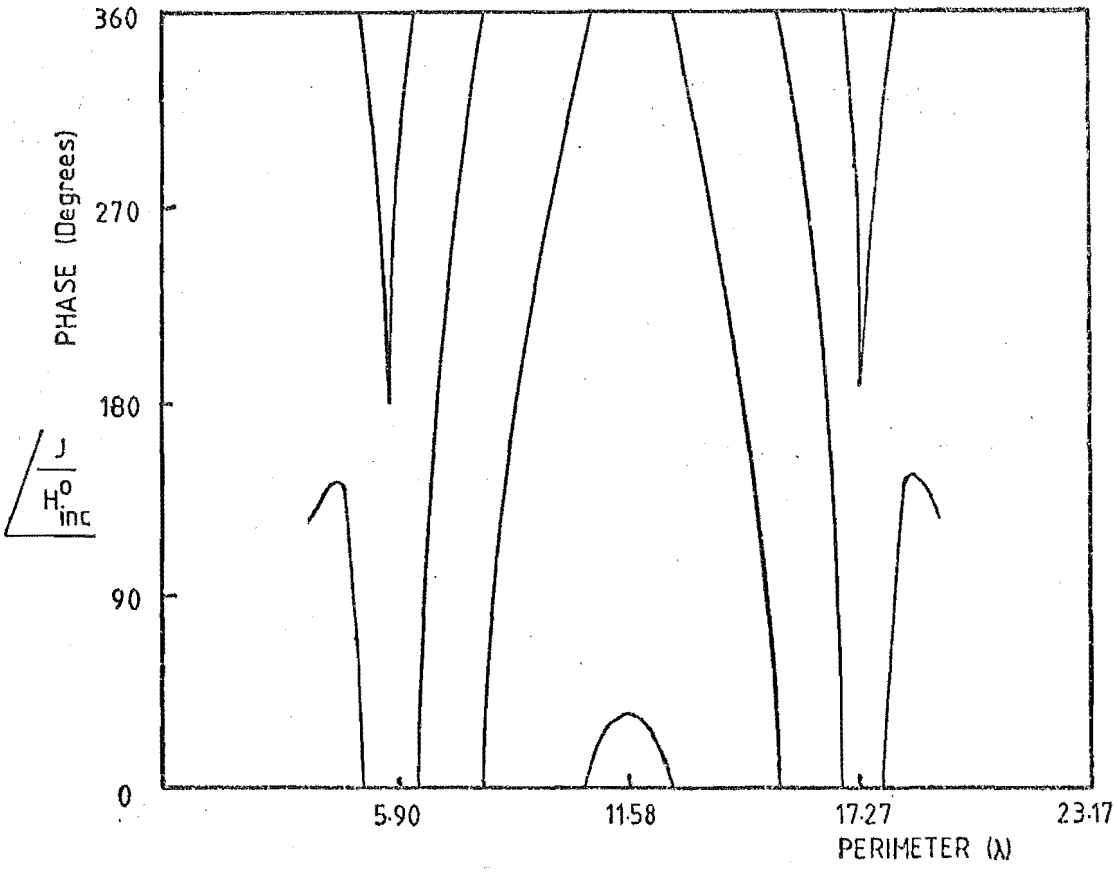

Figure 4.12 Current Densities on Parabolic Reflector, Physical Optics cum Moments Case.

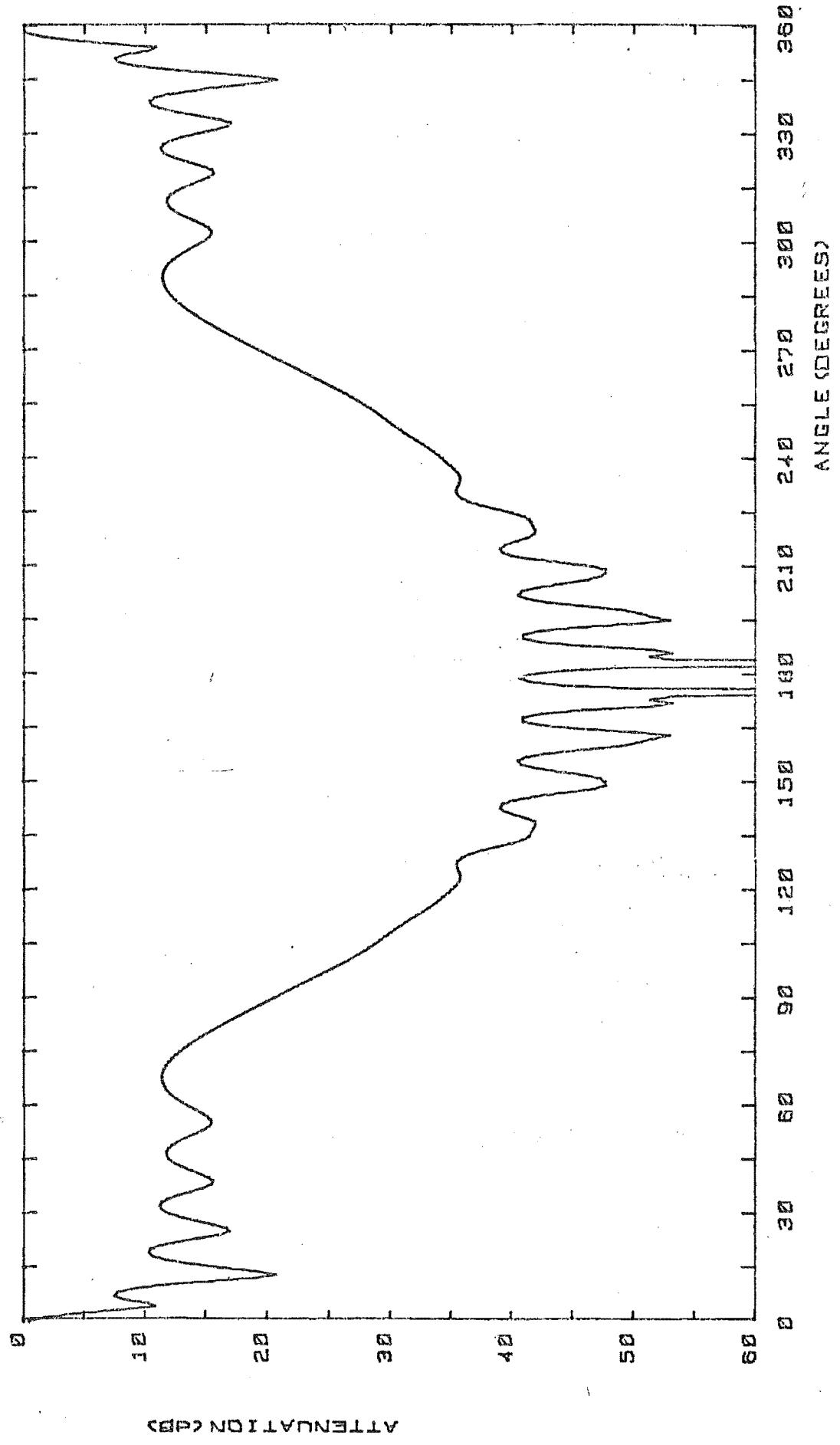

Figure 4.13a) Reflector Field Distribution, Physical Optics cum Moments Description (Intensity).

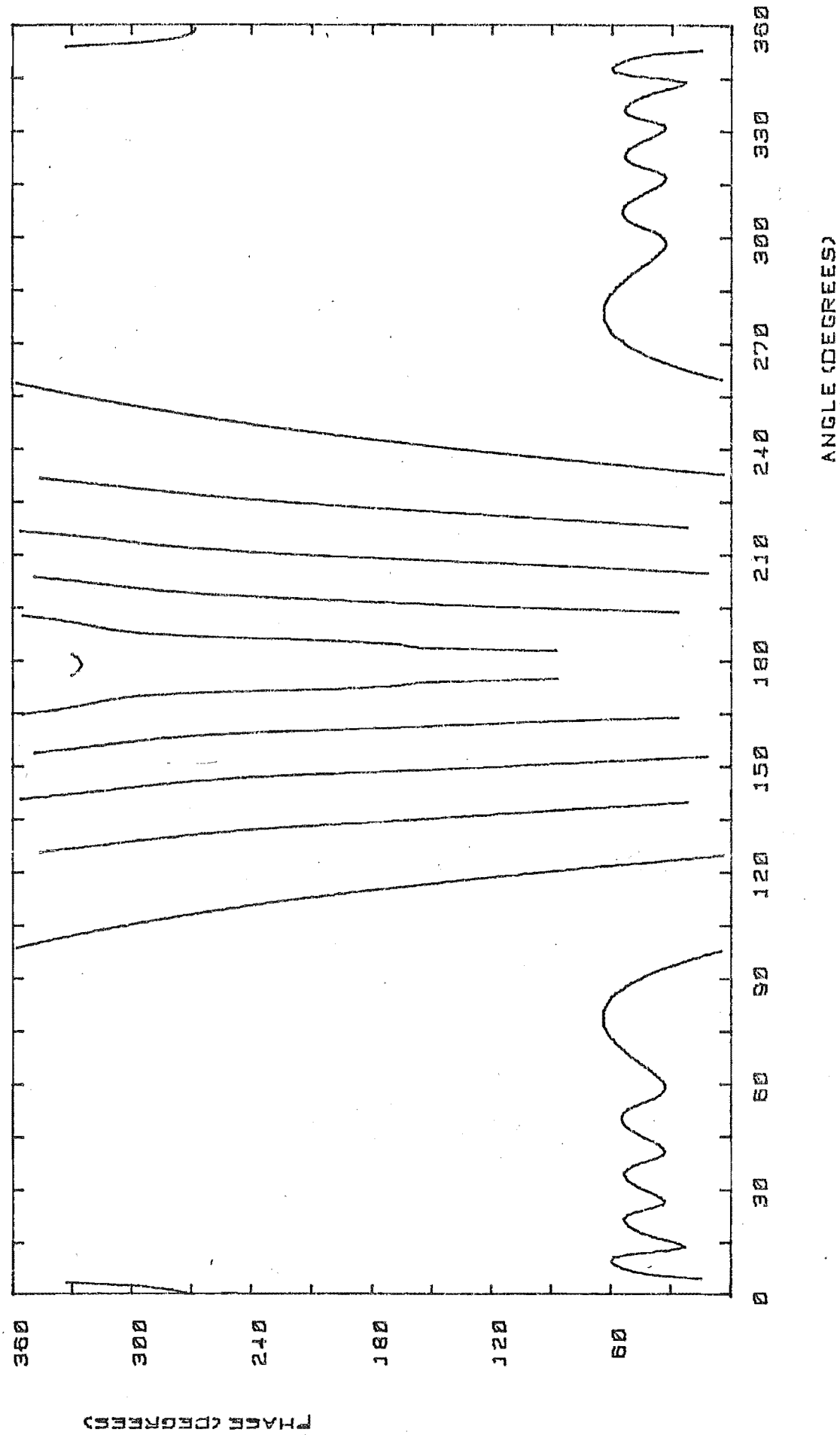

Figure 4.13b) Reflector Field Discription, Physical Optics cum Moments Description (Phase).

edges have an effect but with a reduced aperture from that aspect. The Physical Optics cum Moment Method (PO-MOM) phase pattern is very similar to that of the GTD result. The GTD phase variation can be attributed to the variation of the probe position with respect to the edge sources. In the regions 90^{o} to 135^{o} and 235^{o} to 270^{o} only one GTD edge source illuminates the probe. The PO-MOM modified theory has a similar phase variation as GTD. This suggests that the large currents generated at the edges have the greatest effect upon the phase pattern.

4.1.5 EXPERIMENTAL RESULTS

The unperturbed parabolic reflector was tested in the range described in Section 5.5. The experimental results are given, depicted in Figure 4.14. Measurements were made at every 2^{o}, hence results are not smooth. The results show some symmetry, but with measurements of over 40dB attenuation some variability is apparent.

Lobes appear in the attenuation pattern over nearly all of the rear direction. This suggests extraneous interference other than from the source or the edges. Between 140^{o} and 220^{o} in the rear direction, lobe and null positions match in the Experimental and PO-MOM results. In the forward direction, nulls and lobes match reasonably well, but it appears that the experimental forward lobes are about 3dB lower than the PO-MOM results predict. Experimental investigation of the dipole field produced the explanation for this attenuation of the sidelobes, see Figure 4.14. The dipole field intensity may be approximated by the dashed curve on Figure 4.15a. The region 90^{o} to 270^{o} would correspond to the position of the parabolic reflector if it was present. The dipole field pointing towards the reflector is generally higher than that towards the reflector edges. This taper, purely accidental in nature, will serve to improve the forward looking characteristics of the

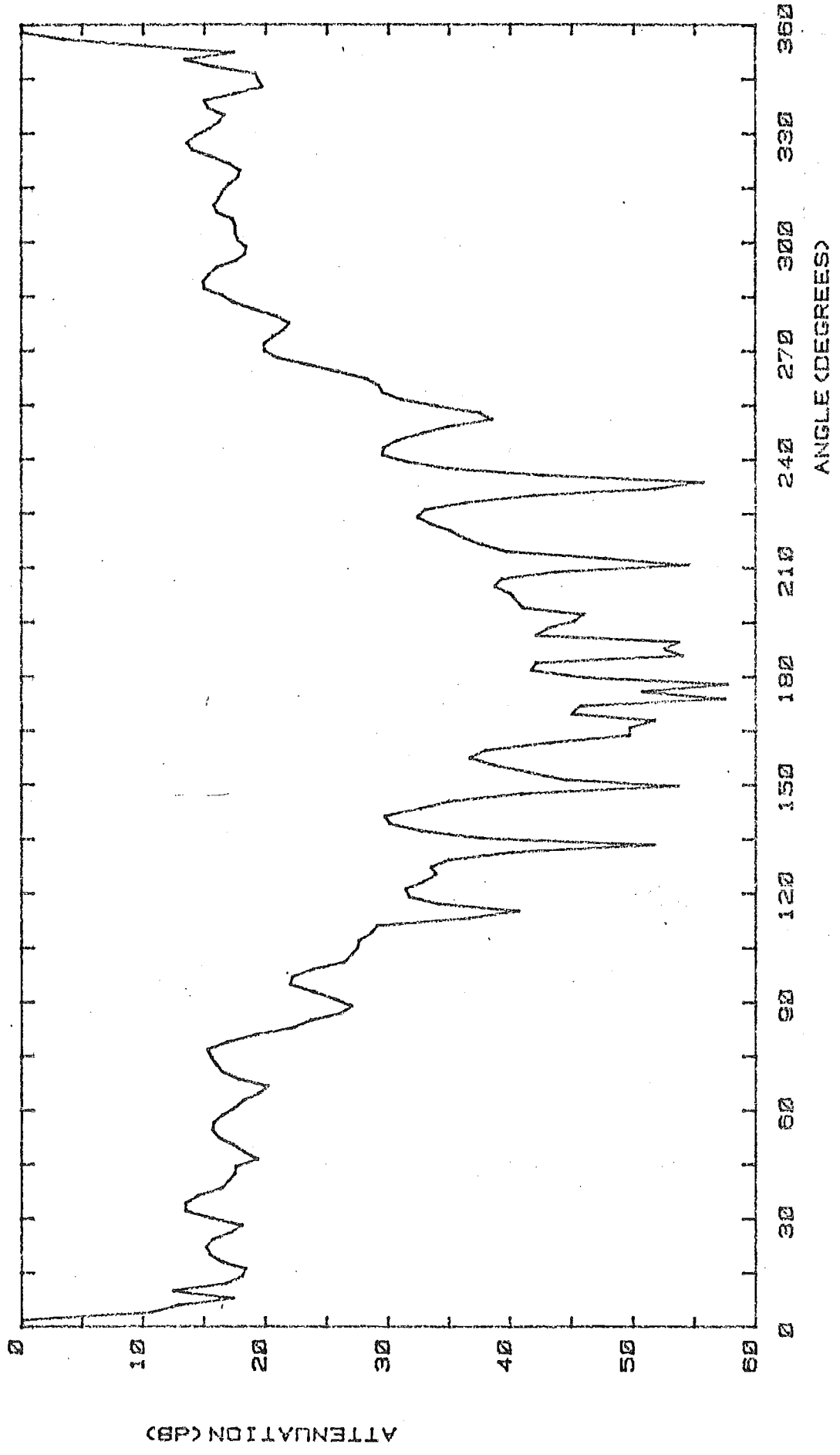

Figure 4.14a) Reflector Field Distribution, Experimental Results, (Intensity).

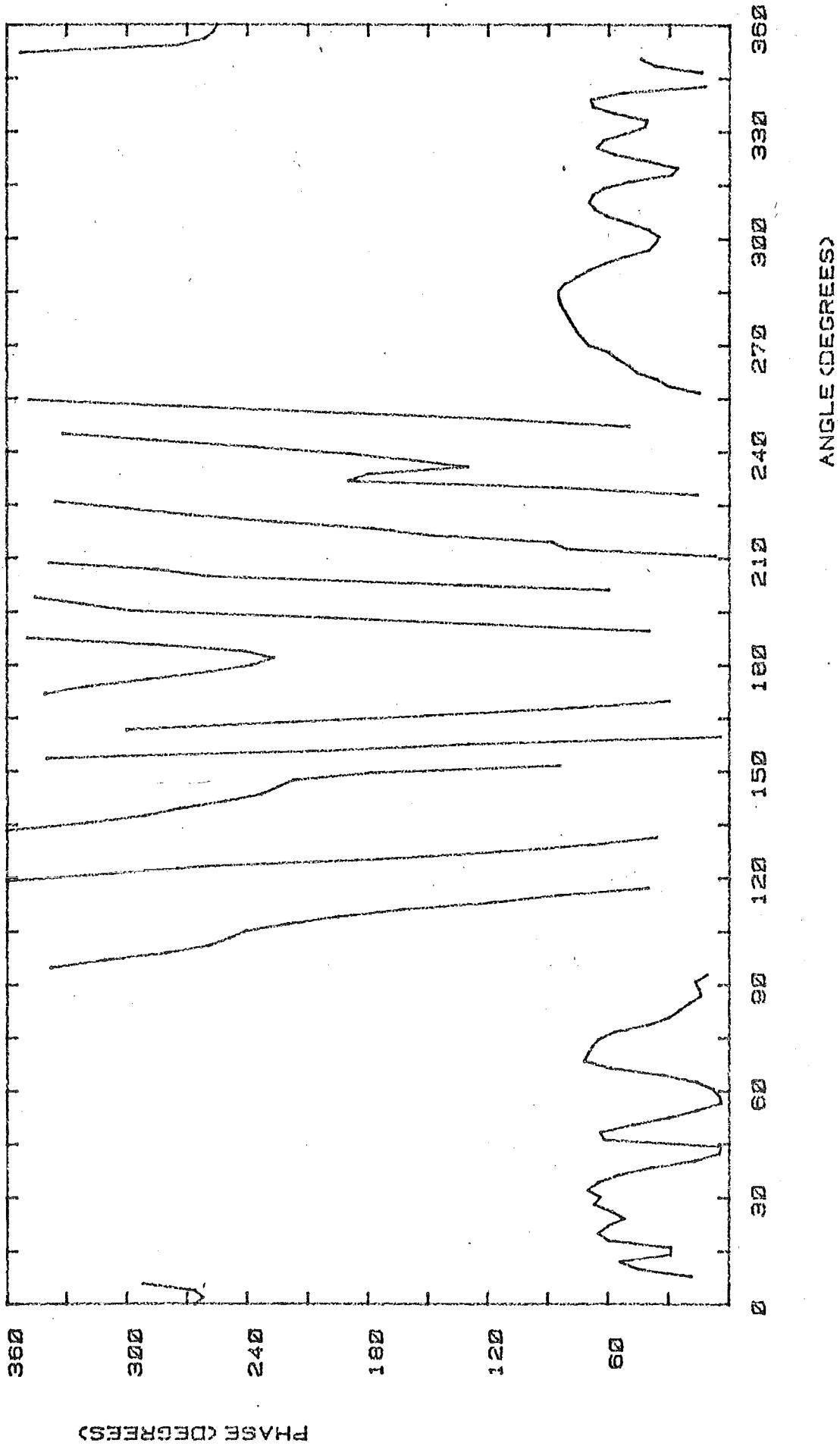

Figure 4.14b) Reflector Field Distribution, Experimental Results, (Phase).

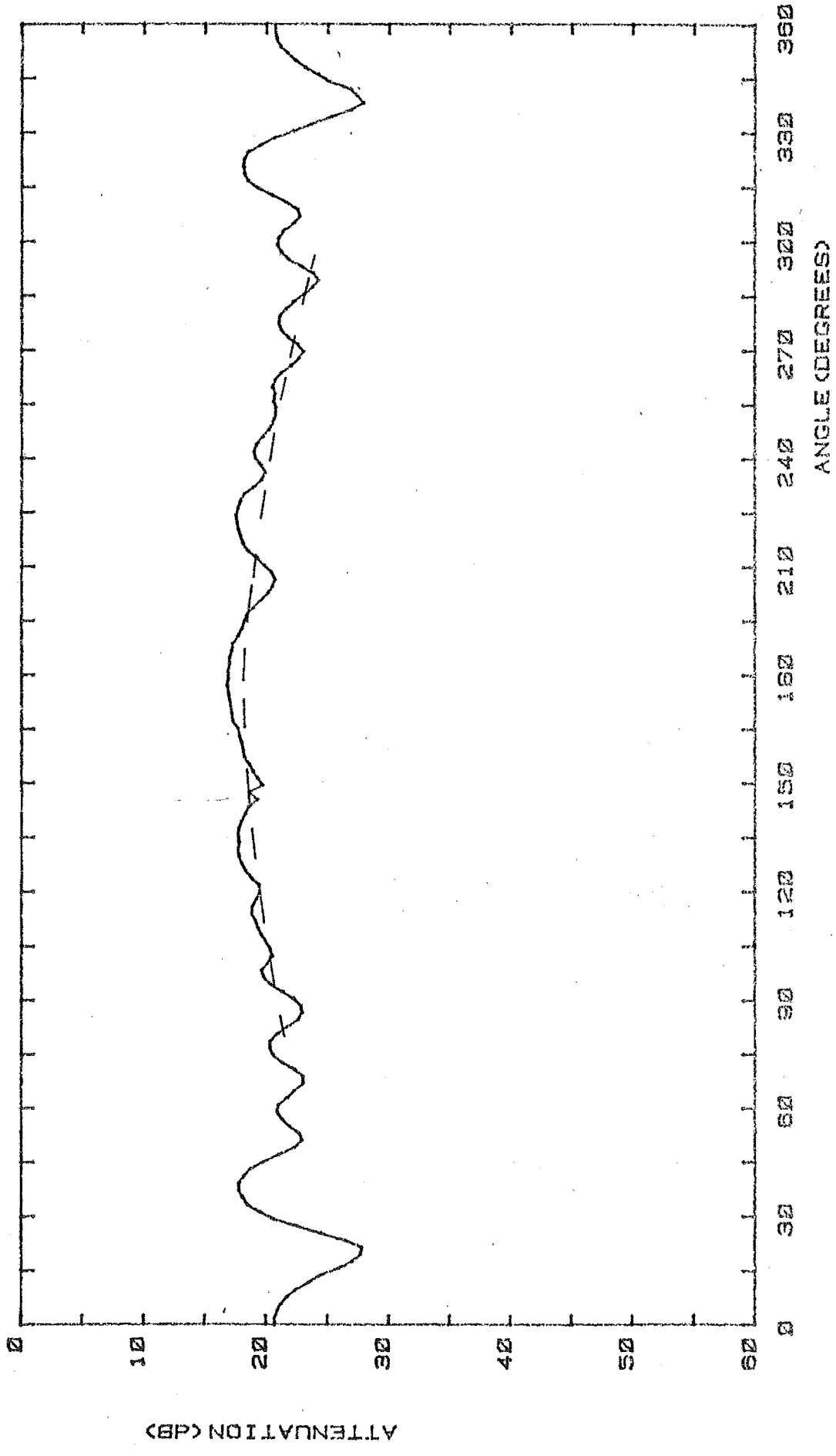

Figure 4.15a) Dipole Field, (Intensity).

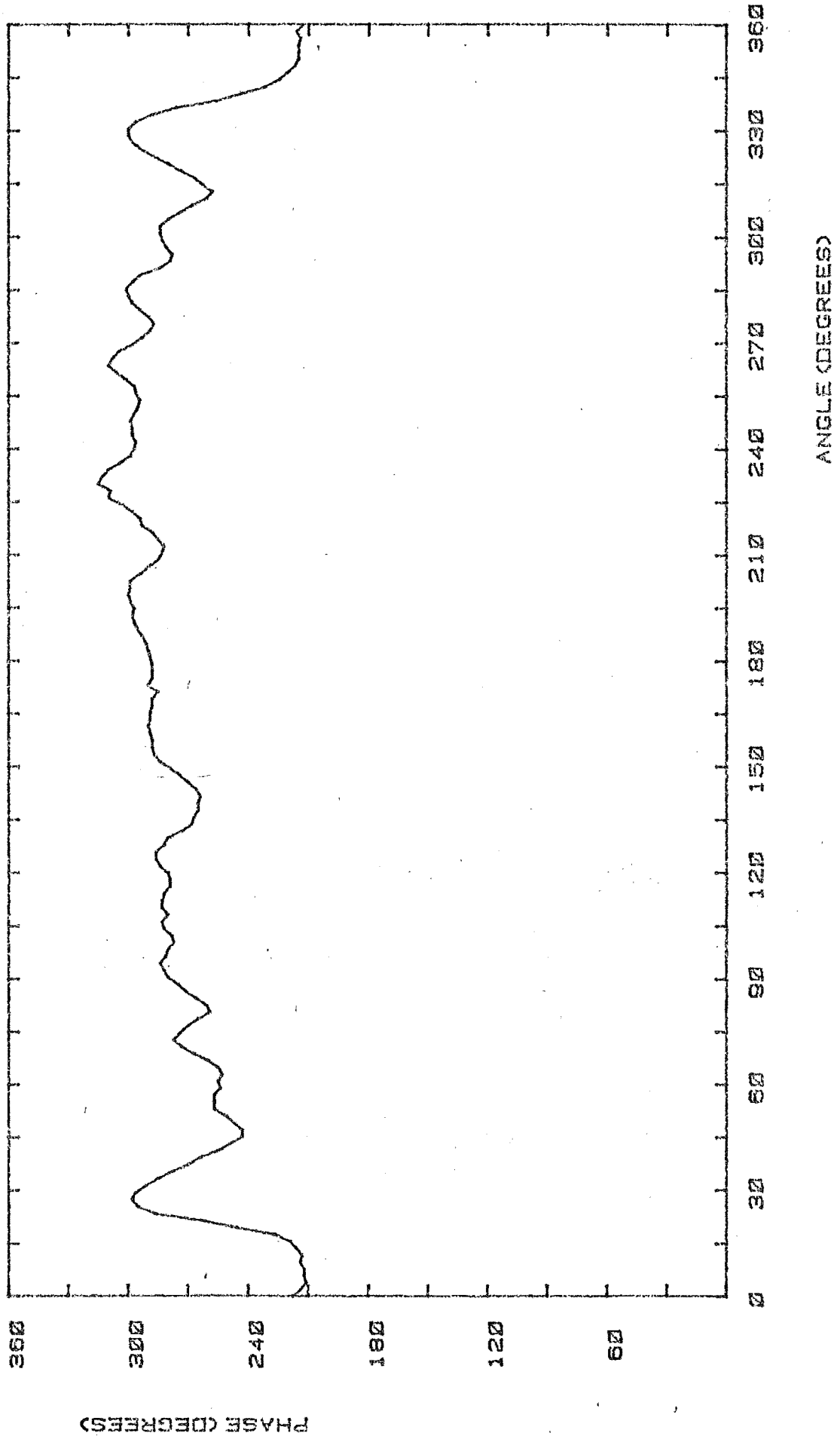

Figure 4.15b) Dipole Field, (Phase).

reflector by lowering the sidelobes which occur from diffraction off the directly radiated truncated edges.

Major discrepancies between PO-MOM theory and Experimental results occur in the regions 90° to 140° and 220° to 270°.

Interferences occur in the Experimental results where only one edge source should be 'visible'. This extra interference can be explained by the effects of the dipole support and feed structures. The perspex support and the coaxial connector (Figure 5.12), affect the dipole forward field (Figure 4.15). Equivalent secondary sources of some consequence on the support system may be set up especially when the support is irradiated by the reflector field. These secondary sources would then be in a position to interfere with the field from the reflector edge sources, especially in the above regions.

The Method of Moments can account for the support, (Andreasen,1965), (Rusch,1975), (Richmond,1965a), where currents are placed in the dielectric and on the coaxial feed, see Figure 4.16. A numerical experiment was run where eight surface sources were placed on the coaxial connector and sixteen dielectric volume sources modelled the perspex support, in concert with the PO-MOM formulation. These results are shown in Figure 4.17. The results are not conclusive, but do show interference effects in the regions where interference was not before. These results may be 'tuned' by the inclusion of more currents about the support and gauging the effects of such currents on the Physical Optics currents on the front of the reflector (Rusch, 1975).

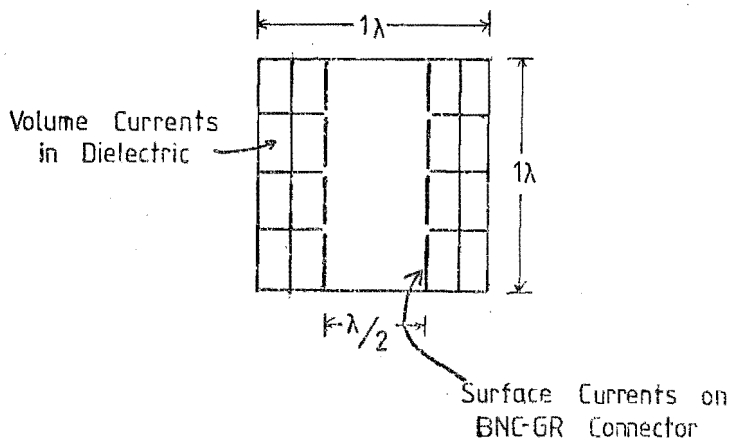

Figure 4.16 Placement of Currents About Reflector Support.

The measured phase shows a basic similarity to the PO-MOM and GTD phase results, but there are differences, especially in the region about 230°. The radiation pattern shows no apparent reason for such a change. The measured results show an overall extra phase change of about 90°. This corresponds to a path length change of about 7mm. It is possible that the range may have had a 7mm discrepancy between extremes of positions as the antenna positioning was very hard to control. Another contribution to the phase change may have been the flexing and unflexing of the coaxial connecting cable.

4.1.6 DISCUSSION

From the comparison with experimental results, in the case of an unperturbed reflector, it appears that the hybrid PO-MOM theory developed in Section 4.1.4 describes the reflector field most accurately.

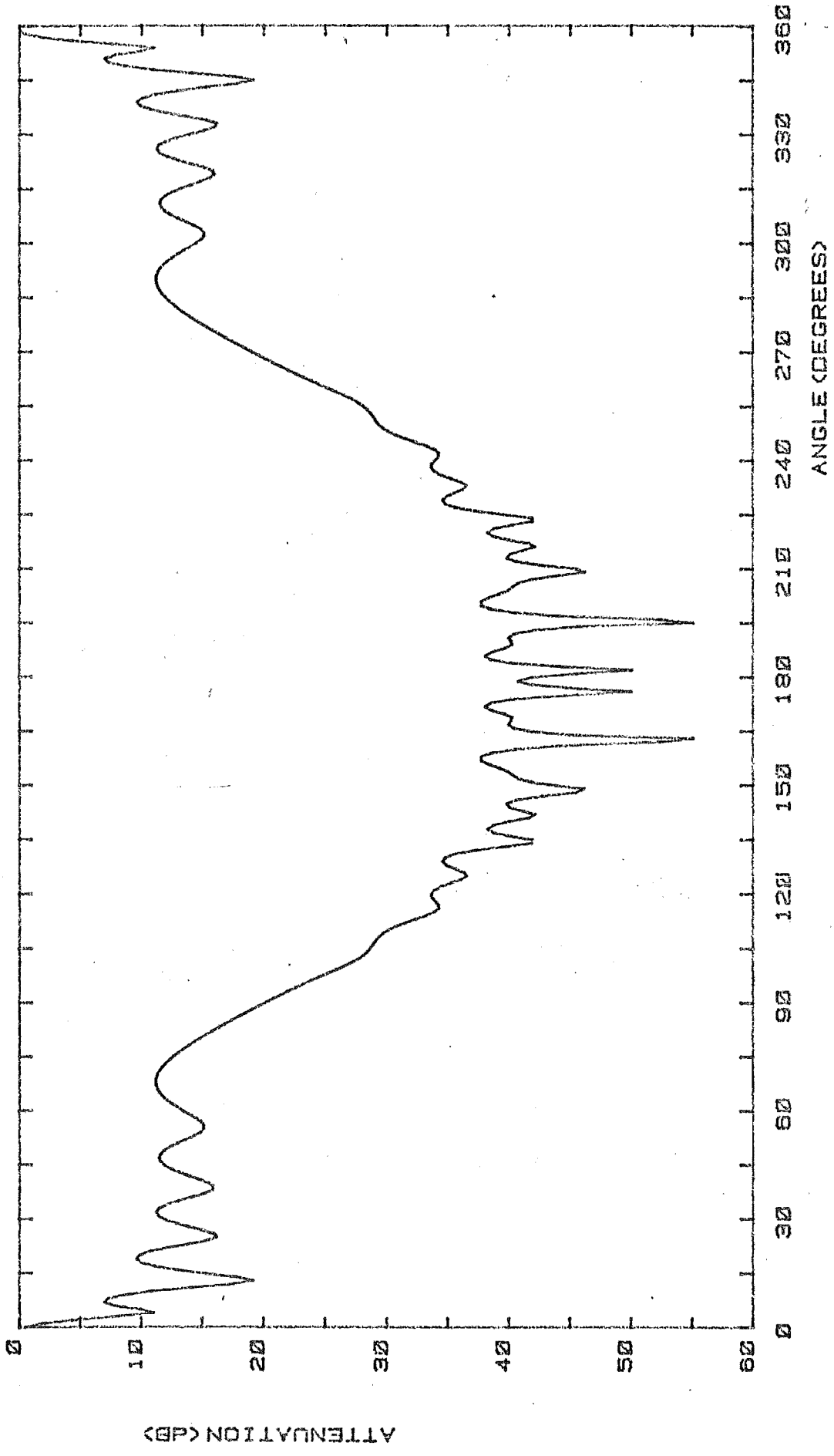

Figure 4.17a) Reflector Field Distribution Taking Support into Account (Intensity).

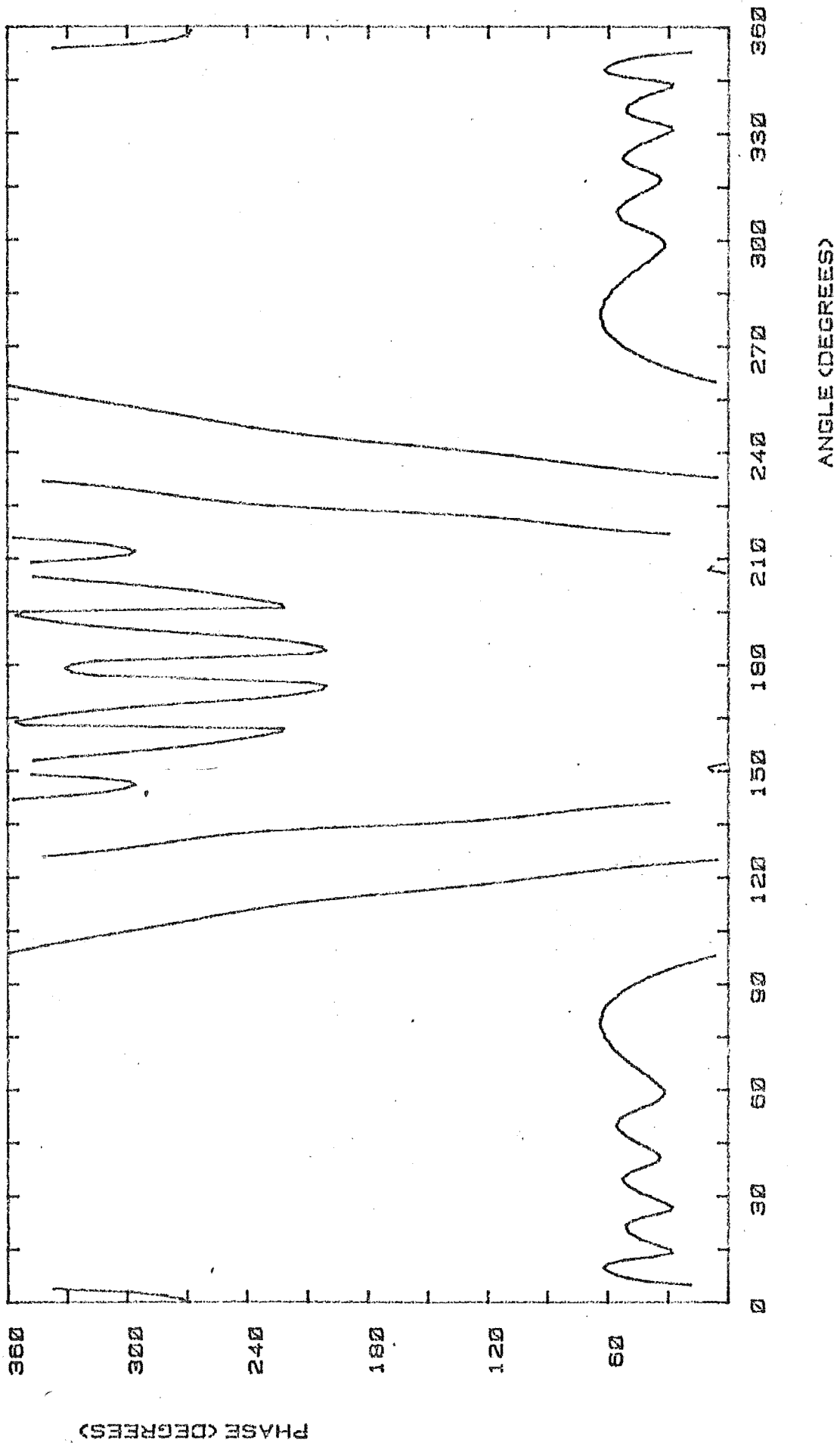

Figure 4.17b) Reflector Field Distribution Taking Support into Account (Phase).

The GTD method is unable to account for wide angle rear-field interferences, especially in the regions 120^{o} to 135^{o} and 225^{o} to 240^{o}, which are covered by PO-MOM theory.

If surface waves from the edges are considered, there are transition regions about the tangent half planes where such diffraction may not be insignificant. For a source on the surface, as in this case, Kouyoumjian (1975) has stated that the angular width of the transition region is,

$$2\phi = (k\rho_g)^{-\frac{1}{3}} \tag{4.23}$$

where k is the wave number $= 2\pi/\lambda$

ρ_g is the radius of curvature of the reflector where the source is situated.

In the case of the parabolic reflector, $2\phi = 0.22$ radians, hence the inclusion of such transition regions would improve the width of the rear interference region to 129^{o} to 231^{o}. The major problem associated with surface wave diffraction is that the surface field is diminished under Dirichlet Boundary Conditions, and the derivative of the diffraction coefficient has to be used. Only in the case of Neumann Boundary Conditions should surface diffraction become significant. (Rusch, 1975).

4.2 PARABOLIC REFLECTORS WITH SLITS

4.2.1 INTRODUCTION

In this section we will study the effects of slits in rear radiation patterns of reflectors. A slit is placed in the reflector as shown in Figure 4.18. The aim of the slit is that its leakage cancels the edge diffracted field in a pre-determined direction.

For an unperturbed parabolic cylinder reflector, as studied in Section 4.1, it was found that the rear field was attenuated in the region of 40dB to the maximum forward signal. This corresponds to about a 20dB attenuation when the field strength is compared with the dipole signal.

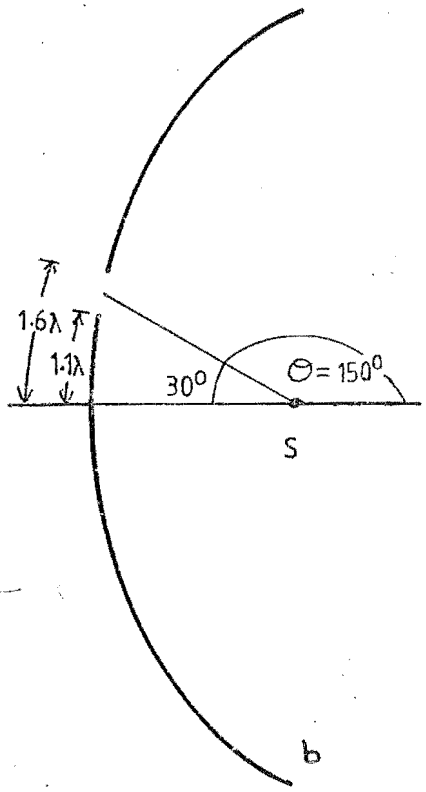

Figure 4.18 Parabolic Reflector, λ/2 slit at 30°.

Referring to our results in Chapter 3, for slit diffraction, we would expect that a slit width of one third of a wavelength would provide enough leakage when its signal is in antiphase to the edge diffracted signal. A major problem associated with a narrow slit is that its transmitted field has a wide major lobe, making it impossible to steer a narrow beam through the reflector in a specific direction.

To test the theories, as well as verifying experimental results, we will study the radiation and phase patterns of a reflector with a

reasonably large slit placed near the rear axis of the reflector. The slit is one half a wavelength in width, placed at 30° away from the rear axis.

4.2.2 EXPERIMENTAL RESULT FOR REFLECTOR WITH SLIT

The half wavelength slit will leak too much energy in the rear direction, and will tend to dominate the resultant field patterns. The geometry of the slit is shown in Figure 4.18, and the resultant measured attenuation and phase are shown in Figure 4.19. The attenuation results show a local maximum about 150°, where the direct field would traverse through the slit. There is also a deep null in the region of 240°, and the forward field is also affected by the reflector modification, appearing to make the forward pattern lopsided. The measured phase has a stationary point at 150°, corresponding to the overpowering effect of the direct field of the dipole, and another stationary point at 230°, near where the deep null occurs. This suggests that the edge diffracted field at edge b, shown on Figure 4.18 must be close to cancelling the slit field and the diffracted field from the opposite edge, as shown by the null at 240°. The problems of phase measurement are covered in Chapter 5, and it must be noted that there might be ambiguity in the phase results where rapid phase changes occur near a null.

The support once again causes problems producing extra interference peaks and nulls in the region of 90° and 270°.

4.2.3 GTD RESULT FOR REFLECTOR WITH SLIT

Equation (4.15), describing the field from an unperturbed reflector was combined with Equation *, describing the field from an inclined plane slit. The plane inclinations were obtained from a study of the tangential planes of the reflector at the slit edges. The resultant

*(3.48)

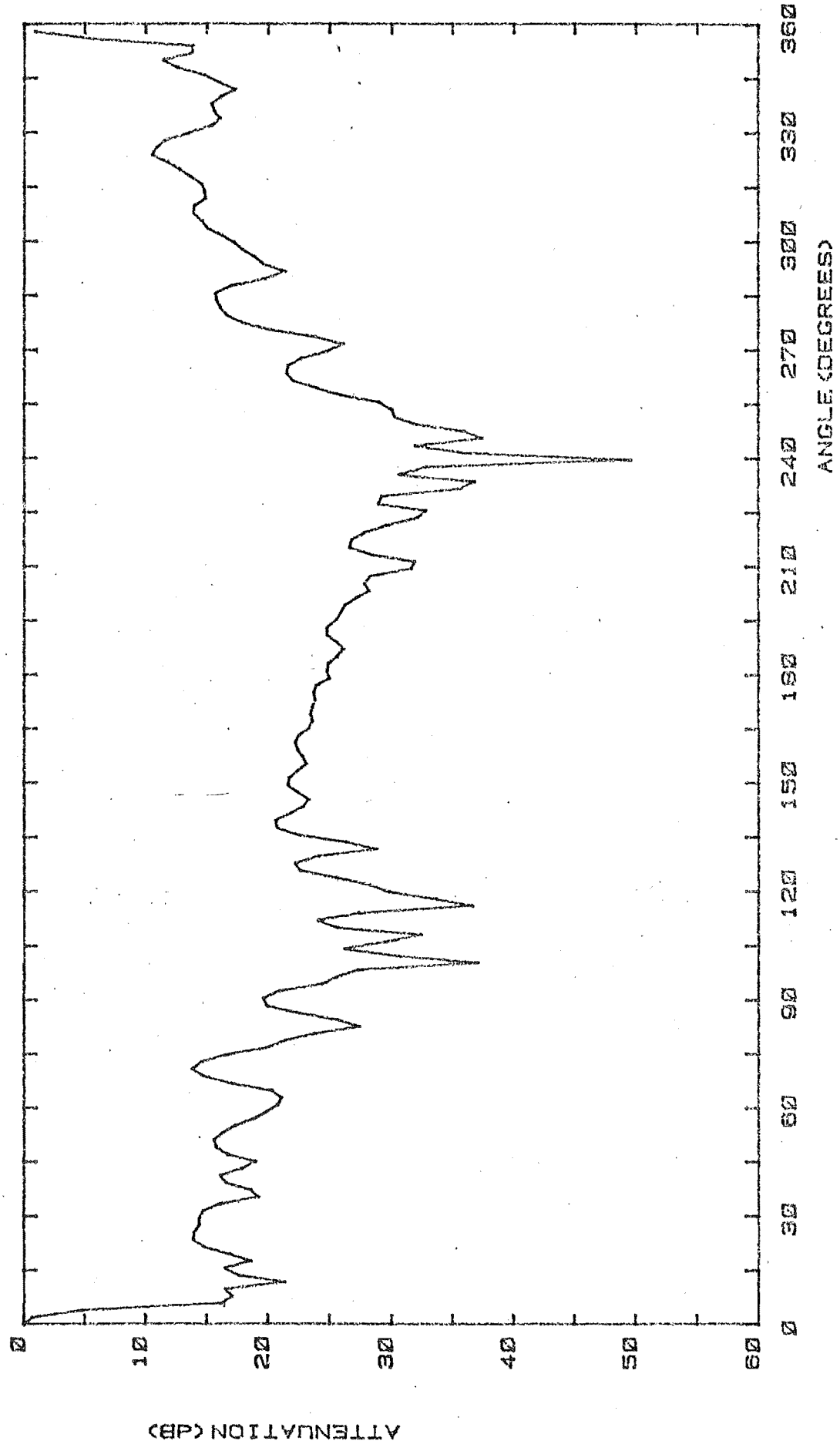

Figure 4.19a) Reflector Field Distribution, $\lambda/2$ Slit at 30^{o}

Experiment Result, (Intensity).

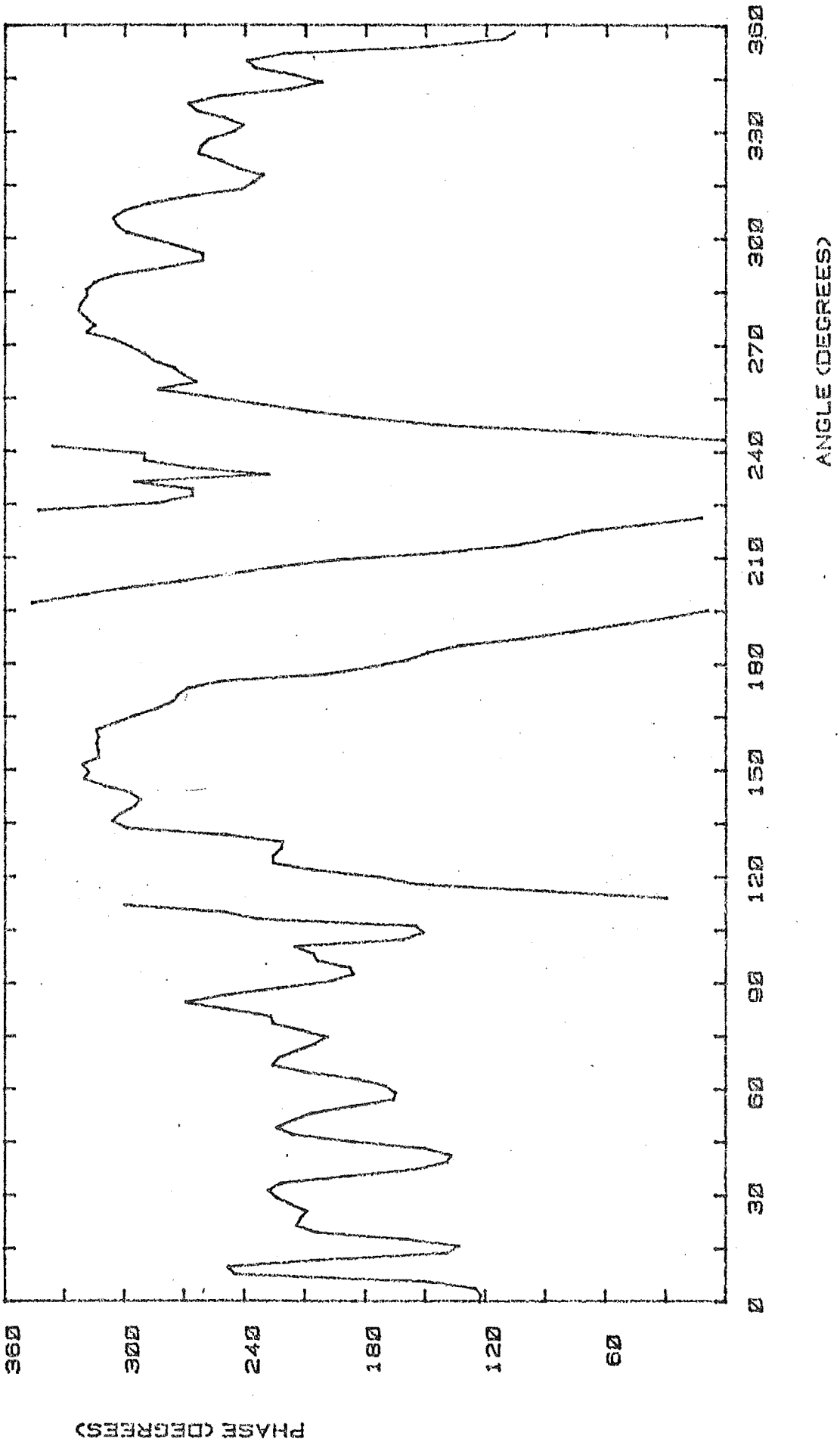

Figure 4.19b) Reflector Field Distribution, $\lambda/2$ Slit at 30°

Experiment Result, (Phase).

field was a superposition of the two formulations along with extra slit to edge couplings. For the E-polarization under study, multiple diffractions between the edges of the parabolic reflector and the slit edges should be very low, as they are angled close to the tangent planes.

The GTD result is shown in Figure 4.20, and can be compared to Figure 4.19. The rear fields show a good match. In this case, where a few extra sources are looking in the rear direction, it appears that the GTD formulation is able to correctly describe the rear field. This is probably because two sources at least can 'see' the probe over most of its locus, providing an interference pattern over a wider region.

The phase shows a total overall change of 720° between ends of the probe locus. This is explained in detail in Section 5.5.5, but briefly the change is caused by the phase algorithm jumping $+180^{\circ}$ at an attenuation null rather than -180°, or vice versa. If this happens twice, an overall error of 720° will occur. Experimental results change in a different manner at 120° and 240°.

4.2.4 METHOD OF MOMENTS RESULT FOR REFLECTOR WITH SLIT

The 220-current filament distribution was modified to account for the slit, and a resultant 212 current distribution was used. The 212 current positions and calculated densities are given in Figures 4.21 and 4.22 respectively. The scatterer matrix took nearly three hours CPU time to invert. The resultant field is presented in Figure 4.23. The attenuation pattern shows agreement with experimental results (Figure 4.19) in the rear direction. The forward field shows a wide deep null at 15° which is not so evident in the Experimental result which has depressed side lobes in the forward direction. The Moments result tends to overemphasise the irregularity found in the rear field of the experiment while GTD global variation is very smooth.

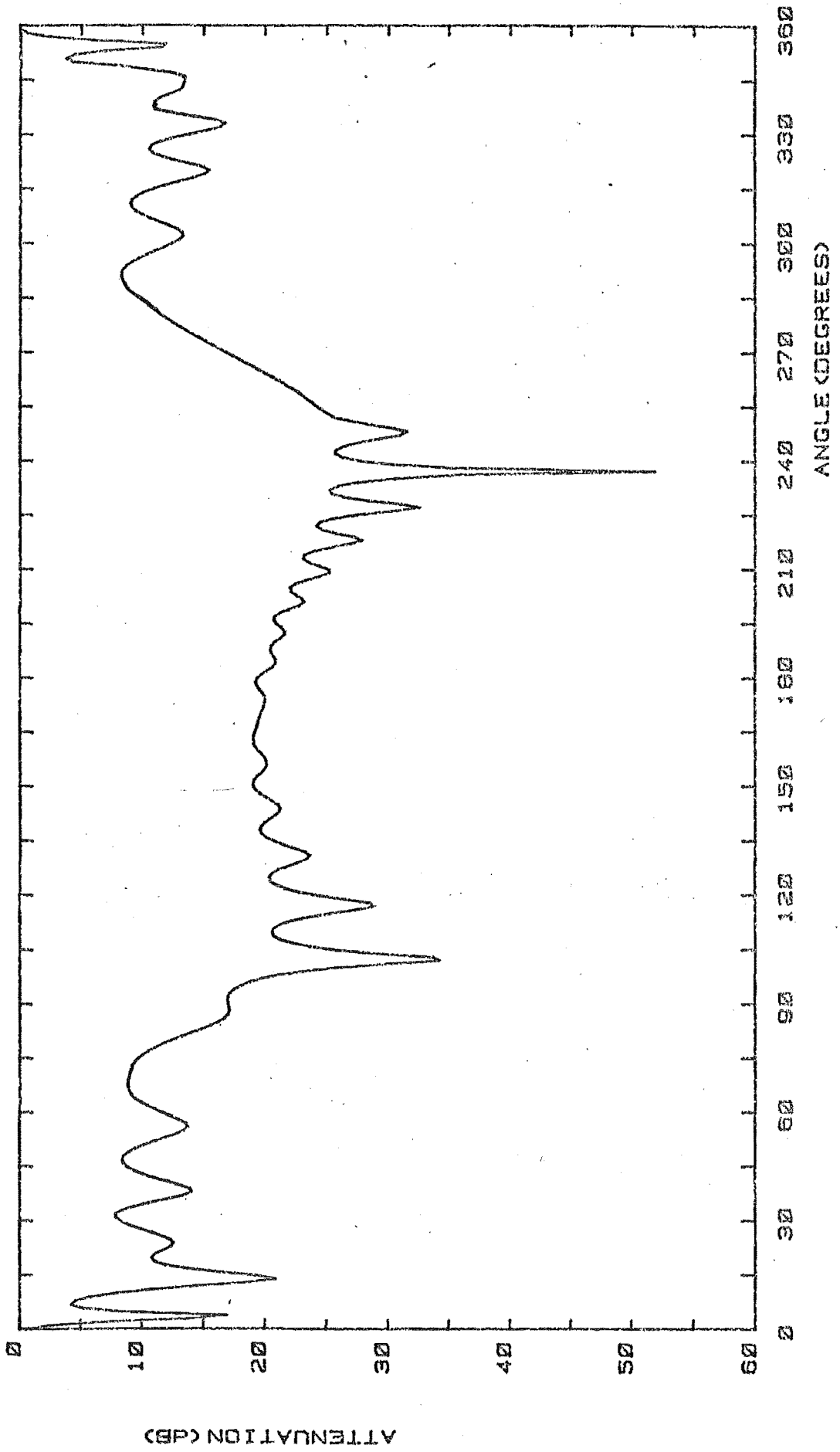

Figure 4.20a) Reflector Field Distribution, $\lambda/2$ Slit at 30°, GTD (Intensity).

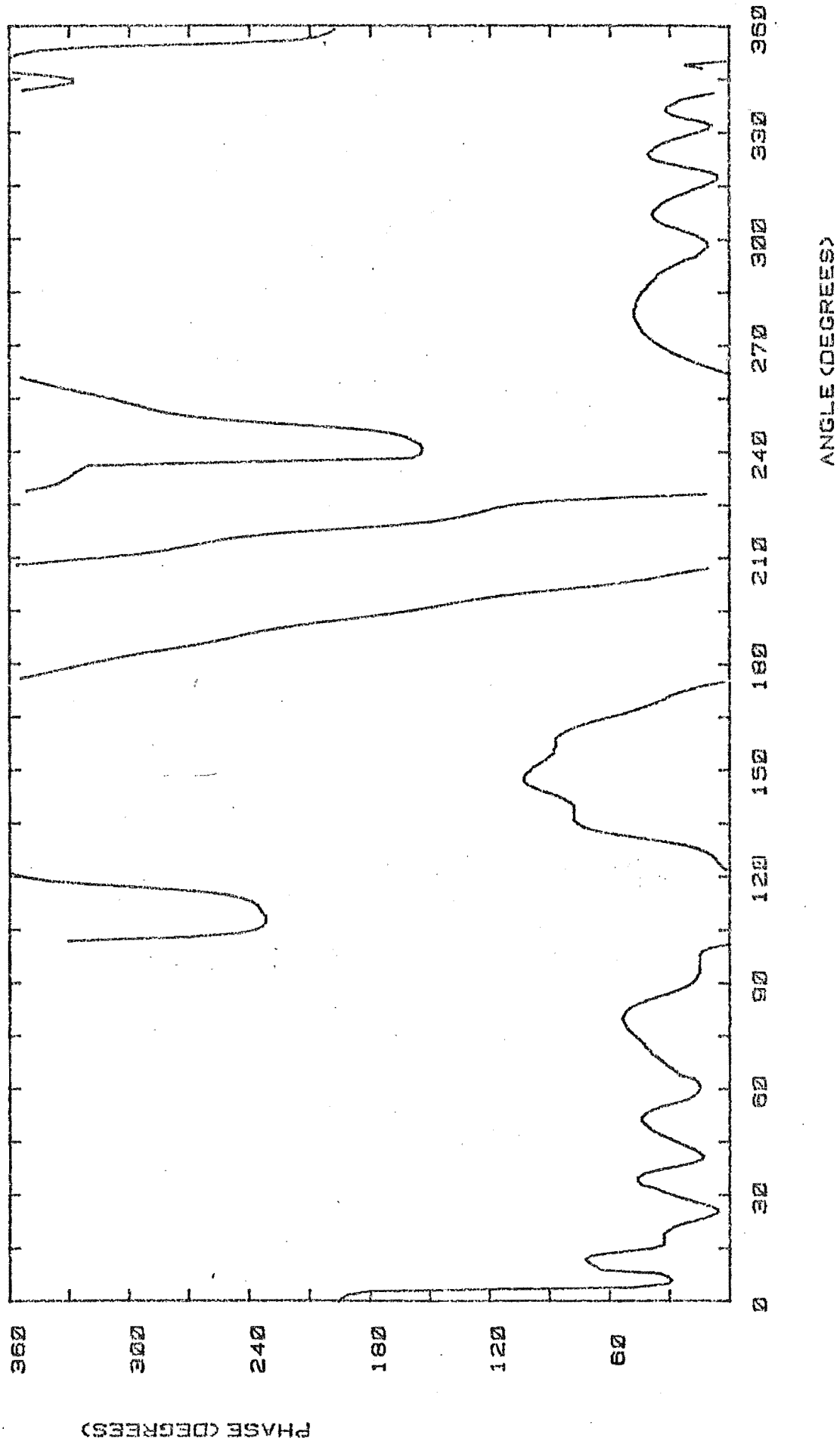

Figure 4.20b) Reflector Field Distribution, $\lambda/2$ Slit at 30°, GTD (Phase).

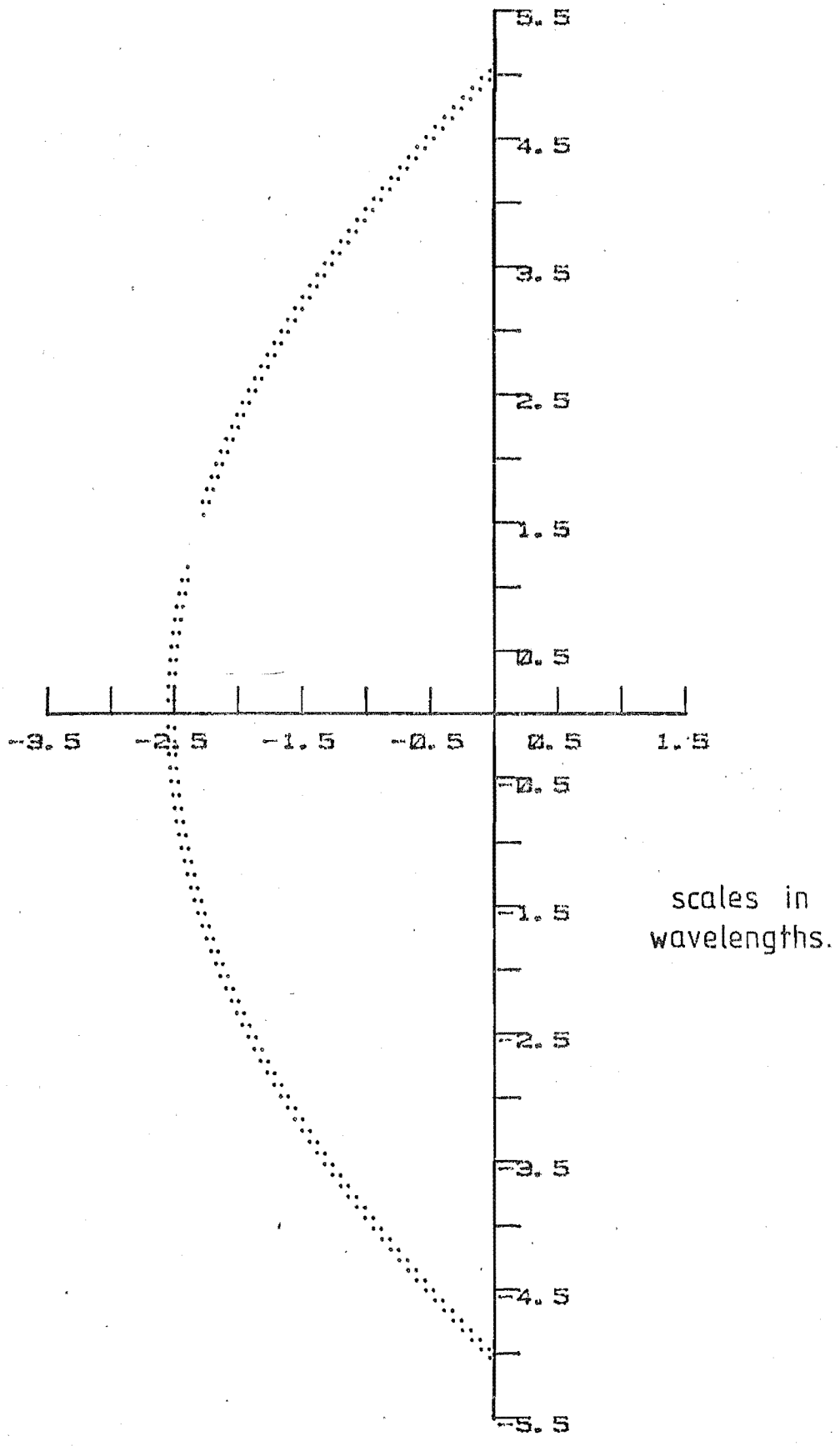

Figure 4.21 Moments Current Distribution on Reflector with $\lambda/2$ Slit at 30°.

This is probably a result of the slowly changing pattern factors of the GTD sources placed at the slit and reflector edges.

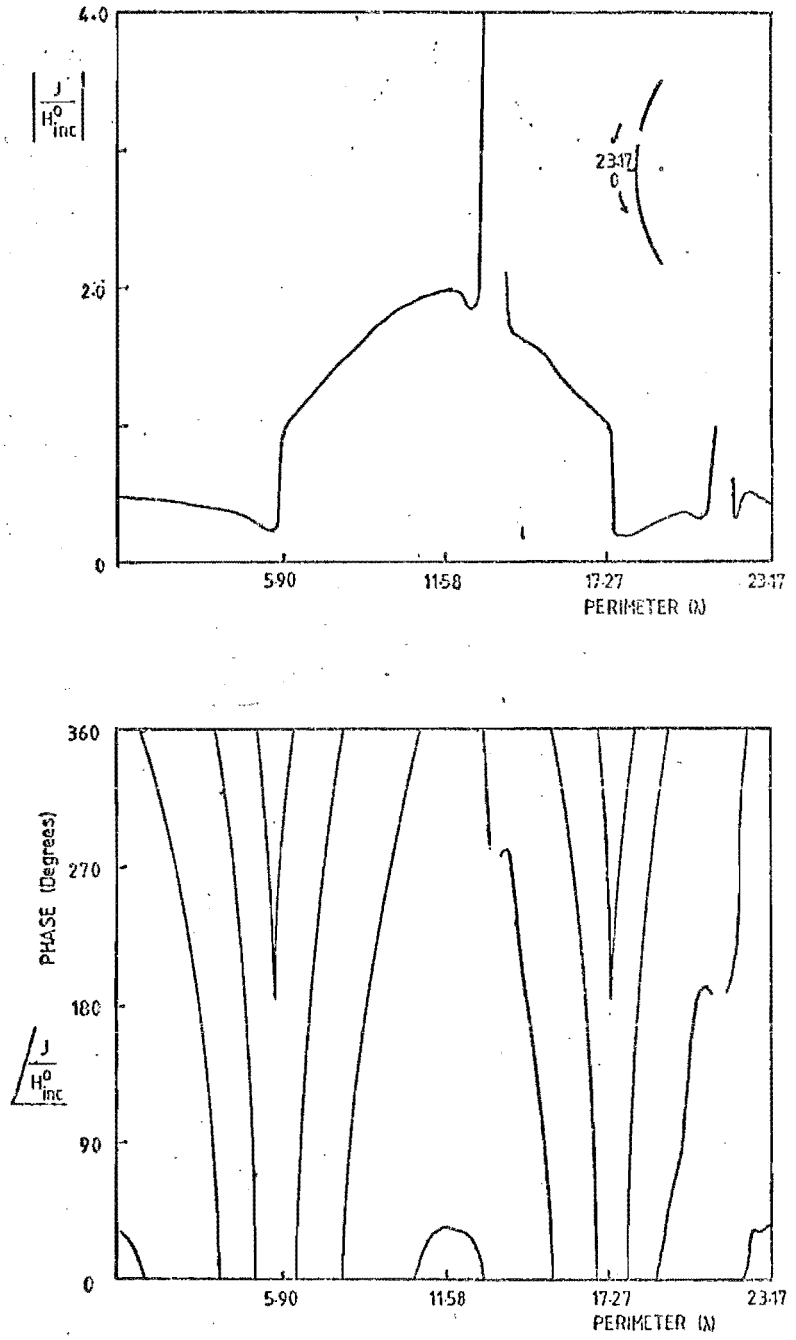

Figure 4.22 Moments Current Density on Reflector with $\lambda/2$ Slit at 30°.

The phase result has a 360° difference between end points of the probe trajectory. Between 120° and 360° the Experiment and Moment results show reasonable agreement, but between 100° and 120° the experimental results show a 360° phase change which the Moments results fail to reproduce.

A major stumbling block associated with large 'moments' problems is the length of solution time. If the currents associated with this example are compared with the currents of the unperturbed reflector,

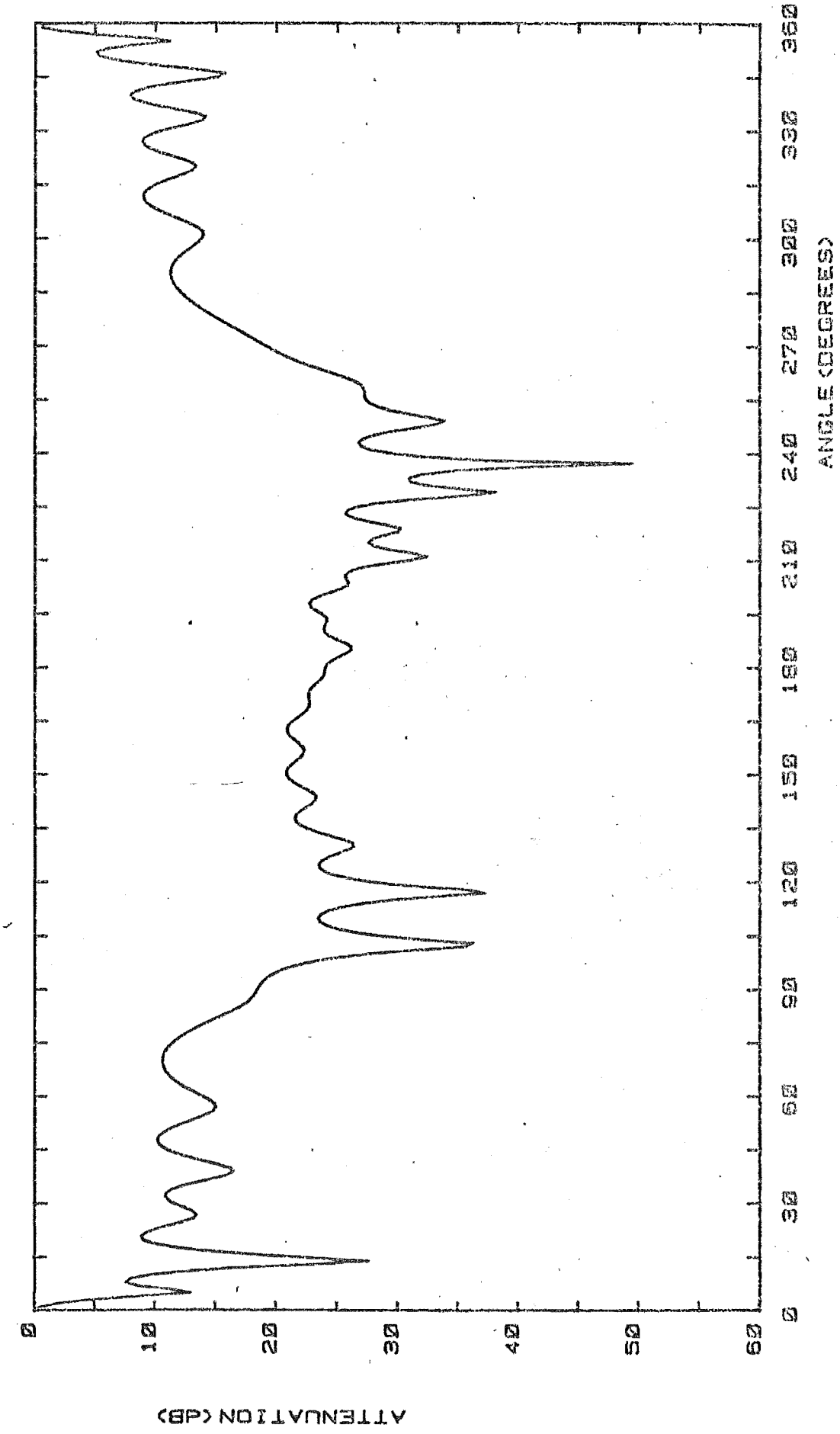

Figure 4.23a) Reflector Field Distribution, $\lambda/2$ Slit at 30°, Moments (Intensity).

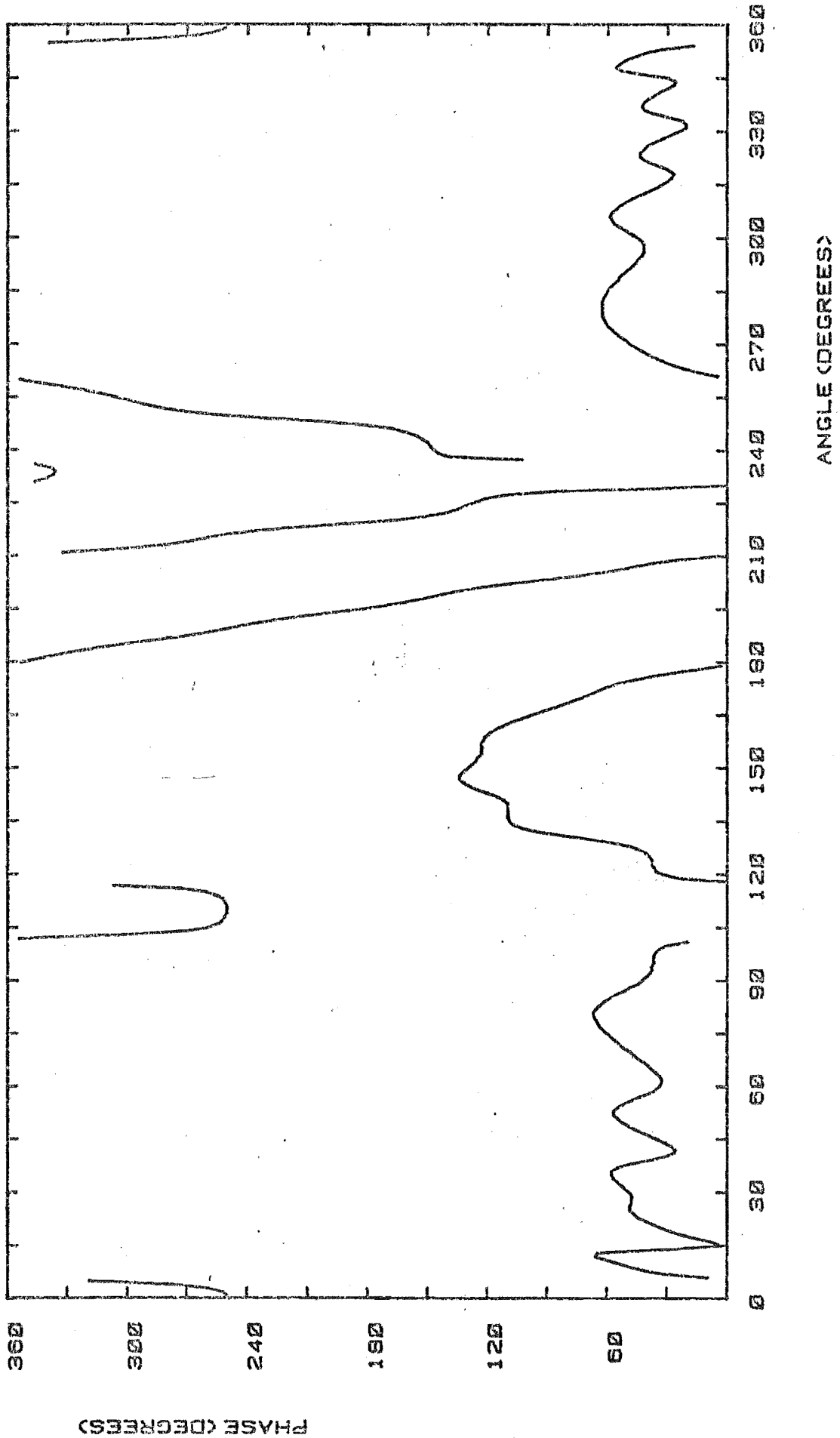

Figure 4.23b) Field Distribution, $\lambda/2$ Slit at 30^{o}, Moments (Phase).

it is found that nearly half of the currents have less than a 2% difference. In the case of other situations where smaller slits are placed at 30^{o}, it may be assumed that these currents will remain unaffected. The <2% changed currents may be shifted into the source vector, reducing the size of the scatterer matrix. When the scatterer matrix is halved, the solution time is cut to one eighth, giving major savings.

A disadvantage of this uncoupling method is that two full sized problems must be solved before any unaffected currents may be found, hence only in the case of many slightly varying problems will the method show real savings.

The half wavelength slit problem was solved again using the uncoupled currents as sources, and the results are in Figure 4.24. The results are very similar to the full scale Moments solution, showing that a small variation of currents has a smaller effect upon the field. The only differences between the Moments and uncoupled Moments solutions occur in the depth of nulls, where the differences of the calculated currents caused by round off errors in the inversion of the scatterer matrix will have their greatest effect.

4.2.5 PHYSICAL OPTICS CUM METHOD OF MOMENTS RESULTS FOR A SLIT IN THE REFLECTOR

The PO-MOM formulation places 55 Moments currents about each edge in the same procedure as in Section 4.1.4. In the example under scrutiny this would mean a 220 by 220 scatterer matrix inversion requiring too great a solution time. A viable alternative is to use an iteration scheme with the following flow path:

a) Assume no slit, and find the unperturbed edge currents using the original PO-MOM formulation in Section 4.1.4.

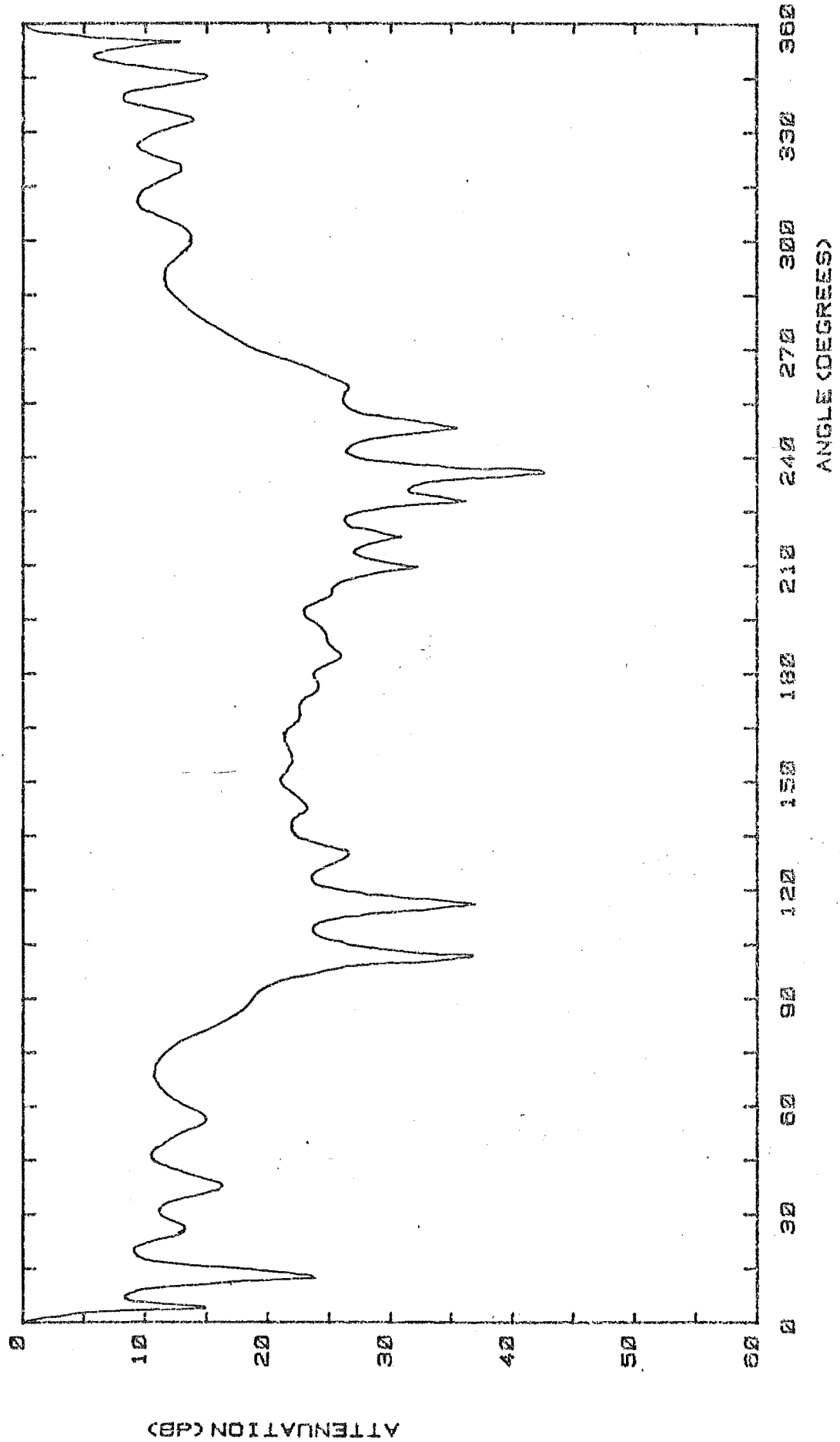

Figure 4.24a) Reflector Field Distribution, $\lambda/2$ Slit at 30°, Uncoupled Moments (Intensity).

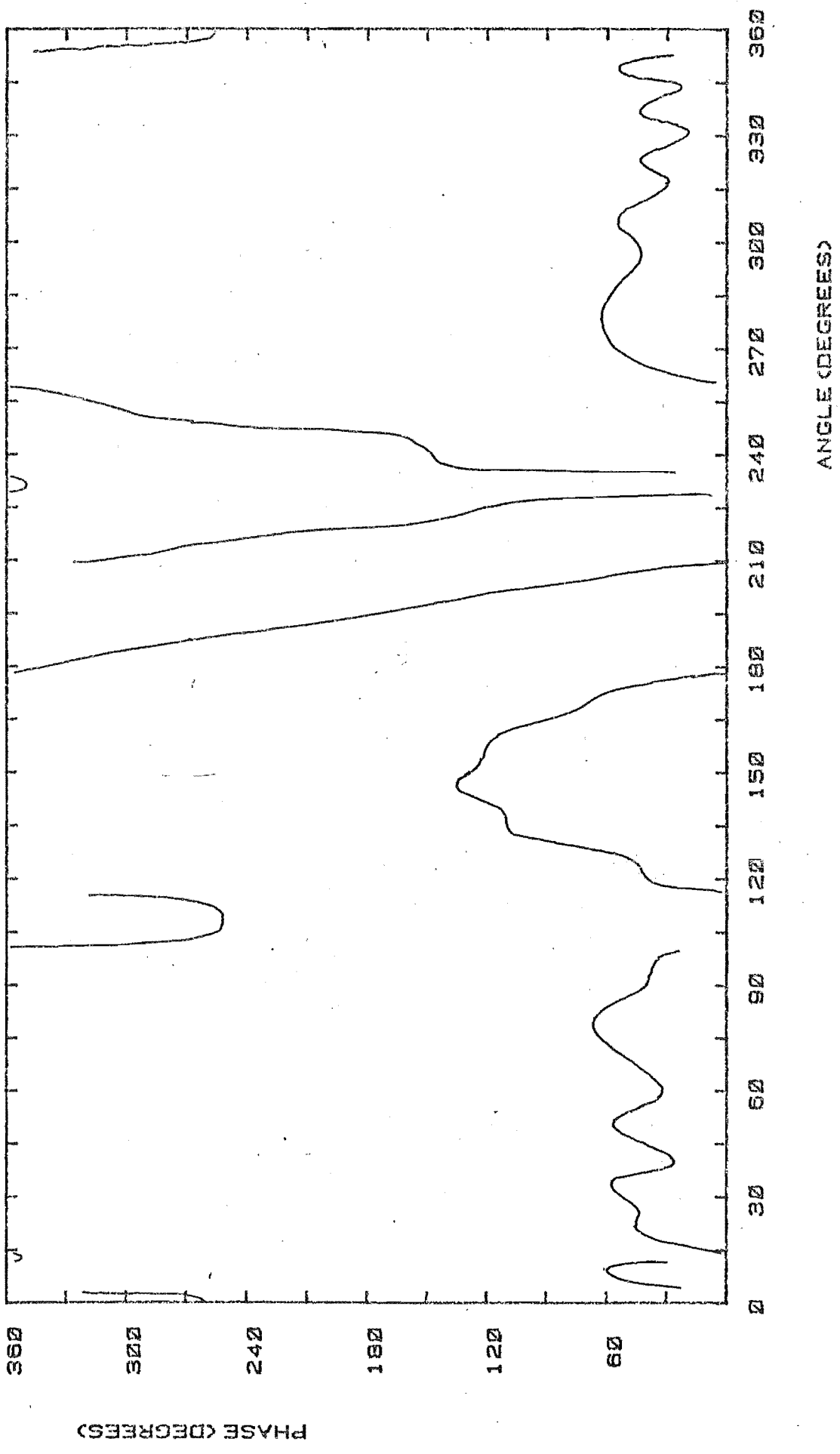

Figure 4.24b) Reflector Field Distribution, $\lambda/2$ Slit at 30°, Uncoupled Moments (Phase).

b) Create a slit, placing moments currents around it, assuming Physical Optics currents and reflector edge currents as sources. Find the slit Moments currents.

c) Use the P.O. currents and slit edge currents as sources. Find the new Moments reflector edge currents. Compare with previous reflector edge currents or previous field calculation. If differences small enough, stop.

d) Use the P.O. currents and reflector edge currents as sources. Find the new Moments slit edge currents. Compare with previous reflector currents or previous field calculation. If differences small enough, stop.

e) Go to step c).

The procedure acts in the same manner as adding in coupling terms in GTD methods. The procedure will normally iterate to a solution, but there is no proof that such a solution is the correct one.

For the present example, the above scheme was used, and run for two iterations. Figure 4.25a shows the slit currents after step b) above and Figure 4.26a,b shows the associated total field. Similarly Figures 4.25b and 4.26c,d are associated with step d) of the second iteration.

The Figures show little variation, hence it can be concluded that the slit is well decoupled from the reflector edges, allowing more or less direct superposition of each field.

The iterated PO-MOM results compare well with experimental and GTD results, in the rear direction. This suggests that the greatest effect comes from edge currents near the slit and reflector edges. The forward field is very similar to the Moments results. This indicates that the calculated front currents away from the edges are close to the

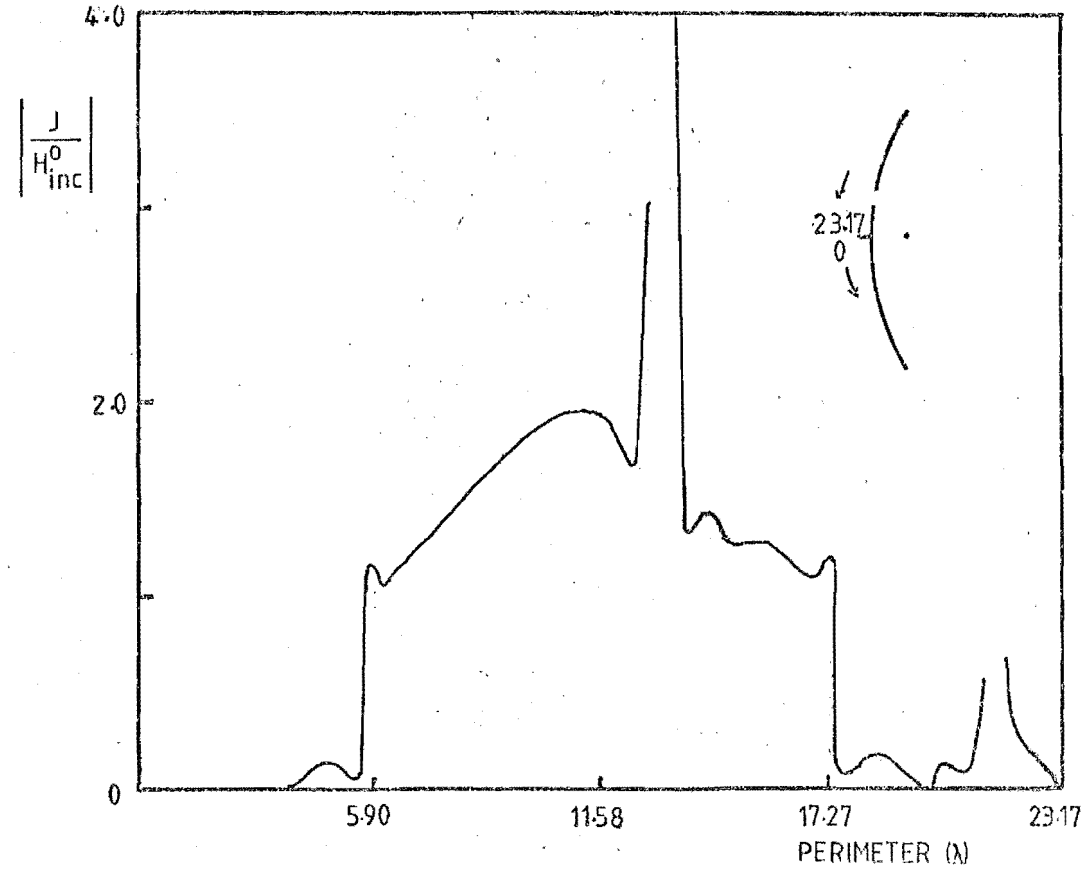

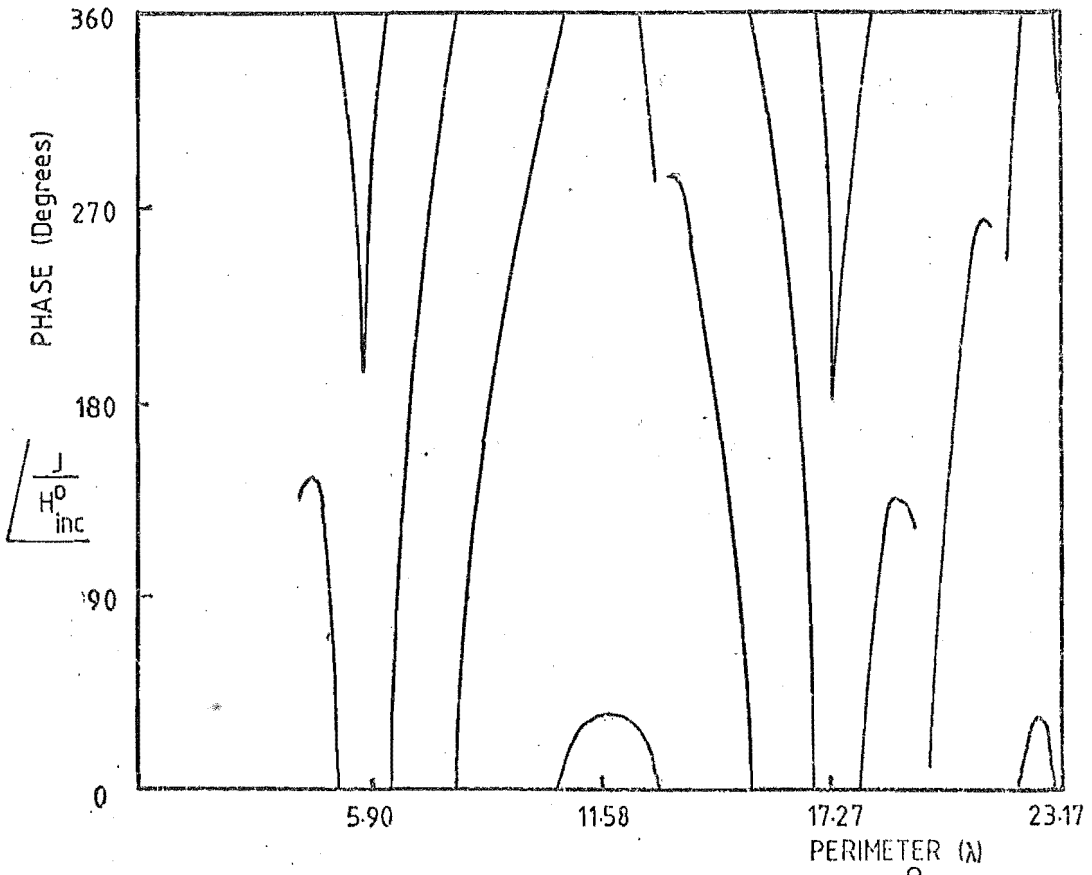

Figure 4.25a) Reflector Surface Currents, λ/2 Slit at 30°, Iterated PO-MOM, 1st Iteration.

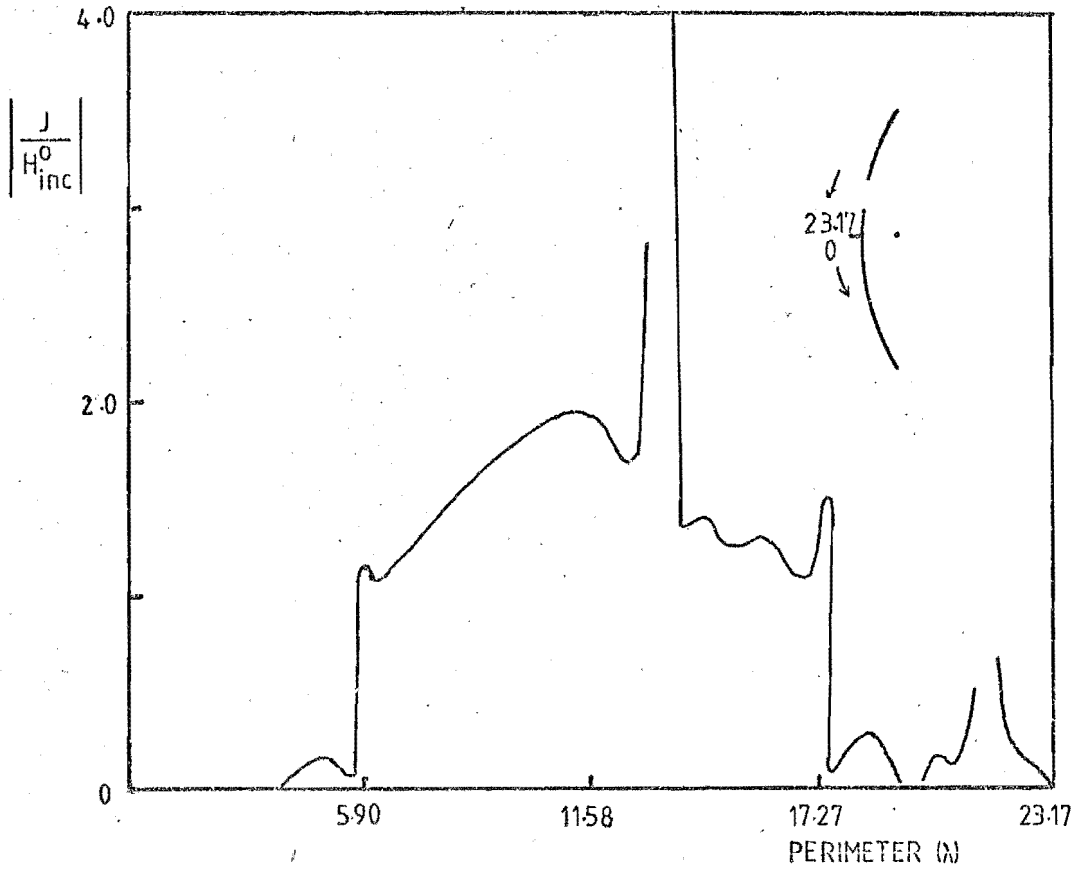

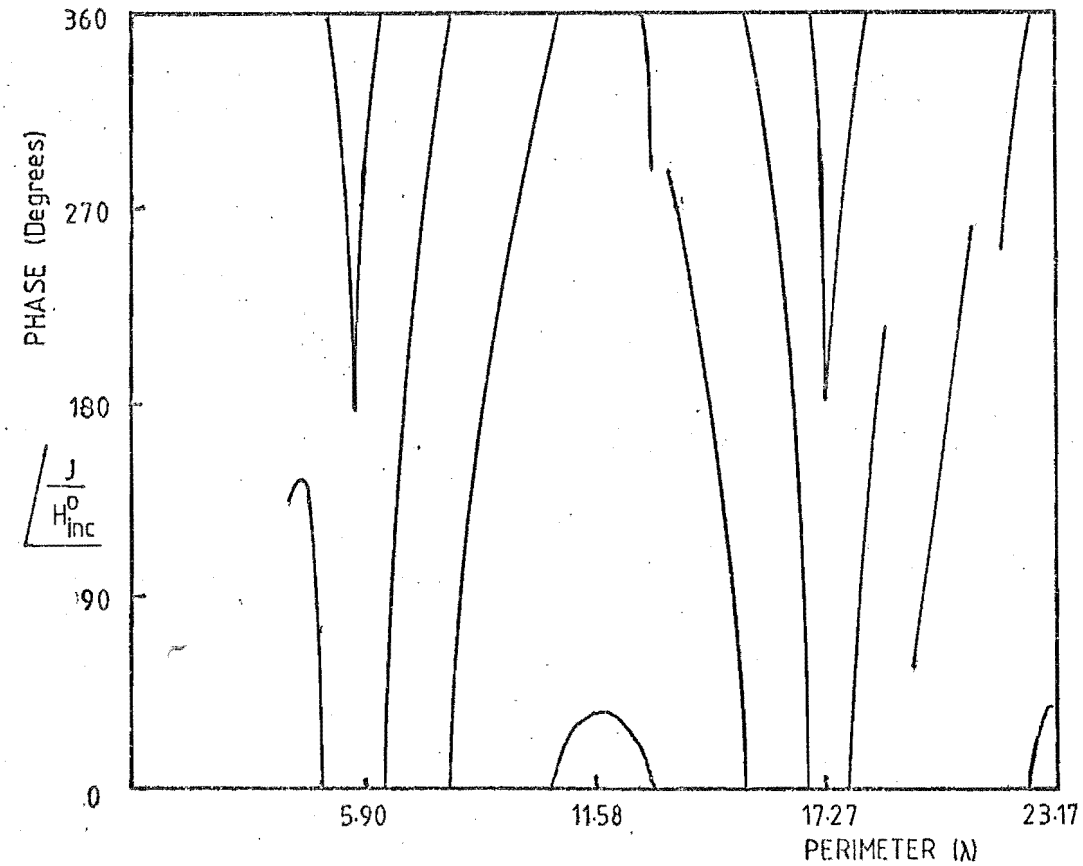

Figure 4.25b) Reflector Surface Currents, λ/2 Slit at 30°, Iterated PO-MOM, Final Iteration.

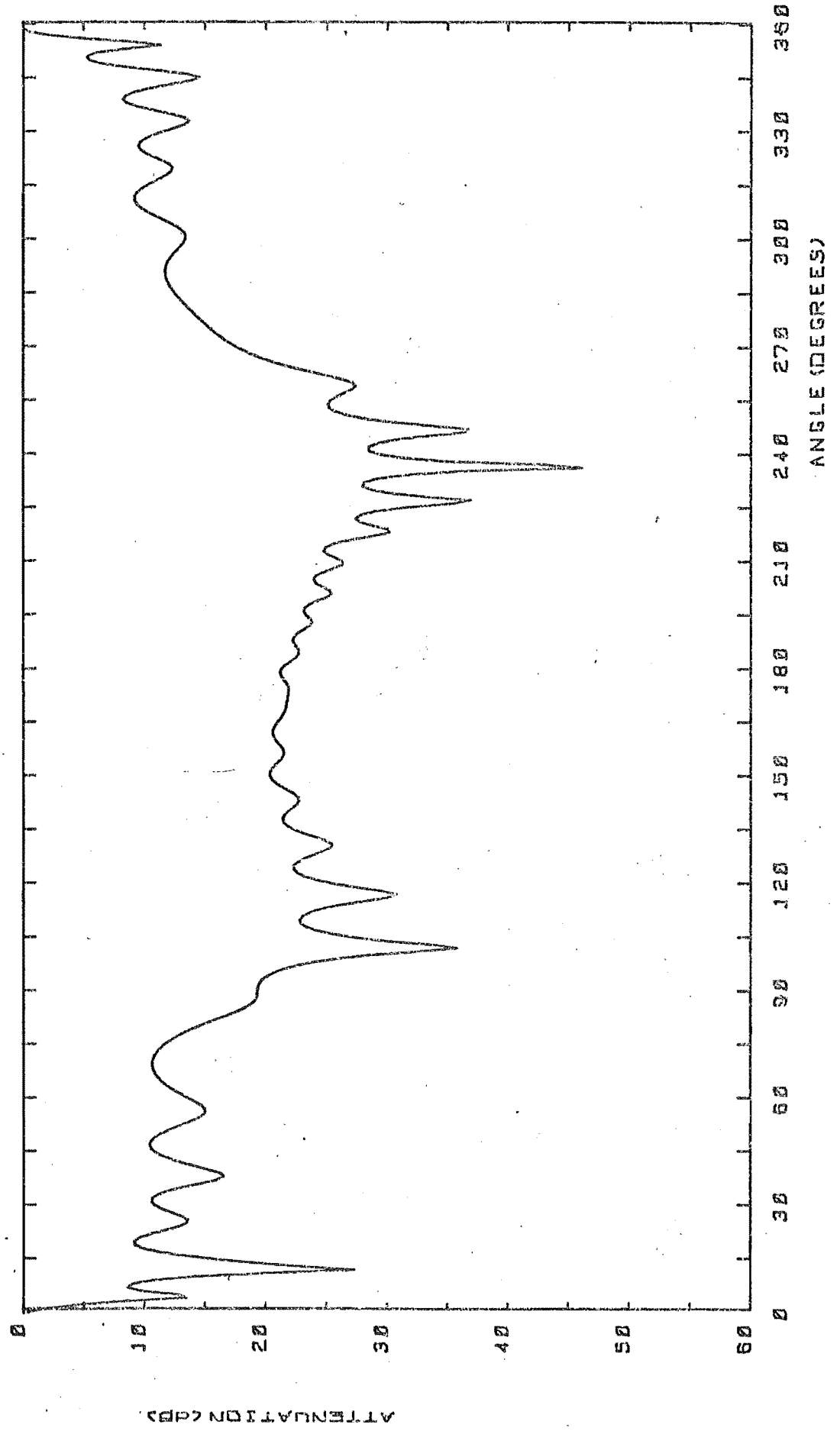

Figure 4.26a) Reflector Field Distribution, $\lambda/2$ Slit at 30°, Iterated PO-MOM, 1st Iteration, (Intensity).

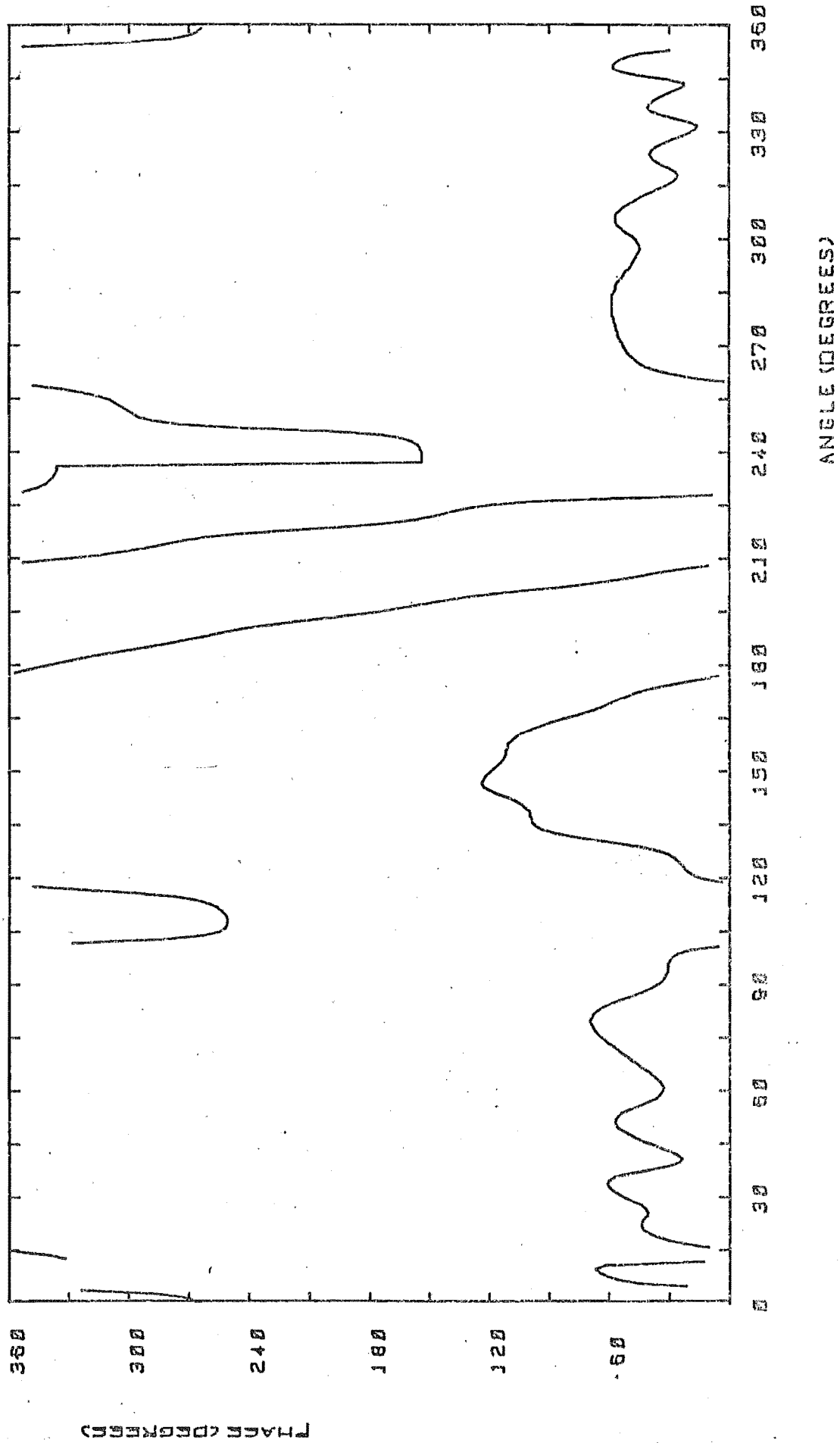

Figure 4.26b) Reflector Field Distribution, $\lambda/2$ Slit at 30^{o}, Iterated PO-MOM, 1st Iteration, (Phase).

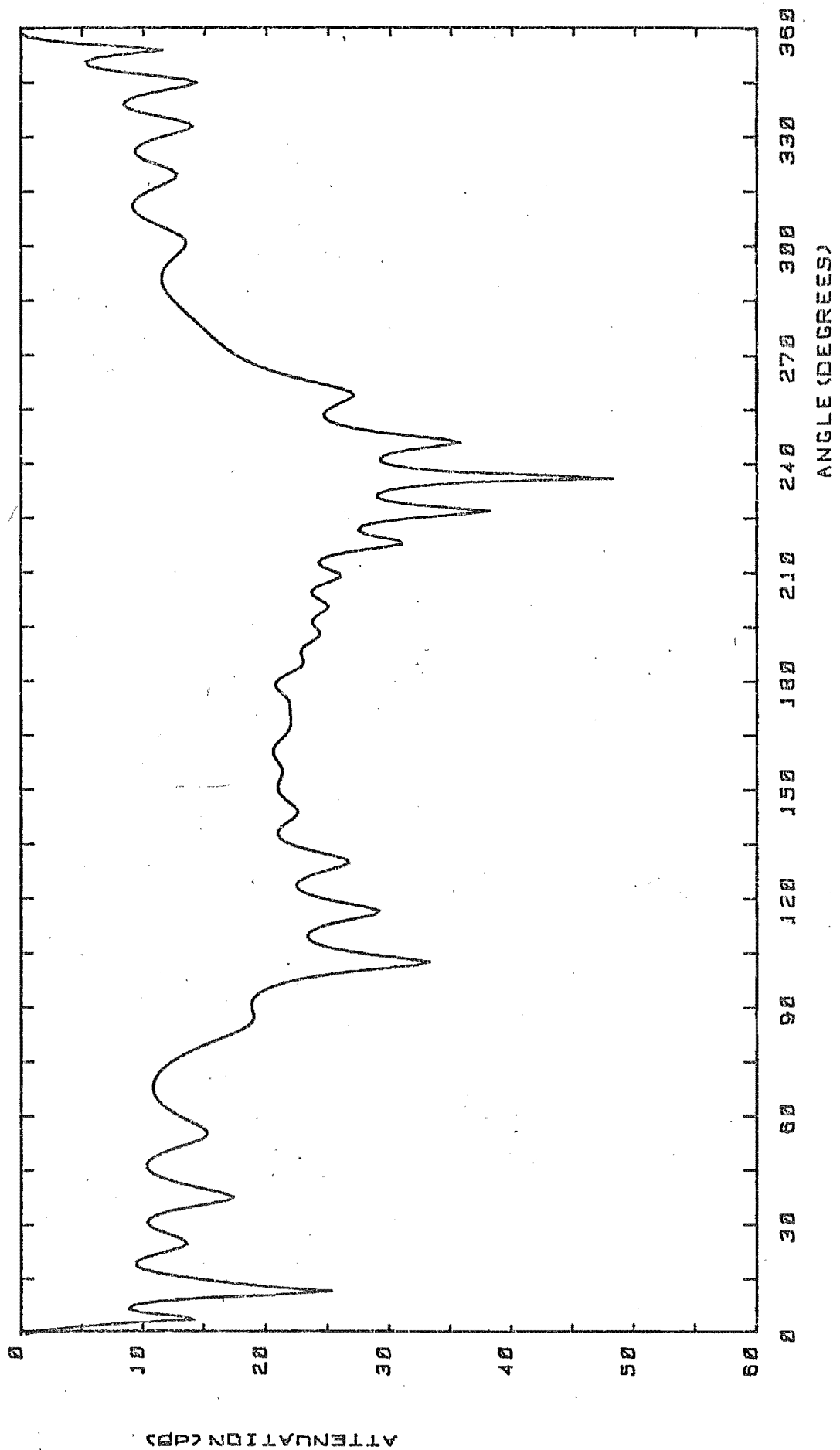

Figure 4.26c) Reflector Field Distribution, $\lambda/2$ Slit at 30°, Iterated PO-MOM, Final Iteration, (Intensity).

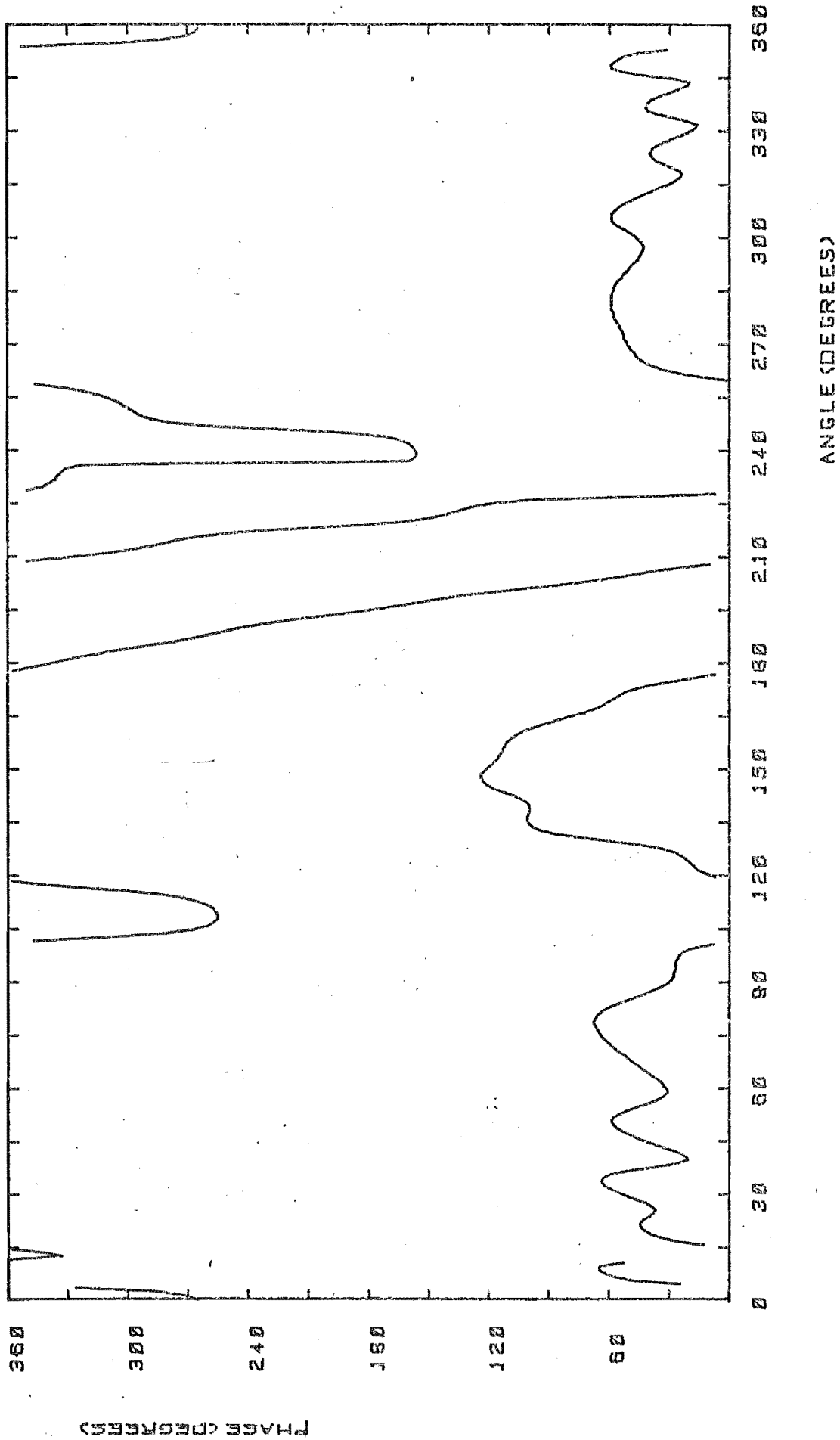

Figure 4.26d) Reflector Field Distribution, $\lambda/2$ Slit at 30°, Iterated PO-MOM, Final Iteration, (Phase).

Physical Optics currents used in the PO-MOM case.

Overall, the PO-MOM formulation combines the forward field of the Moments solution with the GTD rear field in a case where the slit is well decoupled from the reflector edges.

The PO-MOM phase pattern is very similar to the Moments result, with an overall phase change of 360° between extremes of the probe locus. The same errors in the phase occur for the PO-MOM formulation as in the case of the Moments Method.

The PO-MOM iterated formulation involves the inversion of two independent scatterer matrices, rather than one single large scatterer matrix. The Gauss-Jordan inversion routine takes a CPU time proportional to n^3 where n is matrix rank. The larger matrix takes much longer to invert on many machines due to problems storing the matrix array, hence the inversion of two smaller matrices will speed up solution time of the problem many times. The scatterer matrices need to be inverted only once since the current positions are fixed. The only parameters that are changed are the source vectors, dependent upon the results of previous iterations.

4.2.6 DISCUSSION

For this example, for the rear field, it appears that either the GTD or the PO-MOM representations may be of use. The slit appears to be well decoupled from the edges, as shown by the small changes in the slit edge currents in the iterated PO-MOM example. If it is known, or can be proved that the slit is well decoupled, a simple superposition of the GTD fields will provide an adequate result in a fraction of the time that a PO-MOM form would require.

As a general rule, working from experimental results of Chapter 3 where two edges are more than 1½ wavelengths away from each other and if

both can be viewed simultaneously at the probe point it seems reasonable to apply GTD to the problem.

A more stringent test upon the theories might be to place a slit closer to a reflector edge. This will increase slit-edge coupling, and will tend to isolate the opposite edge of the reflector. This situation is covered in the next section.

4.3 OTHER RESULTS

Three other situations were covered by experiment and theory. They were,

a) quarter wavelength slit at 30^{o}

b) half wavelength slit at 70^{o}

c) quarter wavelength slit at 70^{o}.

The smaller slits were tested to find if the lower leakage could actually null the reflector field, and slits were placed at 70^{o} to investigate coupling between slits and edges.

4.3.1 EXAMPLE a)

The slit at 30^{o} is well decoupled from the reflector edges as may be expected from the results of Section 4.2. Results in Figure 4.27 cover experiment, GTD, uncoupled Method of Moments (MOM) and Iterated Physical Optics cum Method of Moments (Iterated PO-MOM). Referring to Chapter 3, the GTD solution for the quarter wavelength slit should have a slight phase inaccuracy, which can be corrected. This would retain the simplicity of the GTD formulation.

Only one iteration was required with the Iterated PO-MOM formulation, due to the slit being so removed from the edges. The PO-MOM results appear to agree most closely with the experimental results.

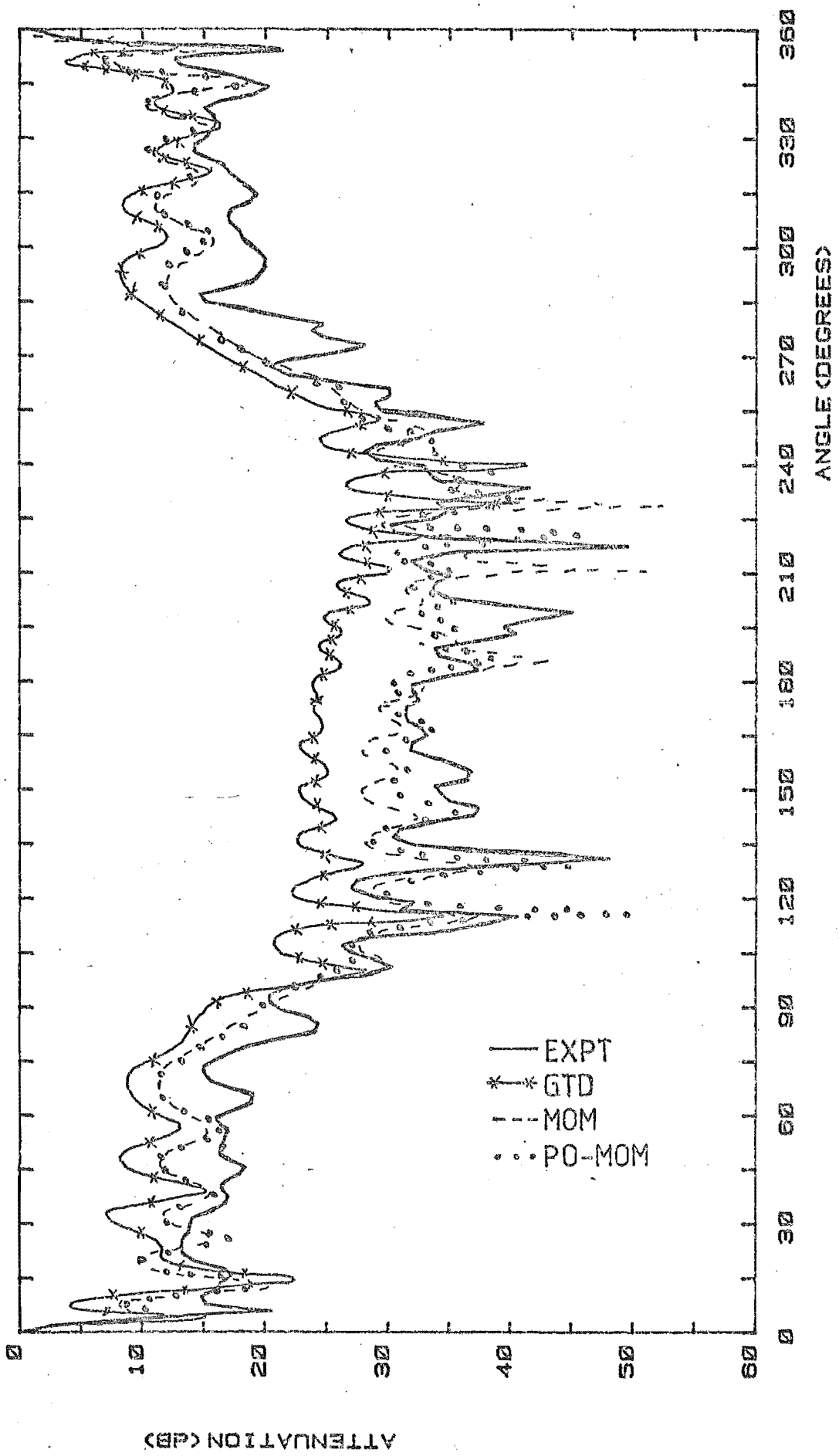

Figure 4.27a) Reflector Field Distribution, $\lambda/4$ Slit at 30^{o}, Experiment, GTD, Uncoupled MOM, Iterated PO-MOM, (Intensity).

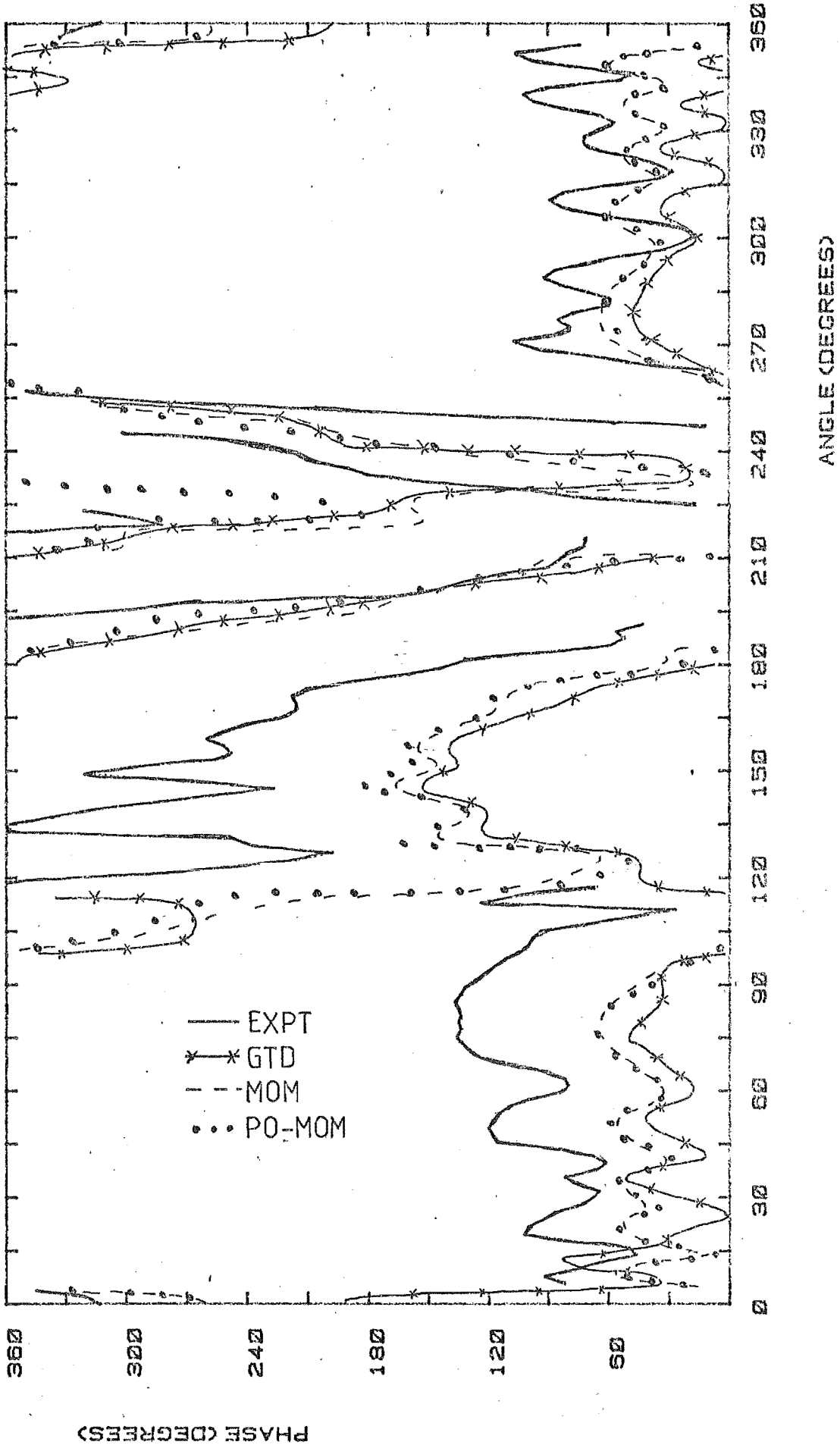

Figure 4.27b) Reflector Field Distribution, λ/4 Slit at 30°, Experiment, GTD, Uncoupled MOM, Iterated PO-MOM, (Phase).

The phase results differ quite markedly. The Iterated PO-MOM representation has a 360^{o} phase change over the probe locus, and there are rapid phase changes associated with nulls at 115^{o} and 130^{o}. The experimental results show equally rapid phase changes, and it appears that the 180^{o} phase change at 115^{o} may be in the opposite direction. This effectively reduces the overall phase change between ends of the probe locus to zero. Another phase jump occurs at 225^{o}. This may be the source of another error.

The uncoupled MOM result produces a group of nulls about 210^{o}, and tends to exagerate the leakage through the slit. The forward field of the MOM form matches closely that of the PO-MOM form. The MOM formulation has one incorrect phase jump at 225^{o}, which can be associated with the extra nulls in that region.

The GTD result does not produce a satisfactory result. Peaks and nulls in the rear field are in approximately the correct places, but are of incorrect values. The phase results show a discrepancy of 360^{o} over the probe locus, probably caused by peculiarities around 115^{o}.

4.3.2 EXAMPLE b)

In this case the slit is about 1.75 wavelengths away from the edge (Figure 4.28). Taking a GTD approach to the problem we might reasonably expect inter-edge interactions between the slit and the nearer reflector edge. The interactions between the reflector edge can be split into two forms, i.e. the coupling caused by surface rays around the convex surface between the reflector edge and the slit, and coupling from diffraction off the edge across the concave face of the reflector to the slit. From the Dirichlet Boundary Conditions, it might be expected that the coupling directly across the concave face might be the greatest, and would swamp the effect of the surface ray. This has been assumed for this example.

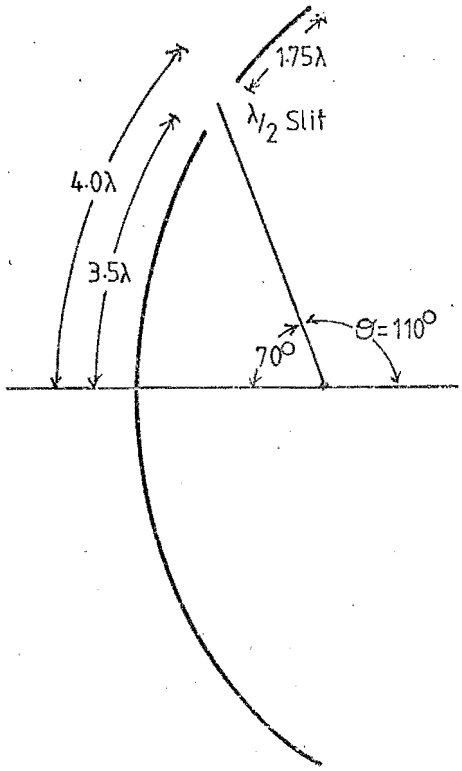

Figure 4.28 $\lambda/2$ Slit at 70° in Parabolic Reflector.

The iteration scheme involving the PO-MOM formulation has been modified to account for two edges close together. The reflector edge and its associated closer slit edge have been brought together for this problem, as the currents about these edges cannot be easily separated into two distinct groups. The iteration scheme of Section 4.2 has to be modified as follows:

a) Place Physical Optics currents over the larger piece of the reflector, disregarding the edges, and use these currents as sources to find the moments currents on the small strip.

b) Use the small strip moments currents and Physical Optics currents away from the edges of the big bit as sources to find the moments edge currents of the big bit. Stop if difference in currents or calculated far field small enough.

c) Use the currents on the big bit as sources to find the moments currents on the small strip. Stop if differences in the currents or the calculated far field small enough.

d) Go to step b).

The iteration scheme above has a cruder starting point than the scheme in Section 4.2, but it has been found that only three iterations are required before currents and field show little variation, the coupling being accounted for very quickly. Changing the starting point by using moments currents at the far away edge of the big bit does not alter the iterated result.

The results for theories and experiment are presented in Figure 4.29. The theoretical results are in poor agreement with each other as well as with experimental results. The best correlation between experiment and theory occurs with the interated PO-MOM solution.

The phase result is confusing. The large number of nulls in the rear direction make it difficult to explain which way the 180° phase shifts go at the nulls, hence both experiment and theory have ended up with an overall phase shift along the probe locus. The Iterated PO-MOM result may have an incorrect phase shift in the region of 110° where the slit field should cause a reversal of phase shift, c.f. the half wavelength at 30° example.

The Moment Method theory results appear to be skewed with respect to experimental and other theoretical results.

The MOM theory predicts deep nulls at 105° and 227°, in each case 5° to one side of the corresponding nulls in the experimental results. In the rear direction nulls and peak positions do not match as well as the iterated PO-MOM results, even when the experiment results are shifted 5° to line up the deep nulls.

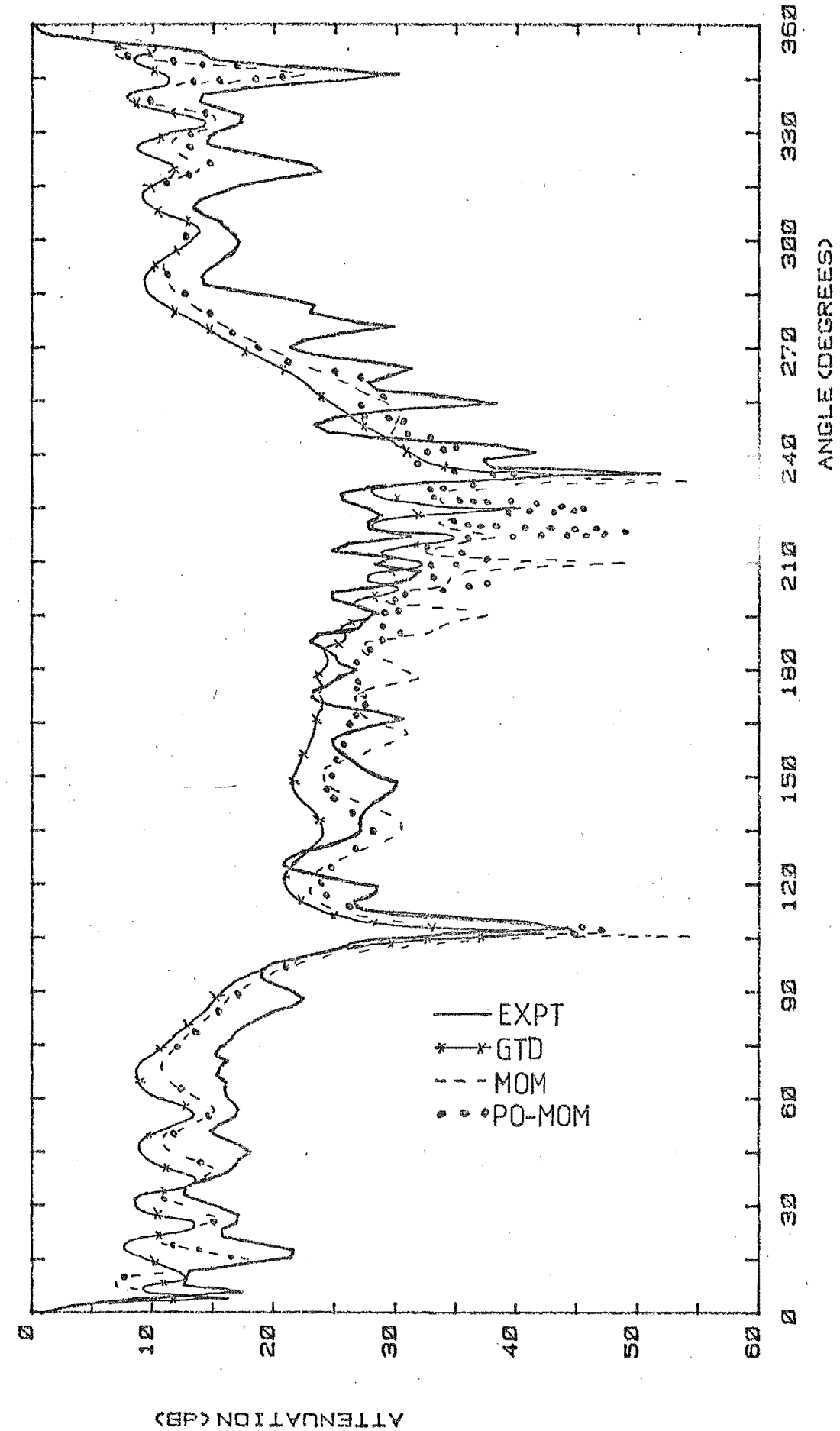

Figure 4.29a) Reflector Field Distribution, $\lambda/2$ Slit at 70°, Experiment, GTD, Moments, Iterated PO-MOM, (Intensity).

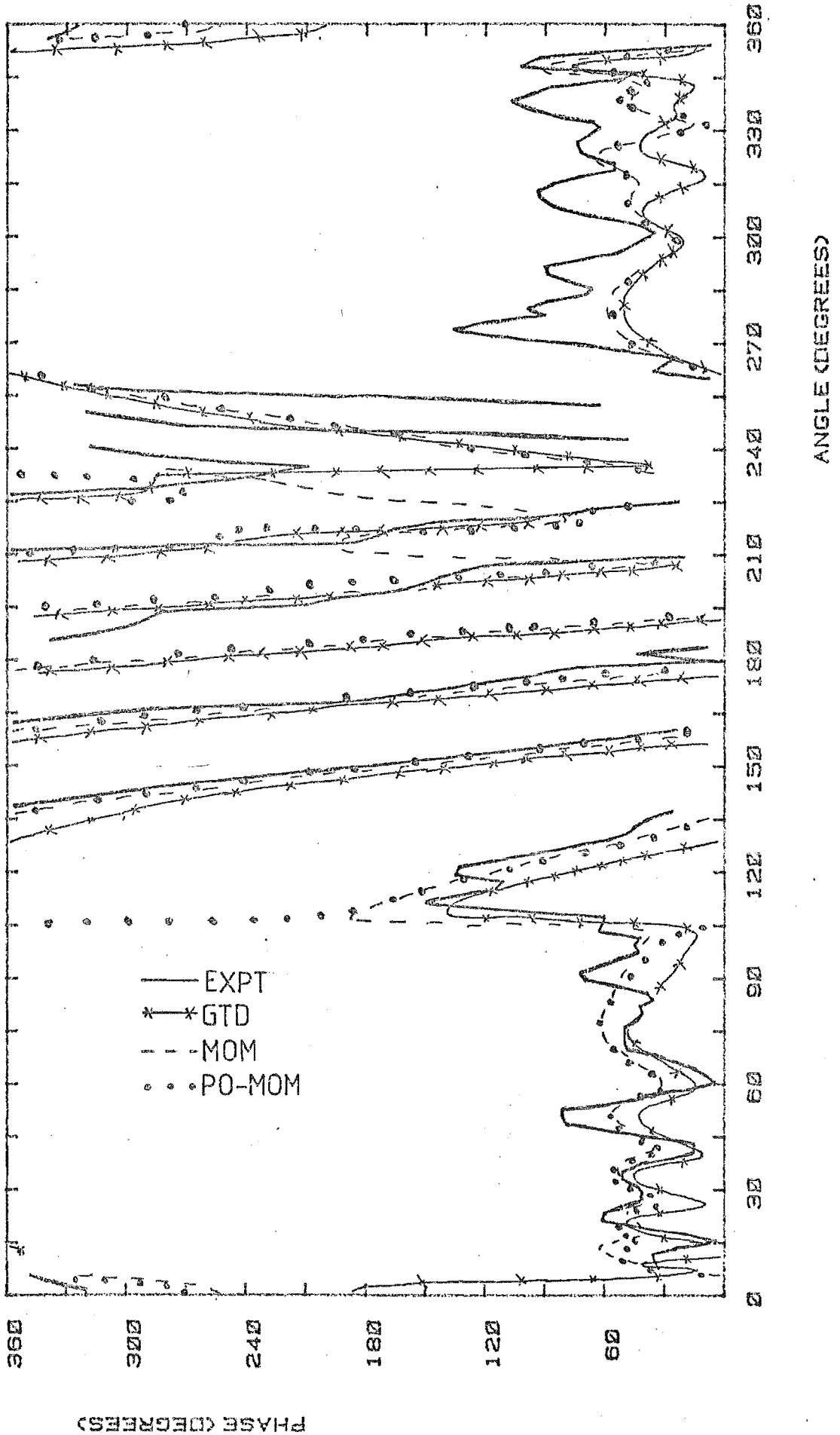

Figure 4.29b) Reflector Field Distribution, $\lambda/2$ Slit at 70°, Experiment, GTD, Moments, Iterated PO-MOM, (Phase).

The MOM phase results show three stationary points in the region of 210°. This is probably caused by the distribution of incorrect currents on the rear of the reflector away from the edges. The uncoupled MOM results are very similar to the MOM results except for a slight variation in null depths.

The GTD result predicts the experiment nulls at 110° and 235°, but the remainder of the rear radiation pattern is not a good assessment of the measured pattern. The bumps and hollows in the rear radiation pattern occur at a high spatial frequency, suggesting widely spaced sources. It appears that the same problem struck in the case of the unperturbed reflector may be occurring here. To circumvent this problem, some form of surface ray diffraction may be necessary.

The GTD phase pattern has the same general form as that of the iterated PO-MOM result, except that about 105° the phase jump at the null is in the opposite direction.

4.3.3 EXAMPLE c)

The quarter wavelength slit at 70° leaks less power in the rear direction in comparison to the same sized slit at 30° because the slit is further away from the source. This lower leakage, along with a stronger edge diffracted signal in the direction of 110° means that the leakage signal is not strong enough to cancel the edge diffracted field. This is evident by the lack of nulls in the experimental rear radiation pattern, see Figure 4.30.

The iterated PO-MOM theory compares quite well with experimental results with peaks and nulls corresponding reasonably well. It was found that three iterations were sufficient for accurate results.

A comparison of the experimental phase and the phase from the iterated PO-MOM solution show major discrepancies, especially in the

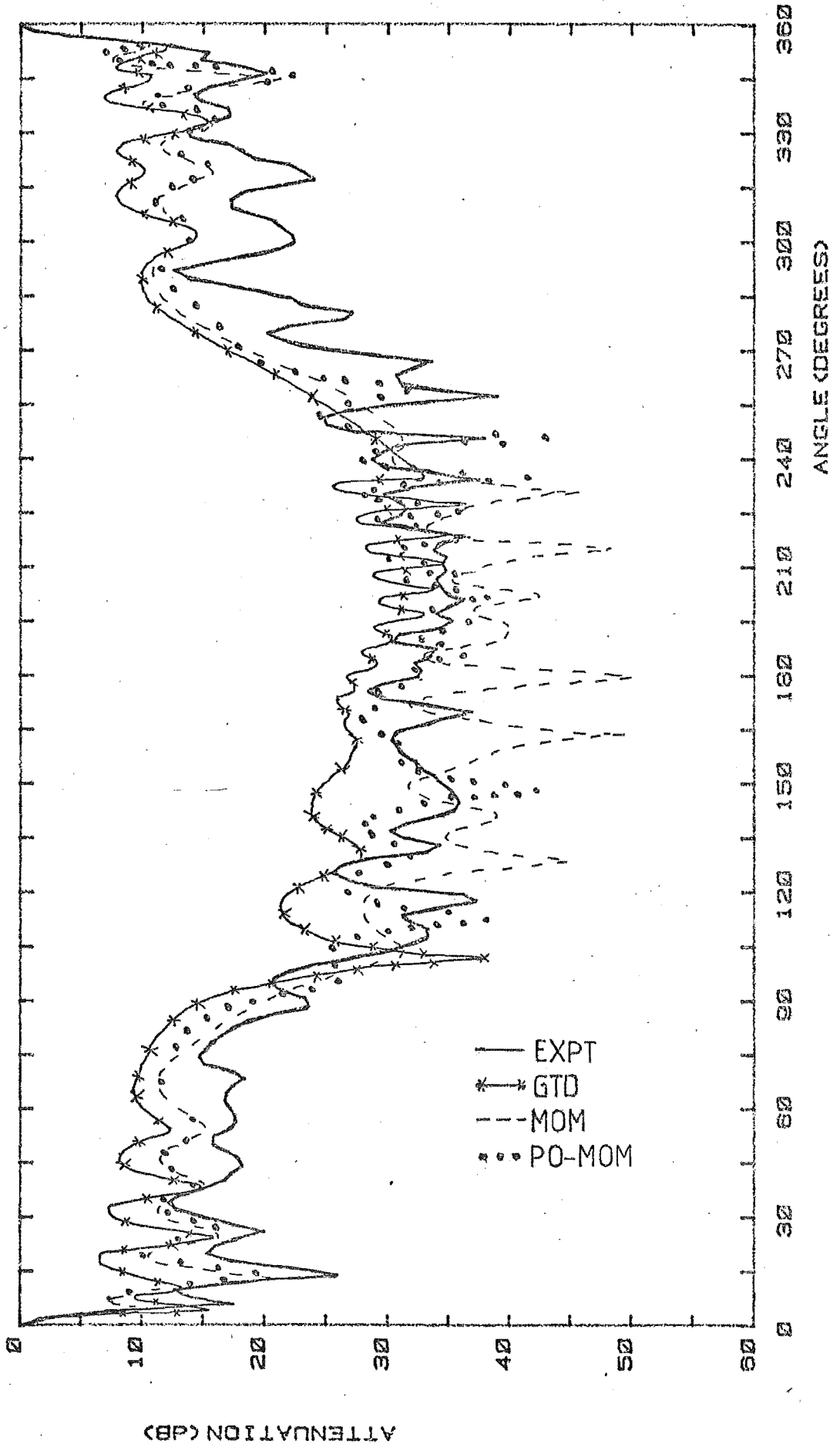

Figure 4.30a) Reflector Field Distribution, $\lambda/4$ Slit at 70°, Experiment, GTD, Uncoupled Moments, Iterated PO-MOM, (Intensity).

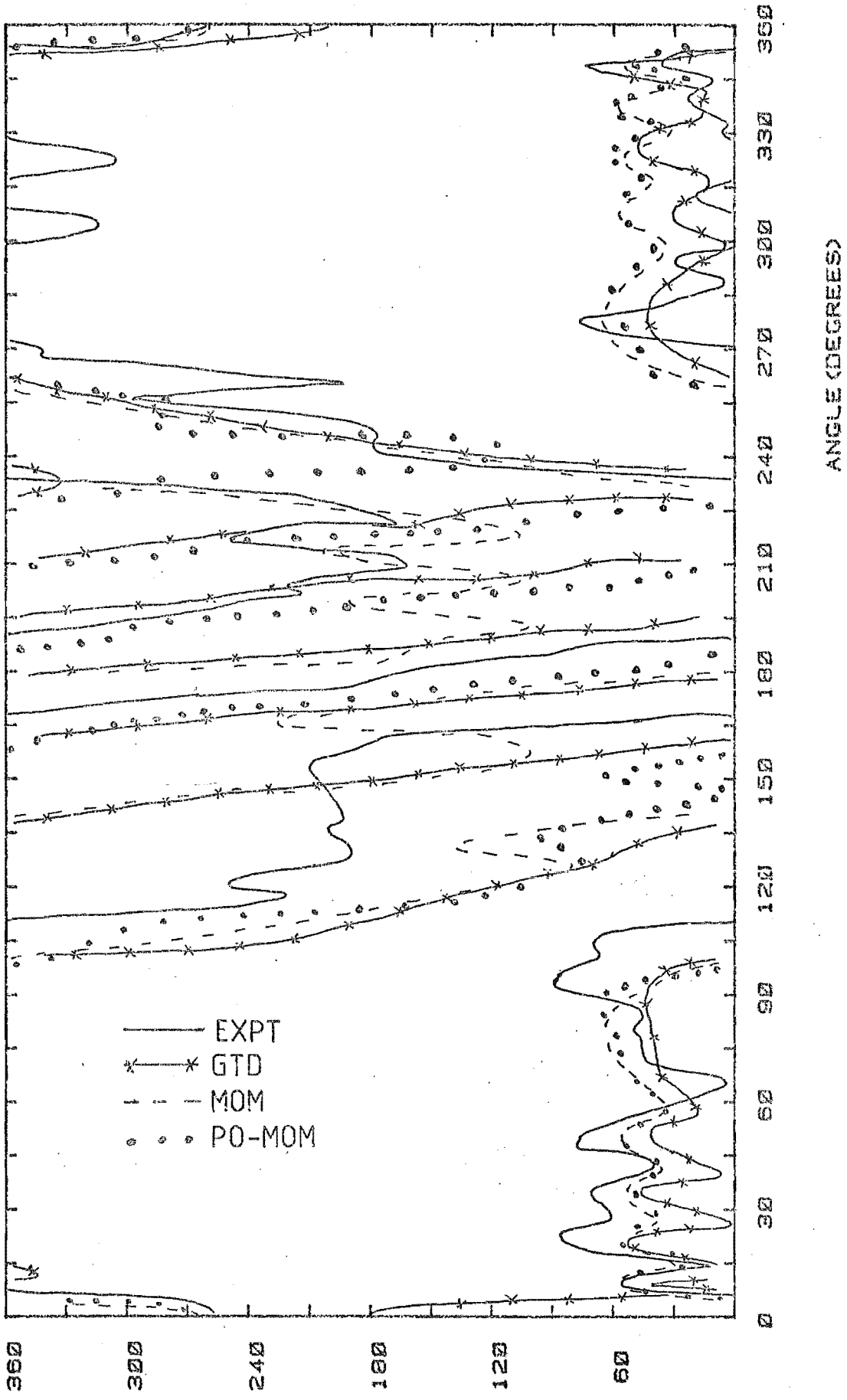

Figure 4.30b) Reflector Field Distribution, $\lambda/4$ Slit at 70°, Experiment, GTD, Uncoupled Moments, Iterated PO-MOM, (Phase).

region about 220°. There is a phase shift over the probe locus for both experiment and theory.

The uncoupled MOM result shows a large number of nulls, in a similar manner to those for the MOM result of the unperturbed reflector. The bumps and hollows of the phase result underlines the effect of incorrect currents on the rear of the reflector. The MOM results are poor and of little use for this example.

The rear radiation pattern for the GTD description is just an attenuated version of the description of Example b). The rear field radiation pattern suffers from the same problems as in the previous example. The GTD phase result does not match well with experiment.

4.4 DISCUSSION

From the previous examples, it appears that the best theoretical description is the iterated PO-MOM. This theory takes into account such problems as coupling effects and the existence of surface travelling waves without added complexity to the theory. Care should be taken, however, to ensure that the PO-MOM currents are placed close together at surface discontinuities where current variation is large and rapid.

In a situation where an aperture in the reflector is reasonably large, i.e. of the order of half a wavelength wide, and is close to the rear axis, the radiation field of the reflector may be described to a reasonable accuracy by either GTD, PO-MOM or MOM theories. The MOM theory produces large spurious currents on the rear of the reflector, and when the slit in the reflector is small, or well off axis, the formulation becomes suspect.

GTD field descriptions are inaccurate when the slit is well off the rear axis, and problems associated with the assumption of tangent planes

at curved edges return for off axis slits.

A problem encountered throughout this chapter has been the difficulty in following of phase shifts at nulls. Where many nulls occur it is a matter of guesswork as to which way the phase changes at a null. Inspection of the phase pattern in the rear direction for an unperturbed parabolic reflector reveals a continuously changing phase at a reasonably rapid rate. If it can be assumed that a slit field pattern may be superimposed upon the reflector field pattern as a first approximation, it is clear that a deep null over a very small angle can be produced. This is shown by example b) in the previous section, where the slit field cancels the rear field in the straight through direction. In this case coupling had to be taken into effect.

Such a null, where the reflector phase varies rapidly will vary in position if the reflector is subject to stress or movement in the wind, hence the antenna must be protected and supported if the null direction is to be maintained.

CHAPTER 5: HOMODYNE EXPERIMENTS

Experientia docet - Experience teaches

Latin Proverb

5.1 MATHEMATICAL DESCRIPTION

Homodyne detection is a form of coherent detection. Coherent detection occurs in the situation where a modulated carrier signal is mixed with a coherently related unmodulated carrier in a non-linear device. In the case of Homodyne Detection, the unmodulated signal carrier frequency is exactly the same frequency as that of the modulated carrier signal.

Homodyne Detection can be thought of as a subset of Heterodyne Detection. (Taub and Schilling, 1971).

Assuming double sideband with carrier amplitude modulation, a modulated carrier signal can be described as:

$$E_1(t) = b\left[k_o+m(t)\right] \cos \omega_{ct}, \tag{5.1}$$

where,

$E_1(t)$ - is an amplitude modulated signal,

b - is the carrier amplitude,

k_o - is a constant, depending upon the amount of suppression of the carrier during modulation,

m(t) - is the modulating signal,

ω_c - is the carrier frequency.

Allow this signal to be mixed in a non-linear device with another signal described by,

$$E_2(t) = A \cos(\omega_{ct}+\phi_u) \tag{5.2}$$

where,

$E_2(t)$ - is the unmodulated carrier signal,

A - is the amplitude of the carrier,

ϕ_u - is the unknown phase difference between the modulated and unmodulated signals.

For the purposes of this derivation we shall assume that the non-linear device has a square law response making the detection process easier to describe. It is possible to model a detector response in the form of a Taylor Power Series, but no advantage would be gained by this procedure as usually the quadratic term of the series would have the greatest effect upon the mixing. Thus, for square law mixing, we find:

$$E^2_{sum}(t) = b^2\left[k_o+m(t)\right]^2\cos^2\omega_{ct} + 2Ab\left[k_o+m(t)\right]\cos\omega_{ct}\cdot \cos(\omega_{ct}+\phi_u) + A^2\cos^2(\omega_{ct}+\phi_u). \quad (5.3)$$

If (5.3) is narrow-band filtered to pass frequency components at the modulation frequency only, then:

$$e_{out} = k_o b^2 m(t) + Abm(t)\cos\phi_u, \quad (5.4)$$

which can be manipulated in two ways to exhibit various properties, i.e.,

$$e'_{out} = K_{sq} \cdot m(t).b^2\left[k_o + {}^{A}/_{b}.\cos\phi_u\right] \quad (5.4a)$$

$$= K_{sq} \cdot m(t).Ab\left[{}^{b}/_{A}\,k_o + \cos\phi_u\right] \quad (5.4b)$$

where K_{sq} is a conversion constant of the square law mixer.

For simplicity m(t) can be considered to be a sinusoidal signal, i.e.,

$$m(t) = \cos\omega_{mt},$$

where ω_m is the modulation frequency.

In the case of Heterodyne Detection of Double Sideband with Carrier (DSWC) modulation the filtered output e_{out} in Equation (5.4) should be made as independent as possible of cos ϕ_u. If e_{out} is arranged as in Equation (5.4a), it becomes clear that, b, the modulated carrier signal amplitude, should be made as large as possible to produce this requirement.

Conversely, in Homodyne Detection of DSWC, the phase relationship between the two signals is known, and may be used to advantage. Thus, if e_{out} is conceived of in the form of Equation (5.4b), obviously A, the unmodulated carrier signal amplitude, should be as large as possible to amplify the effects of cosϕu.

Homodyne detection can be incorporated into measurement systems to estimate phase and amplitude changes of the modulated carrier signal (5.1).

Figure 5.1 is a plot of e_{out} vsϕ_u taken from Equation (5.4b), under the conditions b/A = 0.2. (King 1978). Note $R_o = 1$.

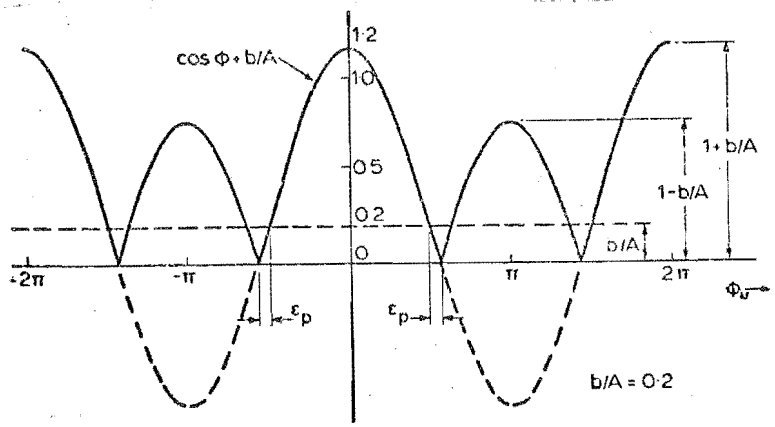

Figure 5.1 Square Law Detector Output, with respect to Phase.

It is assumed that the amplitude A of the unmodulated carrier is well controlled and that ϕ_u, the phase of the mixing signal, can be maintained at any value by changing the phase of the unmodulated signal.

If the phase of the carrier of the unmodulated signal can be adjusted, then the detector output at ω_m can be varied between maxima and nulls. The sizes of the maxima are in a direct relationship with the amplitude of the modulated carrier signal, while the variation in phase of the unmodulated carrier that is required to produce a minimum is a direct measure in the change in the phase of the modulated carrier. (Dyson, 1966).

The peaks in Figure 5.1 are alternately $Ab[1+b/A]$ and $Ab[1-b/A]$ * high, and the minima vary from an integer times $\pi/2$ by an error angle, Ep, given by,

$$Ep = \sin^{-1}\left(\frac{k_o b}{A}\right),$$

hence it is important to have A as large as possible.

The Homodyne Principle is theoretically applicable at any and all carrier and modulation frequencies, provided of course that they are different. Practical filtering considerations limit the spectral spacing of carrier and modulation frequencies, while noise levels limit the lower values of modulated signal amplitude. Maximum heat dissipation characteristics of the detector will impose restrictions on the maximum power level of the unmodulated carrier signal.

5.2 MICROWAVE HOMODYNE DETECTION

Homodyne Detection can be used in a microwave system, subject to the practical limitations alluded to in the previous section. For a microwave point contact diode, the 1N23E, operating in the square law region (King 1978, Jaggard and King 1973), where A=-15dBm, measured

---

* If the suppression constant, k_o is assumed to be unity.

relative to one milliwatt, a 10kHz modulated signal in the region of b=-130dBm can be detected. From Equation (5.4b), it can be calculated that an amplitude measurement error of 3.5% will occur if the ratio of amplitudes b/A is limited to a maximum of -30dB.

Under the same conditions a phase measurement error of about 2 degrees will be found, and an amplitude dynamic range of 85dB will be attainable, for the above values of b,A and b/A.

The detector that was used in the experiments was a point contact 1N23B diode. This detector diode has similar properties to the 1N23E, except that when used as a standard mixer it has a larger noise figure and a higher conversion loss (Microwave Associates Inc. catalogue, SF-4001). These differences are reproduced in Table 5.1, but it should be noted that the properties listed for each diode are only the average values, and that any particular diode may have a better or worse performance.

Diode	Conversion Loss (dB)	Noise Figure (dB)	I.F. Impedance (Ohms)
IN23E	6.0	7.5	335-465
IN23B	6.5	11.4	300-600

Table 5.1 Comparison of Point Contact Diode Properties.

(Noise Figure is defined as,

$$N.F. = \left(\frac{\text{Signal}}{\text{Noise}}\right)\text{input} \Big/ \left(\frac{\text{Signal}}{\text{Noise}}\right)\text{output}$$

therefore a lower noise figure is preferable.)

Figure 5.2a is a drawing of a basic two-channel microwave Homodyne system, (King 1978).

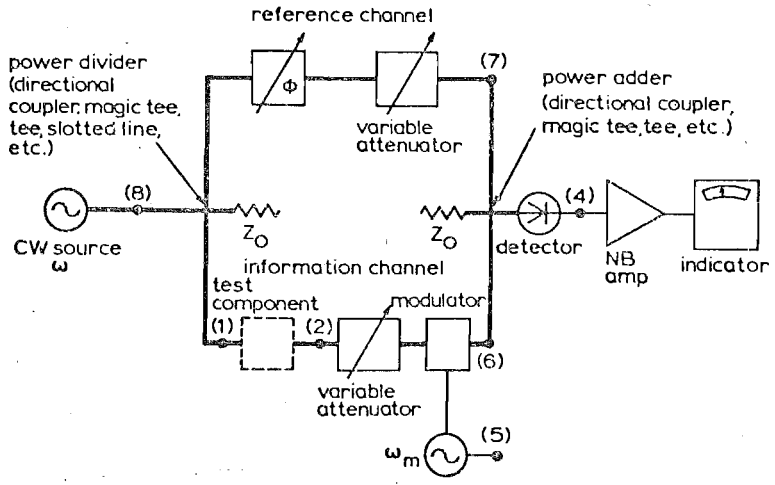

Figure 5.2a Two Channel Microwave Homodyne Circuit, (King 1978, P. 5).

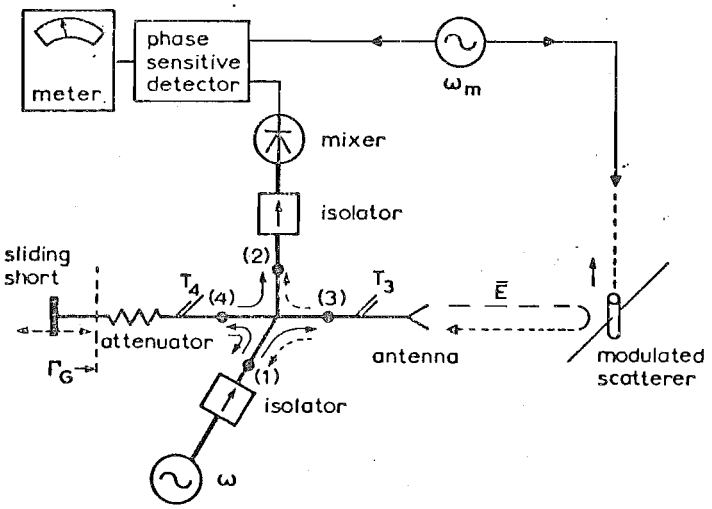

Figure 5.2b Pseudo-Double Channel Microwave Homodyne Circuit, (King 1978, P. 139).

Briefly, in the system of Figure 5.2a a microwave CW signal is split into two channels, one of which is modulated. Each channel undergoes phase and amplitude changes, and are then summed. The summed signal is detected by a point contact diode.

One channel is a fixed reference channel which serves to transmit the unmodulated carrier at a constant attenuation and known relative phase change to be injected into the mixer. The other channel, called the information channel, causes unspecified changes to the signal prior to being modulated. It is vital to ensure that the modulated signal is smaller than the unmodulated signal if the system is to be accurate when the detector is operating in the square law region.

The circuit in Figure 5.2b utilises a four port Magic-T device which has the property of splitting signal from arm 1 into arms 2 and 3 and combining signals from arms 2 and 3 into arm 4. The attenuator and short circuit on arm 2 corresponds to the reference channel in Figure 5.1a, and the 'monostatic' circuit attached to arm 3 is the information channel. This 'Pseudo-Double' Channel system has the same principle of operation as the Double Channel system.

If greater unmodulated signal power can be delivered to the detector, the point contact diode response will become linear, (Jaggard and King, 1973), as shown in Figure 5.3.

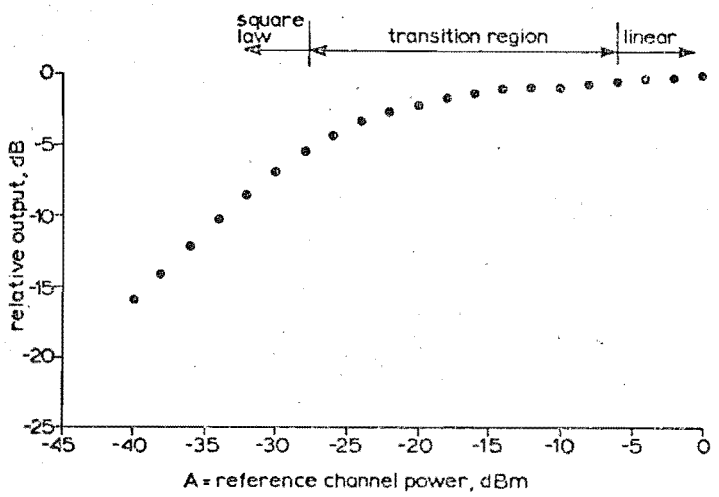

$f = 4{\cdot}8894$ GHz
$f_m = 1$ kHz
$b \cong -70$ dBm
crystal type 1N23E
external bias = 0

Figure 5.3 Point Contact Diode Response.

This affects Equation (5.3). If it is assumed that b<<A, a condition that can be satisfied for most microwave experiments, then the filtered form of Equation (5.3) becomes, retaining all terms at or near the modulation frequency,

$$e_{sum}^2(t) = \left[k_o^2 + 2m(t)k_o + m(t)^2\right]b^2 + 2Ab\left[k_o + m(t)\right]\cos\phi_u + A^2 \qquad (5.5)$$

The square root of (5.5) may be found by a Binomial expansion. If we assume that b<<A, the terms in b^2 in the expansion may be disregarded, hence

$$e_{sum}(t) = b\left[k_o + m(t)\right]\cos\phi_u + A \qquad (5.6)$$

Filtering this result to retain terms at the modulation frequency only gives,

$$e_{out} = k_{lin} \cdot b \cdot m(t) \cdot \cos\phi_u \qquad (5.7)$$

where k_{lin} is the linear mixer conversion gain constant.

This result shows that for a reference channel power that forces the detector into the linear region, the output of the detector becomes independent of A. This is an important result. It means that in the case of amplitude measurements the restriction b/A<-30dB does not have to be adhered to. The amplitude range of the linear law detector now is between the maximum sensitivity and the level of the unmodulated carrier signal, which is typically 0dBm. The increase in A does increase the detector noise level, hence the maximum sensitivity is lowered, typically to -105dBm for a 1N23E diode (King 1978).

The minimum detectable signal is that defined to be 3dB above the noise level, but in the case of phase measurement, where a null is required, a further 20dB of signal is required to ensure that a maximum phase error of five degrees occurs for low level modulated signals.

If a more accurate analysis of the square root of (5.5) by Binomial expansion is carried out, taking terms of order b^2, the output becomes dependent upon,

$$e_{out} = k_{lin}\, b\, m(t) \left[\cos \phi_u + \frac{k_o b}{A} \sin^2 \phi_u\right] \qquad (5.8)$$

From (5.8), when the phase angle ϕ_u=90 degrees it can be seen that the restriction $k_o b/A$<-30dB must be retained to ensure phase measurement accuracy. This 30dB loss for large signals and the 20dB loss for small signals takes a large chunk out of the dynamic range of the system if phase is to be measured. The constant k_o is dependent upon the amount of suppression of the carrier in the modulated signal. For 100% suppression the b/A restriction is unnecessary, increasing the phase dynamic range for large signals by 30dB.

In practical experiments, using the 1N23B diode, it was found that a maximum amplitude dynamic range of 90dB was attained using suppressed carrier amplitude modulation and with the unmodulated signal power set at -7dBm. The corresponding phase dynamic range was 70dB, which was considered acceptable for experimental work.

5.3 PRACTICAL HOMODYNE SYSTEM

Figure 5.2a shows a basic two channel system. The circuits used in this batch of experiments were based on this design, with local variations as required. For initial testing, a Homodyne System pictured in Figure 5.4 was used. Microwave power is produced by a Marconi Sanders wideband klystron source, which can produce about 10mW into a 50 ohm load at 9.2GHz. The signal is isolated from the system by a Ferrite Isolator, and the klystron frequency is accurately measured by a high Q cylindrical cavity Wavemeter.

Beyond the Wavemeter lies a 3dB power splitter, which diverts half the power into a reference channel and the rest into the information channel.

Looking first at the reference channel, which produces the signal in Equation (5.2) at the detector, there is a Calibrated Variable Attenuator, and a variable Phase Shifter which is used to follow nulls introduced by the information channel.

The information channel signal is first attenuated by a factor of 10dB, and is then isolated by a Circulator and a Matched Load. A Variable Attenuator is next, used to cut out leakage from the circuit while the information channel is undergoing changes. During calibration tests, the information channel had various obstructions placed between the Variable Attenuator and a fixed 20dB Attenuator. The nature of these obstructions will be explained later.

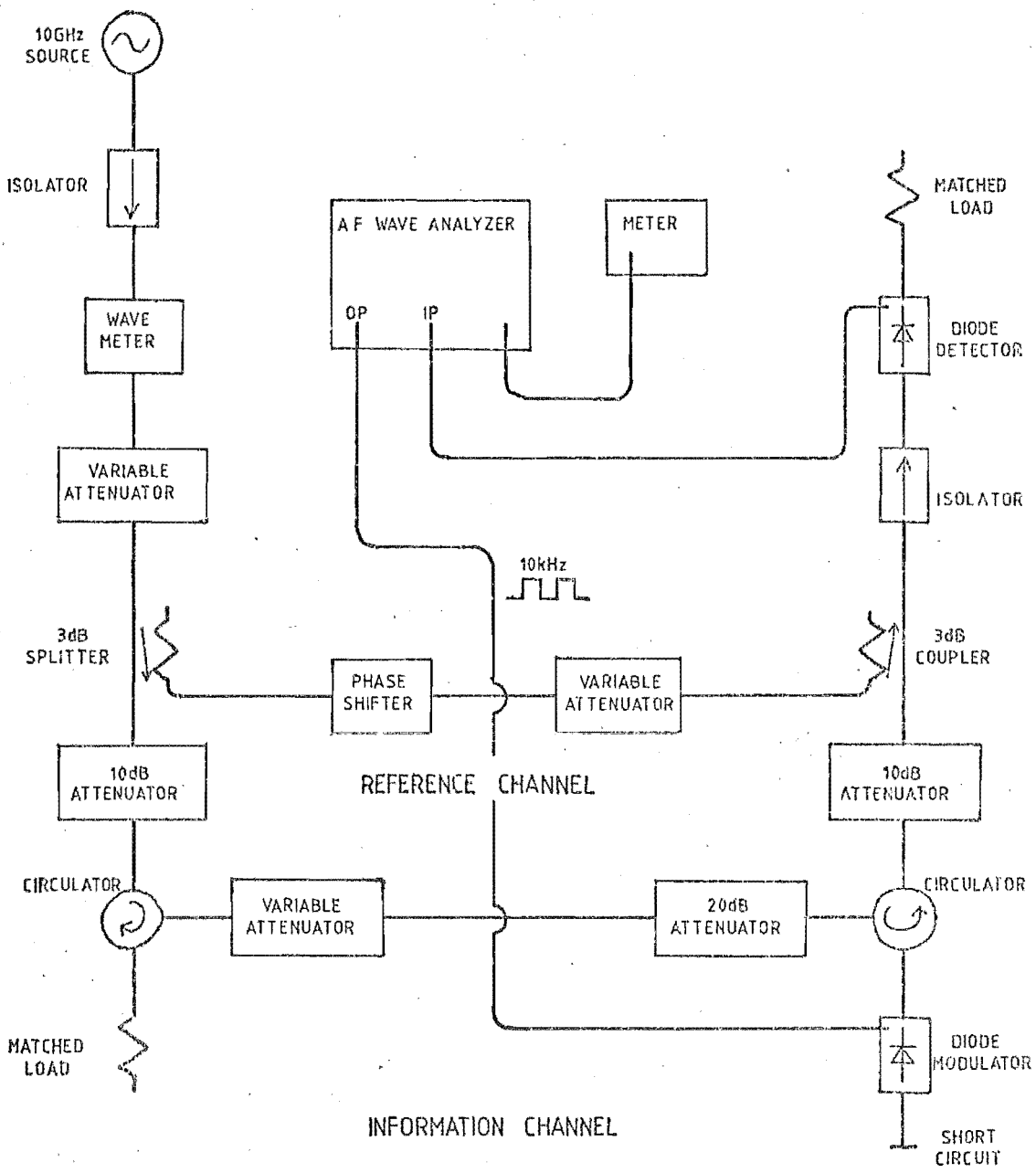

Figure 5.4 Initial Homodyne System.

Beyond the fixed attenuator lies the Diode Modulator. The circulator sends the unmodulated information signal into a tuned Thermistor Mount, which in this case holds a point contact diode. The diode is placed about a quarter of a guide wavelength (λg) in front of the short circuit of the Thermistor Mount. A large amplitude A.F. square wave signal is applied to the diode. When the diode is biased on by the signal, it forms a short circuit across the guide at that point, and when the diode is biased off the diode essentially open circuits, letting signal reflect at the thermistor mount short circuit. The on-off modulation of the diode shifts the reflection point up and down the guide by $\lambda g/4$, changing the phase of the carrier by 180 degrees at the A.F. input frequency. This is equivalent to having a 100% modulation index, causing suppression of the carrier. In this case k_o tends to zero in Equation (5.1) effectively reducing the unwanted term in Equations (5.4b) and (5.8).

The modulator feeds a 10dB Fixed Attenuator. The attenuators either side of the modulator act as buffers to ensure that little modulated signal travels an incorrect path anticlockwise around the information channel.

The two channels are recombined at a 3dB power summer, and the resultant signal is passed through a Ferrite Isolator into a Matched Detector Mount containing a 1N23B point contact diode.

The A.F. side of the system also involves coherent detection. A 10kHz signal is output from a Marconi A.F. Wave Analyser which is fed into a Hewlett Packard phase locked loop. The loop outputs a large amplitude square wave at the same frequency which is fed into the diode modulator in the information channel of the Homodyne Circuit. The detected signal is fed back into the A.F. wave analyser where the A.F. signal power is fed out on a meter. The analyzer has a bandwidth

of 7Hz, hence the detected signal can be assumed to be very narrow band filtered. A dynamic range of 90dB is available on the analyzer at the operating point of the detector, but only 70dB of the range was ever used due to the minimum allowed signal strengths for phase measurement as defined in Section 5.2

An alternative system that was studied was the monostatic arrangement shown in Figure 5.2b, (King 1978). The 4 port Hybrid-T has to be unbalanced to allow transfer of the reference signal via the circuitry on port 4 to the detector circuit on port 2. The variation of short circuit position on the Variable Short Circuit is equivalent to the effects of the phase shifter in the reference channel in a bistatic system. The presence of the short circuit served to produce unwanted signals in other parts of the circuit and to cause a bias in the actual Hybrid junction which was dependent upon the short circuit position. To be able to set up the circuit properly required tuning by the placement of posts in the junction of the Hybrid-T, which was beyond the resources of the department, (Pound 1948).

External tuning to the circuit produced only marginal improvement in performance, while any small change in the klystron frequency would negate the effects of the previous tuning.

The difficulty of tuning the system lead to the abandonment of the circuit. It should be noted that the amplitude dynamic range would be degraded in a monostatic system, especially if an A.F. modulated scatterer is used in free space. The scatterer used was an 1N833 Microwave Diode cut to a half wavelength and fed via high resistance ptfe strands from a large signal A.F. oscillator. The scatterer had the advantage of minimally affecting the measured field, but also had a very low return due to its small modulation index, (King 1978).

The bistatic system underwent calibration tests. The calibrated variable Attenuator was changed between 0 and 40dB with and without a further 30dB of attenuation in the information channel. This save an attenuation range of 70dB. Upon correct tuning of the klystron source the Homodyne system was able to measure the attenuation to within plus or minus 0.5dB over a dynamic range of 60dB, and within plus or minus 1dB from 60 dB to 70 dB attenuation. It was interesting to note that the attenuators caused phase shifts as well as the attenuations, which had to be compensated for by changing the phase in the reference channel.

A phase shifter was placed in the information channel, along with 0dB and 60dB of attenuation. The phase shifter in the reference channel was used to track phase shifts in the information channel. At 0dB attenuation the phase shifters tracked each other accurately. At 60dB attenuation the phase shifters showed a maximum of plus or minus 4 degrees variation from each other. This was considered to be acceptable.

As a further test the system was used to measure phase shifts through various widths of dielectric placed inside the guide. From these measured phase shifts it was possible to calculate the dielectric constants of the pieces of material (Montgomery 1947). Table 5.2 shows the results of this experiment.

Specimen	Width	Measured Phase Change	Calculated Dielectric Constant	Identification
a	3.01mm	31°	3.26	?
b	6.24mm	51°	2.61	Perspex
c	12.42mm	102°	2.62	Perspex

Table 5.2 Results of Dielectric Constant Measurement Experiment.

Von Hippel, (Von Hippel, 1954), has published a refraction index of 2.59 for perspex. These measurements proved the performance of the system, and it was now ready for adaption to experiments.

5.4 SLIT TRANSMISSION EXPERIMENT

The aim of the first experiment was to measure the fields transmitted by slits with inclined planes, as described in Chapter 3. Originally an open area experiment was performed using two large metal sheets as slit planes, but difficulties were encountered in the placement of the sheets due to their size. The range was extremely susceptible to vibration and air movement, making measurements unrepeatable.

It was concluded that a closed range was the only alternative that would be more vibration free, and as an anechoic chamber was unavailable, a parallel plate range was used. Figure 5.5 is some photographs of the range and circuitry associated with it.

A parallel plate waveguide consists of two reflecting surfaces placed parallel to each other within half a free space wavelength. Any wave launched into the system is forced to travel in the TEM mode, giving the impression of free space, with the E plane perpendicular to the surfaces and the H plane at right angles to the direction of propagation. A mathematical description is given as part of an exposition on the separation of variables technique in Chapter 2.

The major disadvantage of such a system is that only one polarization is available, and can only be used over a small bandwidth, restricting experimentation. The parallel plate system does provide greater stability, good sensitivity and a constant transmission environment at a relatively low cost (Donaldson et al, 1978), (Cumming, 1959).

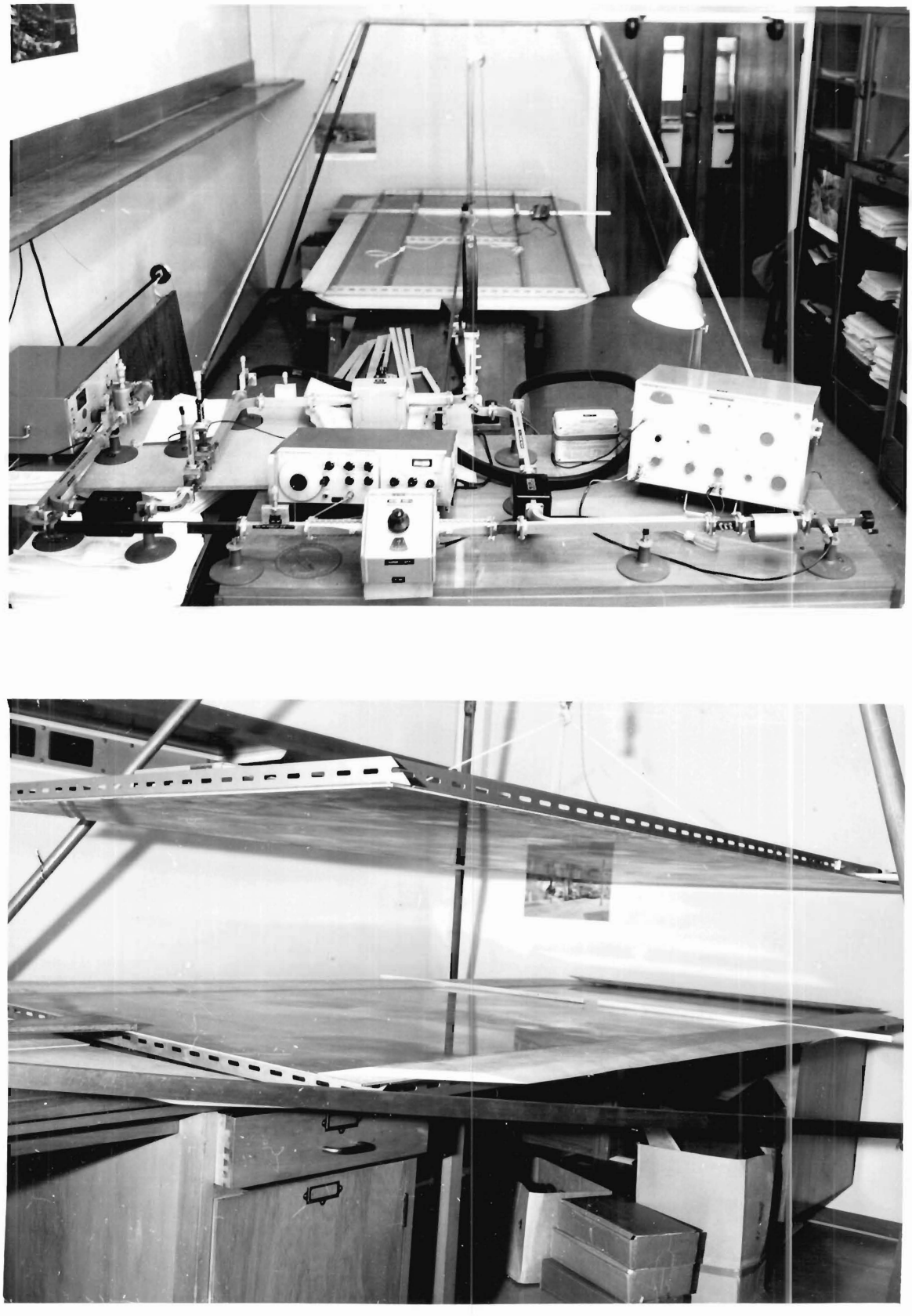

FIGURE 5.5 SLIT TRANSMISSION EXPERIMENT

5.4.1 RANGE DESCRIPTION

The parallel plate guide consists basically of two 2.4m by 1.2m sheets of 8swg hard wrought aluminium alloy (BS1470 type NS5) as seen in Figure 5.5 and 5.6a. The sheets are spaced 12.0mm' apart by Jelutong timber wedges, shaped as in Figure 5.6b. These wedges had a VSWR of 1.04 when measured in a rectangular guide with the TE01 mode at 10GHz.

The source into the parallel plate region was an H-Plane sectoral horn placed at one end of the medium and a probe was placed on a slide in the top plane as shown in Figure 5.6c. The slide was a milled aluminium bar with slots $\lambda/4$ away from the gap in the top plane, placing open circuits at these points. This took away the necessity for a perfect electrical connection between the probe bar and the top plane, allowing the probe bar to slide with ease. The probe construction is shown as Figure 5.6d. The probe had to be large enough to be able to provide a reasonable signal for the detector, while remaining small enough to leave the field that is measuring undisturbed, (Dyson 1973). A compromise was reached in the use of a sewing machine needle.

The slit planes had to be positioned accurately within the guide, 30cm in front of the probe, between the probe and the source. The slit planes also needed to have good electrical contact with the top and bottom planes of the range.

The slit planes were made out of aluminium alloy used in printer's lithoplate, bent into a square c shape. The planes were taped in position on the bottom plane of the range and a combination of the spring in the lithoplate and the weight of the top plane gave good electrical contact between the slit conducting

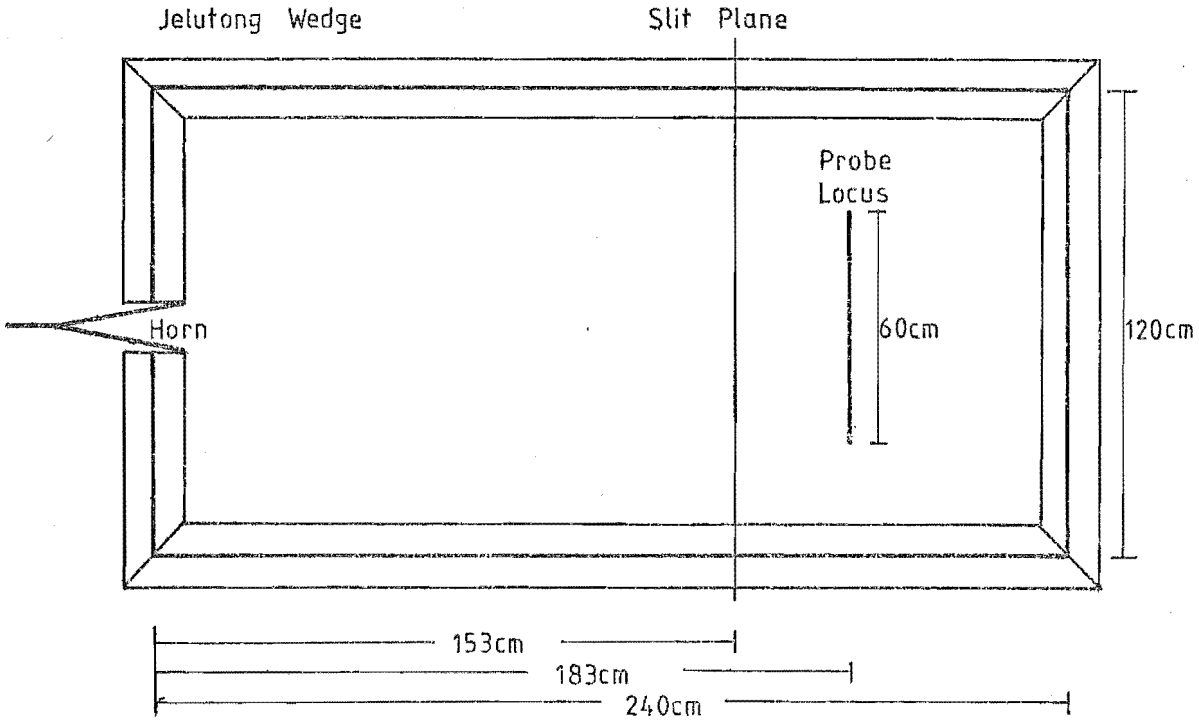

(a) RANGE PLAN

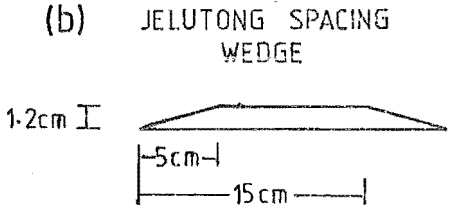

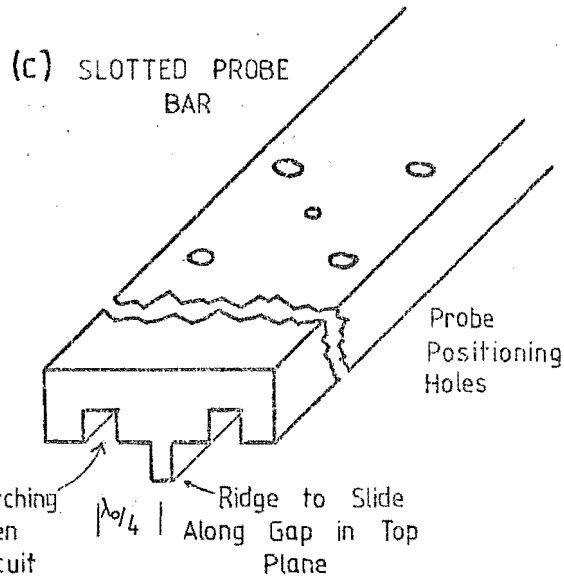

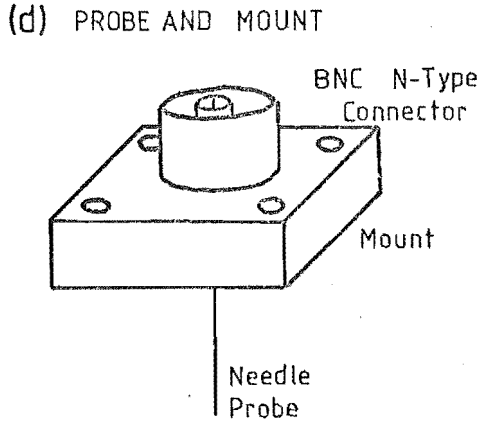

Figure 5.6 Components of Slit Transmission Range.

planes and the range planes. These planes were found to have a leakage of about -60dB. This gave a lower limit of attenuation measurement of -57dB, and a phase measurement dynamic range of 40dB. The leakage figures were taken relative to the maximum intensity of the horn source distribution.

5.4.2 CIRCUIT MODIFICATIONS

Several modifications to the Homodyne Circuit have been made. The most obvious change has been the inclusion of a third, phase checking channel, see Figure 5.7. This channel was normally attenuated out of operation and was only used to check on the frequency drift of the klystron source. Measurements of phase and amplitude of the signal were made at regular intervals. The resultant measured phase drift was converted to a frequency drift, using the known electrical lengths of circuitry and the time between measurements. At its best, the klystron source had a frequency drift of 150kHz/hr but drift could reach 30MHz/hr under draughty conditions. This underlined the need for a constant temperature and draught free environment.

Extra Ferrite Isolators were placed in the circuit at both ends of the information cum phase check channels. This reduced circuit tuning problems and reduced unwanted reflections propagating in the wrong directions. The modulator was shifted to the input of the test channels, in order to reduce reflections at the untuned probe which would retard its effective performance.

The probe was attached to a three meter length of waveguide. The guide was in the circuit for two reasons.

1) To cut out phase change associated with varying path length from the probe to the circuit when the probe is slid along its locus, and

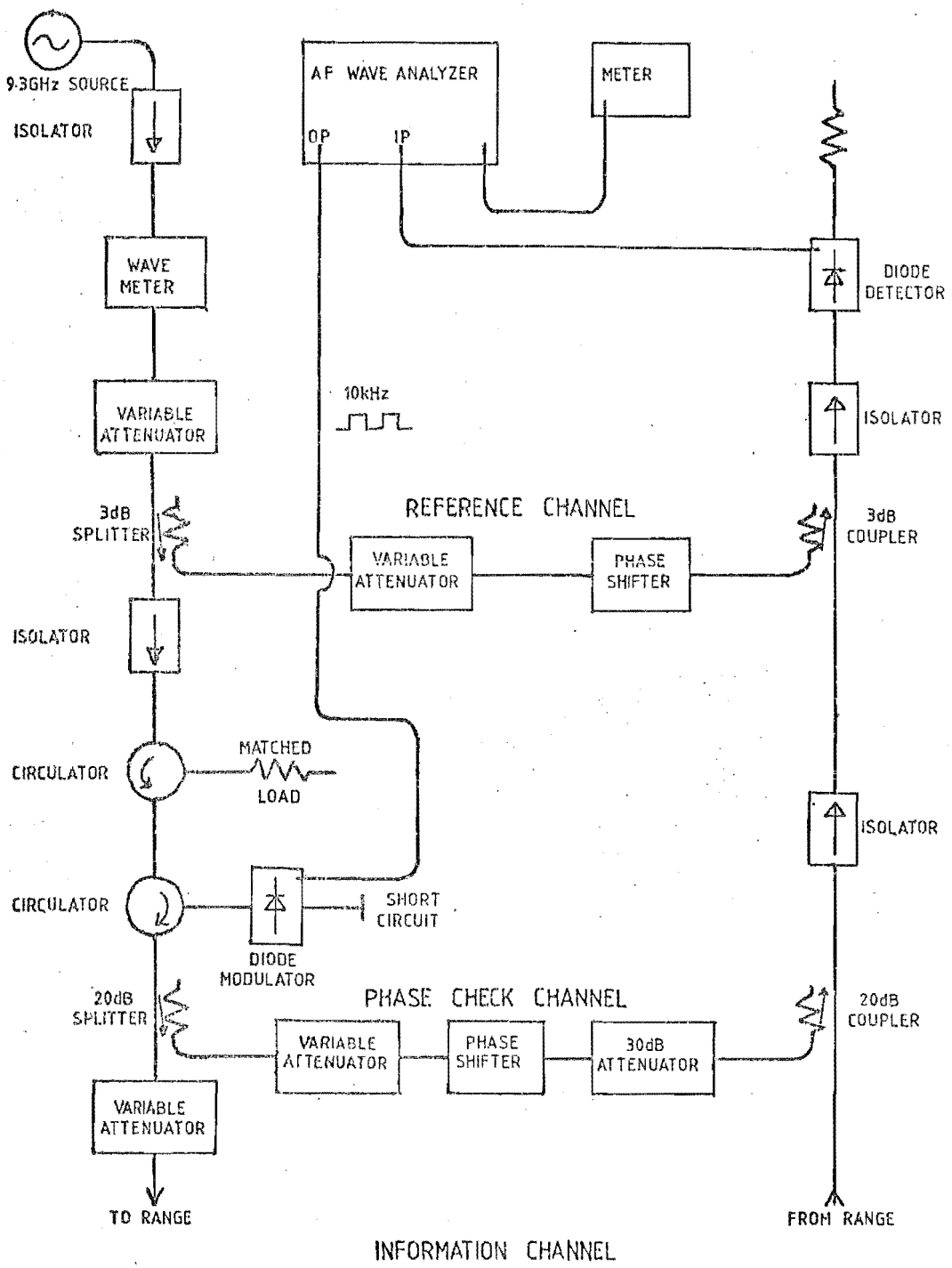

Figure 5.7 Slit Transmission Homodyne System.

2) To ensure that metal is as far away as possible, cutting out spurious reflections into the guide.

5.4.3 RANGE TESTS

The calibration of the range took the form of measurement of the field of the input horn by the probe, the results of which are shown as Figure 5.8a and 5.8b. There are up to 1 dB bumps in the intensity distribution, which were probably caused by a combination of the effects of reflections from the edge of the plates and environmental noise. These measurements were taken during normal working hours and the system was subject to the movements of individuals near the test area. The phase in Figure 5.8b varied 240 degrees between the edges and the centre. For both intensity and phase measurements it is clear that there is a symmetry about the 30cm probe point.

The far field of the horn was calculated (Collin and Zucker, 1969) and these results are portrayed on Figures 5.9a and 5.9b. Agreement between Figures 5.8 and 5.9 is close, proving that the range is accurate.

5.4.4 EXPERIMENTAL PROCEDURE

A child's swing frame supported a pulley to lift the top plane of the range away from the bottom plane, allowing access between the planes for the purpose of shifting the slit planes. Guide pins at each corner of the parallel plane ensured that the top plane was replaced accurately. It should be noted that a 1mm error in the position of the top plane corresponded to a 10 degree change in the measured phase. A modification which could be considered is to turn the range upside down and have the probe on the bottom. Problems could be encountered in positioning the probe.

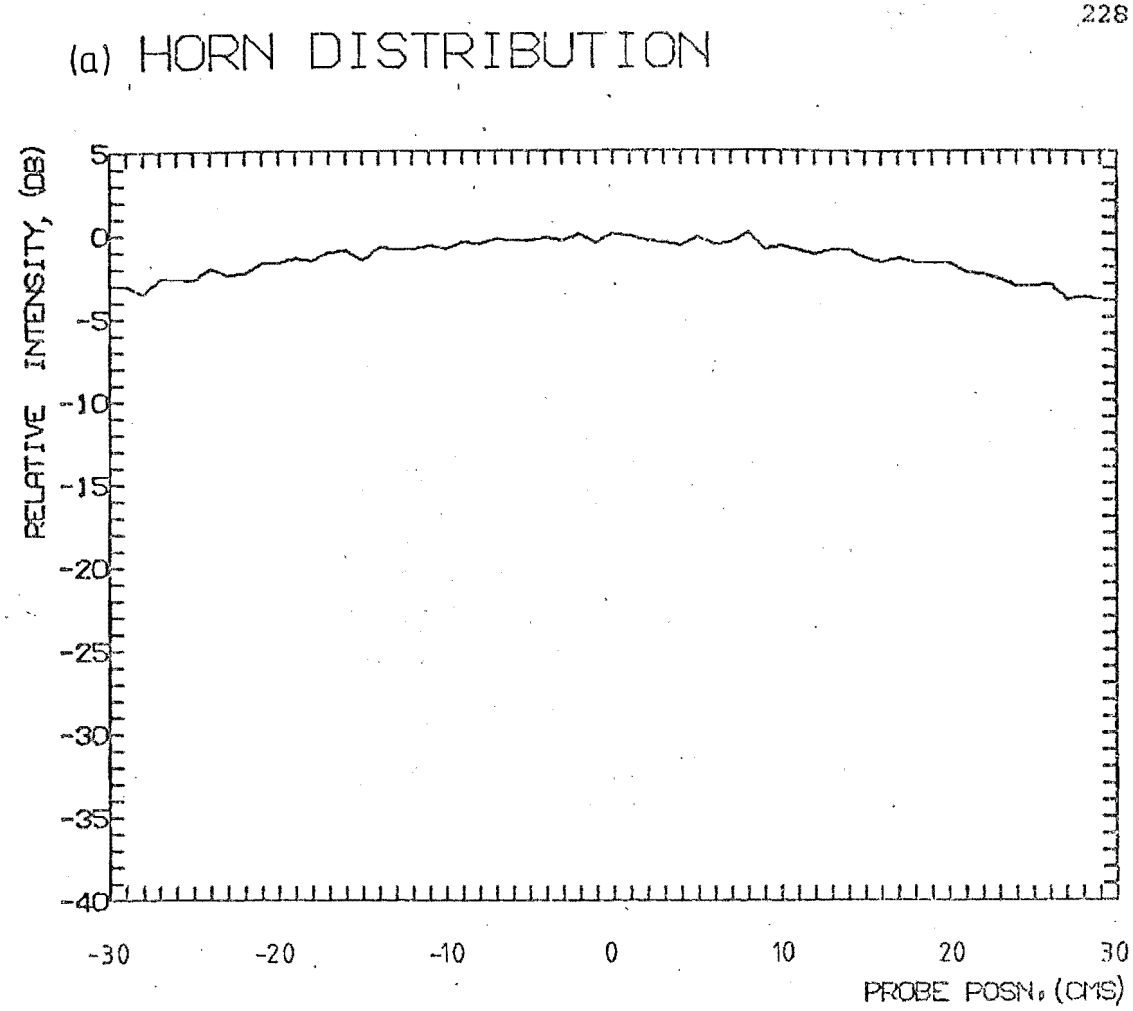

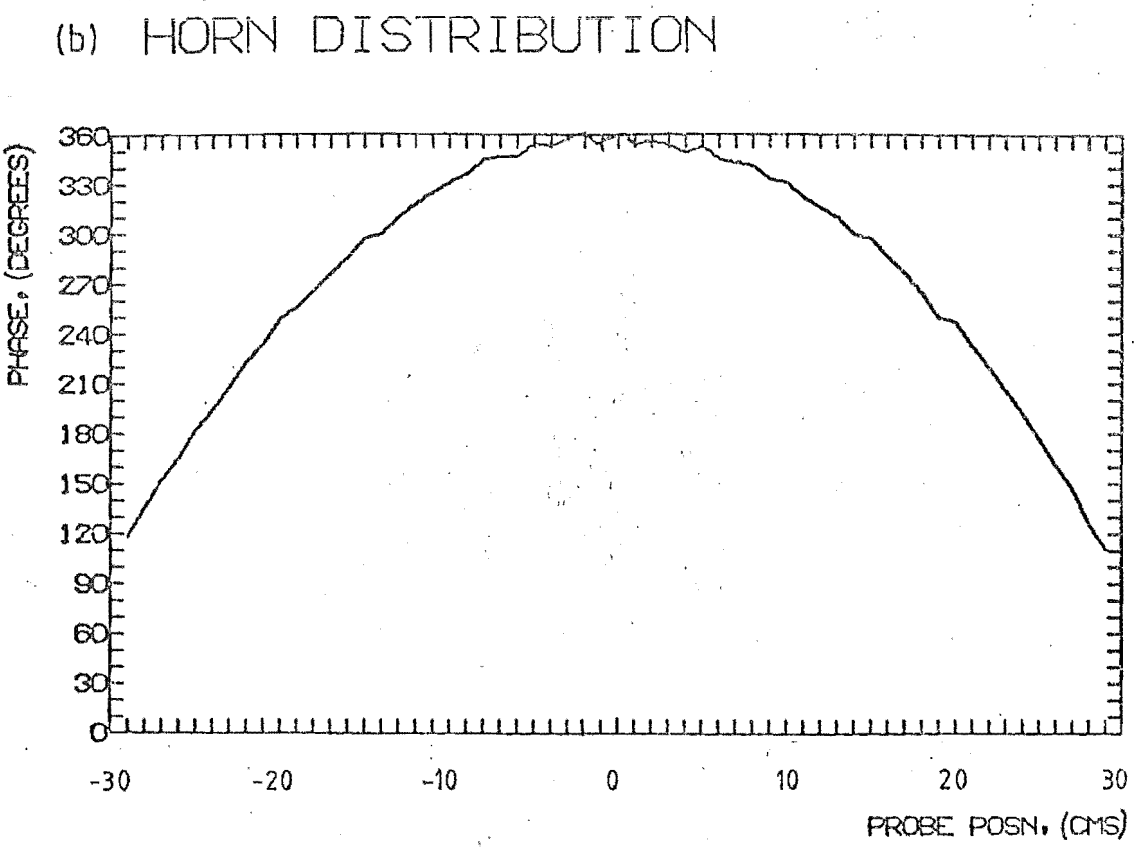

Figure 5.8 Range Calibration Measurement, Horn Distribution.

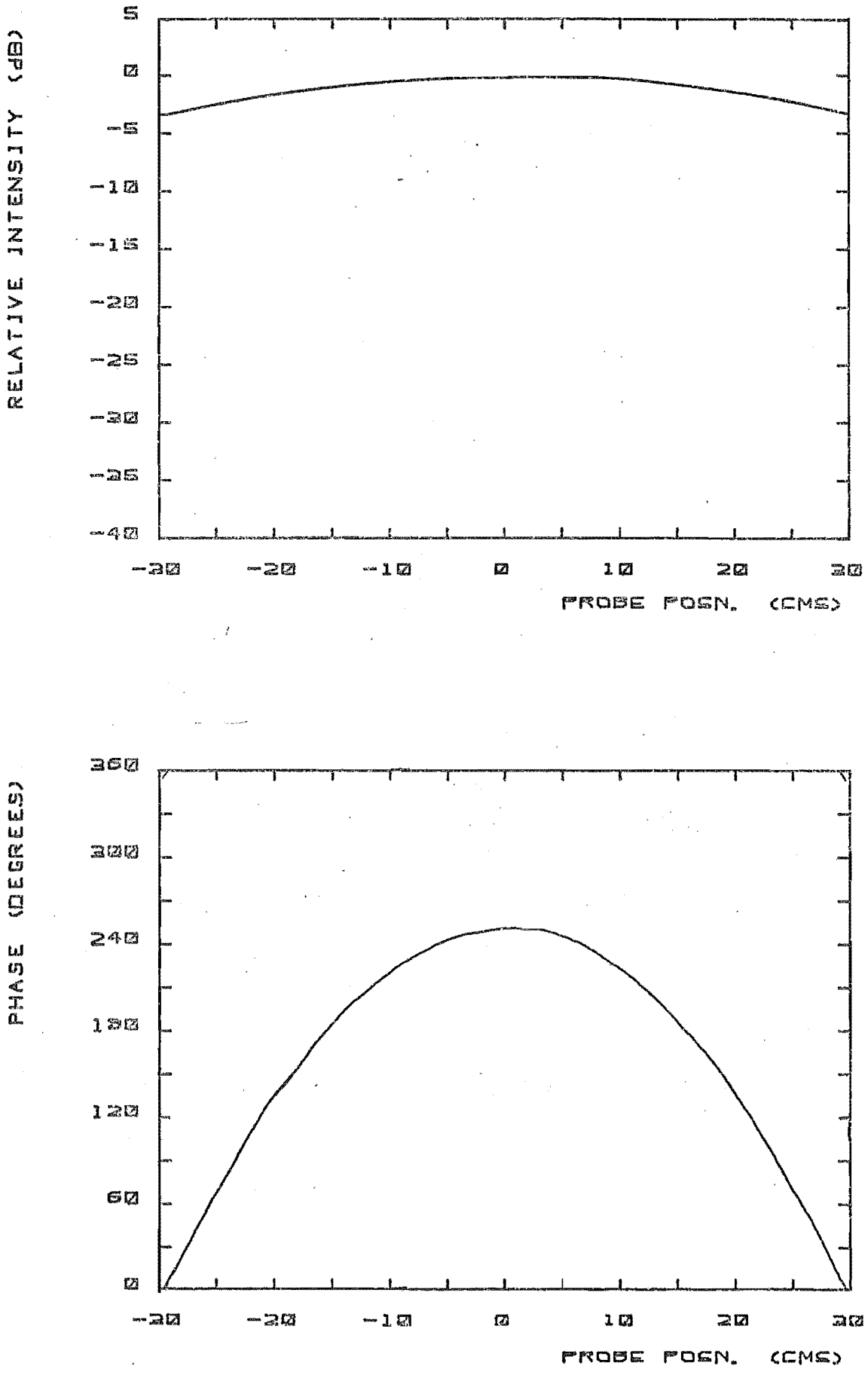

Figure 5.9 Calculated Horn Distribution.

Sixty measurements were taken for each slit tested, each measurement being one centimetre apart along the probe locus. Between each slit measurement run a calibration of the unperturbed field was made to check probe performance. Slit gaps tested were 5, 10, 15, 25, 35, 50 and 65 mm, for 5, 10 and 20 degree concave slit, convex slit and zig slit. The parallel plane slit was tested for the same widths. Each slit was tested twice.

5.4.5 EXPERIMENTAL DATA

Experiment data from each probe position was written directly on to computer coding forms, along with the calibration data. This data was punched on to cards.

The experimental data required was plotted by the Calcomp Plotter on a Burroughs installation at the University of Canterbury.

5.5 PARABOLIC REFLECTOR EXPERIMENT

5.5.1 RANGE DESCRIPTION

The second experiment was to measure the far field radiation and phase patterns of various parabolic cylinder reflector antennas. The antenna range, shown in Figure 5.10 was similar to one used by James (1973) and Smith (1974), but has been dormant for a number of years. Results, especially those of James have been published and accepted by workers, thus it is reasonable to assume that the range can and does satisfy accuracy criteria. They would be,

a) the range antennas must be spaced apart sufficiently to ensure that measurements are made of the far field, and

b) the range must be free of obstructions and nearby reflections.

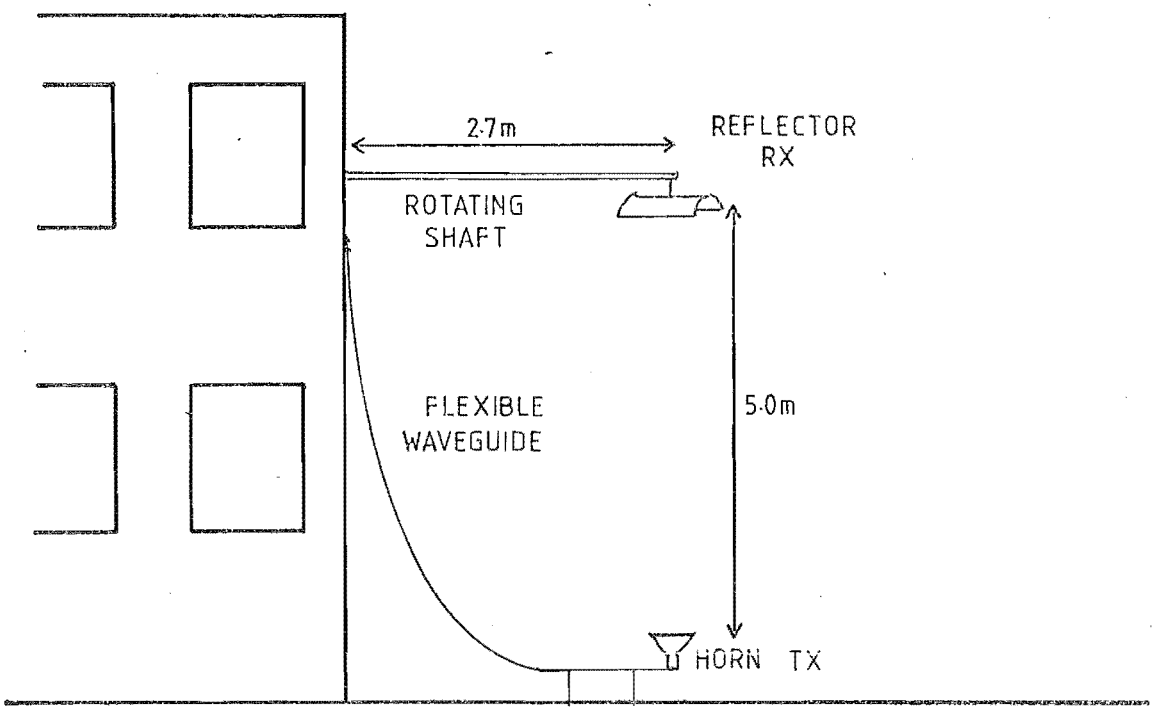

Figure 5.10 Parabolic Reflector Range.

The far field criterion states that for two antennas of apertures d_1 and d_2, they should be spaced a minimum distance S, where (Montgomery, 1947),

$$S = \frac{K(d_1+d_2)^2}{\lambda} \qquad (5.9)$$

Normally K should equal 2, but in the case of experimentation, where a range may be limited in size, values of K in the region of unity are acceptable. For the range in question, S = 5.0m, hence from Equation (5.9) K is approximately 1.1.

The effects of obstructions and reflecting objects are the most difficult problems to deal with. The range had to be positioned from a new window due to the growth of nearby trees in the years since the first prototype range was set up. The building, which the range was parallel to, was the nearest reflecting object, 3m from the centre line of the range. It can be assumed that very little reflection comes from the ground and the support underneath the transmitting horn as the horn leaks very little power out in the reverse direction, and any of that power will be reflected in many directions.

The minimum distance that the antennas can be spaced away from the wall is normally governed by the relation,

$$h = \frac{K(d_2+d_1)^2}{2d_1} \qquad (5.10)$$

Where h is the distance away from the wall and d_1 is the aperture size of the smaller antenna. The relation Equation (5.10) originates in the assumption that the aperture distribution of the source is planar and consequently the first null of the far field occurs at $\sigma = \lambda/d_1$ radians. For a small pyramidal horn, 2.5 wavelengths square, the aperture distribution assumption is patently incorrect. The aperture distribution is cosinusiodal as discussed in Chapter 3, hence instead of finding that h = 1.02m, if $d_2=10\lambda$, $d_1=2.5\lambda$, and K=1.1, it is necessary to move the range as far away from the building as possible to make its effects negligable. It was found that h needed to be greater than 2.7m, before intensity measurements were repeatable over the range of 50dB.

The transmit horn was a 2.5λ x 2.5λ pyramidal horn, connected by flexible waveguide from the input of the information channel of a Homodyne System. The horn, with a standard free

space gain of 17.2dB, was placed 5.0m below the receive parabolic reflector antenna, and was supported by waveguide support brackets as shown in Figure 5.11a.

The receive antenna, Figure 5.11b, was a parabolic cylinder of focal length 7.5cm (2.5λ), with an F/d ratio of 0.25. Its length was 30cm (10λ), ensuring that the H plane effects from interactions of the curved ends were negligable (Ross 1966). The reflector was kept in its shape by two accurately machined brass jigs. The reflector construction is in Figure 5.12a. The feed support is made of perspex, and is placed such as to eliminate unwanted reflections in the rear direction of the reflector. The feed is a thin half wavelength dipole with a quarter wavelength split skirt balun (Dyson 1973) as pictured in Figure 5.12b.

The receive antenna was attached to a boom, 3m in length which was constructed of Tufnol. Inside the boom was a length of WG16 copper waveguide. The antenna was attached to a 25mm diameter Tufnol rotating section which was held by four bushes. The rotating section was geared to allow motor drive, but as the Homodyne System was not automated, the shaft was turned manually. A protractor at the end of the shaft enabled angular positioning of the parabolic antenna.

The boom was extended through an upstairs window, and clamped just inside the building. To increase stability, guy ropes were placed around the boom near the antenna which were secured tightly inside the building. This ensured that the receive antenna aperture plane was perpendicular to the building.

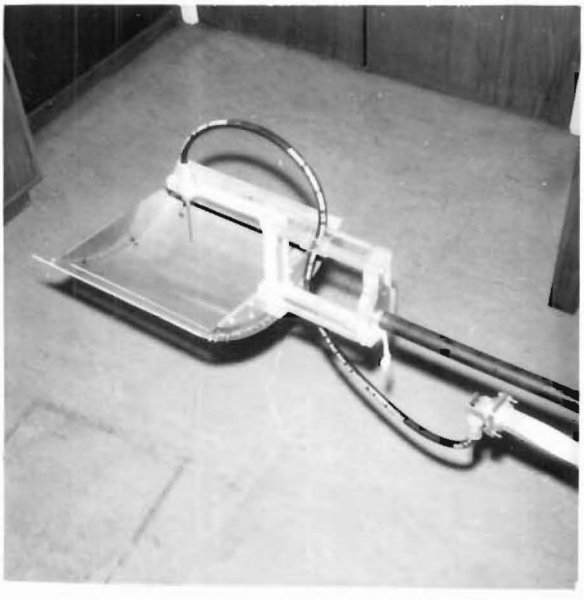

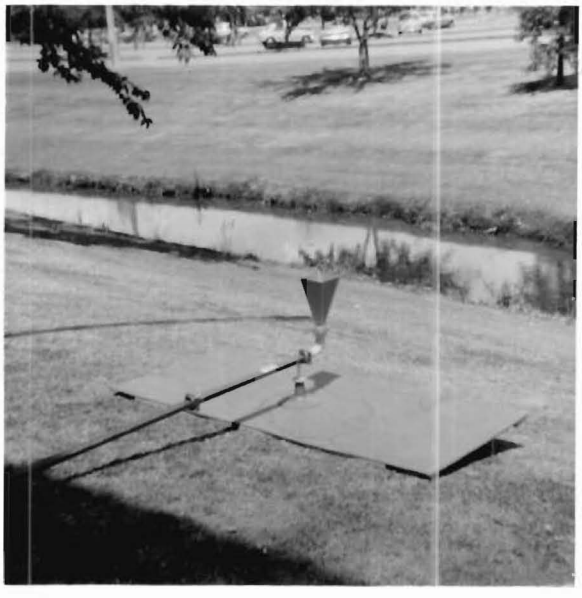

FIGURE 5.11 PARABOLIC REFLECTOR EXPERIMENT

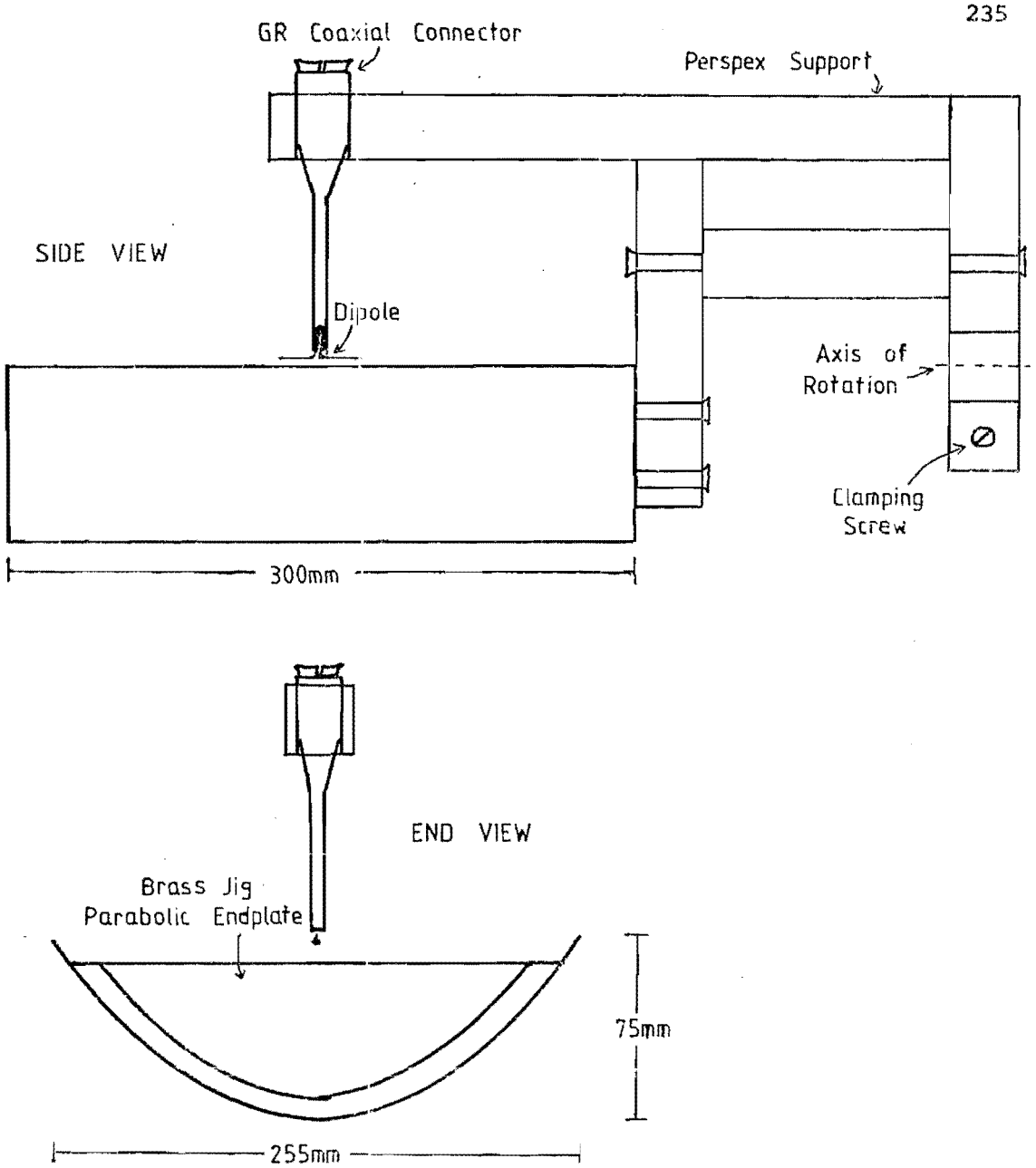

(a) PARABOLIC CYLINDER REFLECTOR ANTENNA

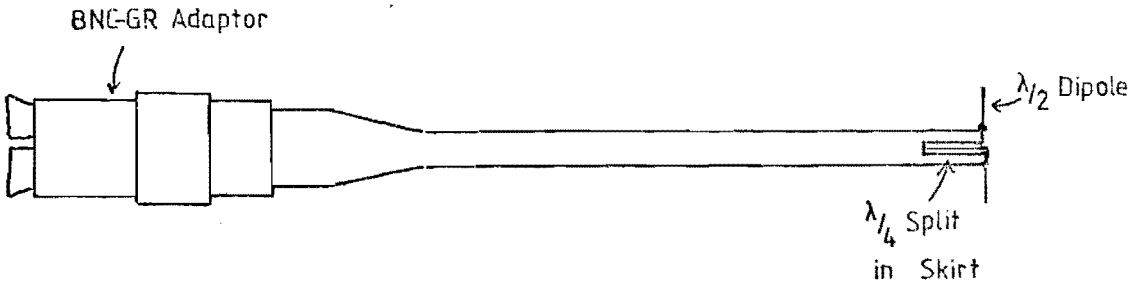

(b) REFLECTOR FEED DIPOLE

Figure 5.12 Reflector Antenna Construction and Support.

5.5.2 CIRCUIT MODIFICATIONS

Because of the larger transmission distance in the range, more power was necessary to give a reasonable information signal. To produce more power a Hewlett Packard wideband microwave amplifier was introduced into the circuit just after the microwave source (Figure 5.13). An isolator was placed between the source and the amplifier to ensure that neither was loaded down by the other. The power output of the amplifier was 1W, hence in order to have linear operation of the detector diode without reverse self bias (King 1978), the reference channel signal power had to be attenuated. This was achieved by replacing the 3dB power splitter and 3dB power adder by a 10dB version of each at the ends of the separate channels. This had the added benefit of directing a greater percentage of the available power into the range.

The modulator was placed at the end of the information channel where it would do the least amount of harm caused by reflections in the circulator. Padding was provided by the 10dB power adder to reduce the effects of unwanted signals.

The power amplifier was found to have too great a noise figure at rated power, due mainly to the age and the poor condition of the Travelling Wave Tube in the amplifier. The power output of the amplifier was set at 100mW, where a more reasonable noise figure was obtained.

An intensity and phase dynamic range of 60dB was obtained.

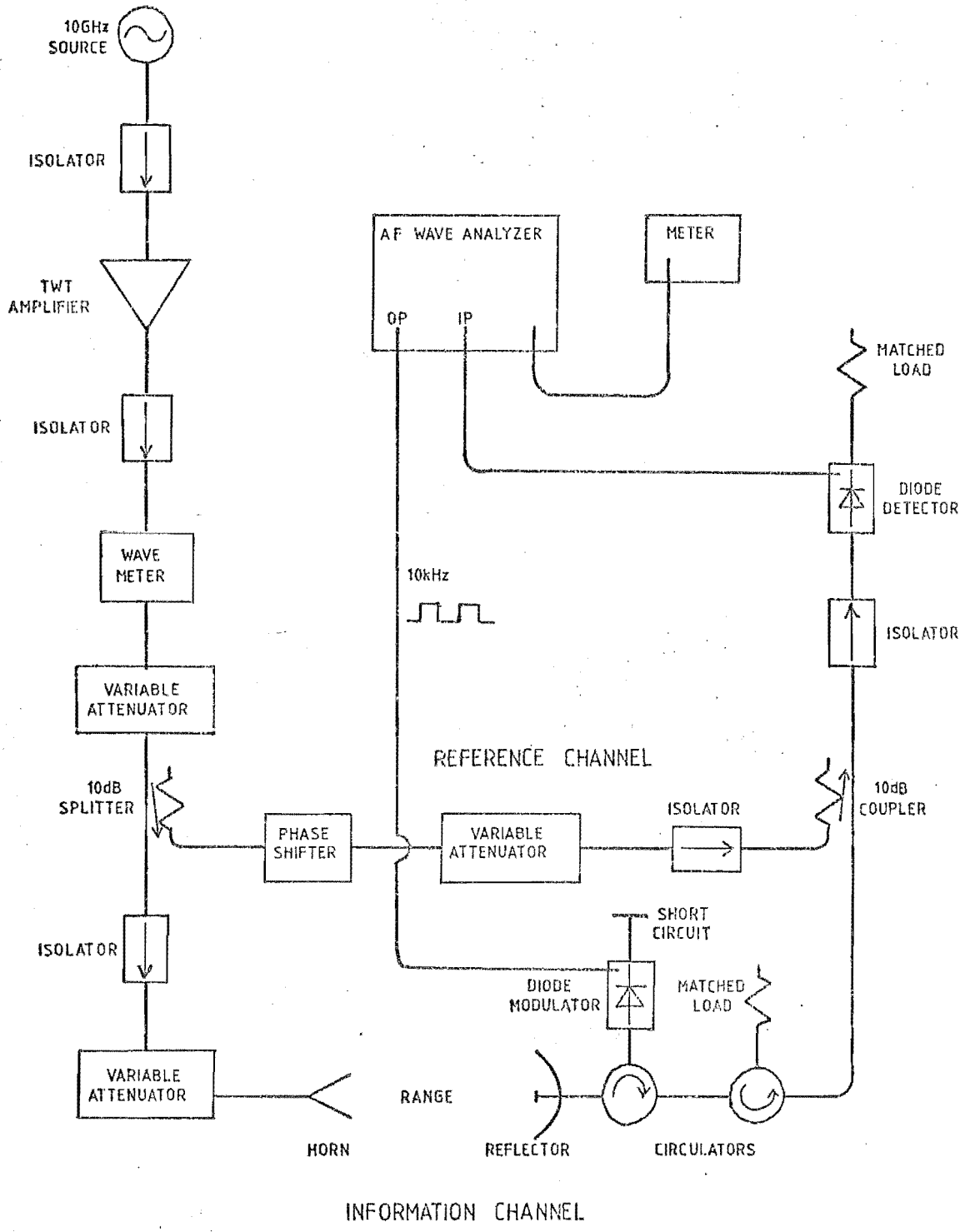

Figure 5.13 Parabolic Reflector Experiment Homodyne System.

5.5.3 RANGE CALIBRATION.

Two standard pyramidal horns were placed on the range, and the intensity pattern of the receive horn was measured and plotted in Figure 5.14. The measured field can be compared from published measurements. (Cross) also shown in Figure 5.14. The range produces known results to a reasonable accuracy.

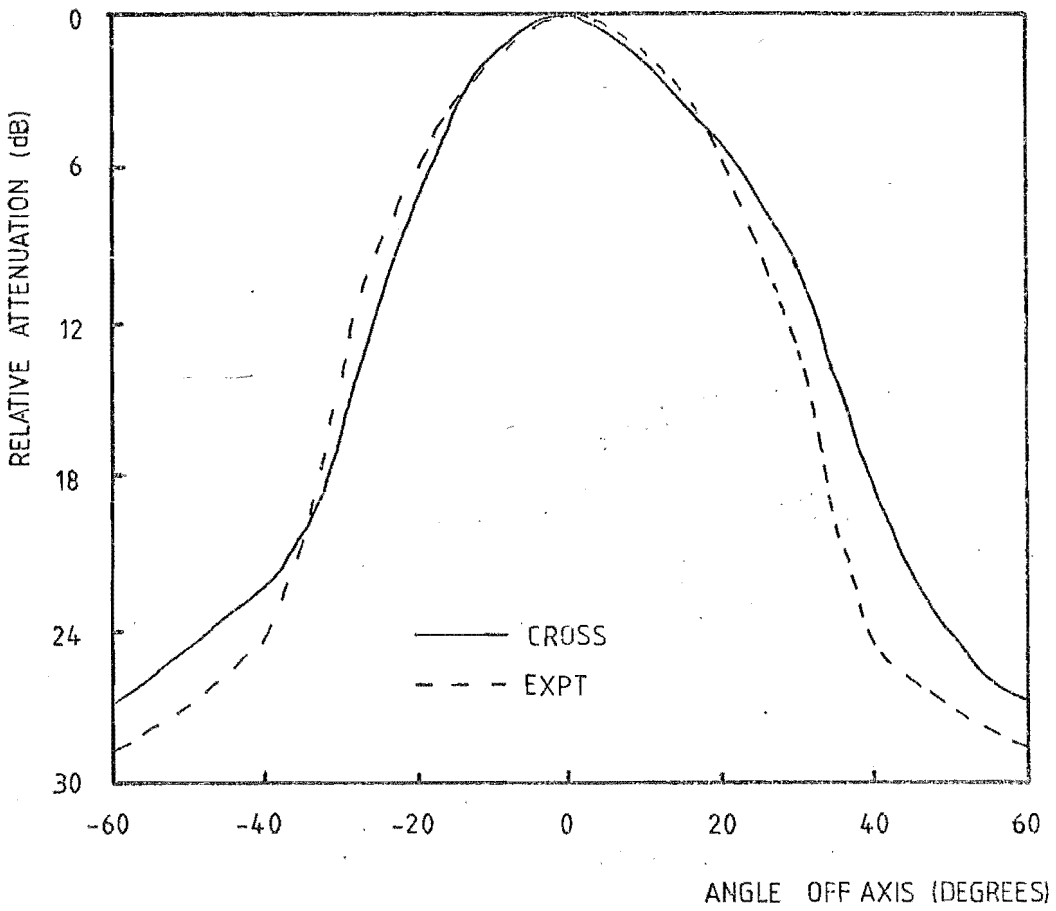

Figure 5.14 Horn Calibration Measurements

The feed dipole was measured in situ, and its intensity and phase patterns are reproduced in Figure 5.15. The regions 270-360 and 0-90 degrees are in the forward direction, if a reflector is attached. It is clear that the dipole field is not constant in this direction, caused by the feeding

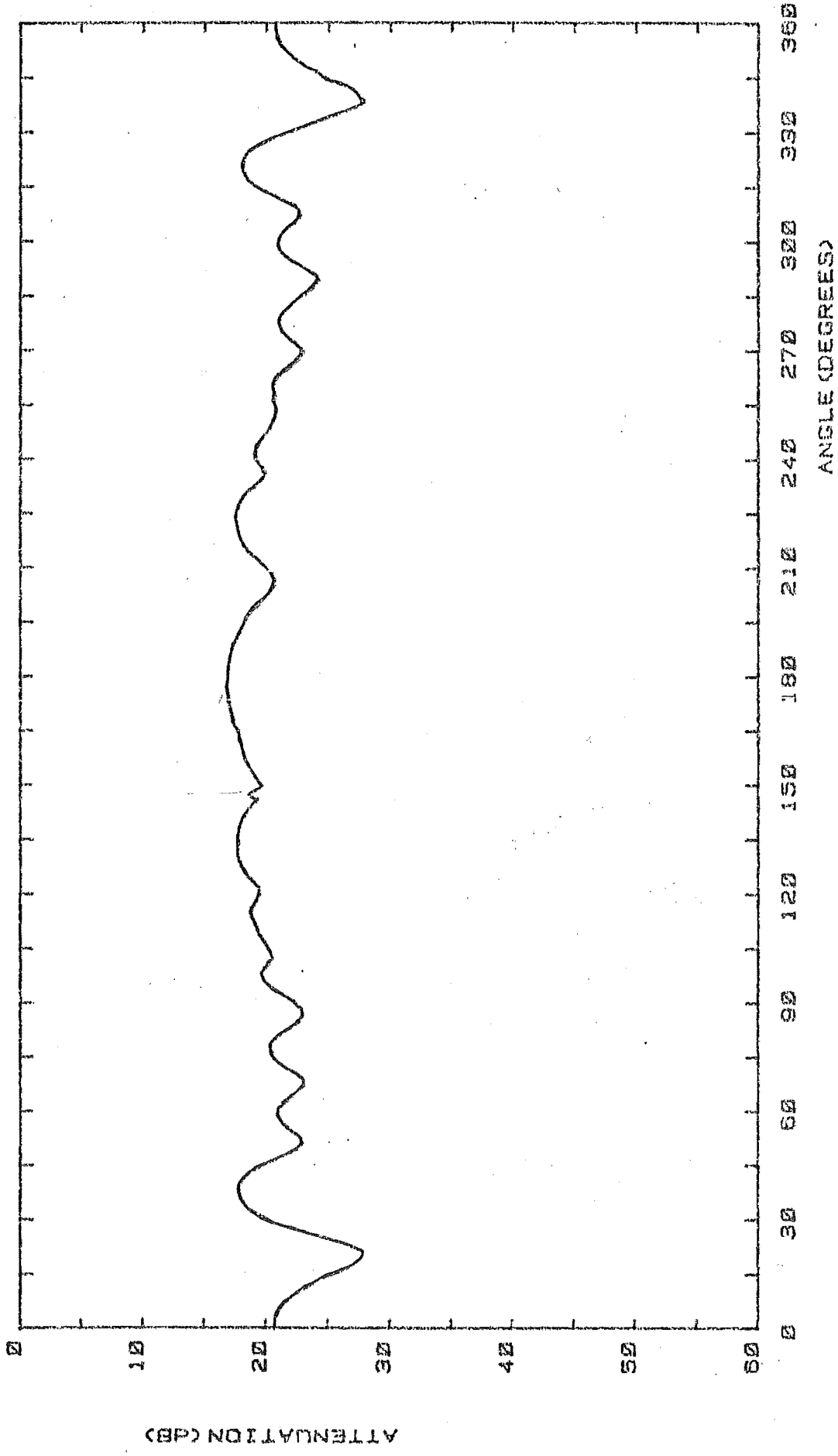

Figure 5.15a In Situ Dipole Measurement, (Intensity).

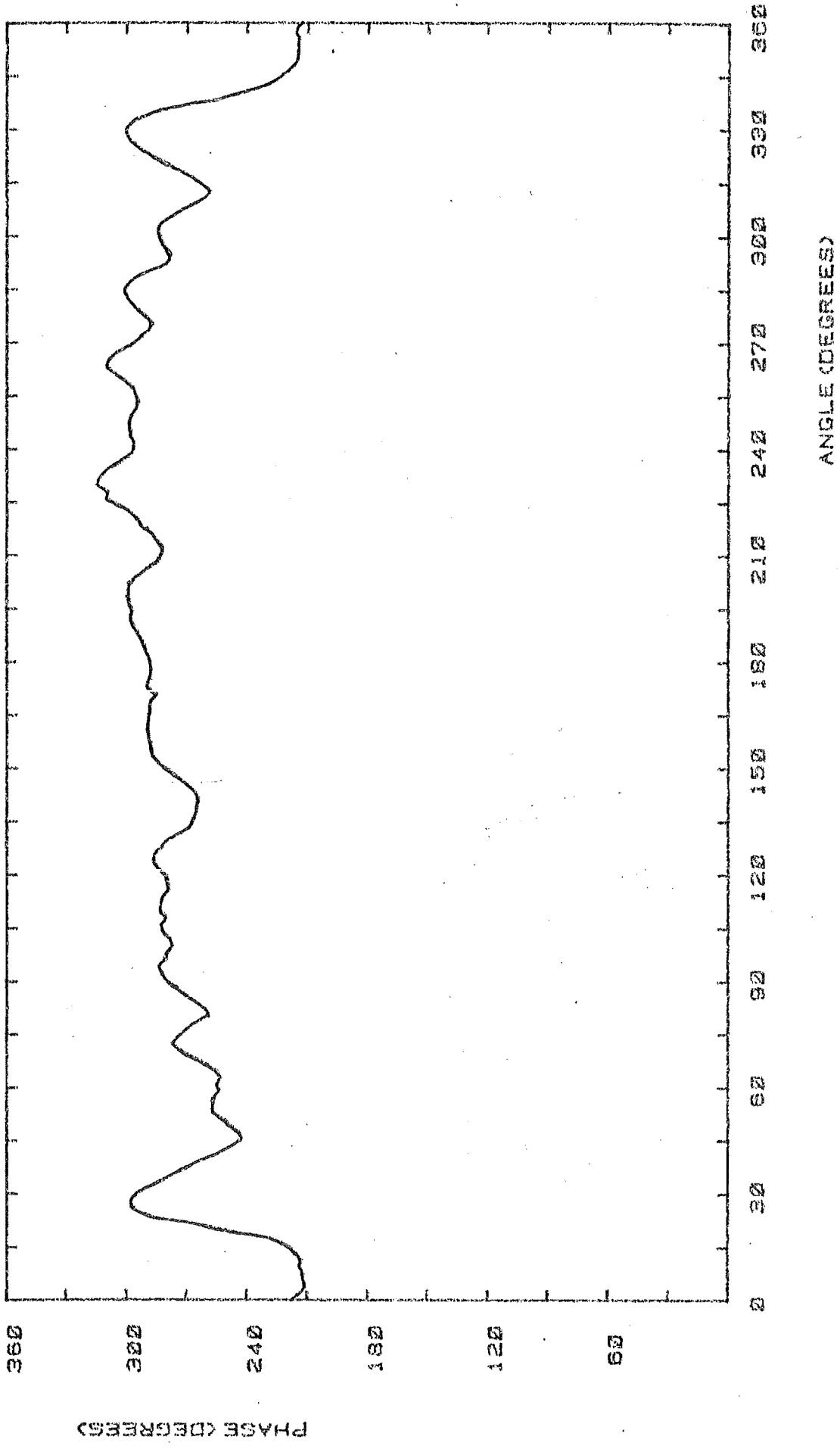

Figure 5.15b In Situ Dipole Measurement, (Phase).

arrangement and the perspex support. Over the region 90-270 degrees the intensity pattern is reasonably constant, hence the reflector will be bathed nearly isotropically. The intensity and phase patterns are quite symmetric, however.

All measurements were repeatable. Many deep nulls in the experiment patterns were carefully inspected, and each time similar repeatable results were obtained.

Measurements had to be taken in still conditions in order to obtain phase accuracy. Antenna movements tended to average out the rapid changes in intensity, masking peaks and nulls. The best times to run the experiment were usually during the night after the wind had been blowing from the North-East during the day. Usually six to seven hours of calm conditions were available. This allowed time for two or three experimental runs.

Automation would have increased the speed of result taking, but may have had the same averaging effect as the wind.

5.5.4 EXPERIMENTAL PROCEDURE

Penduli were used to align the antennas, and a spirit level was used to ensure that the horn was level in both planes. Measurements were taken every two degrees over a range of 360 degrees from the main lobe of the parabolic reflector pattern at 0 degrees to the same lobe at 360 degrees. Every 20 degrees the source was returned as required to make peaks as near to the same size as possible and nulls 180 degrees apart as in Figure 5.1. The system had to be returned continuously to avoid errors, as draughts through the open

window through which the boom was put affected the operating point of the source. The source was insulated as much as possible from environmental changes but clearly the source was subject to temperature changes which could not be combatted without sophisticated oven equipment. It appears that when the source is sufficiently detuned the modulator sends spurious unwanted signals about the system. These signals end up at the detector as an error signal, causing null position variation and peak fluctuations, with similar effects to too great an information channel signal.

Measurements were taken for 5 antennas. They were,

a) unperturbed parabolic reflector,

b) $\lambda/2$ slit at 30 degrees off the rear axis,

c) $\lambda/4$ slit at 30 degrees off the rear axis,

d) $\lambda/2$ slit at 70 degrees off the rear axis,

e) $\lambda/4$ slit at 70 degrees off the rear axis.

5.5.5 PHASE MEASUREMENT PROBLEMS

In Chapter 4 we saw that many problems were encountered with total phase variation over a range of measurements. When there is a null in a radiation pattern, it is usually the result of several sources adding to cancel each other completely. This can be seen in the Phasor Diagrams of Figure 5.16, where the fields of two similar sources are compared along a probe locus.

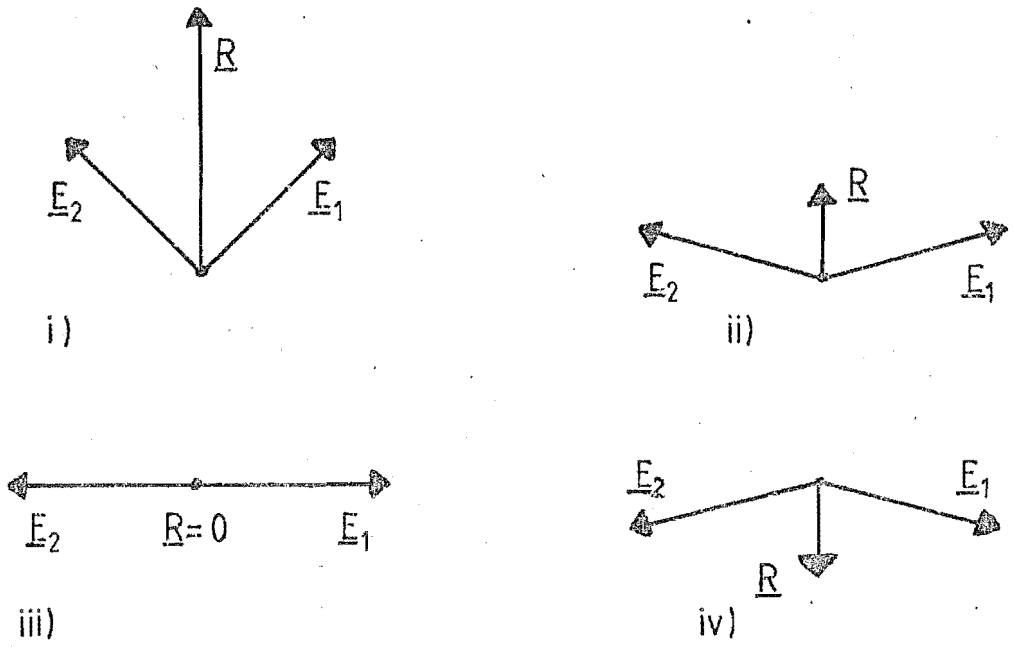

Figure 5.16 Phasor Diagram of Cancellation.

Between ii) and iv) in Figure 5.16, the Resultant changes phase by 180°. The probe position variation may be very small if the field phases vary rapidly, hence a phase change of 'π' can occur within a very small movement of the probe.

In the case of a perturbed parabolic reflector where the slit field can be modelled by one phasor and the unperturbed reflector field by another phasor, the phasors in Figure 5.16 may vary rapidly. The resultant phasor would then be harder to follow.

A question arises, in which direction does the phase change? This becomes important if total phase difference between points is required or if a phase field plot over a closed locus is made.

The direction of phase change can sometimes be detected by studying the direction of phase change either side of a null, but this depends upon the relative size of the constituent phasors. Experimental and theoretical results show inconsistencies caused by assuming the wrong direction of phase change at nulls. It is extremely difficult to isolate which phase changes are correct, and which are incorrect, hence results in Chapter 4 have been left as they stand.

In any other case the direction of phase change at a null may be disregarded as phase over a 2π range only is required.

Measurement of phase in a Homodyne System can involve ambiguities of π radians as well as 2π radians, especially where phase charges of $\pi/2$ occur between measurement points. The phase measurement involves the tracking of nulls of the detector response, as shown in Figure 5.1, and it is quite possible to track unconsciously the other null when the phase shift is too large. The phase shift history can usually provide a good indication of the null position to follow, but if the situation is too confusing the frequency error properties in Section 5.5.4 may be put to good use.

It was mentioned that the frequency error caused variations in the position of the nulls and different sized maxima. With the different sized maxima it is then possible to identify each null over the 360° range of the phase shift in the reference channel. When the phase of the measured field varies rapidly, individual nulls may be more easily tracked. In this case the Homodyne System will still not be able to follow the direction of sudden changes of 180°, as in the case of a null, in a similar manner to phase calculating

algorithms used in the theoretical analyses.

This frequency offset method of phase measurement introduces two problems which must be taken into consideration.

1) The change in frequency will alter the position of the nulls being tracked. This change must be taken into account and recompensated for when attenuation measurements are being taken. The original frequency may be hard to regain as Klystron tuning is not very stable.

2) The phase pattern may be altered with the change in frequency, especially when nulls are being considered. Care must be taken to ensure that the frequency change is as small as possible so that the antenna attenuation and phase pattern is altered to as small an extent as possible.

The frequency offset method was utilized in the measurement of phase over rapidly varying areas. It can be noted that phase errors over the probe locus of experimental results are generally smaller than the errors produced by the phase calculating algorithms of the theories. When this method was used about a null all maxima and minima were measured at both the intended operating frequency and the offset frequency. This increased the length of time required to make an experimental run.

5.6 DISCUSSION

The Homodyne Detection principle has proved to be accurate and reasonably simple to use. All of the circuits used in the experiments had very little tuning, tending to rely heavily on padding by attenuation or buffering by isolation. Result taking was necessarily slow due to the need to measure phase and intensity at each point, requiring the shifting of the phase shifter in the reference channel by 90 degrees each time. Two alternatives present themselves if measurements need to be taken more quickly.

They are,

a) build a servo control system to automatically measure phase and intensity on the present system,

or,

b) build a detection circuit similar to that of Cohn and Weinhouse (1964) using a processing system from King (1978), Chapter 10.

These alternatives were not explored, as a disproportionate amount of time had been spent in the refining of the circuits in use. It should be noted that reasonably intelligent measurement algorithms may be required if phase is rapidly varying with respect to probe position.

CHAPTER SIX: CONCLUSIONS

There was a young man of Japan,
Whose limericks never would scan;
When they said it was so,
He replied, 'Yes I know,
But I always try to get as many words into the last
line as ever I possibly can.'

Anonymous.

In this thesis we have investigated the diffraction of electromagnetic waves by slits, and have assessed the effect of the placement of slits in parabolic cylinder reflector antennas. As a first approximation of slits in parabolic reflectors we have taken inclined plane slits.

Two different descriptions of slit diffraction have been studied, one based on the Geometrical Theory of Diffraction, the other based on a combination of Physical Optics and the Method of Moments.

For the reflector antennas studied here, GTD has provided a good description of wide angle lobes, but has failed under two circumstances, i.e.,

a) where two induced edge sources are within $\lambda/3$ of each other.

b) where the main lobes of the reflector field are being studied.

The GTD method has to be modified to account for different sources, curved edges and curved reflecting planes. These modifications tend to complicate a reasonably simple theory based on Geometrical Optics. Problems may arise from not taking all Geometric Optics ray paths into account, resulting in an incomplete GTD description.

The Method of Moments technique calculates the surface currents induced about diffracting edges and volume currents within dielectric cylinders. If the Moments currents have been placed carefully about points of interest, the method provides a simple solution technique to give a collection of currents which produce accurate far fields. The Moment Method is restricted by the number of surface currents which can be used to model a reflector.

The far field appears to be relatively independent of variations of current sizes and placings, but in the case where two surfaces are close to each other problems may arise.

The Method of Moments can be used in concert with Physical Optics to describe currents over a reasonably sized reflector, and an iteration scheme like those described in Chapters 3 and 4 can be instituted to include currents over many diffracting edges.

A major limitation of the Method of Moments is the length of computer time required to give solutions. One advantage of the method is that it is easy to understand. Another advantage is that it can be applied to any shaped two or three dimensional reflecting or dielectric object without modification or resort to consideration of physically based models, like surface ray propagation or slope wave diffraction. With an expected increase in the availability of computers it is felt that methods based on numerical analyses will provide the key to future electromagnetic problems, (Newsweek, 1980).

It should be noted that the brute force Moment Method calculations employed in this thesis only became possible after the new Electrical Engineering Computer was installed. This massive increase in computing power made these calculations feasible. The use of hybrid procedures have decreased solution times, and in some cases produced more accurate solutions.

A parabolic reflector rear field does not have a particularly simple form, and it is difficult to null the shadow field by allowing leakage through the reflector with narrow slits. Narrow slits leak the correct intensity but over a wide angle, hence a narrower leaked distribution in the rear direction must be found, that will successfully null in specified directions without affecting the physical and electromagnetic properties of the reflector.

APPENDIX A:

SEPARATION OF VARIABLES TECHNIQUE APPLIED TO PARALLEL PLATE WAVEGUIDE

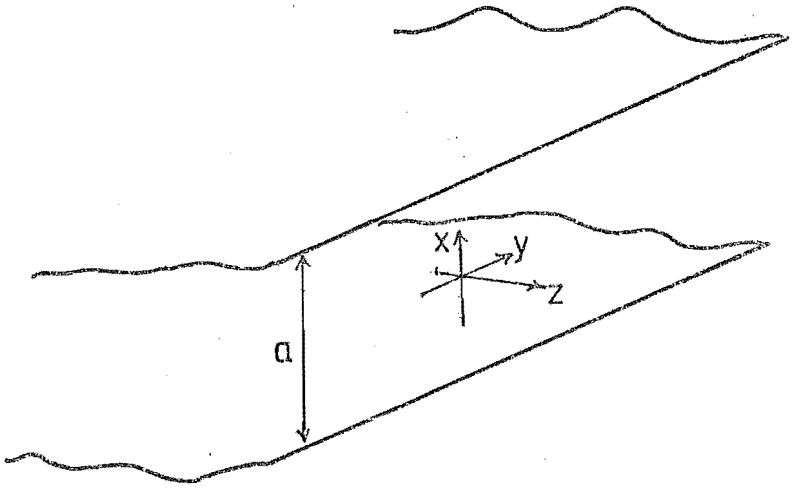

Figure A1. Parallel Plate Waveguide.

For TEM transmission, both the Electric and Magnetic Fields are transverse to the power flow, and the boundary conditions are, (Jordan and Balmain, 1968)

$$E_y = E_z = H_x = 0 \qquad (A.1)$$

where the subscripts refer to the direction the Field Vectors at the surfaces of the parallel plate guide.

Here the E fields are governed by the Dirichlet Boundary conditions, and the H field by the Neumann boundary conditions.

If propagation is in the z direction, assume there is no variation in the y direction. Hence $\frac{\partial E}{\partial y} = \frac{\partial H}{\partial y} = 0$ can be set, i.e. no attenuation, and plane type propagation

Inside the parallel plate waveguide, Maxwell's Source Free Curl Equations apply, i.e.,

$$\nabla \times \underline{E} = -j\omega\mu\underline{H} \ ,$$

$$\nabla \times \underline{H} = j\omega\varepsilon\underline{E} \ , \tag{A.2}$$

along with the free space wave equation,

$$\nabla^2\underline{E} + \beta^2\underline{E} = 0 \ ,$$

$$\nabla^2\underline{H} + \beta^2\underline{H} = 0 \ . \tag{A.3}$$

For the propagation in the z direction, the description

$$e^{-j\beta z}, \tag{A.4}$$

assuming no attenuation, and β varies according to the mode of propagation.

Solving Equation (A.2) it can be found that

$$H_x = \frac{-j\beta}{h^2}\frac{\delta H_z}{\delta x}, \qquad E_x = \frac{-j\beta}{h^2}\frac{\delta E_z}{\delta x},$$

$$H_y = \frac{-j\omega}{h^2}\frac{\delta E_z}{\delta x}, \qquad E_y = \frac{j\omega\mu}{h^2}\frac{\delta H_z}{\delta x}, \tag{A.5}$$

where $h^2 = (-\beta^2 + \omega^2\mu\varepsilon)$.

Equation (A.5) describes a total wave, being the result of $E_z \equiv 0$ and $H_z \equiv 0$.

To obtain an expression for the TEM mode, look first at TM, i.e. transverse magnetic propagation. In this case $H_z = 0$ thus from Equation (A.5) it can be seen that E_y and H_x are zero, leaving H_y, E_x and E_z.

The wave equation reduces to,

$$\frac{d^2H_y}{d_x^2} = -h^2H_y \tag{A.6}$$

Equation (A.6) is a separated ordinary differential equation. Solving Equation (A.6) at $y = y^o$ produces the Simple Harmonic solution, i.e.,

$$H_y^o = (A_1\sin(hx) + A_2\cos(hx)), \tag{A.7}$$

and when propagation is taken into account,

$$H_y = H_y^o\, e^{-j\beta z}$$

$$= (A_1\sin(hx) + A_2\cos(hx))\, e^{-j\beta z} \tag{A.8}$$

H_y however, is free of boundary conditions, but H_y is related to E_z via Equation (A.2), that is,

$$E_z = \frac{-j}{\omega\varepsilon}\frac{dH_y}{dx}$$

$$= \frac{-jh}{\omega\varepsilon}\,(A_1\cos(h2) - A_2\sin(hx))\, e^{-j\beta z} \tag{A.9}$$

Boundary conditions can be applied to Equation (A.9), as $E_z = 0$ when $x = 0$ or $x = a$ thus,

$$E_z = \frac{jm\pi}{\omega\varepsilon a}\, A_2\sin(\frac{m\pi}{a}\cdot x)\, e^{-j\beta z}$$

$$H_y = A_2\cos(\frac{m\pi}{a}\cdot x)\, e^{-j\beta z}$$

$$E_x = \frac{\beta}{\omega\varepsilon}\, A_2\cos(\frac{m\pi}{a}x)\cdot e^{-j\beta z}$$

$$m = 0,\ 1,\ 2,\ \ldots. \tag{A.10}$$

When m = 0, TEM transmission occurs, and all free space constants hold, hence

$$E_x = \sqrt{\frac{\mu}{\varepsilon}}\, H_y = \sqrt{\frac{\mu}{\varepsilon}} \cdot A_2 \cdot e^{-j\beta z} \qquad \text{(A.11)}$$

This is the only* field inside the guide when $a < \lambda/2$.

---

* only propagating field.

APPENDIX B:

METHOD OF MOMENTS SOLUTION TECHNIQUE

In the case of solving linear equations, consider the functional equation, (Harrington, 1968).

$$L(f) = g \tag{B.1}$$

where L is a linear operator

f is field to be determined

g is the known source.

f can be written as a series of functions.

$$f = \sum_n \alpha_n f_n, \tag{B.2}$$

where α_n are undertermined coefficients of assumed f_n basis functions.

Assuming L is a linear functional gives,

$$\sum_n \alpha_n \cdot L(f_n) = g. \tag{B.3}$$

Define a set of testing functions $w_1, w_2, w_3 \ldots$ and take the inner product of Equation (B.3) with each w_m, i.e.,

$$\sum_n \alpha_n < w_m, L(fn) > = < w_m, g > \tag{B.4}$$

Written in matrix form Equation (B.4) can be written as

$$\left[\ell_{mn}\right] \quad \left[\alpha_n\right] = \left[g_m\right] \tag{B.5}$$

where

$$\left[\ell_{mn}\right] = \begin{bmatrix} <w_1, L(f_1)> & <w_1, L(f_2)> & - & - & - & - & - \\ <w_2, L(f_1)> & <w_2, L(f_2)> & - & - & - & - & - \\ \vdots & \vdots & & & - & - & - \end{bmatrix} \tag{B.6}$$

$$[\alpha_n] = \begin{bmatrix} \alpha_1 \\ \alpha_2 \\ \vdots \end{bmatrix}, \quad [g_m] = \begin{bmatrix} \langle w_1, g \rangle \\ \langle w_1, g \rangle \\ \vdots \end{bmatrix} \tag{B.7}$$

solving to find the coefficient matrix

$$[\alpha_n] = [\ell_{mn}]^{-1} \quad [g_m] \quad . \tag{B.8}$$

Hence

$$f = [f_n]^T \quad [\alpha_n] = [f_n]^T \quad [\ell_{mn}]^{-1} [g_m] \tag{B.9}$$

where $[\ell_{mn}]$ is called the scatterer matrix, $[g_m]$ the source matrix, and $[\alpha_n]$ the coefficient matrix.

In the case $f_n = w_n$, the method of solution is referred to as Galerkins method.

The simplest case is when $w_m = f_m = \delta_m$ the Kronecker Delta, and the solution technique is called point matching.

For Dirichlet boundary conditions, split the circumference of the scatterer into little strips, of width ΔCn. Define basis functions f_n in terms of pulse functions to produce the orthogonal representation.

$$f_n(\underline{\rho}) = \begin{cases} 1 & \text{on } \Delta Cn \\ 0 & \text{elsewhere.} \end{cases} \tag{B.10}$$

Applying the moment method to a highly conducting scatterer, we can define the surface currents as

$$\underline{Je}_z = \Sigma \alpha_n f_n, \tag{B.11}$$

assuming the basis functions of Equation (B.10).

Using Equations (B.3), (B.4), (B.5) and (2.97) we obtain the elements of the scatterer matrix, i.e.

$$\ell_{mn} = \frac{k}{4j}\sqrt{\frac{\mu}{\varepsilon}} \int_{\Delta Cn} Ho^{(2)} \left[k\sqrt{(x-x_m)^2+(y-y_m)^2}\right] d\ell, \qquad (B.12)$$

where (x_m, y_m) is the scatter surface current filament position,

(x,y) is the position on the scatterer where the effects of the filament are being measured,

$[\alpha_n]$ is the current coefficient matrix,

$[g_m]$ is the source matrix the elements of which are given by,

$d\ell$ is a path around the surface of the scatterer, c.f. Fig 2.15.

$$g_m = E_z^i (x_m, y_m). \qquad (B.13)$$

The current $\underline{Je}_z$ is then found by the use of Equation (B.9).

The integral in Equation (B.12) can be approximated by,

$$\ell_{mn} = \frac{k}{4j}\sqrt{\frac{\mu}{\varepsilon}}\ \Delta Cn\ Ho^{(2)} \left[k\sqrt{(x_n-x_m)^2+(y_n-y_m)^2}\right] \qquad (B.14)$$

if the element $\underline{Je}_z \Delta Cn$ is treated as a cylindrical filament of current when $m \neq n$. In the case $m=n$, Equation (B.14) has an integrable singularity, and ΔCn can be approximated by a straight line and we can use the small argument formula of the Hankel Function, i.e.,

$$H_o^{(2)}(z) \simeq 1 - j\frac{2}{\pi}\log_e\left(\frac{\gamma z}{2}\right), \qquad (B.15)$$

where $\gamma = 0.5772$ is Euler's constant. Evaluating Equation (B.12) for $m=n$ we obtain

$$\ell_{nn} = \frac{k}{4j}\sqrt{\frac{\mu}{\varepsilon}}\ \Delta Cn.\left[1-j\frac{2}{\pi}\log_e\left(\frac{\gamma k \Delta Cn}{4e}\right)\right] \qquad (B.16)$$

After evaluating the $[\ell_{mn}]$ scatterer matrix the coefficient matrix $[\alpha_n]$ can be found by Equation (B.8). In the case where f_n is defined as in Equation (B.10) the $[\alpha_n]$ matrix will define the currents.

Newmann Boundary Conditions can be treated in a similar manner, see Harrington (Harrington, 1968).

Major Computational problems arise with the solution of Equation (B.8), involving the inversion of the scatterer matrix.

The scatterer matrix is normally a general matrix, where each element is defined, consequently the inversion involves much calculation. If it can safely be assumed that filaments m and n are far enough apart on the surface of a scatterer, their interactions may be neglected, (Kinzel, 1974). This will result in a scatterer matrix with zero elements in the top right hand and bottom left hand corners, depending upon the structure of the scatterer and its matrix. If there are enough zeros, sparsity techniques may be employed, resulting in a faster inversion.

Another solution to the scatterer matrix inversion problem can be found by using Physical Optics currents over smooth portions of the scatterer and placing moments currents where Physical Optics currents would be incorrect. This method is used in the present work. Iterative techniques can reduce each scatterer matrix further.

Where a large irregular scatterer is used, or where a multi-wire problem is under study, the scatterer currents may be split into bands, where elements that interact most strongly are kept to their own scatterer matrices. (Ferguson et al, 1976). The individual scatterer matrices are calculated and an iterative technique between bands is used to find the scatterer currents. Problems arise in the optimization of band size, as there is a trade off between band size and the required number of iterations between bands to allow the problem to settle to a solution.

APPENDIX C:

EXACT SOLUTION TO SCATTERING BY A STRIP OR DIFFRACTION BY A PARALLEL SLIT

This Appendix studies the exact solution of scattering from a strip or diffraction by a slit. This is achieved by solving the Helmholtz Equation in Elliptic Coordinates, with the appropriate Boundary Conditions set at $\xi_1 = 0$. $\xi_1 = 0$ is the coordinate surface which coincides with the strip or the slit, whichever is under study. The Helmholtz Equation, solved in terms of functions of the Elliptic Cylinder, is given as Equation (3.1) giving Mathieu's Equation and the associated Mathieu's Equation. Mathieus Equations are repeated below. The Elliptic Cylinder coordinate system is depicted in Figure 3.2. (Morse and Feshbach, 1953).

$$\frac{-d^2F}{d\xi_1^2} + (b - d^2k^2\cosh^2\xi_1)\ F = 0$$

$$\frac{d^2G}{d\xi_2^2} + (b - d^2k^2\cos^2\xi_2)\ G = 0 \qquad \text{(C.1)}$$

where b is a constant and d is half the interfocal distance of the elliptic coordinate system.

In the case of a line source placed at coordinates (ξ_1^o, ξ_2^o), in circular polar coordinates, the field of such a source would be described by the Greens Function,

$$g(\underline{\rho}^p, \underline{\rho}^o) = \frac{1}{4j} H_o^{(2)} (k|\underline{\rho}^p - \underline{\rho}^o|), \qquad \text{(C.2)}$$

a Hankel Function. (ξ_1^p, ξ_2^p) are the coordinates of a probe.

The Greens Function can be expanded in Elliptic Coordinates as, (Morse and Feshbach, 1953),

$$g(\rho^p,\rho^o) = \pi\Bigg[\sum_{m=0}^{\infty}\left(\frac{1}{M_m^e(h)}\right)\cdot Se_m(h,\cos\xi_2^o)\ Se_m(h,\cos\xi_2^p)$$

$$\cdot\begin{cases} Je_m(h,\cosh\xi_1^o)\cdot He_m(h,\cosh\xi_1^p);\ \xi_1^p>\xi_1^o \\ Je_m(h,\cosh\xi_1^p)\cdot He_m(h,\cosh\xi_1^o);\ \xi_1^o>\xi_1^p \end{cases}$$

$$+\sum_{m=1}^{\infty}\left(\frac{1}{M_m^o(h)}\right)\cdot So_m(h,\cos\xi_2^o)\cdot So_m(h,\cos\xi_2^p)$$

$$\cdot\begin{cases} Jo_m(h,\cosh\xi_1^o)\cdot Ho_m(h,\cosh\xi_1^p);\ \xi_1^p>\xi_1^o \\ Jo_m(h,\cosh\xi_1^p)\cdot Ho_m(h,\cosh\xi_1^o);\ \xi_1^o>\xi_1^p \end{cases}\Bigg] \qquad (C.3)$$

where M_m^e (M_m^o) are even, (odd) order normalizing constants,

$Se_m(a,b)$ are even angular Mathieu Functions, (M.F.'s). of order m,

$So_m(a,b)$ are odd angular M.F.'s, of order m,

$Je_m(a,b)$ are even radial M.F.'s, of order m and 1st kind,

$He_m(a,b)$ are even radial M.F.'s, of order m and 3rd kind,

$Jo_m(a,b)$ are odd radial M.F.'s, of order m and 1st kind,

$Ho_m(a,b)$ are odd radial M.F.'s, of order m and 3rd kind,

and h is defined below Equation (3.16).

The angular Mathieu Functions (M.F.'s) are related to the circular sine and cosine functions, and the even M.F.'s are similar to the cosine functions with zeros at $\xi_2 = \frac{\pi}{2}, \frac{3\pi}{2}$ and are even about $\xi_2 = 0$ and π. The odd M.F.'s correspond to the circular sine function. The radial M.F.'s are related to the Bessel and Hankel Functions associated with the Circular Cylinder coordinate system. The symbols for the radial M.F.'s are chosen to correspond to the Cylindrical Coordinate Bessel Functions.

In the case of a plane source, the 1-dimensional Greens Function is, in Cylindrical Coordinates,

$$g(\ell) = e^{-jk\ell\cos(u-\phi)} = e^{-jk\left[x\cos u + y\sin u\right]} \tag{C.4}$$

i.e., a plane wave proceeding at an angle u with respect to the x-axis of a Cartesian Coordinate System, or the major axis of the ellipse $\xi_1 = \alpha$. The two-dimensional Greens Function may be manipulated to form a plane wave if the source is removed to infinity.

Now deriving the plane wave expansion, set the source point a large distance from the origin in the direction $u+\pi$ to the +ve x axis. The quantity $|\underline{\rho}^p - \underline{\rho}^o|$ becomes $\rho^o + \rho^p\cos(u-\phi)$, with $\rho^o >> \rho^p$, $\xi_2^o \to \phi+\pi$ and $k\rho_o \to h\cosh\xi_1^o$. At large distances from the origin the Elliptic and Cylindrical Coordinate Systems resemble each other closely. Using the relation $Se_m(h,-\cos u) = (-1)^m Se_m(h,\cos u)$, and the asymptotic form for He, Ho which is similar to the Hankel Function expansion for large argument, we have,

$$\frac{1}{4j} H_o^{(2)}(k|\rho_o - \rho_p|) \xrightarrow[\rho_o \to \infty]{} e^{-jk\rho_o} \cdot e^{-jk\rho(\cos(\phi-u))} \cdot (8\pi jk\rho_o)^{-\frac{1}{2}}$$

$$\xrightarrow[\rho_o \to \infty]{} \frac{1}{\sqrt{h\cosh\xi_1^o}} \cdot e^{-jh\cosh\xi_1^o}$$

$$\cdot \left(\sum_{m=0}^{\infty} \frac{Se_m(h,\cos\xi_2^o)}{M_m^e(h)} Se_m(h,\cos\xi_2^p) \cdot Je_m(h,\cosh\xi_1^p) \right.$$

$$\left. + \sum_{m=1}^{\infty} \frac{So_m(h,\cos\xi_2^o)}{M_m^o(h)} So_m(h,\cos\xi_2^p) \cdot Jo_m(h,\cosh\xi_1^p) \right) \tag{C.5}$$

Normalizing to produce the plane wave expansion in Equation (C.4) gives,

$$e^{-jk\rho\cos(\phi-u)} = \sqrt{8\pi}\left[\sum_{m=0}^{\infty} j^m \frac{Se_m(h,\cos\xi_2^o)}{M_m^e(h)} \cdot Se_m(h,\cos\xi_2^p)\, Je_m(h,\cosh\xi_1^p) + \sum_{m=0}^{\infty} j^m \frac{So_m(h,\cos\xi_2^o)}{M_m^o(h)} \cdot So_m(h,\cos\xi_2^p)\, Jo_m(h,\cosh\xi_1^p)\right] \tag{C.6}$$

the expansion of an incident plane wave in elliptic coordinates.

If we study scattering from a strip, the scattering can be related to diffraction through a complementary slit by Babinet's Principle. (Bouwkamp, 1954). If Neumann Boundary Conditions are satisfied at the conducting strip, the scattering is the negative of the diffraction through the slit whose conducting planes are subject to Dirichlet Boundary Conditions.

Similarly the scattered field from a strip under Dirichlet Boundary Conditions is the negative of the diffracted field through the slit with Neumann Boundary Conditions on the conducting planes. The Boundary Conditions are easily set at the coordinate surface which coincides with the strip, hence it is easier to solve for the associated scattering from a strip and apply Babinet's Principle to obtain diffraction through a slit.

As an example we will look at Neumann Boundary conditions at the strip, i.e.,

$$\frac{\partial\psi_{incident}}{\partial\xi_1} + \frac{\partial\psi_{scattered}}{\partial\xi_1} = 0 \quad \text{at the strip.} \tag{C.7}$$

where

$$\left.\frac{\partial\psi_{incident}}{\partial\xi_1}\right|_{\text{at the strip}} = \sqrt{8\pi}\sum_{m=1}^{\infty}(j^m)\cdot\frac{So_m(h,\cos\xi_2^o)}{M_m^o(h)}\cdot So_m(h,\cos\xi_2^p)$$

$$\cdot Jo_m'(h,1) \qquad (C.8)$$

for plane wave incident.

and

$$\left.\frac{\partial\psi_{incident}}{\partial\xi_1}\right|_{\text{at the strip}} = \pi\sum_{m=1}^{\infty}\left(\frac{1}{M_m^o(h)}\right)\cdot So_m(h,\cos\xi_2^o)\cdot So_m(h,\cos\xi_2^p)$$

$$\cdot Ho_m(h,\cosh\xi_1^o)\cdot Jo_m'(h,1) \qquad (C.9)$$

for cylindrical wave incident.

where

$$Jo_m'(h,1) = \left.\frac{\partial\, Jo_m(h,1)}{\partial\xi_1}\right|_{\xi_1 = \text{strip}} \qquad (C.10)$$

No even Mathieu Functions are found as $Je_m'(h,1) = 0$.

The scattered field from the strip source would be outward travelling. Relating the known cylindrical source field, a Hankel Function, with a Function of the Elliptic Cylinder, i.e., the Radial Mathieu Function of the 4th kind, a strip source should be some combination of Radial Mathieu Functions of various orders, i.e.,

$$\psi_{scattered} = \sum_{m=0}^{\infty} B_m\, Ho_m(h,\cosh\xi_1^p) \qquad (C.11)$$

For Neumann Boundary Conditions on the strip,

$$\frac{\partial \psi_{scattered}}{\partial \xi_1} = \sum_{m=1}^{\infty} B_m \, Ho'_m(h,1) \tag{C.12}$$

assuming that B_m is independant of ξ_1.

Hence on the strip, for the plane wave case,

$$\sqrt{8\pi} \sum_{m=1}^{\infty} (j^m) \left[\frac{So_m(h,\cos\xi_2^o)}{M_m^o(h)} \right] So_m(h,\cos\xi_2^p) \cdot Jo'_m(h,1) \tag{C.13}$$

$$+ \sum_{m=1}^{\infty} B_m \, Ho'_m(h,1) = 0$$

Now each B_m $m = 1,2, \ldots$ can be found from Equation (C.13), i.e.,

$$B_m = - \sqrt{8\pi} \, j^m \left[\frac{So_m(h,\cos\xi_2^o)}{M_m^o(h)} \right] \cdot So_m(h,\cos\xi_2^p) \cdot \frac{Jo'_m(h,1)}{Ho'_m(h,1)} \tag{C.14}$$

From Equation (C.14),

$$\psi_{scattered} = \sum_{m=1}^{\infty} B_m \, Ho_m(h,\cosh\xi_1^p)$$

$$= - \sqrt{8\pi} \sum_{m=1}^{\infty} j^m \left[\frac{So_m(h,\cos\xi_2^o)}{M_m^o(h)} \right] \cdot So_m(h,\cos\xi_2^p) \cdot \tag{C.15}$$

$$\frac{Jo'_m(h,1)}{Ho'_m(h,1)} \cdot Ho_m(h,\cosh\xi_1^p) .$$

The diffracted wave from a slit whose conducting planes are subject Dirichlet Boundary Conditions will produce a diffracted wave through the slit which is just the negative of $\psi_{scattered}$.

For a cylindrical source, the coefficients B_m can be found in the same way as for the plane wave source, i.e., the diffracted field through

a slit subject to Dirichlet Conditions for a line source is,

$$\psi_{diffracted} = 4 \sum_{m=1}^{\infty} \left(\frac{1}{M_m^o(h)}\right) . So_m(h,\cos\xi_2^o) . So_m(h,\cos\xi_2^p) . \frac{Jo_m'(h,1)}{Ho_m'(h,1)} \cdot Ho_m(h,\cosh\xi_1^o) . Ho_m(h,\cosh\xi_1^p) . \tag{C.16}$$

In the case of Dirichlet Boundary Conditions being applied at the strip, the following relation holds,

$$\psi_{incident} + \psi_{scattered} = 0 \quad \Big| \text{at the strip,} \tag{C.17}$$

and the scattered field is

$$\psi_{scattered} = \sum_{m=0}^{\infty} C_m He_m(h,1) \tag{C.18}$$

The same procedure leading to the production of B_m can be followed to find C_m, which in this case will be dependant upon even Mathieu Functions since $Jo_m(h,1) = 0$.

Computer routines are available (Clemm, 1969), which produce Mathieu Functions of the Stratton Normalization (the ones used in this study) without too much difficulty. It will be noticed that the fields are described by infinite series, hence some error will be incurred by terminating the series at some pre-determined value of m. The Mathieu Functions themselves are infinite series of trigonometric functions or Bessel Functions hence there is another source of error. It should be noted that the trigonometric and Bessel Functions are defined as infinite series themselves.

Slits up to two wavelengths wide have been treated by the Exact theory of this Appendix, and the series have been truncated at m=12. This appears to be satisfactory as results in Chapter 3 match these of the GTD formulation.

Morse and Feshbach (1953) have tabulated Mathieu Functions for up to $h = 3$, which corresponds to a slit or strip about 0.9λ wide. For such a configuration they state that terms up to $m = 4$ are sufficient to give an accurate result. Different normalizations may give a more rapid result.

The original work on the exact solution of diffraction through a slit was done by Morse and Rubenstein, (Morse and Rubenstein, 1938). Their theory was correct, but it appears that some of their results were wrong, (Leeb, 1973). Other workers who have used Mathieu Function representations for electromagnetics problems are Hsu, (1960); Leeb, (1973); McLachlan, (1947); Stratton et al., (1941); and Nimura and Shibayama (1951).

The exact theory can only be applied to plane slits, as the elliptic cylinder coordinate system is incapable of modelling planes that are not in the plane of the slit.

APPENDIX D

TRANSMISSION THROUGH SLITS FORMED BY INCLINED PLANES

BY

E.J. Hamilton and V. Kerdemelidis

Department of Electrical Engineering,
University of Canterbury,
Christchurch, New Zealand.

To be published in IEEE Transactions on Antennas and Propagation.

SUMMARY

The phase and the amplitude of electromagnetic fields transmitted through two-dimensional slits are investigated both theoretically and experimentally. The slits are formed by two inclined perfectly conducting planes. The approximate theory employed is based on the modification of the high frequency diffraction by a half-plane (modified GTD). The experimental measurements were performed using a parallel-plate range.

Results indicate that the effect of the relative inclinations of the planes tends to be of importance only for the cases of narrow slits, i.e. $\lambda/3$ or less.

INTRODUCTION

A finite reflector antenna suffers loss of energy due to diffraction over the edges of the reflector [1]. Several workers have investigated the effects of modifying the reflector edge with the purpose of reducing leakage [2] - [4], while others have suggested placing screens behind the reflector [5]. The placement of holes near the rim of the reflector to allow an amount of energy to leak through, in some phase relation to the energy diffracted at the edge, is a suggestion [6] that needs further study. To investigate this last possibility, a slit was placed in the reflector parallel to the cylindrical axis of a parabolic cylinder reflector antenna and near its edge. This slit allows field leakage in back directions and forms the basis for the work reported here.

To implement this geometry, we set out first to investigate the phase and amplitude transmission properties of various slits. There have been many treatises on the diffraction by planar slits, e.g. [7]-[13]. A slit in a parabolic cylinder reflector would differ from planar slits because the forming planes on either side of the slit do not share the same plane as the gap between them. Transmission through non-planar slits has also been considered in the past [14]-[16], using the variational

principle and Kirchhoff integrals for relatively wide slits. (We thank the reviewers for bringing these references to our attention). The approach adopted in the present work is similar to GTD in that we consider the slit as a result of two edges and not as an aperture as in the Kirchhoff approximation.

In this paper, in addition to the amplitude, we also determine the relative phase of the transmitted fields. Thus, in the analyses that follow the slit in a parabolic cylinder is approximated by an aperture formed by two inclined planes and we investigate the effects on transmitted fields of the aperture size of the slit and the relative inclinations of the planes which form it. The theoretical results are compared with experiment.

THEORY

Figure 1 shows a slit with inclined planes. In this figure, η_1 and η_2 are the angles of inclination of planes Σ_1 and Σ_2 with respect to the aperture plane of the slit. Both η_1 and η_2 are positive when the planes are inclined towards the source, and are negative when the planes are inclined away from the source. Two image sources occur, one for each plane. In the case $\eta_1 = \eta_2 = 0$, the images coincide.

Born and Wolf [17] describe diffraction by a half plane of fields generated by a cylindrical line source. Following the reasoning of Keller [12], a slit can be thought of as a pair of half planes brought close together. Thus the diffraction by a slit can be initially described as the independent superposition of the two individual diffractions by the half planes.

In this work the half-plane edges are assumed to be line sources with certain pattern factors as in GTD. The main difference between this approach and (Keller's) GTD is that the diffracted field representation uses a Fresnel Integral similar to the classical Sommerfeld solution while

Keller uses only the first term in the asymptotic expansion of the Fresnel Integral. As a result the diffraction coefficients do not exhibit singularities at reflection and shadow boundaries.

In the present approach to the slit diffraction, a source geometrical optics term is included allowing the observation point to be positioned anywhere - providing the source is more than one wavelength away from the slit [17]. In the Keller theory the probe must be placed at relatively large distances away from the slit.

Assume that the electric field is parallel to the edges and that the exponential time dependence, $\exp(+j\omega t)$, is suppressed. Then the addition of the effects of two half-plane diffracted fields, as found from Born and Wolf, produces (neglecting interaction between the half planes):

$$E_T = E_S + D_1 + D_2 \,, \tag{1}$$

where (see Fig. 1),

$$\begin{aligned} E_S &= 0 \qquad \text{in Region E} \\ &= \frac{e^{-jkr_{SP}}}{(8\pi jkr_{SP})^{1/2}} \qquad \text{in Region H} \\ &= 0 \qquad \text{in Region G} \end{aligned} \tag{2}$$

D_1 is the diffracted field from the edge of half plane Σ_1

D_2 is the diffracted field from the edge of half plane Σ_2 .

Where D_1 and D_2 are defined as,

$$D_1 = \frac{-e^{-j(kr_{Q1P}-\pi/4)}}{(8\pi jk(r_{Q1P}+r_1+r_{1P}))^{1/2}} \cdot F[k(r_1+r_{1P}-r_{Q1P})]$$

$$-B_1 \cdot \frac{e^{-j(kr_{SP}-\pi/4)}}{(8\ jk(r_{SP}+r_1+r_{1P}))^{1/2}} \cdot F[k(r_1+r_{1P}-r_{SP})] \tag{3}$$

$B_1 = -1$ for P in region E

$= +1$ for P in regions H, G,

and similarly,

$$D_2 = \frac{-e^{-j(kr_{Q2P}-\pi/4)}}{(8\ jk(r_{Q2P}+r_2+r_{2P}))^{\frac{1}{2}}} \cdot F[k(r_2+r_{2P}-r_{Q2P})]$$

$$-B_2 \cdot \frac{e^{-j(kr_{SP}-\pi/4)}}{(8\ jk(r_{SP}+r_2+r_{2P}))^{\frac{1}{2}}} \cdot F[k(r_2+r_{2P}-r_{SP})] \qquad (4)$$

$B_2 = -1$ for P in region G

$= +1$ for P in regions E,H

and

$$F[\gamma] = \frac{1-j}{\sqrt{2}} - \int_0^{\gamma} \frac{e^{-jt}}{\sqrt{t}}\, dt \qquad (5)$$

Previous work [18] has shown that multiply diffracted rays are only significant for aperture sizes smaller than two wave-lengths.

As usual, in a multiple diffraction formulation, we assume that the edges of a slit act as secondary sources of waves, which are then diffracted at the opposite edge. One cross-slit term is often found sufficient to provide a good approximation to the diffraction pattern, although all cross-slit terms can be calculated. The scattered field where cross-slit terms are taken into account will be derived now.

Figure 2 shows the sources, S_1 and S_2 at edges of planes Σ_1 and Σ_2, along with the corresponding image sources I_1 and I_2.

Now, define:

R_1 as the source strength of S_1 at edge 1 towards edge 2, caused by source S.

R_2 as the source strength of S_2 at edge 2 towards edge 1, caused by source S.

C_1 as the field at P from S_2 on edge 2 which is diffracted off edge 1.

C_2 as the field at P from S_1 on edge 1 which is diffracted off edge 2.

V_1 as the source strength from edge 1 diffracted towards edge 2, caused by a source S_2 on edge 2.

V_2 as the source strength from edge 2 diffracted towards edge 1, caused by a source S_1 on edge 1.

From the above definitions a ray which travels a path from the source, via edge 1, then edge 2 to P would be described as R_1C_2, and thus multiple diffraction can be described.

The total field beyond the slit is a sum of the contributions from each edge, and can be described as

$$E_T = E_S + D_1 + D_2 + \frac{C_1(R_2+R_1V_2)}{(1-V_1V_2)} + \frac{C_2(R_1+R_2V_1)}{(1-V_1V_2)} \tag{6}$$

where

$$R_1 = \left\{ \frac{-e^{-j(kr_{Q1Y}-\pi/4)}}{\sqrt{8\pi jk(r_{Q1Y}+r_{1Y}+r_1)}} \cdot F[k(r_{1Y}+r_1-r_{Q1Y})] \right.$$

$$\left. - \frac{e^{-j(kr_{SY}-\pi/4)}}{\sqrt{8\pi jk(r_{SY}+r_{1Y}+r_1)}} \cdot F[k(r_{1Y}+r_1-r_{SY})] \right\} \cdot \frac{\sqrt{8\pi jkr_{1Y}}}{e^{-jkr_{1Y}}} \tag{7}$$

where Y is an 'arbitrary' field point in the aperture plane as shown in Fig. 2. The field is evaluated at Y and then the source field strength is found, assuming that the diffracted field has a cylindrical dependence. In computations it has been assumed that the points Y and Z are 6 wavelengths from the slit centre. Also

$$R_2 = \left\{ \frac{-e^{-j(kr_{Q2Z}-\pi/4)}}{\sqrt{8\pi jk(r_{Q2Z}+r_{2Z}+r_2)}} \cdot F[k(r_{2Z}+r_2-r_{Q2Z})] \right.$$

$$\left. - \frac{e^{-jkr_{SZ}-\pi/4)}}{\sqrt{8\pi jk(r_{SZ}+r_{2Z}+r_2)}} \cdot F[k(r_{2Z}+r_2-r_{SZ})] \right\} \cdot \frac{\sqrt{8\pi jkr_{2Z}}}{e^{-jkr_{2Z}}} \tag{8}$$

and

$$C_1 = \frac{-e^{-j(kr_{I2P}-\pi/4)}}{\sqrt{8\pi jk(r_{I2P}+C+r_{1P})}} F[k(r_{1P}+C-r_{I2P})] - \frac{e^{-j(kr_{2P}-\pi/4)}}{\sqrt{8\pi jk(r_{2P}+C+r_{1P})}} F[k(r_{1P}+C-r_{2P})] \tag{9}$$

$$C_2 = \frac{-e^{-j(kr_{I1P}-\pi/4)}}{\sqrt{8\pi jk(r_{I1P}+C+r_{2P})}} F[k(r_{2P}+C-r_{I1P})] - \frac{e^{-j(kr_{1P}-\pi/4)}}{\sqrt{8\pi jk(r_{1P}+C+r_{2P})}} F[k(r_{2P}+C-r_{1P})] \tag{10}$$

$$V_1 = \left\{\frac{-e^{-j(kr_{I2Y}-\pi/4)}}{\sqrt{8\pi jk(r_{I2Y}+C+r_{1Y})}} F[k(r_{1Y}+C-r_{I2Y})] - \frac{e^{-j(kr_{2Y}-\pi/4)}}{\sqrt{8\pi jk(r_{2Y}+C+r_{1Y})}} F[k(r_{1Y}+C-r_{2Y})]\right\} \cdot \frac{\sqrt{8\pi jkr_{1Y}}}{e^{-jkr_{1Y}}} \tag{11}$$

$$V_2 = \left\{\frac{-e^{-j(kr_{I1Z}-\pi/4)}}{\sqrt{8\pi jk(r_{I1Z}+C+r_{2Z})}} F[k(r_{2Z}+C-r_{I1Z})] - \frac{e^{-j(kr_{1Z}-\pi/4)}}{\sqrt{8\pi jk(r_{1Z}+C+r_{2Z})}} F[k(r_{2Z}+C-r_{1Z})]\right\} \cdot \frac{\sqrt{8\pi jkr_{2Z}}}{e^{-jkr_{2Z}}} \tag{12}$$

Thus for parallel polarization equations (7) to (12), in combination with equations (2), (3), and (4) can be used to evaluate equation (6), and in the case of perpendicular polarization, add rather than subtract the two terms in Equations (3), (4) and (7) to(12).

It should be noted that it is assumed that the probe is not within a secondary reflection region, where reflections of a secondary edge source off the opposite plane would need to be taken into account. The above situation does not occur in the experiment presented in this paper.

If the probe does enter such region, the signs of the first terms in Equations (9) to (12) need to be changed, and a reflection term from S_1 or S_2 needs to be incorporated. Tan, [16]-[18], has shown, experimentally, that these reflections will affect the transmission, especially from $\eta_1 = \eta_2 = -45^\circ$ to $\eta_1 = \eta_2 = -90^\circ$.

Equation (6) describes the field diffracted by a slit for the case of the incident wave provided by a single cylindrical source. In the actual experiment we used a sectoral horn source whose aperture distribution was approximated by an array of five line sources with a cosinusoidal amplitude array pattern and a square law phase pattern [19]. The electrical field

in the aperture of the horn used in the theoretical verification of the experiment was assumed to be:

$$E_H = A \cos\left(\frac{\pi y}{a}\right) \cdot e^{-jky^2/2\ell_1}, \tag{13}$$

where

A is an arbitrary constant

a is the aperture width of the horn in the H plane

y a cartesian axis across the width of the aperture,

and y=0 is at the centre

ℓ_1 is the length of the sectoral horn

and each source strength, in the case of five sources, is then given by

$$E_{HN} = A \cos\left(\frac{\pi(N-3)}{6}\right) \cdot e^{-jk[a(N-3)/6]^2/2\ell_1}, \tag{14}$$

for N=1,2,3,4,5.

To modify the cylindrical description into a horn description requires the summation of the diffracted fields caused by the sources described in Equation (14), i.e.,

$$E_T^{HORN} = \sum_{N=1}^{5} E_{HN} \times \left\{E_S^N + D_1^N + D_2^N + \frac{C_1^N(R_2^N+R_1^N V_2^N)}{(1-V_1^N V_2^N)} + \frac{C_2^N(R_1^N+R_2^N V_1^N)}{(1-V_1^N V_2^N)}\right\} \tag{15}$$

Where the superscript, N, implies that the distances associated with each source need to be calculated individually.

Equation (15) was used to calculate the diffraction patterns covered by the experiment. In the case of a parallel plane slit, these results can be checked by the use of Mathieu functions, [10],[20]. The exact or Mathieu function solution is for a cylindrical source. The field diffracted by the slit for the case of the horn excitation is approximated by the use of the factors in Equation (14). Each cylindrical diffraction pattern is multiplied by an appropriate term in Equation (14) and then summed to produce the horn diffraction.

Figure 3 shows a comparison of the amplitude and phase of the transmitted fields for slit widths ranging from 1/6th of the wavelength to two wavelengths. The probe point is 9.15 wavelengths away from the slit centre. It can be seen that the intensities of fields obtained by the two theories match closely, while phase angle differences occur for slit widths of a third of a wavelength or less. It should be noted that in the derivation of Equations (6) and (15) the slit edges were assumed to be in each others far fields. Thus for narrow slits the analytical results would be expected to show divergences from measured values. While the exact field representation is very time-consuming to compute, as the Mathieu functions are calculated by a slowly convergent series, calculations for up to two wavelength slit widths can be reasonably accomplished using an algorithm developed by Clemm [21].

EXPERIMENTAL

A parallel plate range was used to measure the electric fields behind the slits. The planes of the wave guide range were spaced within one half of a wavelength apart to ensure that the wave within the range was confined to the TEM mode with the E-plane perpendicular to the planes of the guide, [13],[22], [23]. This limits measurements to polarizations parallel to slits. The planes were spaced by wedges made of Jelutong timber, without any coatings. In a rectangular waveguide such a wedge was found to have a VWSR of 1.04. The wedge shaping is unusual, with wedges at both ends. These wedges give low reflectivity, while attenuation in the timber further reduces the reflected wave from the distant edge.

An untuned probe is allowed to slide over a distance of 60cm on a T shaped bar 56λ away from, and at right angles to, the horn axis.

The reflecting planes were made of pieces of printer's lithoplate, bent into a square C shape and placed about 47λ away from the horn source.

The metal bent easily but was rigid enough to remain in contact with both planes of the guide. The thickness of the lithoplate was 0.31mm, i.e. about one hundredth of a wavelength at the operating frequency, (9.12 GHz).

Both intensity and phase of the transmitted field were measured by the use of a Homodyne Detection System [24]. This system allows one to accurately measure intensity over a dynamic range of 60db, and can be used to measure phase change to within 1 degree.

THEORETICAL AND EXPERIMENTAL RESULTS

Field distributions were measured for various combinations of η_1 and η_2 varying between $+20^\circ$ to -20°, and for slit widths between one sixth of a wavelength and two wavelengths. (These results are available on request from the authors).

Figures 3, 4, and 5 show how experimental results compare with theory. In Figure 3, the experimental data is depicted together with results obtained from equation (15) and the exact solution. The theory developed correlates well with the exact formulation and the experiment over a wide range of slit widths. The main difference between experimental results and those obtained using the approximate theory occur in the phases for slit widths less than one third of a wavelength.

The transmission from a slit with $\eta_1 = \eta_2 = 20^\circ$ is indicated in Fig. 4. Variations between measured and calculated phase are apparent for slit widths less than 1/3rd of a wavelength. These phase errors may be attributed to the theory. The measured electric field intensity follows the calculated intensities quite well. Note how transmission calculated using equation (1) is inaccurate for slit widths less than one and a half wavelengths.

The experimental results for two slits,

$$\eta_1 = \eta_2 = +20^\circ \text{ and } \eta_1 = \eta_2 = -20^\circ,$$

are compared in Figure 5. In the field intensity measurements the largest

variations occur at the smallest slit widths. The concave slit with $\eta_1 = \eta_2 = 20^\circ$ tends to channel more power through as compared with the convex slit. In this graph are also included the calculations for the same slits using Equation (15).

DISCUSSION AND CONCLUSIONS

From the data obtained for amplitude of transmission and phase it is clear that the approximate theory and experiment give comparable results over a wide range of slit widths. The theory is an extension of the half-plane diffraction theory of Born and Wolf, and is reasonably simple to use.

To apply the observed and computed results to the case of back radiation from a parabolic reflector, we need to be able to control both the phase and amplitude of the leaked wave. We have seen that the transmitted wave phase lag from a slit is controllable over the region 40° to 140°, but the price is a large variation of the transmitted field intensity. It may be possible to control the intensity independently of phase by the use of a pattern of relatively closely-spaced slits, which may be positioned to provide the correct phase with respect to the energy back-scattered from the reflector edges in predetermined directions. This is the next step in our programme.

Finally, we conclude that for wider slits the transmission is relatively unaffected by the angle of inclination of the reflection planes, and is more dependent upon the size of the aperture.

REFERENCES

[1] Morris, G; 'Coupling Between Closely Spaced Back-to-Back Paraboloidal Antennas', IEEE Trans. Antennas and Propagation, Vol. AP-28, No. 1, p.60, Jan. 1980.

[2] Cornbleet, S; 'Progress in Microwave Communication Antennas in the U.K.', Microwave J., Vol. 10, No. 12, p. 84, 1967.

[3] Lewin, L; 'Main-Reflector-Rim Diffraction in Back Direction', Proc. IEE, Vol. 119, p. 1100, 1972.

[4] James, G.L.; 'Electromagnetic Effects of Edges', Ph.D. Thesis, Electrical Engineering, University of Canterbury, 1973.

[5] Corona, P; D'amrosio, G; Franceschetti, G; 'Reflector Antennas with Very High Front-to-Back Ratio Theory and Experiment on Models', Proc. European Microwave Conference, Stockholm, Sweden, 23-28 August 1971.

[6] Sletten, C.J.; Blacksmith, P.; 'The Paraboloidal Mirror', Appl. Optics, Vol. 4, p. 1239, 1965.

[7] Asvestas, J.S.; Kleinman, R.E.; 'The Strip', in 'Electromagnetic and Acoustic Scattering by Simple Shapes', Bowman, et al, Eds. North-Holland Publishing Co., Amsterdam, p. 181, 1969.

[8] Karp, S.N.; Russek, A; 'Diffraction by a Wide Slit', J. Appl. Phys., Vol. 27, No. 8, p. 886, Aug. 1956.

[9] Menendez, R.C.; Lee, S.W.; 'On the Role of the Geometrical Optics Field in Aperture Diffraction', IEEE Trans. on AP, Vol. AP-25, No. 5, p. 688, Sept. 1977.

[10] Morse, P.M.; Rubenstein, P.J.; 'The Diffraction of Waves by Ribbons and by Slits', Physical Review, Vol. 54, p. 895, Dec. 1938.

[11] Yu, J.S.; Rudduck, R.C.; 'On Higher-Order Diffraction Concepts Applied to a Conducting Strip', IEEE Trans. AP, Vol. AP-15, No. 5, p. 662, Sept. 1967.

[12] Keller, J.B.; 'Diffraction by an Aperture', J. Appl. Phys., Vol. 28, No. 4, p. 426, April 1957.

[13] Hongo, K; Ishii, G.; 'Diffraction of an Electromagnetic Plane Wave by a Thick Slit', IEEE Trans. AP, Vol. AP-26, No. 3, p. 495, May 1978.

[14] Tan, H.S.; 'Some Results of the Variational Principle in Non-Planar Diffraction', Proc. Phys. Soc., Vol. 91, p. 248, 1967.

[15] Tan, H.S.; 'On Kirchhoff's Theory in Non-Planar Scalar Diffraction', Proc. Phys. Soc., Vol. 91, p. 768, 1967.

[16] Tan, H.S.; 'Diffraction by a Slit Aperture Formed by Two Inclined Surfaces', Aust. J. Phys., Vol. 21, p. 661, 1968.

[17] Born, M; Wolf, E; 'Principles of Optics', 1959, p. 577-581.

[18] Ryan, C.E.; 'A Geometrical Theory of Diffraction Analysis of the Radar Cross Section of a Sectionally Continuous Second Degree Surface of Revolution', Technical Report-2430-4, Electro Science Lab., Dept. of E.E., Ohio State University, March 1968.

[19] Compton, R.T. Jr.; Collin, R.E.; 'Open Waveguides and Small Horns', in 'Antenna Theory, part 1', Chapter 15, Collin, R.E.; Zucker, F.J.; Eds., McGraw-Hill, 1969.

[20] Hsu, H.P.; 'Aperture Fields in the Diffraction by a Slit', J. Appl. Phys., Vol. 31, No. 10, p. 1742, Oct. 1960.

[21] Clemm, D.S.; 'Characteristic Values and Associated Solutions of Mathieu's Differential Equation', Comms. A.C.M., Vol. 12, No. 7, p. 399, July 1969, and Correction Vol. 13, p. 750, 1970.

[22] Row, R.V.; 'Microwave Diffraction Measurements in a Parallel-Plate Region', J. Appl. Phys., Vol. 24, No. 12, p. 1448, Dec. 1953.

[23] Cumming, W.A.; 'Radiation Measurements at Radio Frequencies: A Survey of Current Techniques', Proc. IRE, Vol. 47, No. 5, p. 705, May 1959.

[24] King, R.J.; 'Microwave Homodyne Systems', Peregrinus Press, for the IEE, IEE Electromagnetic Waves Series 3, 1978.

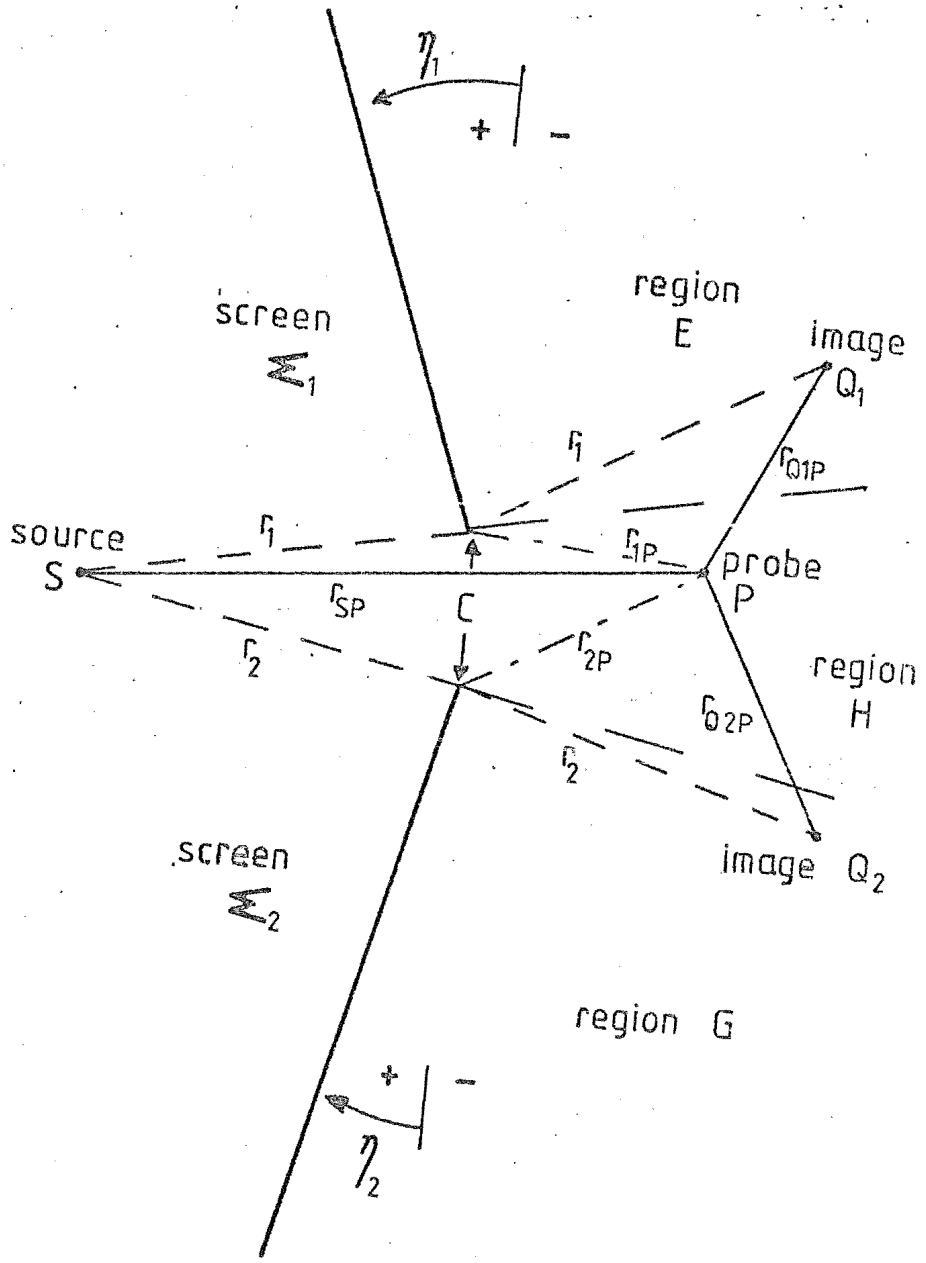
η_1
+
−
screen
Σ_1
region
E
image
Q_1
r_1
r_{Q1P}
source
S
r_1
r_{1P}
probe
P
r_{SP}
C
r_2
r_{2P}
region
H
r_{Q2P}
r_2
screen
Σ_2
image Q_2
region G
+
−
η_2

FIGURE 1

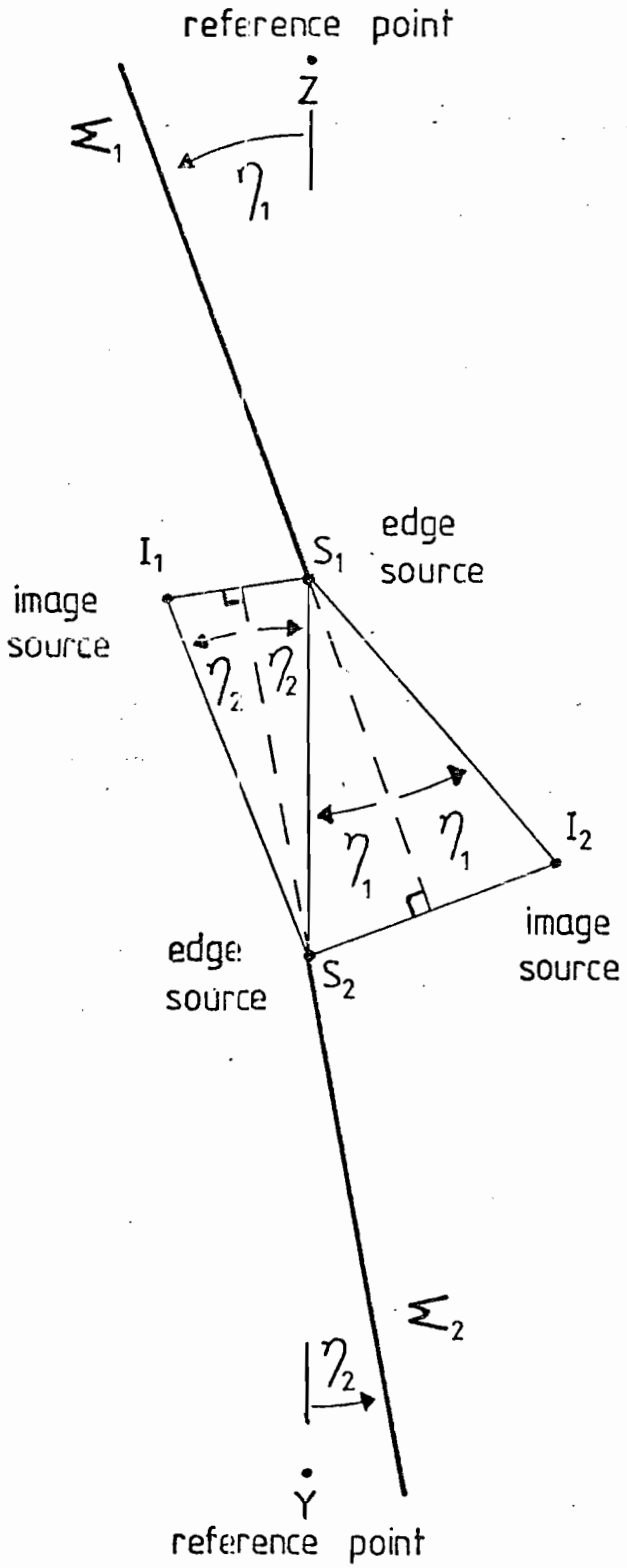
reference point
Z
Σ_1
η_1
I_1
S_1
edge source
image source
η_2
η_2
η_1
η_1
I_2
image source
edge source
S_2
Σ_2
η_2
Y
reference point

FIGURE 2

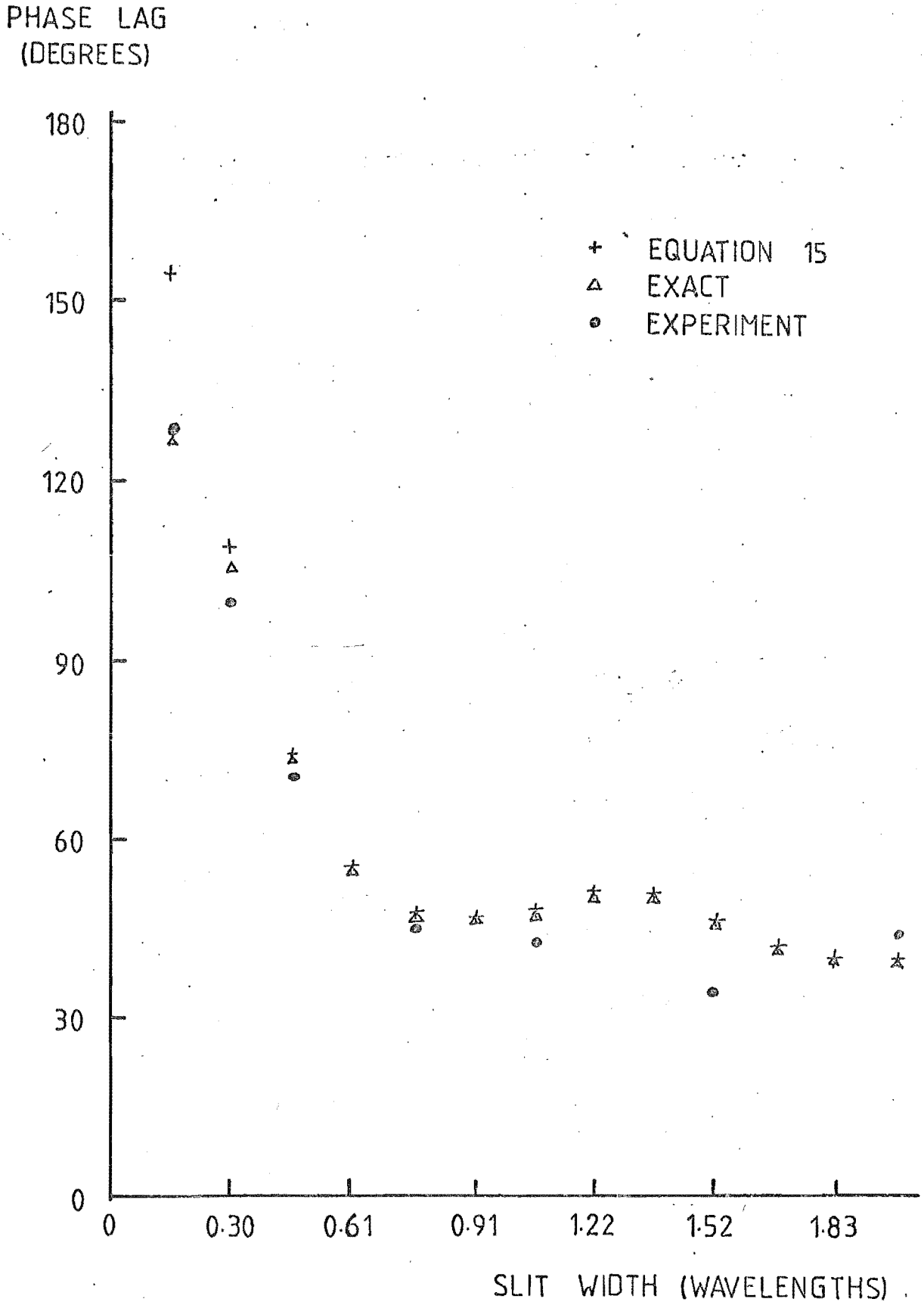
PHASE LAG
(DEGREES)
180
150
120
90
60
30
0
0
0·30
0·61
0·91
1·22
1·52
1·83
SLIT WIDTH (WAVELENGTHS)
EQUATION 15
EXACT
EXPERIMENT

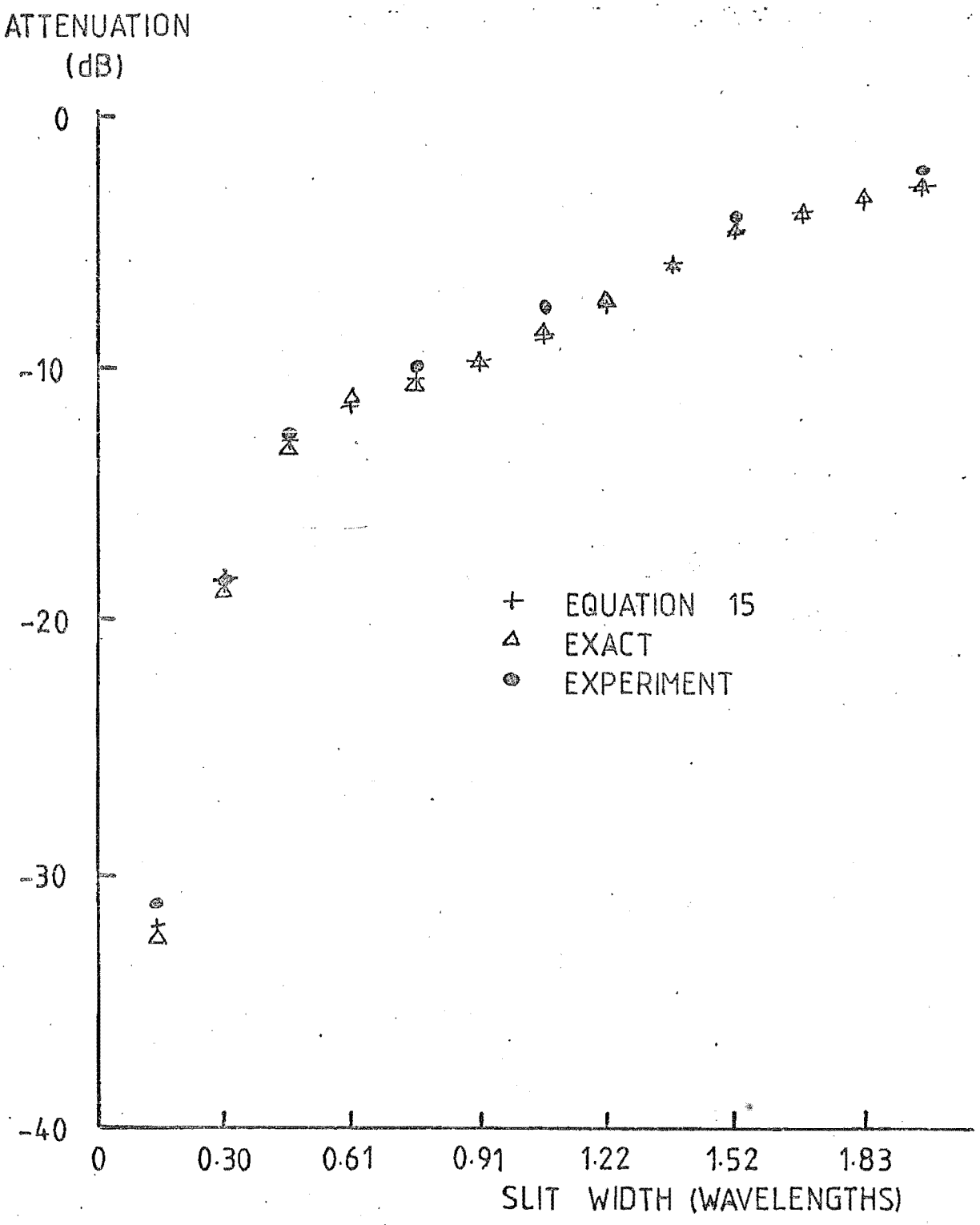
ATTENUATION
(dB)
0
-10
-20
-30
-40
0
0·30
0·61
0·91
1·22
1·52
1·83
SLIT WIDTH (WAVELENGTHS)
EQUATION 15
EXACT
EXPERIMENT

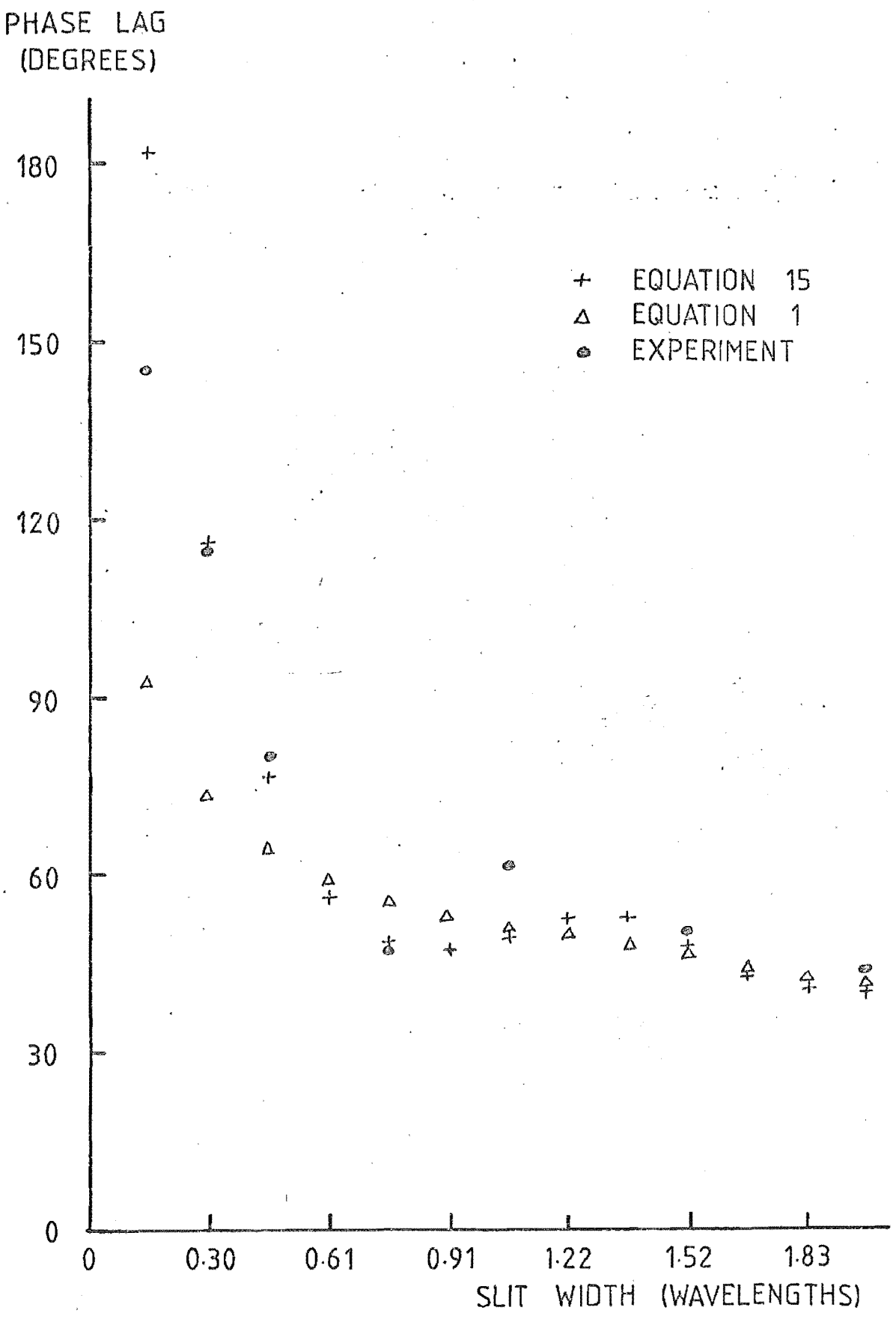
PHASE LAG
(DEGREES)
180
150
120
90
60
30
0
0
0·30
0·61
0·91
1·22
1·52
1·83
SLIT WIDTH (WAVELENGTHS)
EQUATION 15
EQUATION 1
EXPERIMENT

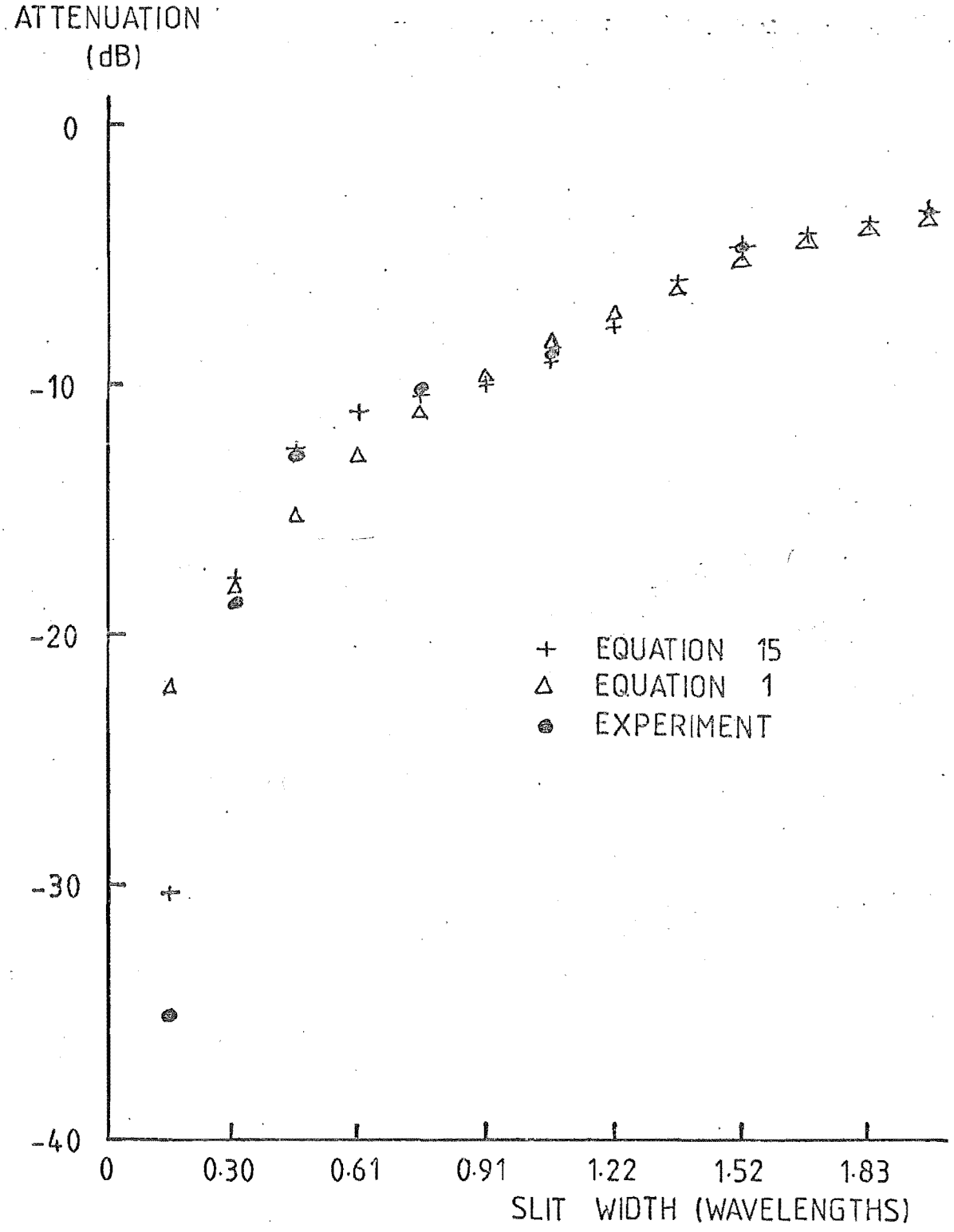
ATTENUATION
(dB)
0
-10
-20
-30
-40
0
0·30
0·61
0·91
1·22
1·52
1·83
SLIT WIDTH (WAVELENGTHS)
EQUATION 15
EQUATION 1
EXPERIMENT

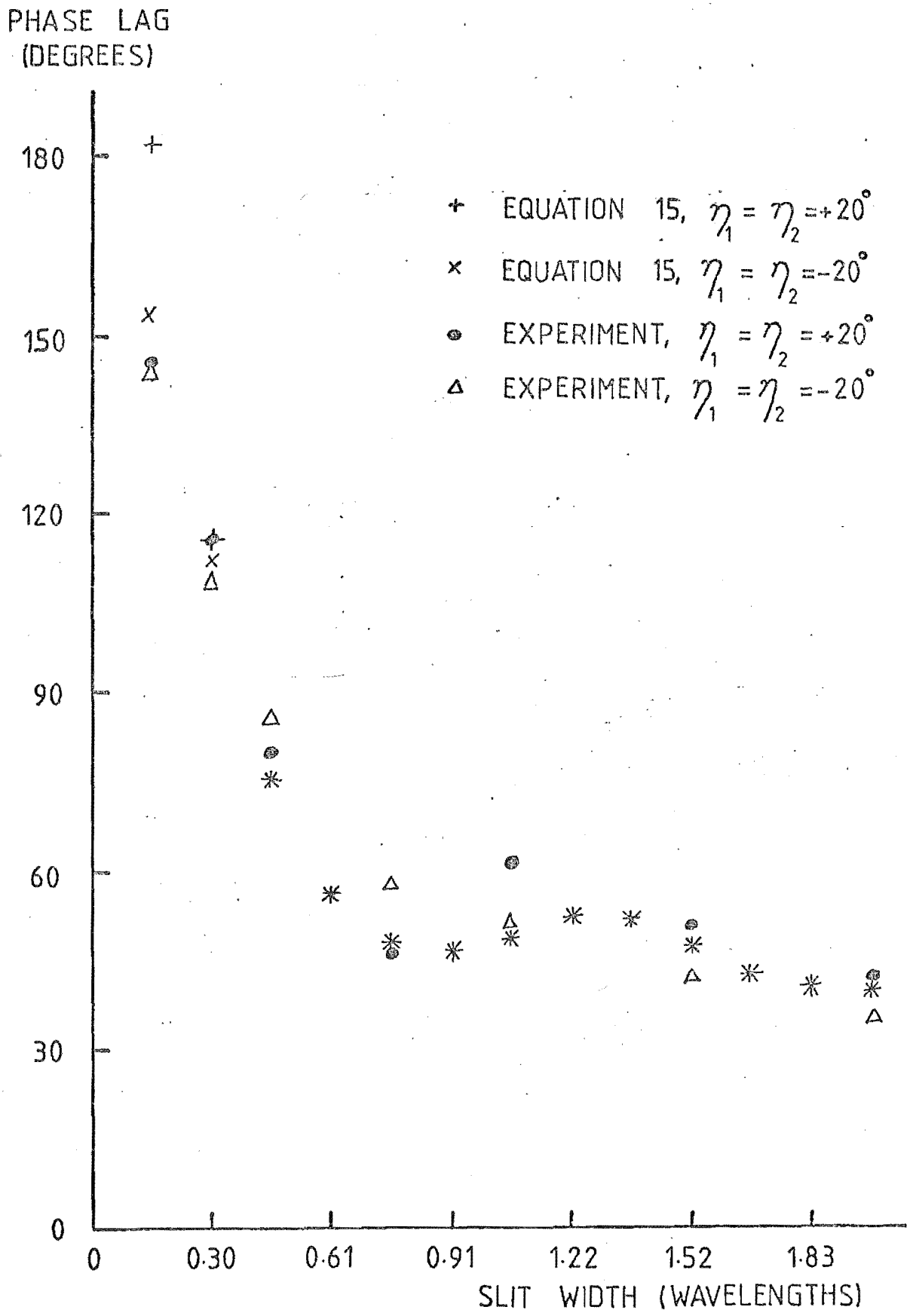
PHASE LAG
(DEGREES)
180
150
120
90
60
30
0
0
0·30
0·61
0·91
1·22
1·52
1·83
SLIT WIDTH (WAVELENGTHS)
EQUATION 15, $\eta_1 = \eta_2 = +20^\circ$
EQUATION 15, $\eta_1 = \eta_2 = -20^\circ$
EXPERIMENT, $\eta_1 = \eta_2 = +20^\circ$
EXPERIMENT, $\eta_1 = \eta_2 = -20^\circ$

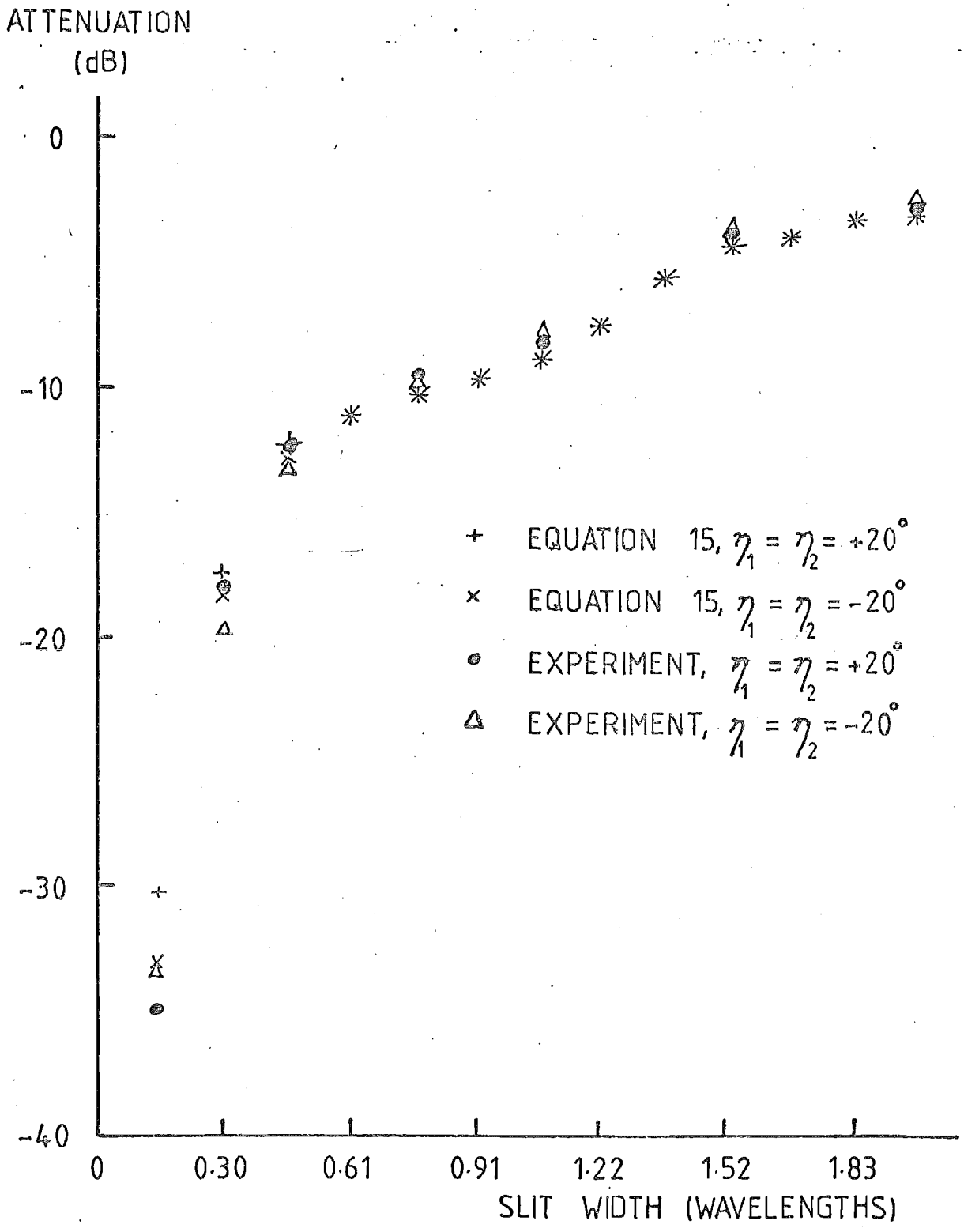
ATTENUATION
(dB)
0
-10
-20
-30
-40
0
0·30
0·61
0·91
1·22
1·52
1·83
SLIT WIDTH (WAVELENGTHS)
+ EQUATION 15, $\eta_1 = \eta_2 = +20^\circ$
× EQUATION 15, $\eta_1 = \eta_2 = -20^\circ$
EXPERIMENT, $\eta_1 = \eta_2 = +20^\circ$
EXPERIMENT, $\eta_1 = \eta_2 = -20^\circ$

LIST OF CAPTIONS FOR FIGURES

Figure 1 Slit with inclined planes.

Figure 2 Source location in cross-slit diffraction

Figure 3a Comparison of transmitted phase lag through a parallel plane slit, Equation 15, Exact and Experiment.

Figure 3b Comparison of transmitted intensity through a parallel plane slit, Equation 15, Exact, and Experment.

Figure 4a Comparison of transmitted phase lag through a concave inclined plane slit ($\eta_1=\eta_2=20^\circ$), Equation 15, Equation 1, Experiment.

Figure 4b Comparison of transmitted intensity through a concave inclined plane slit ($\eta_1=\eta_2=20^\circ$), Equation 15, Equation 1, Experiment.

Figure 5a Comparison of transmitted phase lag through concave and convex inclined plane slits, ($\eta_1=\eta_2=20^\circ$ and $\eta_1=\eta_2=-20^\circ$), Equation 15 and Experiment.

Figure 5b Comparison of transmitted intensity through concave and convex inclined plane slits, ($\eta_1=\eta_2=20^\circ$ and $\eta_1=\eta_2=-20^\circ$), Equation 15 and Experiment.

REFERENCES

AFFIFI, M.S. (1966)

'Radiation from the paraboloid of revolution', from 'Electromagnetic Wave Theory, Part 2', J. Brown, ed, Pergamon, Oxford, P 669.

AHLUWALIA, D.S.; LEWIS, R.M.; BOERSMA, J. (1968)

'Uniform asymptotic theory of diffraction by a plane screen', SIAM, J. Appl. Math, Vol 16, P 783.

ANDREASEN, M.G. (1964)

'Scattering from parallel metallic cylinders with arbitrary cross sections', IEEE Trans. on Antennas and Propagation, Vol AP-12, No 6, P 746.

ANDREASEN, M.G. (1965)

'Scattering from cylinders with arbitrary surface impedance', Proc IEEE, Vol 53, August, P 812.

AZARBAR, B.; SHAFAI, L. (1978)

'Application of Moment method to large cylinder reflector antennas', IEEE Trans. on Antennas and Propagation, Vol AP-26, No 3, P 500.

BECKMANN, P. (1968)

'The depolarization of electromagnetic waves', Golem, Colorado, P 105.

BLANCH, G. (1966)

'Numerical aspects of Mathieu Eigenvalues', Rend. Circ. Matem. Palermo, Series II, Vol 15, P 51.

BORN, M.; WOLF, E. (1959)

'Principles of Optics', 2nd Ed., Pergamon, Oxford, P 581.

BOUWKAMP, C.J. (1954)

'Diffraction Theory', Rep. Prog. Phys., Vol 17, P 35.

BOWMAN, J.J.; SENIOR, T.B.A.; USLENGHI, PLE. (1960)

'Electromagnetic and Acoustic Scattering by Simple Shapes', North-Holland, Amsterdam, Chapter 4, 'The Strip'.

BUCCI, O.M.; FRANCESCHETTI, G. (1980)

'Rim loaded reflector antennas', IEEE Trans on Antennas and Propagation, Vol AP-28, No 3, P 297.

BURNSIDE, W.D.; YU, C.L.; MARHEFKA, R.J. (1975).

'A technique to combine the Geometrical Theory of Diffraction and the Moment Method', IEEE Trans on Antennas and Propagation, Vol AP-23, No 4, P 551.

CASHMAN, J.D.; KOUYOUMJIAN, R.G.; PATHAK, P.H. (1977)

'Comments on "A uniform Geometrical Theory of Diffraction for an edge in a perfectly conducting surface"', IEEE Trans. on Antennas and Propagation, Vol AP-25, P 447.

CLEMM, D.S. (1969)

'Characteristic values and associated solutions of Mathieu's Differential Equations, Comms. ACM, Vol 12, No 7, P 396, and correction, Vol 13, P 750.

CLEMMOW, P.C. (1966)

'The Plane-Wave Spectrum Representation of Electromagnetic Fields', Pergamon, Oxford, P 82.

COHN, S.B.; WEINHOUSE, N.P. (1964)

'An automatic microwave phase-measurement system', Microwave J., Vol 7, No 2, P 49.

COLLIN, R.E.; ZUCKER, F.J.; EDS. (1969)

'Antenna Theory', Inter-University Electronics Series, Vol 7, McGraw-Hill, N.Y., Chapter 15.

CORNBLEET, S. (1967)

'Progress in microwave communication antennas in the U.K.', Microwave J., Vol 10, No 12, P 84.

CORONA, P.; D'AMROSIO, G.; FRANCESCHETTI, G. (1971)

'Reflector Antennas with very high front-to-back ratio, theory and experiment on models', Proc. European Microwave Conference, Stockholm, Sweden, 23-28 August.

CROSS, A.W. (Circa 1960)

'Experimental Microwaves', Sanders, P 170.

CUMMING, W.A. (1959)

'Radiation measurements at radio frequencies: A survey of current techniques', Proc IRE, Vol 47, No 5, P 705.

DONALDSON, E.E.; FREE, W.R.; ROBERTSON, D.W.; WOODY, J.A. (1978)

'Field measurements made in an enclosure', Proc IEEE, Vol 66, No 4, P 464.

DYSON, J.D. (1966)

'The measurement of phase at VHF and Microwave Frequencies', IEEE Trans on Microwave Theory and Techs., Vol MTT-14, No 9, P 410.

DYSON, J.D. (1973)

'Measurements of near fields of antennas and scatterers', IEEE Trans. on Antennas and Propagation, Vol AP-21, No 4, P 446.

EKELMAN, E.P.; THIELE, G.A. (1980)

'A hybrid technique for combining the Moment Method treatment of wire antennas with the GTD for curved surfaces', IEEE Trans on Antennas and Propagation, Vol AP-28, No 6, P 831.

FERGUSON, T.R.; LEHMAN, T.H.; BALESTRI, R.J. (1976)

'Efficient Solution of large moments problems: Theory and small problem results', IEEE Trans. on Antennas and Propagation, Vol AP-24, No 2, P 230.

HAMILTON, E.J.; KERDEMELIDIS, V. (1981)

'Transmission through slits formed by inclined planes', To be published in IEEE Trans on Antennas and Propagation.

HARRINGTON, R.F. (1967)

'Matrix methods for fields problems', Proc IEEE, Vol 55, No 2, P 136.

HARRINGTON, R.F. (1968)

'Field computations by Moment Methods', Macmillan Series in Electrical Science, Macmillan, N.Y., Chapter 3.

HSU, H.P. (1960)

'Aperture fields in the diffraction by a slit', J. Appl. Phys., Vol 31, No 10, P 1742.

INCE, E.L. (1932)

'Tables of the elliptic cylinder functions', Proc. Roy. Soc. Edinburgh, Vol 52, P 355.

JAGGARD, D.L.; KING, R.J. (1973)

'Sensitivity and dynamic range considerations for Homodyne Detection Systems', IEEE Trans. on Inst. and Meas., Vol IM-24, No 4, P 331.

JAMES, G.L. (1973)

'Electromagnetic Effect of Edges', PhD Thesis, University of Canterbury.

JAMES, G.L. (1976)

'Geometrical Theory of Diffraction for Electromagnetic Waves', Peregrinus, IEE Em waves series, No 1, London.

JAMES, G.L.; KERDEMELIDIS, V. (1973)

'Reflector antenna radiation pattern analysis by equivalent edge currents', Trans IEEE Antennas and Propagation, Vol AP-21, No 1, P 19.

JORDAN, E.C.; BALMAIN, K.G. (1968)

'Electromagnetic Waves and Radiating Systems', 2nd Edition, Prentice-Hall, N.J., P 177.

KARP, S.N.; KELLER, J.B. (1961)

'Multiple diffraction by an aperture in a hard screen', Optica Acta, Vol 8, No 1 PP 61.

KELLER, J.B. (1957)

'Diffraction by an aperture', J. Appl. Phys., Vol 28, No 4, P 426.

KELLER, J.B. (1962)

'Geometrical theory of diffraction', J. Opt. Soc. America, Vol 52, No 2, P 116.

KELLER, J.B.; LEVY, B.R. (1959)

'Decay exponents and diffraction coefficients for surface waves on surfaces of non-constant curvature; IRE Trans. on Antennas and Propagation, Vol AP-7, (Special Supplement) P S52.

KING, R.J. (1978)

'Microwave Homodyne Systems', Peregrinus, IEE Em waves series, No 3, London.

KNOP, C.M.; OSTERLAG, E.L. (1977)

'A note on the asymptotic Physical Optics solution to the scattered fields from a paraboloidal reflector', IEEE Trans. on Antennas and Propagation, Vol AP-25, No 4, P 531.

KOUYOUMJIAN, R.G. (1975)

'The Geometrical Theory of Diffraction and its application', Topics in Applied Physics, Vol 3; 'Numerical and Asymptotic Techniques in Electromagnetics', R. Mittra, ed, Springer-Verlag, N.Y., N.Y., P 167.

KOUYOUMJIAN, R.G.; PATHAK, P.H. (1974)

'Geometrical Theory of Edge Diffraction'; Proc IEEE, Vol 62, No 10, P 1438.

KRAUS, J.D. (1953)

'Electromagnetics', McGraw-Hill, NY, P 541.

KRITIKOS, H.N. (1963)

'The extended aperture method for the determination of shadow region radiation of parabolic reflectors', IEEE Trans. on Antennas and Propagation, Vol AP-11, No 4, P 400.

LEE, S.W.; DESCHAMPS, G.A. (1976)

'A Uniform Asymptotic Theory of electromagnetic diffraction by a curved wedge', IEEE Trans. on Antennas and Propagation, Vol AP-24, No 1, P 25.

LEEB, W. (1973)

'Diffraction by narrow slits', Applied Optics, Vol 12, No 12, P 2806.

LEWIN, L. (1972)

'Main-reflector-rim diffraction in back direction', Proc IEE., Vol 119, P 1100.

MACDONALD, H.M. (1902)

'Electric Waves', Cambridge University Press.

MACDONALD, H.M. (1915)

'A class of diffraction problems', Proc. London. Math. Soc., Vol XLVI, Jan 14, P 410.

MCLACHLAN, N.W. (1947)

'Theory and Application of Mathieu Functions', Oxford Press.

MEI, K.K.; VAN BLADEL, J.G. (1963a)

'Low frequency scattering by rectangular cylinders', Trans. IEEE on Antennas and Propagation, Vol AP-11, No 1, P 52.

MEI, K.K.; VAN BLADEL, J.G. (1963b)

'Scattering by perfectly conducting rectangular cylinders', Trans IEEE on Antennas and Propagation, Vol AP-11, No 2, P 183.

MENENDEZ, R.C.; LEE, S.W. (1977)

'On the role of the geometrical optics field in aperture diffraction', IEEE Transactions on Antennas and Propagation, Vol AP-25, No 5, P 688.

MILLAR, R.F. (1955)

'An approximate theory of the diffraction of an electromagnetic wave by an aperture in a plane screen' Proc IEE, Vol 103C, P 177.

MILLAR, R.F. (1956a)

'The diffraction of an electromagnetic wave by a circular aperture', Proc. IEE, Vol 104C, P 87.

MILLAR, R.F. (1956b)

'The diffraction of an electromagnetic wave by a circular aperture', Proc. IEE, Vol 104C, P 240.

MONTGOMERY, C.G. (1947a)

'Techniques of Microwave Measurements', MIT Radiation Laboratory Series, McGraw-Hill, NY, Chapter 10.

MONTGOMERY, C.G. (1947b)

Ibid, P 900

MORSE, P.M.; FESHBACH, H. (1953)

'Methods of Theoretical Physics', Parts 1 and 2, McGraw-Hill, NY.

MORSE, P.M.; RUBENSTEIN, P.J. (1938)

'The diffraction of waves by ribbons and by slits', Physical Review, Vol 54, P 895. Also see Leeb (1973).

MOULLIN, E.B. (1949)

'Radio Aerials', Clarendon Press, Oxford, P 199.

MOULLIN, E.B. (1954)

'On the current induced in a conducting ribbon by a current filament parallel to it', Proc IEE, Vol 101, Part IV, P 7.

MOULLIN, E.B.; PHILLIPS, F.M. (1952)

'On the current induced in a conducting ribbon by the incidence of a plane electromagnetic wave', Proc IEE, Vol 99, Part IV, P 137.

NEWSWEEK. (1980)

'Machines that think', a series of articles in the issue 30 June.

NIMURA, T.; SHIBAYAMA, K. (1951)

'The radiation impedance of ribbon type sound radiators and the vibromotive force on them', Rep. Res. Inst. Elect. Comm. Tohoku. University, Series B (Technology), Vol 3, No 1, P 77.

PLONSEY, R. (1958)

'Diffraction by cylindrical reflectors', Proc IEE, Vol 105, Part C, P 312.

PLONUS, M.A.; WILLIAMS, R.; WANG, S.C.H. (1978)

'Radar cross section of curved plates using geometrical and physical diffraction techniques', IEEE Trans. on Antennas and Propagation, Vol AP-26, No 3, P 488.

POUND, R.V. (1948)

'Microwave Mixers', MIT Radiation Laboratory Series, McGraw-Hill, N.Y., Sections 6.5 and 6.6, P 269.

RAHMAT-SAMII, Y.Y.; MITTRA, R. (1977)

'A spectral domain interpretation of high frequency diffraction phenomena', IEEE Trans. on Antennas and Propagation, Vol AP-25, No 5, P 676.

RICHMOND, J.H. (1965a)

'Scattering by a dielectric cylinder of arbitrary cross section shape', IEEE Trans. on Antennas and Propagation, Vol AP-13, No 3, P 334.

RICHMOND, J.H. (1965b)

'Digital computer solutions of the rigorous equations for scattering problems', Proc IEEE, Vol 53, No 8, P 796.

ROSS, R.A. (1966)

'Radar cross section of rectangular flat plates as a function of aspect angle', IEEE Trans on Antennas and Propagation, Vol AP-14, No 3, P 329.

ROW, R.V. (1954)

'Microwave diffraction measurements in a parallel-plate region', J. Appl. Phys., Vol 24, No 12, P 1448.

RUBINOWICZ, A. (1938)

'On the anomalous propagation of phase in the focus', Physical Review, Vol 54, P 931.

RUSCH, W.V.T. (1975)

'Reflector Antennas', Topics in Applied Physics, Vol 3; 'Numerical and Asymptotic Techniques in Electromagnetics', R. Mittra, ed, Springer-Verlag, N.Y.

RUSCH, W.V.T.; LUDWIG, A.C. (1973)

'Determination of the maximum scan-gain contours of a beam-scanning paraboloid and their relation to the Petzval Surface', IEEE Trans. on Antennas and Propagation, Vol AP-21, No 2, P 141.

RUSCH, W.V.T.; SØRENSEN, O. (1975)

'The Geometrical Theory of Diffraction for axially symmetric reflectors', IEEE Trans. on Antennas and Propagation, Vol AP-23, No 3, P 414.

RYAN, C.E. (1968)

'A Geometrical Theory of Diffraction analysis of the radar cross section of a sectionally continuous second degree surface of revolution', Technical Report-2430-4, Ohio State University, Electro Science Lab., Dept. of Electrical Engineering.

SILVER, S. (1949)

'Microwave Antenna Theory and Design', MIT Radiation Laboratory Series, McGraw-Hill, NY.

SLETTEN, C.J.; BLACKSMITH, P. (1965)

'The paraboloid mirror', Applied Optics, Vol 4, No 10, P 1239.

SMITH, B.A. (1974)

'Some Methods of Selectively Reducing Back Radiation in Parabolic Reflector Antennas', M.E. Thesis, University of Canterbury, 1974.

SOMMERFELD, A. (1954)

'Optics', Academic Press, N.Y., P 246.

STRATTON, J.A. (1941)

'Electromagnetic Theory', McGraw-Hill, N.Y. P 54.

STRATTON, J.A.; MORSE, P.M.; CHU, L.J.; HUNTER, R.A. (1941)

'Elliptic cylinder and spheroidal wave functions', M.I.T. Press, J. Wiley.

TAN, H.S. (1967a)

'Some results of the variation principle in non-planar diffraction', Proc. Phys. Soc., Vol 91, P 248.

TAN, H.S. (1967b)

'On Kirchoff's Theory in non-planar scalar diffraction', Proc. Phys. Soc., Vol 91, P 768.

TAN, H.S. (1968)

'Diffraction by a slit aperture formed by two inclined surfaces', Aust. J. Phys., Vol 21, P 661.

TAUB, H.; SCHILLING, D.L. (1971)

'Principles of Communication Systems', McGraw-Hill, Kogakusha, Tokyo.

THIELE, G.A.; NEWHOUSE, T.H. (1975)

'A hybrid technique for combining Moment Methods with the Geometrical Theory of Diffraction', IEEE Trans. on Antennas and Propagation, Vol AP-23, No 1, P 62.

TSAI, L.L.; WILTON, D.R.; HARRISON, M.G.; WRIGHT, R.H. (1972)

'A comparison of Geometrical Theory of Diffraction and integral equation formulation for analysis reflector antennas', IEEE Transactions on Antennas and Propagation, Vol AP-20, No 6, P 705.

UFIMTSEV, P. Ya (1962)

'Method of edge waves in the Physical Theory of Diffraction', Report FTD-HC-23-259-71, National Technical Information Service.

VAN BLADEL, J.G. (1977)

'Low-Frequency asymptotic techniques', Chapter 1 of 'Modern Topics in Electromagnetics and Antennas', Peregrinus.

VON HIPPEL, A.R.. (Ed). (1954)

'Dielectric Materials and Applications', Technology Press of the MIT, Wiley, N.Y., P 334.

WATERMAN, P.C. (1965)

'Matrix formulation of Electromagnetic scattering', Proc. IEEE, Vol 53, No 8, P 805.